Endwall Contouring Using Numerical Optimization in Combination with the Ice Formation Method

A thesis accepted by the Faculty of Aerospace Engineering and Geodesy of the University of Stuttgart in partial fulfillment of the requirements for the degree of Doctor of Engineering Sciences (Dr.-Ing.)

by
Dipl.-Ing. Sven Winkler
born in Waldshut, Germany

Committee chair:	Prof. Dr.-Ing. habil. Bernhard Weigand
Committee member:	Prof. Phillip M. Ligrani, Ph.D.
Date of defence:	May 9, 2016

Institute of Aerospace Thermodynamics
University of Stuttgart
2016

To my parents Josef and Sonja,
my brother Jens,
and my love Julia

Acknowledgements

I am very grateful to Prof. Dr.-Ing. habil. Bernhard Weigand for giving me the opportunity to carry out this work at ITLR and for his constant support throughout this endeavor. His enthusiasm for this project and his inherently positive attitude provided a very pleasant working environment which I deemed greatly valuable for performing my work.

Moreover, I am also very thankful to Prof. Philipp M. Ligrani, Ph.D., for our cooperation during the last years and for being the co-referee of my work.

Special thanks go also to my project partner Kristian Haase who not only provided me with ice contours from his experiments but also has been a reliable colleague and friend throughout my time at ITLR.

In addition, I gratefully acknowledge the financial support of the Deutsche Forschungsgemeinschaft (DFG) and the Forschungsvereinigung Verbrennungskraftmaschinen e.V. (FVV) for this project. I would also like to thank the working group which accompanied our project and consulted us from an industrial point of view. In this respect, I would especially like to thank Dr. Ewald Lutum and Stefanie Jost-Köstering for their technical and organizational management.

Furthermore, I would like to thank my students who contributed their student works to our project: Andreas Grybos, Ryusuke Daniel Kambara Martin, Gabriele Frank, Janosch Brucker, Anton Kierig, Rostyslav Lyulinetskyy, and Timon Hitz.

I would also like to thank all my colleagues at ITLR, from whom many have become good friends over the years, for the great working environment and the good discussions about professional issues and beyond. I enjoyed the time at the institute very much and it has created some very valuable memories.

The greatest thanks of all go to my family, especially to my parents, my brother and my beloved Julia. You gave me the encouragement and strength necessary to carry out this endeavor and your support made many things much easier.

Stuttgart, May 2016 Sven Winkler

Contents

List of Figures **xi**

List of Tables **xvii**

Nomenclature **xix**

Abstract **xxv**

Kurzfassung **xxvii**

1 Introduction **1**
1.1 Motivation . . . 2
1.2 The Ice Formation Method: A Review . . . 3
1.3 State of the Art in Turbine Endwall Contouring . . . 6
1.4 Objectives and Thesis Outline . . . 9

2 Theoretical Background **11**
2.1 The Ice Formation Method . . . 12
2.2 Secondary Flows in Guide Vane Passages . . . 15
2.3 Governing Equations of Fluid Dynamics . . . 18
2.4 Numerical Methods . . . 19
2.4.1 Grid Generation . . . 20
2.4.2 Finite Volume Method . . . 21
2.4.3 Assessment of Numerical Errors . . . 25
2.5 Turbulence Modeling . . . 26
2.5.1 Reynolds-Averaged Navier-Stokes Equations . . . 26
2.5.2 Turbulence Models . . . 27
2.6 Numerical Optimization . . . 33
2.6.1 The NSGA-II . . . 33

2.6.2 Endwall Geometry Creation . . . 38
2.7 Parameters for Results Evaluation . . . 41

3 Methodology **45**
3.1 Experimental Setup . . . 46
3.1.1 Vane Profile . . . 46
3.1.2 Test Facility and Experiments . . . 47
3.2 Numerical Setup . . . 49
3.2.1 Flat Endwall Baseline . . . 49
3.2.2 Ice Contours . . . 54
3.2.3 Numerical Optimization . . . 57
3.3 Considered Cases . . . 60
3.3.1 Ice Contours - Short Cooling Length . . . 61
3.3.2 Ice Contours - Long Cooling Length . . . 64
3.3.3 Numerical Optimization from Flat Endwall . . . 64

4 Results Ice Contours Short Cooling Length **67**
4.1 Flat Endwall Baseline . . . 68
4.2 Ice-contoured Endwalls . . . 72
4.2.1 Heat Transfer . . . 72
4.2.2 Entropy Production . . . 84
4.3 Endwall Contours from Numerical Optimization . . . 88
4.3.1 Reducing Global Endwall Heat Transfer . . . 88
4.3.2 Reducing Vane Passage Endwall Heat Transfer . . . 93

5 Results Other Cases **99**
5.1 Ice Contour Long Cooling Length . . . 100
5.1.1 Heat Transfer . . . 101
5.1.2 Flow Field . . . 102
5.2 Optimization from Flat Endwall Baseline . . . 108

6 Results at Design Reynolds Number **117**
6.1 Flat Endwall Baseline . . . 118
6.2 Ice Contours Short Cooling Length . . . 119
6.2.1 Ice-contoured Endwalls . . . 119
6.2.2 Optimized Endwall Contour OC_{IFM} . . . 124
6.3 Optimization from Baseline . . . 124

7 Conclusion and Outlook **127**

Bibliography **131**

A Appendix **I**
A.1 NSGA-II Operators . . . II
A.1.1 Binary Tournament Selection . . . II

A.1.2 Simulated Binary Crossover (SBX) Operator III
A.1.3 Mutation Operator IV
A.2 Grid Convergence Index V
A.3 Long Copper Inlay VIII
A.4 Non-dimensional Temperature Ratio VIII
A.5 Sutherland's Law IX
A.6 Validation endwall heat transfer IX
A.7 Ice Contours Short Cooling Length X
A.7.1 $Re_C = 34{,}000$ X
A.7.2 $Re_C = 49{,}900$ XI
A.7.3 $Re_C = 71{,}400$ XII
A.8 Entropy Production Rates XIII
A.8.1 $Re_C = 34{,}000$ XIII
A.8.2 $Re_C = 71{,}400$ XIII
A.9 Contour Optimized with Respect to Vane Passage Heat Tranfer . . . XIV
A.9.1 Bézier Curves after Optimization XIV
A.9.2 Average Heat Transfer Coefficients XV
A.10 Optimized Endwall Contour OC_{BSL} XVI
A.10.1 Bézier Curves after Optimization XVI
A.10.2 Average Heat Transfer Coefficients XVII
A.11 Optimized Endwall Contour $OC_{BSL,2}$ XVIII
A.11.1 Bézier Curves after Optimization XVIII
A.11.2 Average Heat Transfer Coefficients XX
A.12 Overview of Created Endwall Contours XXI
A.13 Publications and Related Work XXIII

List of Figures

1.1 Combustion chamber with flat turbine inlet temperature profile 3
1.2 Bowley's elbow with initial geometry and ice-contoured geometry [40] . 4
1.3 Carlson's cylinder in crossflow with initial cooled cylinder and cylinder with ice [13] and the ice contour at a cylinder endwall junction from LaFleur and Langston [44] 4
1.4 Original Energy Efficient Engine (E3) endwall geometry and ice-contoured E3 endwall by LaFleur et al. [45] 5
1.5 Separating web of a 180° bend: Experimental ice contour and numerically optimized geometry from Zehner et al. [82, 83] 6
1.6 Contoured endwalls of Harvey et al. [29], Brennan et al. [12], and Nagel and Baier [59] 7
1.7 Optimized endwall contour for Pack-B airfoil, from Praisner et al. [65] . 7
1.8 Endwall contour for symmetric airfoils from Laveau et al. [50] and optimized contour for vane endwall from Saha and Acharya [68] 8
1.9 Heat transfer optimized endwall contour of Panchal et al. [62] 9

2.1 Ice formation in planar channel flow 12
2.2 Dimensionless ice-layer profiles for planar channel flow; data from [74] . 14
2.3 Formation of horseshoe vortex at cylinder on endwall, after [8] 15
2.4 Flow features in guide vane row 16
2.5 Oil flow visualization on vane endwall [23] 17
2.6 Interaction of neighboring passage vortices downstream of vane row . . 17
2.7 Grid quality criteria: Angle ϑ between line connecting cell centroids and surface normal, wall normal growth rate, and cell aspect ratio . . . 20
2.8 Generic cell of numerical grid with its neighboring cells 22
2.9 Decomposition of generic variable $\varphi(t)$ 26
2.10 Non-dimensional velocity profile in the near-wall region 32

2.11 Relation between decision variables and goal functions for two-dimensional optimization problem . . . 34
2.12 NSGA-II: Functionality for single-objective optimization . . . 36
2.13 Processes used to generate the offspring population . . . 37
2.14 Work flow used to create the endwall contours from the individuals of the optimization process . . . 38
2.15 Generic cubic Bézier Curve defined by the four control points P_0 - P_3 . 39
2.16 C^1-steady joining of two Bézier curves . . . 40

3.1 Vane profile used for this study with characteristic parameters . . . 46
3.2 Experimental test facility . . . 47
3.3 Linear cascade test section . . . 48
3.4 Periodic solution domain for the numerical simulations . . . 49
3.5 Grid used for spatial discretization of the solution domain . . . 50
3.6 GCI study for flat endwall baseline: Darcy friction factor f and htc in plane located in vane wake flow . . . 52
3.7 Boundary conditions for numerical solution domain . . . 53
3.8 Distribution of static pressure coefficient around vane profile of Ligrani and Jin [52]: numerical prediction and experimental data . . . 54
3.9 Laser triangulation method and laser scanning of ice layer . . . 55
3.10 Solution domain with digitized ice layer as lower endwall . . . 56
3.11 Distribution of heat transfer coefficient on ice contour obtained from numerics and from experiments by using one-dimensional heat conduction and ice layer thickness . . . 56
3.12 Generic parametrization of endwall contour . . . 58
3.13 Procedure used to assign the fitness to an individual . . . 58
3.14 Convergence behavior of area-averaged heat transfer coefficient for different flow field initialization techniques . . . 59
3.15 Ice contours short cooling length: Solution domain . . . 61
3.16 Ice contours short cooling length: Parametrized contour in isometric and top view with Bézier curves, edges of transition region, edges from ice layer, and curve junctions . . . 62
3.17 C^1-steadiness at junction of two curves, merge position of transition regions and parametrized contour, and rear suction side with edge from ice layer and polynomial function . . . 63
3.18 Ice contours short cooling length: Optimization space . . . 63
3.19 Ice contour long cooling length: Solution domain . . . 64
3.20 Optimization flat endwall: Param. contour in isometric and top view with Bézier curves and edges of transition region . . . 65
3.21 Optimization from flat endwall: Optimization space . . . 65

4.1 Numerical oil flow visualization on flat endwall . . . 68
4.2 Distribution of heat transfer coefficient for flat endwall . . . 69
4.3 Vortex system for flat endwall baseline . . . 69

4.4 Flat endwall baseline: Heat transfer and path lines at leading edge and at suction side of the vane 70
4.5 Flat endwall baseline: Heat transfer and velocity component in z-direction at rear pressure side and downstream of vane 71
4.6 Average heat transfer reductions of ice-contoured endwalls compared to flat endwall baseline 73
4.7 Ice-contoured endwall with short cooling length at $Re_C = 49{,}900$ and $\Theta = 12.2$ ($\mathrm{IC_{IFM}}$): Height levels and three-dimensional view 74
4.8 *htc* distribution for ice-contoured endwall $\mathrm{IC_{IFM}}$ and *htc* ratio of contoured to flat endwall at $Re_C = 49{,}900$ 75
4.9 Vortex system for ice-contoured endwall $\mathrm{IC_{IFM}}$ at $Re_C = 49{,}900$ 75
4.10 Vortex cores for contour $\mathrm{IC_{IFM}}$ and for flat endwall at $Re_C = 49{,}900$ . . 76
4.11 Distribution of heat transfer coefficient and near-endwall flow field for baseline and ice contour $\mathrm{IC_{IFM}}$ in cross-sections Ψ_1 and Ψ_2 77
4.12 Distribution of heat transfer coefficient and near-endwall flow field for baseline and ice contour $\mathrm{IC_{IFM}}$ in cross-sections Ψ_3, Ψ_4, and Ψ_5 79
4.13 Height levels, *htc* distribution, and iso-surfaces of $\lambda_2 = -4{,}000$ for ice contours at $Re_C = 34{,}000$, $\Theta = 8.5$ and $Re_C = 71{,}400$, $\Theta = 12.2$ 81
4.14 Trapezoidal endwall contour with elevation h in vane passage 82
4.15 Averaged heat transfer difference with respect to baseline for a trapezoidal endwall with vane passage being elevated by height h 83
4.16 Endwall heat transfer coefficient distribution and passage vortex core at $Q = 8{,}000$ for trapezoidal endwall with $h = 8\,\mathrm{mm}$ at $Re_C = 49{,}900$. 83
4.17 Average reductions in heat transfer and entropy production rates due to molecular heat transfer with respect to baseline at $Re_C = 49{,}900$ . . 85
4.18 Local, cross-section averaged entropy production rates due to mean and turbulent heat transfer for $\mathrm{IC_{IFM}}$ at $Re_C = 49{,}900$ 86
4.19 Ratio of entropy production rates due to molecular heat transfer for ice contour $\mathrm{IC_{IFM}}$ to trapezoidal endwall at $h = 8\,\mathrm{mm}$ ($Re_C = 49{,}900$) . 87
4.20 Average heat transfer reductions for endwall contours optimized on the basis of ice-contoured endwalls at $Re_C = 49{,}900$ 88
4.21 Height levels of endwall contours optimized on the basis of ice-contoured endwalls at $Re_C = 49{,}900$ 89
4.22 Average *htc* for all endwall contours created over the 20 generations of the numerical optimization process, referred to flat endwall baseline . 90
4.23 Bézier splines B_1-B_5 for endwall contour $\mathrm{OC_{IFM}}$, optimized from ice-contoured endwall at $Re_C = 49{,}900$ and $\Theta = 12.2$ 91
4.24 Endwall contour $\mathrm{OC_{IFM}}$, optimized on basis of ice-contoured endwall at $Re_C = 49{,}900$ and $\Theta = 12.2$ 92
4.25 Distribution of heat transfer coefficient on endwall and passage vortex as $Q = 8{,}000$ for optimized endwall contour $\mathrm{OC_{IFM}}$ at $Re_C = 49{,}900$ . . 92
4.26 Endwall contour optimized with respect to minimum vane passage heat transfer; based on ice contour at $Re_C = 49{,}900$ and $\Theta = 8.5$ 94

4.27 Distribution of heat transfer coefficient for contour optimized with respect to minimum vane passage heat transfer, flat endwall baseline, and *htc* ratio of both contours at $Re_C = 49{,}900$ 95
4.28 Recirculation zone at rear suction side for contour optimized for vane passage heat transfer from ice contour at $Re_C = 49{,}900$ and $\Theta = 8.5$. 96
4.29 Vertical velocity component close to rear pressure side for contour optimized with respect to minimum vane passage heat transfer and flat endwall baseline at $Re_C = 49{,}900$ 96

5.1 Ice-contoured endwall with long cooling length at $Re_C = 49{,}900$ and $\Theta = 12.2$: height levels and three-dimensional view 100
5.2 *htc* distribution for ice contour long cooling length at $Re_C = 49{,}900$ and $\Theta = 12.2$ and flat endwall baseline 102
5.3 Vortex cores and corresponding path lines for ice-contoured endwall with long cooling length at $Re_C = 49{,}900$ and $\Theta = 12.2$ and flat endwall baseline 103
5.4 Vertical velocities at leading edge for ice contour with long cooling length at $Re_C = 49{,}900$ and $\Theta = 12.2$ and flat endwall baseline 104
5.5 Distribution of static pressure coefficient C_p, path lines and velocity profiles in near-endwall region in front of vane leading edge for baseline and ice-contoured endwall with long cooling length at $Re_C = 49{,}900$. 105
5.6 PIV measurements of vertical velocity component at vanes' leading edges for baseline and experimental ice layer with long cooling length at $Re_C = 49{,}900$ and $\Theta = 12.2$ [26] 107
5.7 Endwall contour optimized from flat baseline at $Re_C = 49{,}900$ 109
5.8 Three-dimensional view of endwall contour $\mathrm{OC_{BSL}}$ at $Re_C = 49{,}900$. 109
5.9 Distribution of heat transfer coefficient for optimized endwall $\mathrm{OC_{BSL}}$, flat endwall baseline and *htc* ratio of both contours at $Re_C = 49{,}900$. 111
5.10 *htc* distribution and vortex system in terms of $Q = 8{,}000$ for endwall contour $\mathrm{OC_{BSL}}$ and baseline at $Re_C = 49{,}900$ 112
5.11 Near endwall flow with velocity and thermal boundary layer in front of vane for baseline and optimized contour $\mathrm{OC_{BSL}}$ at $Re_C = 49{,}900$. 113
5.12 Endwall contour optimized from flat endwall baseline with extended optimization space at $Re_C = 49{,}900$ 114
5.13 *htc* distribution for optimized endwall $\mathrm{OC_{BSL,2}}$ and flat baseline at $Re_C = 49{,}900$ 115
5.14 *htc* distribution with vortex system as $Q = 8{,}000$ and path lines of recirculation zone for contour $\mathrm{OC_{BSL,2}}$ at $Re_C = 49{,}900$ 116

6.1 Distribution of heat transfer coefficient for flat baseline at experimental, $Re_C = 49{,}900$, and design Reynolds number $Re_C = 200{,}000$ . . . 118
6.2 Average heat transfer reductions of ice-contoured endwalls with short cooling length at design Reynolds number 120

6.3 *htc* distribution for ice-contoured endwall IC_{IFM} and flat endwall baseline at $Re_C = 200{,}000$ 121
6.4 Total pressure coefficient along numerical domain for ice-contoured endwall IC_{IFM} and flat endwall baseline at design Reynolds number . 122
6.5 Vane passage *htc* distribution for optimized endwall contour OC_{BSL} and flat baseline at design Reynolds number 125

A.1 Binary tournament selection for a population of six individuals II
A.2 Probability density function used to determine the variable β_i^Q IV
A.3 GCI study for flat endwall baseline; Positions P1 and P2, and plane in vane wake flow used for calculation of GCI VII
A.4 Linear cascade test section with long copper inlay VIII
A.5 Bézier splines B_1-B_5 for endwall contour optimized with respect to minimum vane passage heat transfer; optimized from ice-contoured endwall at $Re_C = 49{,}900$ and $\Theta = 8.5$ XIV
A.6 Bézier splines B_1-B_8 for optimized contour OC_{BSL} at $Re_C = 49{,}900$. XVI
A.7 Bézier splines B_1-B_3 for optimized contour $OC_{BSL,2}$ at $Re_C = 49{,}900$ XVIII
A.8 Bézier splines B_4-B_8 for optimized contour $OC_{BSL,2}$ at $Re_C = 49{,}900$. XIX

List of Tables

3.1 Parameters of vane profile 46
3.2 GCI study for flat endwall baseline: Grid parameters 51
3.3 GCI study for flat endwall baseline: Results for axial and crosswise velocity components, static temperature T and area-averaged endwall heat transfer coefficient 52
3.4 Settings for NSGA-II 60

4.1 Heat transfer coefficients area-averaged over endwall segments for ice-contoured endwall $\mathrm{IC}_{\mathrm{IFM}}$ and flat endwall baseline at $Re_C = 49{,}900$ . . 80
4.2 Heat transfer coefficients area-averaged over endwall segments for contour $\mathrm{IC}_{\mathrm{IFM}}$ and trapezoidal endwall with $h = 8\,\mathrm{mm}$ at $Re_C = 49{,}900$. 84
4.3 Averaged rates of terms contributing to entropy production for ice-contoured endwalls short cooling length and baseline at $Re_C = 49{,}900$. 85
4.4 Percentaged difference of area-averaged endwall heat transfer with respect to baseline for ice-contoured endwall $\mathrm{IC}_{\mathrm{IFM}}$ and endwall contour $\mathrm{OC}_{\mathrm{IFM}}$ optimized on basis of it 93

6.1 Average *htc* for endwall segments of flat baseline at experimental Reynolds number ($Re_C = 49{,}900$) and at design Reynolds number ($Re_C = 200{,}000$) 119
6.2 Difference in average *htc* with respect to baseline for endwall segments of ice-contoured endwall $\mathrm{IC}_{\mathrm{IFM}}$ at experimental ($Re_C = 49{,}900$) and design Reynolds number ($Re_C = 200{,}000$) 120
6.3 Total pressure coefficients with percentaged difference to baseline for ice-contoured endwalls with short cooling length at design Reynolds number 122
6.4 Averaged rates of terms contributing to entropy production for ice-contoured endwall $\mathrm{IC}_{\mathrm{IFM}}$ and baseline at $Re_C = 200{,}000$ 123

6.5 Percentaged difference in average *htc* with respect to baseline for endwall segments of optimized endwall OC_{IFM} at experimental (Re_C = 49,900) and design Reynolds number (Re_C = 200,000) 124

A.1 Data set of GCI study for flat endwall baseline VII
A.2 Endwall heat transfer predicted by numerical simulation and calculated from ice layer thickness in experiment IX
A.3 Averaged rates of terms contributing to entropy production for ice-contoured endwalls and baseline at Re_C = 34,000 XIII
A.4 Averaged rates of terms contributing to entropy production for ice-contoured endwalls and baseline at Re_C = 71,400 XIII
A.5 Heat transfer coefficients area-averaged over endwall segments for contour optimized with respect to vane passage heat transfer, based on ice-contoured endwall with short cooling length at Re_C = 49,900 and Θ = 8.5 XV
A.6 Heat transfer coefficients area-averaged over endwall segments for optimized contour OC_{BSL} at Re_C = 49,900 XVII
A.7 Heat transfer coefficients area-averaged over endwall segments for optimized contour OC_{BSL} at design Reynolds number Re_C = 200,000 XVII
A.8 Heat transfer coefficients area-averaged over endwall segments for optimized contour $OC_{BSL,2}$ at Re_C = 49,900 XX
A.9 Heat transfer coefficients area-averaged over endwall segments for optimized contour $OC_{BSL,2}$ design Reynolds number Re_C = 200,000 . . XX
A.10 Overview of endwall contours created with the Ice Formation Method and with numerical optimization XXI
A.11 Overview of endwall contours created with the Ice Formation Method and with numerical optimization (Continued from page before) . . XXII

Nomenclature

Latin Characters

A	Area	m^2
B	Freezing parameter	–
	Bernstein polynomial	–
C	True chord length of vane profile	m
$C(t)$	Parametric description of Bézier curve	–
C_{ax}	Axial chord length of vane profile	m
C_μ	Eddy viscosity constant	–
C_p	Static pressure coefficient	–
c_p	Specific heat at constant pressure	$\mathrm{J\,kg^{-1}\,K^{-1}}$
D	Decision variable	–
d	Dimension of optimization problem	–
e	Grid error for GCI study	–
f	Body force	N
	Darcy friction factor	–
	Fitness of individual	–
g	Gene of individual	–
$\mathcal{H}$	Hessian matrix	–
h	Elevation height for trapezoidal endwall	m
	Half channel height	m
	Height laser triangulation method	m
	Height of grid cell	m
	Order of Bézier curve	–
	Specific enthalpy	$\mathrm{J\,kg^{-1}}$
htc	Convection heat transfer coefficient	$\mathrm{W\,m^{-2}\,K^{-1}}$
i	Index of Bernstein polynomial	–
	Counter variable	–
i, j	Spatial directions for Einstein notation	–

J	Coefficient matrix	–
k	Thermal conductivity	$\mathrm{W\,m^{-1}\,K^{-1}}$
	Turbulence kinetic energy	$\mathrm{m^2\,s^{-2}}$
L	Characteristic length	m
L_{ice}	Thickness of ice layer	m
l	Turbulent length scale	m
M	Number of goal functions	–
m	Mass	kg
	Number of generations	–
$\dot{m}$	Mass flow rate	$\mathrm{kg\,s^{-1}}$
N	Number of grid cells for GCI study	–
	Number of individuals	–
n	Number of genes	–
n_x, n_y, n_z	Unit vectors	–
P	Control point of Bézier curve	–
	Parent individual	–
	Pitch between adjacent vanes	m
$\mathcal{P}$	Probability density function	–
p	Apparent order for GCI study	–
	Static pressure	$\mathrm{N\,m^{-2}}$
p_{cross}	Crossover probability	–
p_{mut}	Mutation probability	–
Q	Sum of eigenvalues of $S_{ij}^2 + \Omega_{ij}^2$	–
	Offspring individual	–
$q(p)$	Function for GCI study	–
q''	Heat flux	$\mathrm{W\,m^{-2}}$
R	Specific gas constant	$\mathrm{J\,kg^{-1}\,K^{-1}}$
r	Grid refinement ratio for GCI study	–
	Heat of fusion	$\mathrm{J\,kg^{-1}}$
S	Coefficient for Sutherland equation	K
	Span of vane profile	m
	Source term	$[S]$
	Surface of control volume	$\mathrm{m^2}$
S_{ij}	Mean rate of strain tensor	$\mathrm{m\,s^{-2}}$
$\dot{S}$	Entropy production	$\mathrm{W\,K^{-1}\,m^{-3}}$
$\dot{S}_{\mathrm{Diss,mol}}$	Entropy production due to molecular dissipation	$\mathrm{W\,K^{-1}\,m^{-3}}$
$\dot{S}_{\mathrm{Diss,turb}}$	Entropy production due to turbulent dissipation	$\mathrm{W\,K^{-1}\,m^{-3}}$
$\dot{S}_{\mathrm{Heat,mol}}$	Entropy production due to molecular heat conduction	$\mathrm{W\,K^{-1}\,m^{-3}}$
$\dot{S}_{\mathrm{Heat,turb}}$	Entropy production due to turbulent heat conduction	$\mathrm{W\,K^{-1}\,m^{-3}}$
$\dot{S}_{\mathrm{total}}$	Total entropy production	$\mathrm{W\,K^{-1}\,m^{-3}}$
s	Factor for GCI study	–
	Specific entropy	$\mathrm{J\,kg^{-1}\,K^{-1}}$
T	Static temperature	K
Tu	Turbulence intensity	–

t	Bézier curve parameter	–
	Time	s
u	Random number for binary crossover and mutation	–
u_{exit}	Velocity magnitude at vane passage exit cross-section	$\mathrm{m\,s^{-1}}$
u_1, u_2, u_3	Velocity components	$\mathrm{m\,s^{-1}}$
V	Velocity magnitude	$\mathrm{m\,s^{-1}}$
	Volume	$\mathrm{m^3}$
	Volume of grid cell for GCI study	$\mathrm{m^3}$
$\underline{V}$	Velocity vector	$\mathrm{m\,s^{-1}}$
V_τ	Friction velocity	$\mathrm{m\,s^{-1}}$
V^+	Dimensionless velocity	–
w	Width of grid cell	m
x, y, z	Spatial directions	m
$[x]$	Dimension of quantity x	
y	Wall distance of grid cell	m
y^+	Dimensionless wall distance of grid cell	–
y_1	Wall distance of first grid cell	m
y_1^+	Dimensionless wall distance of first grid cell	–

Greek characters

α	Metric for simulated binary crossover	–
	Thermal diffusivity	$\mathrm{m^2\,s^{-1}}$
β	Angle laser triangulation method	$^\circ$
	Weighting factor for simulated binary crossover	–
Γ	Diffusion coefficient	–
γ	Flow turning angle of vane profile	$^\circ$
δ	Displacement laser triangulation method	m
	Ice-free height	m
	Weighting factor for mutation	–
δ_{ij}	Kronecker delta	–
ϵ	Difference between grids for GCI study	–
	Eddy dissipation rate	$\mathrm{m^2\,s^{-3}}$
ζ	Coordinate in wake perpendicular to outflow direction	m
η_C	Crossover distribution index	–
η_m	Distribution index for mutation	–
Θ	Temperature ratio	–
ϑ	Angle of surface normal and line connecting cell centroids	$^\circ$
λ_2	Second eigenvalue of $S_{ij}^2 + \Omega_{ij}^2$	–
μ	Dynamic viscosity	$\mathrm{kg\,m^{-1}\,s^{-1}}$
ν	Kinematic viscosity	$\mathrm{m^2\,s^{-1}}$
ρ	Mass density	$\mathrm{kg\,m^{-3}}$
σ_{ij}	Viscous stress tensor	$\mathrm{kg\,s^{-2}\,m^{-1}}$
τ_W	Wall shear stress	$\mathrm{N\,m^{-2}}$
Φ	Dissipation function	$\mathrm{s^{-2}}$

ϕ	Generic variable	$[\phi]$
φ	Generic variable per unit mass	$[\phi]\,\mathrm{kg}^{-1}$
Ψ_i	Cross-sections in vane passage	$-$
ψ	Dimensionless cross-section width	$-$
Ω	Vorticity	s^{-1}
Ω_{ij}	Spin tensor	$\mathrm{m\,s}^{-2}$
ω	Specific eddy dissipation rate	s^{-1}

Acronyms

B	Bézier curve
BSL	Flat endwall baseline
CDS	Central Differencing Scheme
CFD	Computational Fluid Dynamics
CV	Control Volume
DNS	Direct Numerical Simulation
FMG	Fast Multi-Grid Initialization
FVM	Finite Volume Method
GCI	Grid Convergence Index
G0	Fine grid for GCI study
G1	Intermediate grid for GCI study
G2	Coarse grid for GCI study
HV	Horseshoe Vortex
$\mathrm{IC}_{\mathrm{IFM}}$	Ice contour short cooling length at $Re_C = 49{,}900$ and $\Theta = 12.2$
IFM	Ice Formation Method
NSGA-II	Non-sorted Genetic Algorithm II
$\mathrm{OC}_{\mathrm{BSL}}$	Optimized endwall contour based on flat endwall baseline
$\mathrm{OC}_{\mathrm{BSL,2}}$	Optimized endwall contour based on flat endwall baseline with enlarged optimization space
$\mathrm{OC}_{\mathrm{IFM}}$	Optimized endwall contour based on $\mathrm{IC}_{\mathrm{IFM}}$
PS	Pressure Side
PV	Passage Vortex
PIV	Particle Image Velocimetry
SS	Suction Side
SST	Shear Stress Transport

Subscripts

air	Relating to air properties
bulk	Relating to bulk properties
C	Centroid of grid cell
CI	Copper inlay
CS	Cross-section
EW	Endwall
exp	Experiment
f	Freezing

ice	Relating to ice properties
in	Inlet of numerical domain
N, E, S, W	Cardinal directions labeling cell centroids
n, e, s, w	Cardinal directions labeling cell surfaces
num	Numerical
out	Outlet of numerical domain
t	Turbulent
tot	Total variable
W	Wall
water	Relating to water properties
∞	Incident flow condition

Superscripts

$\underline{(\ldots)'}$	Fluctuating quantity
$\overline{(\ldots)}$	Time-averaged quantity
$\widehat{(\ldots)}$	Mass-flow averaged quantity

Non-dimensional numbers

Bi	Biot number	$= htc\,L/k_{\text{ice}}$
Nu	Nusselt number	$= htc\,L/k_{\text{air}}$
Pr	Prandtl number	$= \nu/\alpha$
Re	Reynolds number	$= VL/\nu$
Re_C	Reynolds number based on vane chord length	$= VC/\nu$

Abstract

Nowadays, modern standards ask for highly efficient technical devices to meet customer expectations. In this context, a high thermal efficiency is demanded for gas turbines, which is since many years achieved by employing high turbine inlet temperatures. This, however, yields a high thermal loading of e. g. the turbine endwalls. One way to reduce this loading is the application of contoured endwalls between the turbine vanes. These influence flow and heat transfer close to the endwall in a favorable way and thus reduce the heat load on the endwall.

The present work deals with the creation of such endwall contours with the goal to reduce average endwall heat transfer. Thereby, two methods were used to generate the contours: the Ice Formation Method (IFM) and numerical optimization. For the IFM, experimental ice layers were digitized and used as endwall contours in numerical simulations. These ice layers resulted from the study of Haase [26] in which they were created in a water channel test facility with experimental Reynolds numbers up to $Re_C = 71{,}400$. In the numerical optimizations, the endwall contour in the vane passage was parametrized with Bézier curves and a genetic algorithm in combination with CFD simulations was employed to generate endwall contours with reduced heat transfer. While the IFM was assumed to be a global optimization method with entropy production as goal function, the numerical optimization allowed to select the goal function, here heat transfer, and the region for optimization, e.g. the entire endwall or only the endwall of the vane passage.

Within the scope of this thesis, different heat transfer optimized endwall contours were created and compared to the flat endwall baseline to assess their heat transfer performance. First, heat transfer on the endwall was carefully analyzed for the flat baseline and the underlying flow features were identified. Next, nine ice-contoured endwalls were created from experimental ice layers, which grew on a cooled copper inlay (termed *short cooling length* in this work) during the experiment, and their endwall heat transfer was evaluated and compared to the baseline, which showed a global reduction of average heat transfer for all these contours. For one contour, the changes in heat transfer and the flow field were outlined in detail. Furthermore,

entropy production rates were determined for these contours and compared to the baseline. This validated the assumption that the IFM causes a reduction of entropy production. The ice-contoured endwalls were also used as starting geometries for a subsequent numerical optimization. The latter yielded contours which further reduced global heat transfer.

To reduce heat transfer especially in the vane passage, another ice-contoured endwall with enlarged cooling length was examined. For this ice contour, a longer cooled copper inlay (termed *long cooling length*) was used in the experiment to create an ice contour that reaches further up- and downstream of the vane passage than the previously generated ice contours. However, the so created contour could not achieve the desired heat transfer reduction. In contrast, numerical optimizations with a parametrization based on the flat endwall yielded endwall contours with a significant reduction of heat transfer in the vane passage.

Finally, heat transfer characteristics for the created endwall contours were analyzed for the design Reynolds number of $Re_C = 200{,}000$. This analysis was done numerically by determining endwall heat transfer from CFD simulations at the design Reynolds number. For the ice-contoured endwalls heat transfer reductions were even higher at this Reynolds number, while the numerically optimized contours featured approximately the same reductions in heat transfer as for the Reynolds numbers at which they were created.

The present work showed, that under specific conditions, the IFM generates contours that reduce global endwall heat transfer for the investigated vane/endwall flow. However, the definition of a proper reference case was difficult, since the growing ice layer in the experiment changes the state of the boundary layer and makes comparisons at the same flow conditions infeasible. The numerical optimization proved successful in creating endwall contours with reduced heat transfer rates. It allows for both endwall contours with reduced global heat transfer and contours with heat transfer being reduced in the vane passage only.

Kurzfassung

Um heutzutage die Erwartungen von Kunden erfüllen zu können werden hoch effiziente technische Geräte verlangt. Von Gasturbinen wird in diesem Zusammenhang ein hoher thermischer Wirkungsgrad verlangt, welcher seit vielen Jahren unter anderem durch die Verwendung hoher Turbineneintrittstemperaturen erreicht wird. Dies führt jedoch zu einer starken thermischen Belastung von z.B. den Turbinen-Seitenwänden. Eine Möglichkeit um diese Belastung zu reduzieren ist die Verwendung konturierter Seitenwände zwischen den Turbinen-Leitschaufeln. Diese beeinflussen Strömung und Wärmeübergang in Wandnähe auf günstige Art und Weise und können so die Wärmelast auf die Seitenwand reduzieren.

Die vorliegende Arbeit beschäftigt sich mit der Erzeugung solcher Seitenwandkonturen mit dem Ziel, den gemittelten Seitenwand-Wärmeübergang zu senken. Dabei kamen zwei Methoden zum Einsatz: die Eisformationsmethode und eine numerische Optimierung. Im Falle der Eisformationsmethode wurden experimentell erzeugte Eisschichten digitalisiert und in numerischen Simulationen als Seitenwandkonturen verwendet. Diese Eiskonturen stammen aus der Arbeit von Haase [26], in der sie in einem Wasserkanal bei experimentellen Reynolds Zahlen von bis zu $Re_C = 71{,}400$ erzeugt wurden. Für die numerische Optimierung wurde der Bereich der Seitenwand im Schaufelkanal mit Bézier-Kurven parametrisiert und es wurde ein genetischer Algorithmus in Kombination mit CFD Simulationen benutzt um Seitenwandkonturen mit verringertem Wärmeübergang zu erzeugen. Während die Eisformationsmethode als globales Optimierungsverfahren mit dem Ziel einer Entropiereduktion angenommen wurde, erlaubte die numerische Optimierung die Auswahl von sowohl der Zielfunktion, hier Wärmeübergang, als auch des Bereichs für die Optimierung, z.B. die gesamte Seitenwand oder nur der Bereich innerhalb der Schaufelpassage.

Im Rahmen dieser Arbeit wurden verschiedene wärmeübergangsoptimierte Seitenwandkonturen erzeugt und mit dem Referenzfall der flachen Seitenwand verglichen, um ihr Wärmeübergangsverhalten zu bestimmen. Dazu wurde zunächst der Wärmeübergang für eine flache Seitenwand untersucht und es wurden die zu Grunde liegenden Strömungsphänomene identifiziert. Danach wurden neun eiskonturierte

Seitenwände auf Basis von experimentellen Eisschichten erzeugt, welche während der Experimente auf einer gekühlten Kupferfläche (in dieser Arbeit *short cooling length* genannt) entstanden, und deren Wärmeübergangsverhalten untersucht und mit der flachen Seitenwand verglichen. Hierbei konnte eine globale Reduktion des gemittelten Seitenwandwärmeübergangs für alle neun Konturen festgestellt werden. Für eine dieser Konturen wurden die Veränderungen von Strömung und Wärmeübergang durch die Konturierung detailliert untersucht.

Des Weiteren wurden für diese Konturen die zugehörigen Entropieproduktionsraten bestimmt und mit dem Referenzfall der flachen Seitenwand verglichen. Damit konnte die Annahme bestätigt werden, dass die Eisformationsmethode die Produktion von Entropie in der Strömung reduziert. Diese Eiskonturen wurden außerdem als Ausgangsgeometrien für eine weiterführende numerische Optimierung verwendet. Letztere ergab Seitenwandkonturen, welche den Wärmeübergang noch weiter senken.

Um den Wärmeübergang speziell im Bereich des Schaufelkanals zu reduzieren, wurde eine weitere eiskonturierte Seitenwand mit erweiterter Kühlfläche untersucht. Hierbei wurde im Experiment eine verlängerte kühlbare Kupferfläche verwendet um eine Eiskontur zu erzeugen, die sich weiter stromauf und stromab des Schaufelkanals erstreckt als die zuvor erzeugten Eiskonturen. Diese Eiskontur konnte jedoch nicht die erwünschte Wärmeübergangsreduktion erreichen. Im Gegensatz dazu, ergaben numerische Optimierungen mit einer Parametrisierung auf Basis der flachen Seitenwand, Seitenwandkonturen die eine deutliche Reduktion des Wärmeübergangs im Schaufelkanal aufwiesen.

Abschließend wurde das Wärmeübergangsverhalten der erzeugten Seitenwandkonturen bei der Auslegungs-Reynolds-Zahl von $Re_C = 200{,}000$ untersucht. Diese Untersuchung wurde numerisch durchgeführt in dem der Seitenwandwärmeübergang mittels CFD Simulationen bei der Auslegungs-Reynolds-Zahl bestimmt wurde. Für die eiskonturierten Seitenwände ergaben sich bei dieser Reynolds Zahl sogar höhere Wärmeübergangsreduktionen als bei den experimentellen Reynolds Zahlen. Die numerisch optimierten Seitenwände wiesen hingegen ähnliche Wärmeübergangsreduktionen auf wie für die Reynolds Zahlen, bei denen sie erzeugt wurden.

Die vorliegende Arbeit zeigte, dass die Eisformationsmethode, unter bestimmten Bedingungen, Seitenwandkonturen erzeugt, welche den globalen Wärmeübergang für die untersuchte Schaufel-Seitenwand-Strömung verringern. Die Definition eines eindeutigen Referenzfalles war jedoch schwierig, da die im Experiment wachsende Eisschicht den Grenzschichtzustand ändert und somit einen Vergleich bei gleichen Strömungsbedingungen unmöglich macht. Die numerische Optimierung erwies sich als erfolgreich um Seitenwandkonturen mit reduzierten Wärmeübergangsraten zu erzeugen. Sie erlaubt es sowohl Seitenwandkonturen zu erzeugen die den Seitenwand-Wärmeübergang global senken als auch Konturen zu erzeugen, die den Wärmeübergang im Bereich des Schaufelkanals reduzieren.

1 Introduction

Contents:
Motivation for the present work - Review of pertinent literature concerning the Ice Formation Method and endwall contouring - Objectives of this work and structure of the thesis

1.1 Motivation

The rapid growth of world economy and today's environmental consciousness have led to high economical and ecological standards for technical devices. To meet these standards, designers constantly perform research to increase the devices' efficiencies. In terms of fluid flow devices, this normally means to either reduce pressure loss or to reduce heat transfer and hence cooling requirements. Both can be achieved by optimizing flow characteristics through modification of the flow restraining geometry.

The classical approach for such a design optimization is to progressively change the flow geometry, based on the flow features of the current design and their analysis. For example, if a flow device exhibits local hot spots due to impinging flow which require heavy cooling, the geometry can be modified in such a way that the flow structure changes and impingement is diminished. This would reduce the required cooling and thus increase the device's efficiency. However, such an approach is tedious and very unidirectional, that is the direction in which the geometry will be optimized is predetermined by the most obvious drawback of the current design. This means that only a small subset of the entire optimization space is considered, i. e. only few geometries of all possible ones are investigated. Hence, this approach does not allow for substantial design innovations.

In the past decades, another approach has been used more and more for design optimization of technical flow devices: numerical optimization algorithms, such as genetic algorithms. On the basis of a parametrization of the investigated geometry by decision variables, these methods automatically create a sequence of design variants and analyze them with respect to a specified goal function, e. g. minimum pressure loss or minimum heat transfer. The optimization algorithms thereby create each new design variant in consideration of the performance of all previous geometries. In this vein, these algorithms incorporate the entire optimization space and finally find a geometry that is optimum for the considered flow problem and the specified goal function. However, this is only possible if the decision variables are chosen carefully enough so that the parametrization can reproduce any possible geometry from the optimization space. Hence, the geometry parametrization is a crucial part of such optimizations.

A different methodology for the optimization of technical devices are natural optimization methods. They utilize the fact that systems in nature always seek to reduce losses and hence aspire to a minimum energy dissipation in steady-state. In this state, entropy production, which turns the systems exergy into anergy, becomes minimum and the system retains a maximum of exergy. For fluid flow devices, such a natural optimization method is the Ice Formation Method. It uses a baseline geometry of the flow device, which is cooled below the freezing point and exposed to water flow. As a consequence, an ice layer develops, which represents a naturally optimized geometry with minimum entropy production as goal function. This optimization method is free of restrictions, i. e. the resulting geometry simply arises from the prevailing flow features without any other input like a parametrization of the geometry. Thus, the method takes the entire optimization space into account for finding an optimized

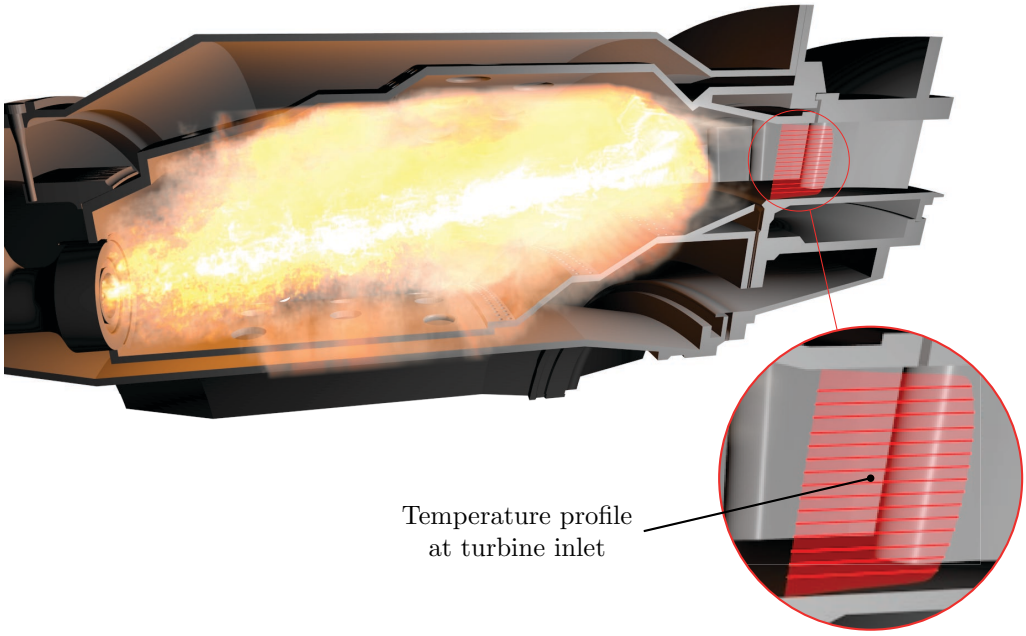

Figure 1.1: Combustion chamber with flat turbine inlet temperature profile

geometry. However, the method's goal function is not selectable but preset to loss reduction and hence minimum entropy production. For fluid flow devices, this means that the method optimizes the geometry either with respect to pressure loss or with respect to heat transfer, depending on which of the two is the dominant source of loss in the flow.

In the field of turbomachinery, optimization methods are widespread and often used for the turbine stages. As Fig. 1.1 shows, modern gas turbines use in their combustion chambers high temperatures to increase thermal efficiency and flat temperature profiles with steep temperature gradients at the wall to reduce peak temperatures and hence pollutants. This leads to high thermal loads on the turbine's vanes and blades. In addition, the vane endwall junction induces secondary flows with complex vortical structures, which further increase heat loads for the vane endwalls. These vortical structures are also responsible for much of the vanes' pressure losses. Therefore, designers apply optimization methods to these endwalls in order to create endwall geometries which reduce pressure loss and heat transfer and hence improve the efficiency of the gas turbine.

1.2 The Ice Formation Method: A Review

The freezing of water to ice in convective flows occurs in many technical applications involving water flow. This phenomenon has been studied intensively for pipe and channel flow applications. For pipe flows, Bilenas and Jiji [7], as well as Oezisik

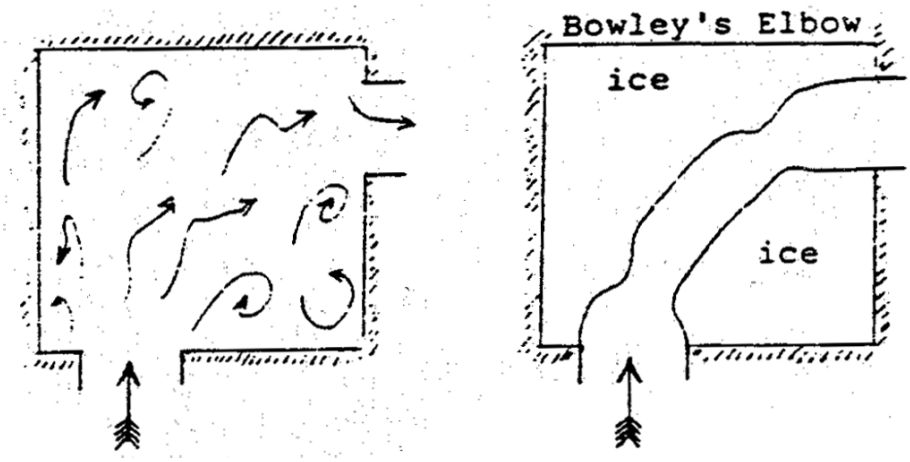

Figure 1.2: Bowley's elbow with initial geometry (left) and ice-contoured geometry (right) [40]

and Mulligan [61] studied analytically the freezing of water to ice, while Chida [17] and Gilpin [25] both investigated the blockage effect due to ice growth and derived criteria for the freeze-shut of pipes. For channel flows, ice formation was investigated for channels with straight walls (Weigand and Beer [75]), curved walls (Braun and Beer [11]) and diverging walls (Neumann and Beer [60]).

In 1965, Bowley [10] was the first one to use the formation of ice in water flow as a tool for optimizing a flow geometry. He generated an optimized 90°-elbow by only prescribing its inlet and outlet position, so that the flow restraining geometry

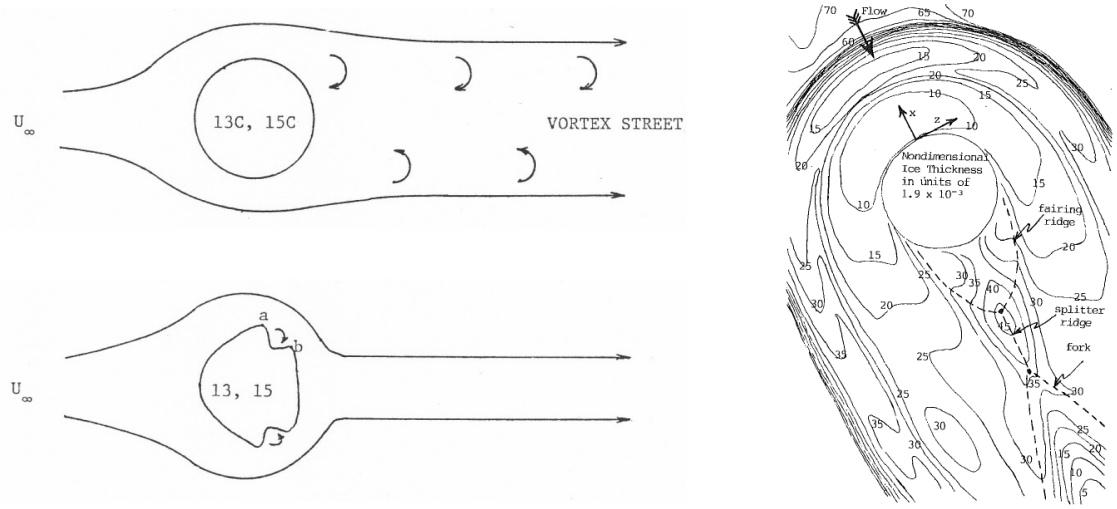

Figure 1.3: Carlson's cylinder in crossflow with initial cooled cylinder (upper left) and cylinder with ice (lower left) [13] and the ice contour at a cylinder endwall junction from LaFleur and Langston [44] (right)

developed in-between in terms of the forming ice (see Fig. 1.2). Carlson [13] created ice layers on cooled cylinders in water cross-flow in order to find geometries that reduce drag. Figure 1.3 (left) shows the resulting ice contours. These had ellipsoidal shapes, which delay flow detachment and thus reduce drag.

In the 1990s, LaFleur did extensive research on ice formation in water flow and developed this natural optimization approach into the *Ice Formation Method (IFM)*. At first, he applied it to a cylinder/hull juncture together with Langston [43] and showed that the resulting ice layers only depend on the flow Reynolds number and the cooling of the wall, i. e. its temperature. In following works, he investigated ice formation for a flat plate Couette flow [41] both analytically and numerically. He could show that in steady-state, the resulting ice layers represent geometries with minimum energy dissipation and that this is linked to reduced entropy production rates. Then, as shown in Fig. 1.3 (right), LaFleur and Langston [44] applied the Ice Formation Method to a complex three-dimensional flow around a cylinder/endwall junction. By ice-contouring the endwall, they created an endwall geometry that reduces drag by 18% compared to a flat endwall.

LaFleur et al. [45] also used the IFM with turbomachinery components by applying it to the second vane endwall of the Energy Efficient Engine (E3) turbine with the goal to reduce endwall heat transfer. The generated endwall ice contour, as shown in Fig. 1.4 (right), reduces the average Stanton number by about 24% compared to the original endwall of the E3-turbine, however, this Stanton number was 10% higher than for a flat endwall. In a later study, LaFleur [42] also investigated total pressure loss for this endwall contour and found that it features a slightly increased total pressure loss than the original endwall of the E3-turbine. This shows both the advantages and disadvantages of the IFM. It creates flow optimized geometries with reduced energy dissipation as goal function, however, this goal function is always a blend between pressure loss and heat transfer and depends on the flow problem.

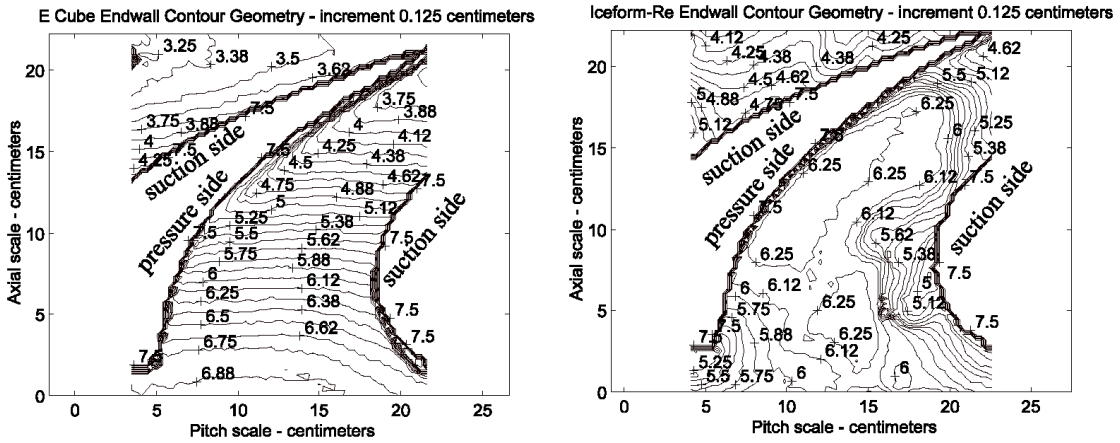

Figure 1.4: Original Energy Efficient Engine (E3) endwall geometry (left) and ice-contoured E3 endwall by LaFleur et al. [45] (right)

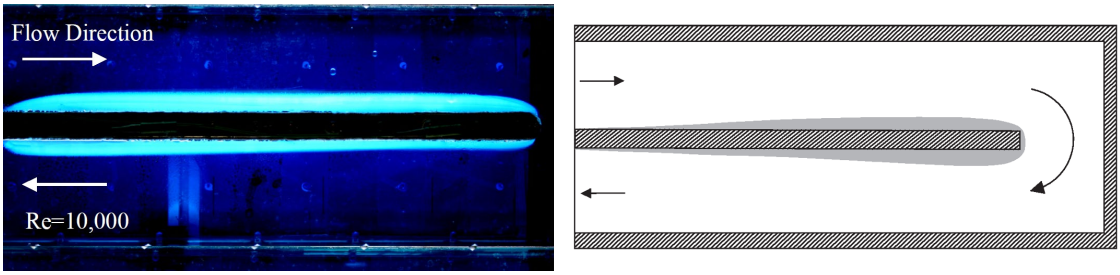

Figure 1.5: Separating web of a 180° bend: Experimental ice contour and numerically optimized geometry from Zehner et al. [82, 83]

Zehner et al. [83] and Steinbrueck et al. [73] used the IFM and augmented it by numerical optimization using a genetic algorithm. In this vein, they optimized the separating web of a 180° bend, as found for internal cooling of gas turbine blades, with respect to pressure loss (see Fig. 1.5). They first created ice contours on the web experimentally using the IFM and then used these as starting points for numerical optimizations. While the IFM created pre-optimized geometries without restrictions on the optimization space, the subsequent numerical optimization allowed them to chose the desired goal function of minimum pressure loss. Compared to the baseline web geometry, their optimized geometry reduces pressure loss by 25%.

1.3 State of the Art in Turbine Endwall Contouring

In the recent development of gas turbine technology, designers started to contour the endwalls between the vanes and blades of turbine stages in order to improve engine efficiency. Such endwall contours have different local heights in axial and circumferential direction and thus directly alter the flow and thermal fields near the endwall. This adds further degrees of freedom to the turbine design and allows for optimization with respect to flow or heat transfer aspects. Most often, researchers use a design system to mathematically describe the endwall geometry and seek endwall contours that improve certain flow features, such as total pressure loss, exit angle deviation or even stage efficiency. Just lately, designers started to apply turbine endwall contouring also to reduce heat transfer rates at the endwalls in order to lower thermal stresses and cooling requirements and thus increasing turbine efficiency.

Harvey et al. [29] (Fig. 1.6, left) created contoured endwalls for the rotor profile of the linear cascade at Durham University. They produced 36 different endwall contours using a product of two curves in axial and circumferential direction and analyzed these contour's flow fields with CFD. The latter predicted a significant reduction of secondary flow loss and exit angle deviations for their final contour. Brennan et al. [12] (Fig. 1.6, middle) redesigned the endwall between the high pressure turbine vanes of the Rolls-Royce Trent 500 engine. They created a total of 72

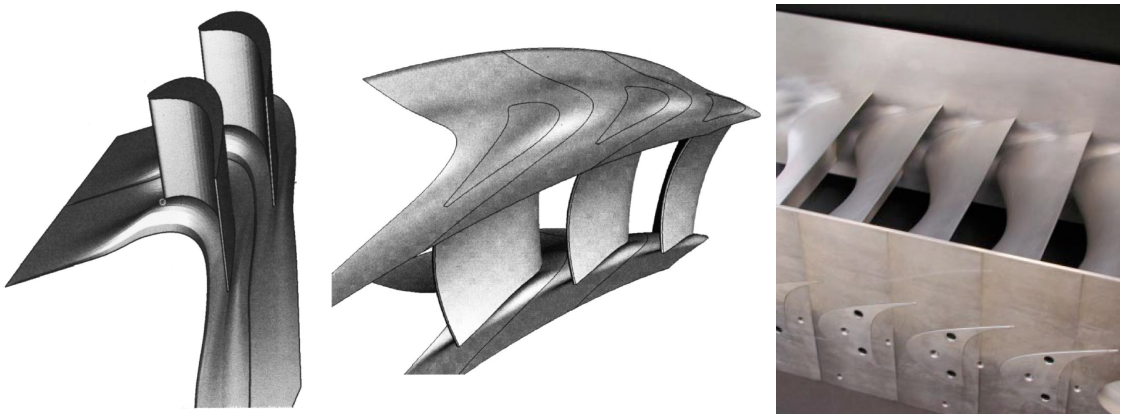

Figure 1.6: Contoured endwalls of Harvey et al. [29] (left), Brennan et al. [12] (middle), and Nagel and Baier [59] (right)

endwall contours with the program FAITH, which used sinusoidal shapes in circumferential direction and B-splines in axial direction at six positions along the profile's mean camber line. By analyzing the created contours with CFD simulations, they identified a final endwall contour which improves stage efficiency by 0.4%. For one conventional and two high-lift low pressure turbine airfoils, Praisner et al. [65] created contoured endwalls with the goal to reduce mass-average total pressure loss. To describe the geometry of their endwalls, they used cubic splines in both the axial and circumferential direction. Combining a gradient-based optimization algorithm with three-dimensional CFD, they then simulated as many as 1,000 design iterations for each profile. All optimized endwall contours reduce total pressure loss, up to a maximum reduction of 12%. For one of these profiles, the Pratt & Whitney PAK-B airfoil shown in Fig. 1.7, Knezevici et al. [37] performed measurements using

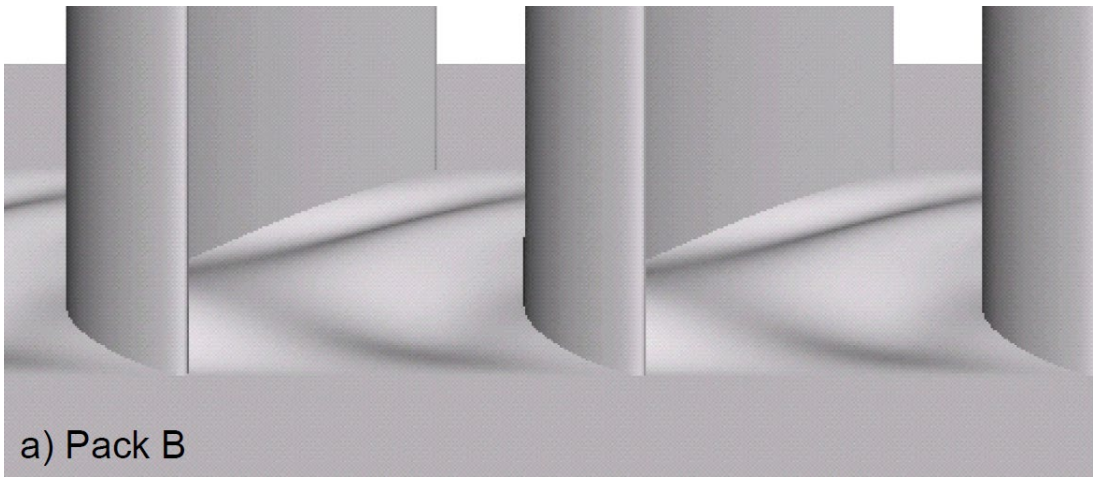

Figure 1.7: Optimized endwall contour for Pack-B airfoil, from Praisner et al. [65]

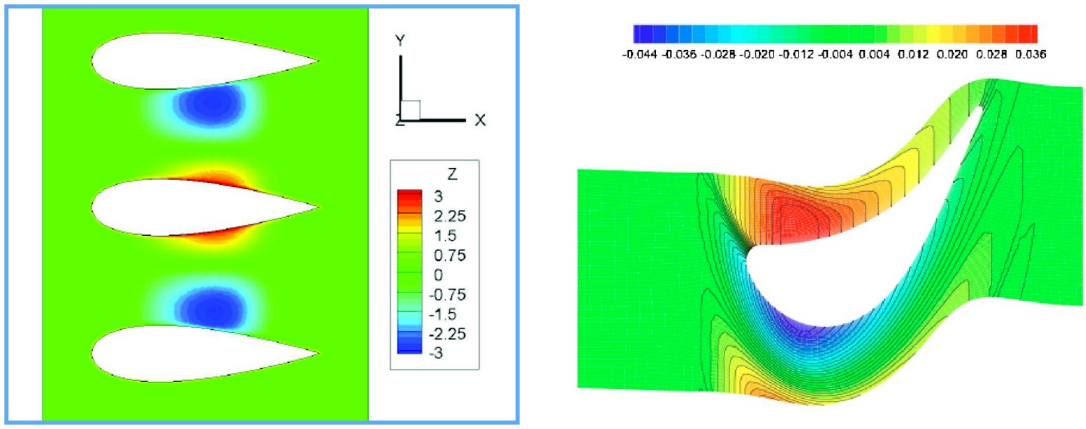

Figure 1.8: Endwall contour for symmetric airfoils from Laveau et al. [50] (left) and optimized contour for vane endwall from Saha and Acharya [68](right)

Praisner's contoured endwall. The experiments showed that the application of the endwall contour results in lower losses and reduces secondary kinetic energy. Nagel and Baier [59] (Fig. 1.6, right) developed an integrated endwall/airfoil design using a gradient method in combination with CFD. Results predicted the so created blade/endwall geometry to significantly reduce total pressure loss and secondary kinetic energy; experiments verified these findings.

Laveau et al. [50] performed heat transfer measurements in a linear cascade with symmetric airfoils and contoured endwalls in the passage between the airfoils. The endwalls, shown in Fig. 1.8 (left), featured a basic contouring with one hill and one trough in the passage. Results showed reductions in heat transfer in divergent regions and increased heat transfer in convergent regions. CFD simulations revealed that the increased heat transfer is caused by a smaller core of the horseshoe vortex with higher intensity, whereas the heat transfer reductions are due to a larger core of the horseshoe vortex with reduced intensity. Lynch et al. [53] performed heat transfer measurements for the endwall contours of Praisner et al. [65] for the Pack-B low pressure airfoil. They found that the contoured endwall featured slightly lower overall heat transfer than the flat endwall. However, heat transfer rates were locally decreased by up to 20% for regions with high heat transfer, for example along the blade pressure side. Endwall oil flow visualization showed that this can be attributed to the fact that the contouring reduces the strength of the passage vortex. Saha and Acharya [68] were the first ones to systematically create turbine endwall contours to reduce endwall heat transfer. By scaling and multiplying analytical profiles in axial and circumferential direction, they created nine different endwall geometries and analyzed these using CFD. The simulations predicted their final contour (see Fig. 1.8, right) to reduce the area-averaged Nusselt number by 8% compared to the flat endwall baseline. For the endwall of a high pressure turbine blade, Panchal et al. [62] used an automated optimization loop with minimum average heat flux through the endwall as goal function. They analyzed the resulting heat transfer optimized

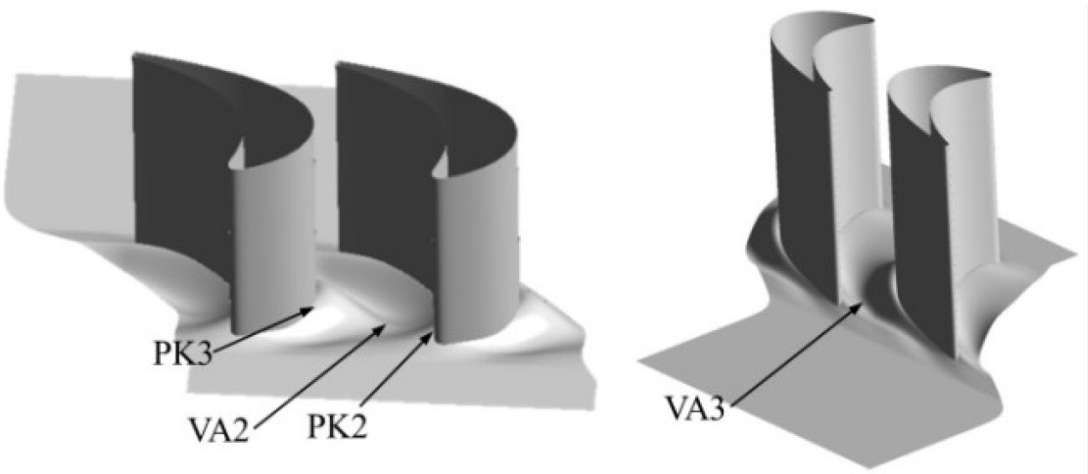

Figure 1.9: Heat transfer optimized endwall contour of Panchal et al. [62]

contour (see Fig. 1.9) experimentally using an infrared thermography technique and found a reduction of 15.6% for the average heat transfer coefficient. However, the contour also significantly increased the maximum heat transfer coefficient near the blade's leading edge.

1.4 Objectives and Thesis Outline

These days, the optimization of existing technical devices has become essential in product design to consistently improve device efficiency. In the field of turbomachinery, the contouring of the endwalls between the turbine vanes proved to be an effective method for such an optimization. The goal of this thesis is to generate novel turbine endwall contours which reduce endwall heat transfer. To create these contours two optimization approaches are employed: the Ice Formation Method, with experimental ice layers being taken from the study of Haase [26], and numerical optimization. The resulting endwall contours are carefully examined with respect to their flow field and heat transfer behavior and compared to a flat endwall as baseline. In this way, it can be investigated how geometric features change the flow structures in the vicinity of the endwall and thus affect endwall heat transfer.

This thesis is organized in seven chapters. Subsequent to this introduction, chapter 2 first describes the *fundamentals of the Ice Formation Method* and the *secondary flow features in guide vane passages*. The chapter continues by describing the *governing equations of fluid dynamics* and the *numerical methods* used to perform the CFD simulations and the numerical optimizations of this work. Chapter 3 shortly comments on the *experimental setup* used in the study of Haase [26] to create the experimental ice layers and then describes in depth the methodology used to obtain the *numerical setup* of this work. The chapter closes by introducing the *considered cases* of this study. In chapter 4, results for the most fundamental case of this work, the

ice-contoured endwalls with short cooling length, are presented. In the experiments of Haase [26], the underlying ice contours for this case were created on a cooled copper inlay that reaches from one chord length upstream of the vane leading edge to one chord length downstream of the trailing edge. After showing flow and heat transfer behavior for the flat endwall baseline, the chapter analyzes these parameters for the ice-contoured endwalls. Based on these results, entropy production rates are calculated for these contours and compared to the baseline. In the last part of this chapter, endwall contours are presented which were created by performing subsequent *numerical optimizations* on the ice-contoured endwalls. Chapter 5 presents the *results for the other cases* of this study: an ice-contoured endwall created from experiments with a longer cooling length (the cooled copper inlay here ranged from four axial cords upstream of the vane to four axial chords downstream of it), and endwall contours obtained from numerical optimizations based on the flat endwall. For these contours, the chapter explores how the contouring affects the near endwall flow and thus changes the heat transfer behavior. Chapter 6 finally analyzes the contours created in this study at the *design Reynolds number* of the used vane profile. The thesis ends with Chapter 7 *Conclusion and Outlook* summarizing the main findings and giving a short outlook.

2

Theoretical Background

Contents:
Fundamentals of the Ice Formation Method and the secondary flow features in turbine guide vanes - Presentation of governing fluid dynamic equations and numerical methods to solve them - Effects of turbulence and models to account for these - Genetic algorithm and Bézier curves used in the numerical optimization - Parameters for evaluating the results of this study

2.1 The Ice Formation Method

The formation of ice is a phenomenon that is well known from nature. Whenever the temperature of water is below its freezing temperature, the water changes its phase from liquid water to solid ice. In many technical applications such as pipe and channel flows, ice formation also plays an important role, especially in combination with convective flow. The specific characteristic of such an ice formation process is that the convective flow interacts with the ice layers, which form at undercooled surfaces of the flow geometry. Whereas the cooled surface extracts heat from the water and causes a solidification to ice, the flow introduces heat to the ice due to convective heat transfer and causes a melting of the ice. In many cases, these two processes balance each other after some time and the ice/water-interface reaches steady-state conditions, i. e. keeps its geometry. This state is characterized by a minimum energy exchange between the two phases and features a minimum in entropy production. To introduce the topic, the next paragraph presents the formation of ice layers in water flow using the example of a planar channel flow. This basic example is intended to give the reader an understanding of the physical background of the ice formation in convective flow. It shall facilitate the comprehension of the ice formation process for the complex case of the vane passage flow investigated in this work.

In general, a problem involving two phases is described by formulating equations for both phases separately and applying coupling equations that describe the interaction between them. For a planar channel flow with ice layers on its cooled walls, as shown in Fig. 2.1, the water phase is described by the conservation equations for mass, momentum, and energy, whereas for the ice phase only the energy equation is needed to account for heat conduction in the ice. Assuming the water as an incompressible, Newtonian fluid with constant fluid properties and a laminar boundary layer type

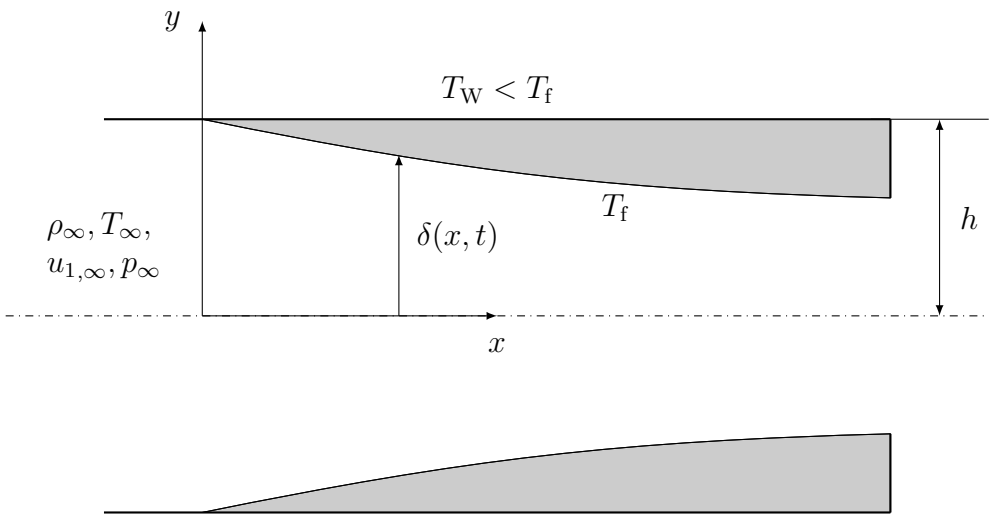

Figure 2.1: Ice formation in planar channel flow

flow, the conservation equations for mass, momentum, and energy take the following forms [74]

$$\frac{\partial u_1}{\partial x} + \frac{\partial u_2}{\partial y} = 0\,, \tag{2.1}$$

$$u_1\frac{\partial u_1}{\partial x} + u_2\frac{\partial u_1}{\partial y} = -\frac{1}{\rho}\frac{\partial p}{\partial x} + \nu\frac{\partial^2 u_1}{\partial y^2}\,, \tag{2.2}$$

and

$$u_1\frac{\partial T_{\text{water}}}{\partial x} + u_2\frac{\partial T_{\text{water}}}{\partial y} = \alpha\frac{\partial^2 T_{\text{water}}}{\partial y^2}\,, \tag{2.3}$$

where u_1 and u_2 denote the velocity components in x- and y-direction, p is the static pressure, T_{water} the static water temperature; ρ, ν, and α are, respectively, the density, kinematic viscosity, and thermal diffusivity of water. Note that in these equations, heat conduction in x-direction is neglected. Furthermore, the momentum equation in y-direction reduces to $\partial p/\partial y = 0$. The associated boundary conditions for the water phase are

$$\begin{aligned}
x &= 0: \quad p = p_\infty, \quad u_1 = u_{1,\infty}, \quad u_2 = 0, \quad T_{\text{water}} = T_\infty \\
y &= 0: \quad \frac{\partial T_{\text{water}}}{\partial y} = \frac{\partial u_1}{\partial y} = u_2 = 0 \\
y &= \delta: \quad u_2 = \frac{\rho_{\text{water}} - \rho_{\text{ice}}}{\rho_{\text{water}}}\frac{\partial \delta}{\partial t}, \quad u_1 = -u_2\frac{\partial \delta}{\partial x}, \quad T_{\text{water}} = T_{\text{f}}\,,
\end{aligned}$$

with ρ_{water} and ρ_{ice} being the densities of water and ice, δ the ice-free channel height, T_{f} the freezing temperature of water and the index ∞ denoting inlet values. Assuming constant properties for the ice phase and negligible axial conduction, the energy equation for the ice phase becomes

$$\frac{\partial^2 T_{\text{ice}}}{\partial y^2} = 0 \tag{2.4}$$

with the following boundary conditions

$$\begin{aligned}
y &= \delta: \quad T_{\text{ice}} = T_{\text{f}} \\
y &= h: \quad T_{\text{ice}} = T_W\,,
\end{aligned}$$

where T_{ice} is the static temperature of the ice layer, T_W the temperature of the wall, and h the channel's half height. In addition to these equations for the two phases water and ice, two further coupling conditions are needed to fully describe the ice formation problem. The first equation is an integral conservation of mass, that accounts for the fact that the water freezes to ice

$$u_{1,\infty}h = \int_0^\delta u_1\,\mathrm{d}y - \frac{\rho_{\text{water}} - \rho_{\text{ice}}}{\rho_{\text{water}}}\int_0^x \frac{\partial \delta}{\partial t}\,\mathrm{d}x\,. \tag{2.5}$$

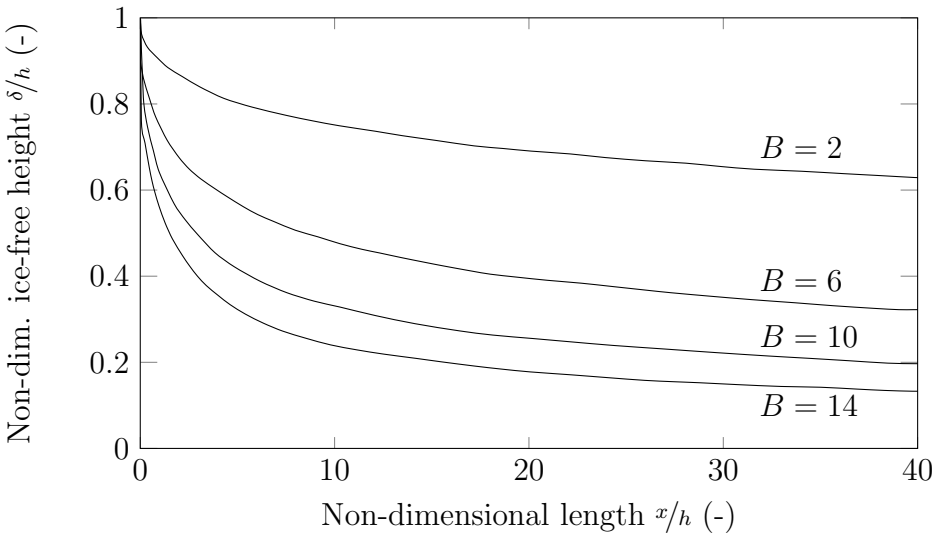

Figure 2.2: Dimensionless ice-layer profiles for planar channel flow; data from [74]

The second coupling equation describes an energy balance at the water/ice-interface ($y = \delta$) and takes the form

$$k_{\text{ice}} \frac{\partial T_{\text{ice}}}{\partial y} - k_{\text{water}} \frac{\partial T_{\text{water}}}{\partial y} = \rho_{\text{ice}} r_{\text{ice}} \frac{\partial \delta}{\partial t} \,, \tag{2.6}$$

where k_{ice} and k_{water} denote the thermal conductivities of ice and water, and r_{ice} is the heat of fusion. This interface energy equation states that the difference of heat conducted in the ice and water phase equals the heat arising from the phase change. In steady-state, the term on the right-hand side of the equation is zero and the heat fluxes in the ice and water phase equal each other.

For steady-state, Weigand and Beer [74] solved the system of equations above in the combined hydrodynamic and thermal entrance region. Figure 2.2 shows the resulting steady-state ice layers for a Reynolds number of $Re = 1{,}800$ and a Prandtl number of $Pr = 12$. The results are plotted in dependence on the dimensionless freezing parameter B, which was first defined by Oezisik and Mulligan [61] as

$$B = \frac{k_{\text{ice}}}{k_{\text{water}}} \frac{T_{\text{f}} - T_W}{T_\infty - T_{\text{f}}} \,. \tag{2.7}$$

This parameter relates the wall temperature to the water temperature at the inlet and hence is a metric for the thickness of the forming ice layer, which increases with rising values of B.

As the paragraph above showed, for simple flows, such as the flow in a flat plate channel or in a pipe, the problem of ice formation in convective flow can be fully described and analytically solved. However, for more complex problems like the three-dimensional flow through a turbine guide vane passage, as considered in this work, the problem becomes complicated, especially due to the presence of turbulence

and three-dimensional effects. Hence, no analytical solution exists for this type of flow and it can only be approached experimentally or numerically.

2.2 Secondary Flows in Guide Vane Passages

The secondary flows in guide vane rows of turbomachines have been vastly researched over the past decades [47,48,56,70,71]. Sieverding [72] and Langston [46] both give a comprehensive review on the secondary flow phenomena and the models derived from them. This section discusses the most important of these secondary flow features. It starts by explaining the formation of the horseshoe vortex around the leading edge, then describes the vortex structures in a single vane passage and concludes with describing the interactions of the vortices in a vane passage row.

Boelcs [8] studied the effects leading to the formation of the horseshoe vortex in a boundary layer flow approaching a cylinder. The circular cylinder thereby represents a fundamental geometric approximation of a vane profile leading edge and allows for investigation of the horseshoe vortex without the influence of the asymmetric

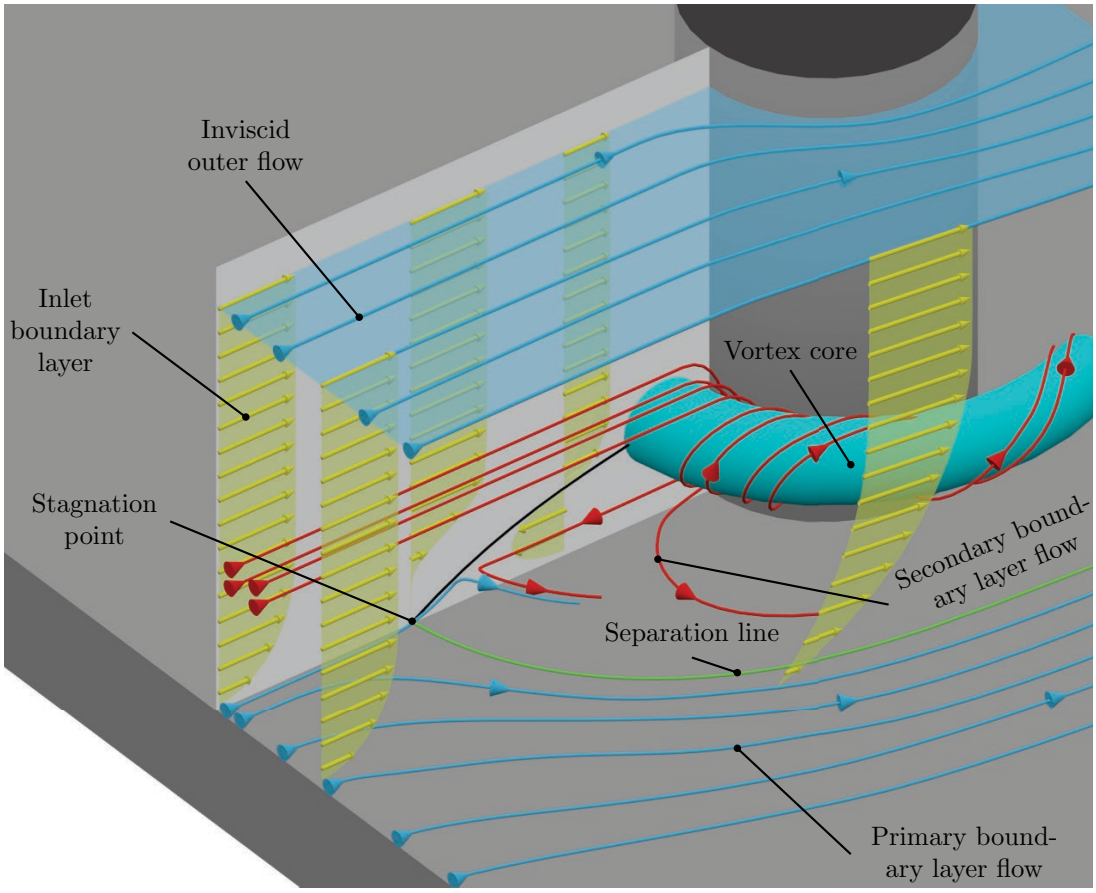

Figure 2.3: Formation of horseshoe vortex at cylinder on endwall, after [8]

pressure distribution of a vane profile. Figure 2.3 illustrates the flow phenomena around the cylinder. The cylinder's blockage effect slows down the approaching flow and converts its kinetic energy into static pressure. For the low momentum boundary layer this causes stagnating and reversed flow on the endwall upstream of the cylinder. Directly at the cylinder, the increase in static pressure is higher outside the boundary layer due to higher velocities and therefore a higher total pressure of the free stream flow. This causes a downwards pressure gradient and hence fluid flow towards the endwall. Therefore, the fluid rolls up into the horseshoe vortex at the front part of the cylinder. Upstream of the vortex core, the near endwall flow of the recirculation zone is deflected around the cylinder and forms a secondary boundary layer. The latter is divided from the primary endwall boundary layer at the separation line.

The horseshoe vortex described above is the main source for the vortex system in a vane cascade. However, in a vane row the vortex is significantly altered by the crosswise pressure gradient which exists in the vane passage between the pressure side of a vane profile and the adjacent vane's suction side. Figure 2.4 illustrates the vortex system in such a vane passage. It shows that the crosswise pressure gradient deflects the pressure side leg of the horseshoe vortex towards the suction side of the adjacent vane profile. In addition, this pressure gradient initiates a crossflow on the endwall between pressure and suction side of the vane passage. On its way through the passage, the pressure side leg is constantly fed by this crossflow and evolves into the passage vortex. This is the strongest and largest vortex of this flow

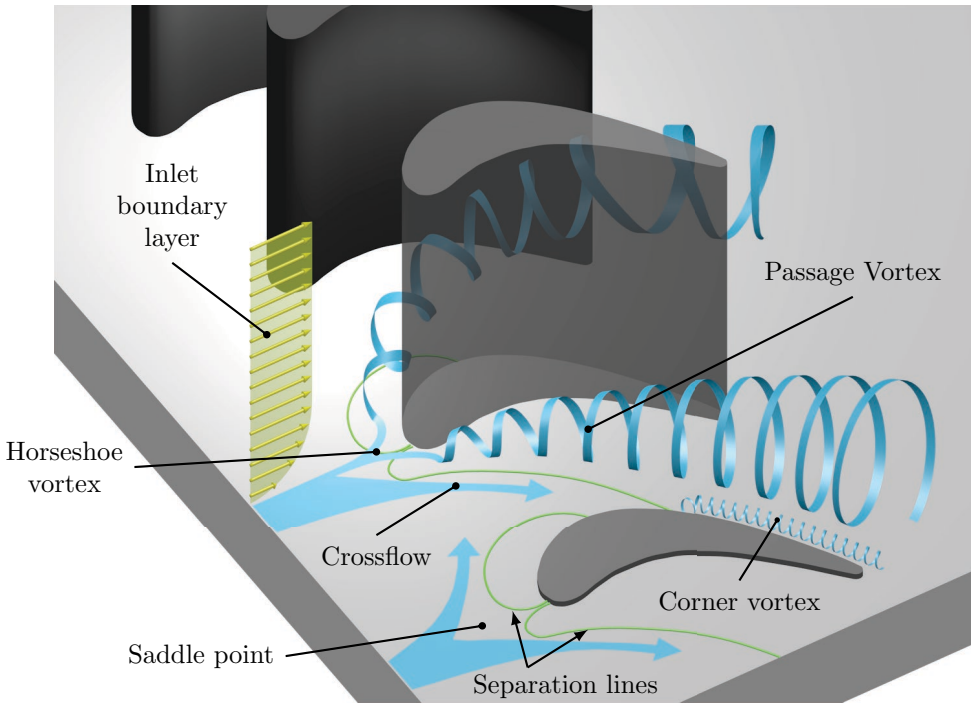

Figure 2.4: Flow features in guide vane row

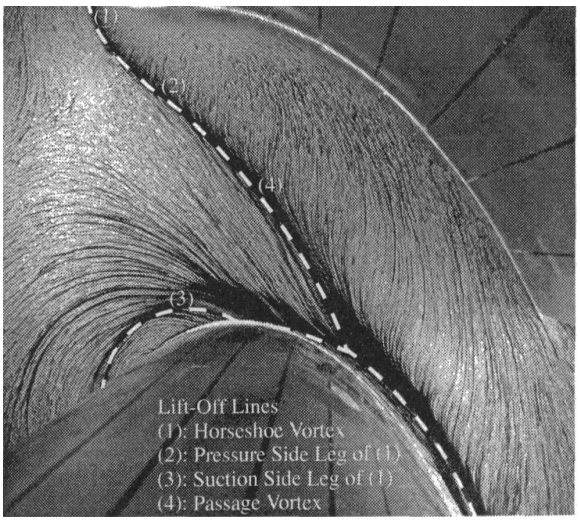

Figure 2.5: Oil flow visualization on vane endwall [23]

configuration. Therefore, the passage vortex also displaces the suction side leg of the horseshoe vortex. That is, the suction side leg moves upwards and hence away from the endwall as it travels along the vane profile. In addition, at their outer edges, the pressure and suction side legs of the horseshoe vortex deflect parts of the incoming boundary layer. This causes a saddle point region upstream of the vane, consisting of separation lines which divide the vortex legs from the remaining flow. At the position where the separation line of the pressure side leg encounters the neighboring vane, a further vortex occurs, the corner vortex.

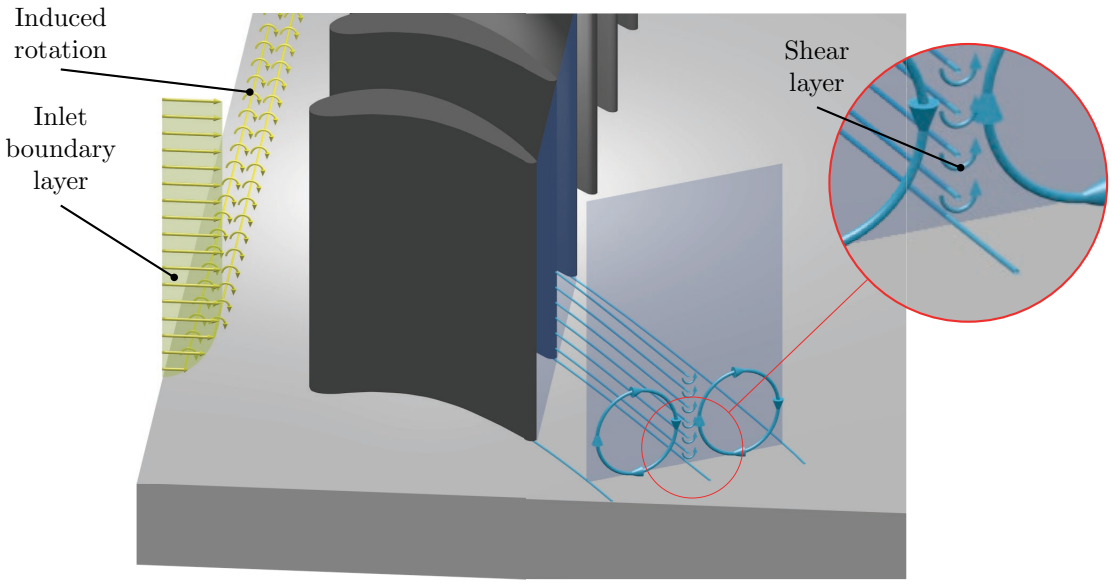

Figure 2.6: Interaction of neighboring passage vortices downstream of vane row

To show how these flow features affect the flow at the vane endwall, Friedrichs et al. [23] used an oil flow visualization technique to illustrate path lines on the endwall. Figure 2.5 shows the obtained result. The image clearly indicates the separation lines of the pressure and suction side legs of the horseshoe vortex and the passage vortex.

Due to its strength, the passage vortex only decays slowly and hence also dominates the flow downstream of the vane row. As Fig. 2.6 shows, this leads to an interaction of the passage vortices from neighboring vane passages. Hawthorne described this phenomenon in [30]. Since the neighboring vortices have the same direction of rotation, they induce vertical velocities with opposite sign in the region where they interact. This causes a shear layer inbetween the neighboring passage vortices, which leads to the formation of a small secondary vortex at the endwall.

2.3 Governing Equations of Fluid Dynamics

The flow characteristics of a fluid are governed by three physical principles: conservation of mass, momentum, and energy. These are mathematically described by their conservation equations. In general, such equations state that only two processes can cause a change of a physical variable in a control volume (CV): the production or destruction of the variable by sources/sinks within the control volume or the transport of the variable into or out of the CV by fluxes over its boundary. These fluxes can be divided into convective and diffusive fluxes. The former are associated with a mass-flux and describe the transport of the physical variable by the mean flow. The latter represent the transport of the variable by statistical fluctuations of the molecules. This process is linked to a non-uniform distribution of the variable and hence the existence of a concentration gradient. Mathematically, for a control volume CV, the conservation equation of a generic variable ϕ with its mass-specific value $\varphi = \phi/m$ is expressed as [69]

$$\iiint_{\mathrm{CV}} \underbrace{\frac{\partial}{\partial t}\left(\rho\varphi\right)}_{\substack{\text{Change}\\ \text{in time}}} \mathrm{d}V = \iiint_{\mathrm{CV}} \left[\underbrace{\frac{\partial}{\partial x_j}\left(\Gamma \frac{\partial \varphi}{\partial x_j}\right)}_{\text{Diffusive flux}} - \underbrace{\frac{\partial}{\partial x_j}\left(\rho u_j \varphi\right)}_{\text{Convective flux}} + \underbrace{S_\varphi}_{\substack{\text{Sources/}\\ \text{sinks}}} \right] \mathrm{d}V \,, \tag{2.8}$$

where t indicates time and ρ is the fluid's density; Γ is the diffusion coefficient, S are sources or sinks and x_j and u_j are, respectively, the spatial coordinates and velocity components in the j-th direction. For a stationary flow, in which the flow variables do not change with time, the conservation equation reduces to a balance equation. In this case, all fluxes through the CV's surface and all sources/sinks inside the CV balance each other. In differential form, this balance equation is written, using Einstein summation convention, for the generic variable φ as

$$\frac{\partial}{\partial x_j}\left(\rho u_j \varphi\right) = \frac{\partial}{\partial x_j}\left(\Gamma \frac{\partial \varphi}{\partial x_j}\right) + S_\varphi \,. \tag{2.9}$$

For the physical quantity mass m, with $\phi = m$ and $\varphi = 1$, this balance equation becomes the *Continuity Equation*. Since mass can neither be created nor destroyed, this equation does not have a source term. Furthermore, there is no diffusive flux of mass, the transport of mass is always linked to a mass flux. This yields

$$\frac{\partial}{\partial x_j}\left(\rho u_j\right) = 0\,. \tag{2.10}$$

Considering the conservation of momentum ($\phi_i = mu_i$, $\varphi_i = u_i$) and assuming a Newtonian fluid, the balance equation turns into the *Navier-Stokes-Equations*

$$\frac{\partial}{\partial x_j}\left(\rho u_j u_i\right) = \frac{\partial}{\partial x_j}\left(\mu \frac{\partial u_i}{\partial x_j}\right) - \frac{\partial p}{\partial x_i} + f_i\,. \tag{2.11}$$

In the equation above, μ is the dynamic viscosity of the fluid, p its static pressure and f_i the body force in the i-th direction. Note that the velocity gradient causes a diffusive flux of momentum, whereas both the static pressure gradient and the body force f_i constitute source terms for momentum. By using the caloric equation of state $\mathrm{d}h = c_p\,\mathrm{d}T$, the *Energy Equation* for a fluid is written as

$$\frac{\partial}{\partial x_j}\left(\rho u_j c_p T\right) = \frac{\partial}{\partial x_j}\left(k \frac{\partial T}{\partial x_j}\right) + u_i \frac{\partial p}{\partial x_i} + \mu\Phi\,, \tag{2.12}$$

with c_p being the heat capacity at constant pressure, T the static temperature, k the thermal conductivity of the fluid, and Φ the dissipation function. A diffusive flux of thermal energy occurs due to work done by both pressure forces and by heat conduction. The last term on the right-hand side of the equation represents a source for thermal energy. It describes the conversion of kinetic energy into thermal energy by the action of viscous forces. This phenomenon is known as dissipation.

In order to make the system of equations solvable, a further equation is needed, which describes the relation between the state variables of the fluid. For an ideal gas, this is the *Thermal Equation of State*

$$p = \rho R T\,, \tag{2.13}$$

where R is the specific gas constant.

2.4 Numerical Methods

The governing equations are a set of coupled, non-linear partial differential equations and hence can only be solved analytically for a few simple flow problems. For all other flows, numerical methods are used to obtain an approximate solution of the system of equations. Such methods use the following approach. First, they divide the solution domain into a discrete number of control volumes CV. Then, the system

of equations is converted into algebraic equations by discretizing the convective and diffusive fluxes of the equations, formulated for each CV. Finally, the discretized equation system is solved iteratively. The following sections in brief describe those methods relevant for this work; for more detail the reader is referred to standard literature [2, 22, 69].

2.4.1 Grid Generation

In a finite volume method approach, the process of grid generation separates the solution domain into cells, each representing a control volume limited by its surfaces. Every cell holds discrete values for all flow variables, usually stored in its center, and exchanges information with its neighboring cells via fluxes through their surfaces. The accuracy of the numerical solution strongly depends on the correct calculation of these fluxes. Besides the method used for their discretization (see next section), the geometry of the grid cells plays an important role for the determination of the surface fluxes. In this regard, the angle ϑ between the normal vector of a surface that separates two cells and the line connecting their cell centers is especially important for the flux calculation. Figure 2.7 (left) illustrates this angle using the example of two neighboring cells. The ideal cell geometry is a cuboid with all neighboring surfaces being perpendicular to each other and ϑ becoming zero. Every deviation from this ideal geometry introduces an error in the calculation of the surface fluxes.

Since the solution domains of complex geometries can hardly be discretized by cuboids, quality criteria are defined for the grid cells to keep the introduced errors low. One quality criterion, which is a measure for the angle ϑ in all spatial directions, is the skewness of the cells, or equivalently, the minimum angle between its neighboring faces. This angle should always be larger than 20°. Two further quality criteria that address the grid generation in boundary layers are the wall normal cell growth rate, Fig. 2.7 (middle), and the cell aspect ratio, Fig. 2.7 (right). In contrast to the flow outside the boundary layer, flow variables change rapidly near walls, causing high gradients in this region. Thus, it is common to use cells with small height at the

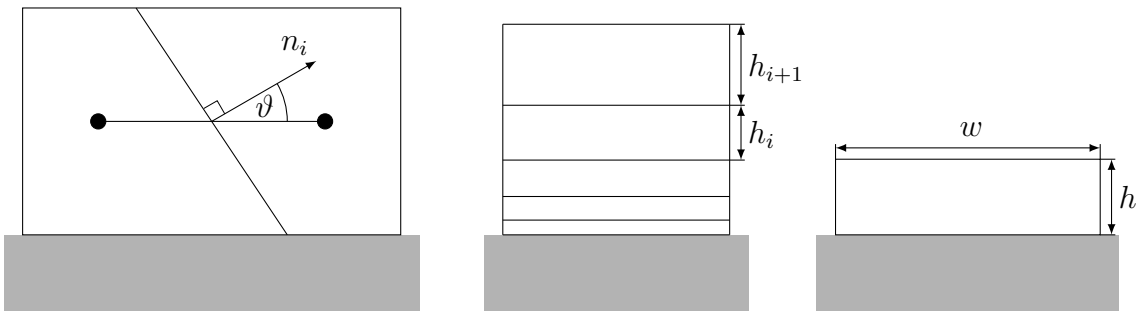

Figure 2.7: Grid quality criteria: Angle ϑ between line connecting cell centroids and surface normal (left), wall normal growth rate (middle), and cell aspect ratio (right)

wall to resolve the steep gradients and gradually grow the cell height with increasing distance from the wall. For reasons of numerical precision, this growth rate should not exceed a value of $h_{i+1}/h_i = 1.25$. The aspect ratio describes the ratio of the longest edge of a cell to its smallest one and should be below $w/h = 1{,}000$ for the used numerical solver. This criterion is important at walls, where gradients are high in wall normal direction but low parallel to the wall, resulting in thin long cells.

In the present work, I created all grids with the grid generator CENTAUR [15]. It allows for the automatic generation of grids with specified quality criteria and can hence be efficiently integrated in the numerical optimization process used to create the optimized endwall contours. The program constructs the volumetric grids in three steps. First, a surface mesh is generated on each wall, with cells being clustered in regions with high gradients, e.g. at the vane endwall junction. In the second step, this surface mesh is extruded in wall normal direction to resolve the wall boundary layers with prismatic cells. The remaining solution domain is in the third and final step filled with tetrahedral cells. For all grids of the present work, I chose the settings for grid generation in such a way that the dimensionless near wall distance of the first cells at walls was $y_1^+ \approx 1$ and the aforementioned quality criteria were fulfilled.

2.4.2 Finite Volume Method

The Finite Volume Method (FVM) is a popular approach in CFD, which formulates the conservation equations for each cell of the numerical grid as control volume CV. Taking into account initial and boundary conditions, the resulting system of equations is then solved while the convective and diffusive fluxes over all cell surfaces are explicitly calculated. Hence, the method is by definition conservative, that is, all balance equations are satisfied locally for every cell of the grid as well as globally for the entire solution domain. The mathematical basis for the FVM is the generic transport equation in integral form, see Eq. (2.8). Since I only simulated stationary flows in this work, this equation becomes

$$\iiint_{\mathrm{CV}} \Bigg[\underbrace{\frac{\partial}{\partial x_j}\left(\Gamma \frac{\partial \varphi}{\partial x_j}\right)}_{\text{Diffusive flux}} - \underbrace{\frac{\partial}{\partial x_j}\left(\rho u_j \varphi\right)}_{\text{Convective flux}} + \underbrace{S_\varphi}_{\substack{\text{Sources/}\\ \text{sinks}}} \Bigg] \mathrm{d}V = 0\,, \tag{2.14}$$

where CV indicates the control volume, i.e. the volume of each cell of the numerical mesh. Using the Gaussian divergence theorem, the convective and diffusive fluxes through the cell surfaces are transformed from volume to surface integrals, yielding

$$\underbrace{\iint_S \left(\Gamma \frac{\partial \varphi}{\partial x_j}\right) \mathrm{d}S}_{\text{Diffusive flux}} - \underbrace{\iint_S \left(\rho u_j \varphi\right) \mathrm{d}S}_{\text{Convective flux}} + \underbrace{\iiint_{\mathrm{CV}} S_\varphi \, \mathrm{d}V}_{\text{Sources/ sinks}} = 0\,, \tag{2.15}$$

with S being the cell surface.

As stated before, the system of equations is not solvable in its partial differential formulation. Hence, the derivatives in the diffusive fluxes as well as the surface and volume integrals are numerically discretized to convert the system of equations into an algebraic formulation. Furthermore, the method assumes all flow variables constant across each cell of the numerical grid and stores their values in the cell centroid. However, for calculating the convective and diffusive fluxes through the cell's bounding surfaces, the flow variables are needed at the surface itself. This requires the use of a numerical interpolation scheme, that determines the values for the flow variables at the surface from the values at the cell centroids. Finally, the flow variables need to be integrated over the control volume. The following paragraphs outline the numerical discretization methods used in this work for differentiation, interpolation and integration of the governing equations.

Numerical Differentiation The numerical differentiation is used to approximate the spatial gradients of the diffusive flux terms at cell faces and to calculate the derivatives of certain variables, for example the velocity, at cell centroids. Both gradient types are derived by exploiting information from the neighboring cells. Figure 2.8 shows a generic cell of the numerical grid and the cells surrounding it. The cell and face centers are shown as dots and crosses, respectively, and are labeled with north (N, n), east (E, e), south (S, s), and west (W, w).

The CFD Program ANSYS® Fluent used in this work determines the spatial gradients at the cell faces with a central differencing scheme (CDS). Assuming a linear variation of the generic variable φ, this yields the variable's derivative at the eastern cell face in Fig. 2.8 as

$$\left(\frac{\partial \varphi}{\partial x}\right)_{\mathrm{e}} = \frac{\varphi_{\mathrm{E}} - \varphi_{\mathrm{C}}}{x_{\mathrm{E}} - x_{\mathrm{C}}} \,. \tag{2.16}$$

The derivatives at the other cell faces are calculated accordingly; due to the linear variation, this discretization scheme is second-order accurate.

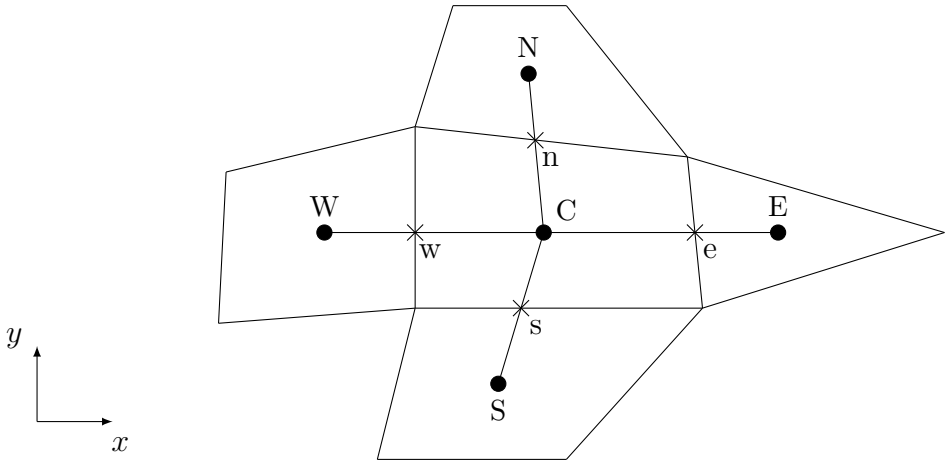

Figure 2.8: Generic cell of numerical grid with its neighboring cells

To calculate necessary gradients at the cell centroid, Fluent uses a cell-centroid-based least square approximation. In two dimensions, the gradient at the cell centroid C takes the form

$$\left(\frac{\partial\varphi}{\partial x_i}\right)_{\mathrm{C}} = \left(\frac{\partial\varphi}{\partial x}\right)_{\mathrm{C}} n_x + \left(\frac{\partial\varphi}{\partial y}\right)_{\mathrm{C}} n_y \,, \tag{2.17}$$

with n_x and n_y being the unit vectors in the two spatial directions x and y. Assuming again a linear variation of the flow variables, this gradient can be expressed with the values at the cell centroids of two neighboring cells. For the eastern, neighboring cell of Fig. 2.8, this gradient becomes

$$\left(\frac{\partial\varphi}{\partial x_i}\right)_{\mathrm{C}} \cdot \overline{\mathrm{CE}} = \varphi_{\mathrm{E}} - \varphi_{\mathrm{C}} \,, \tag{2.18}$$

where $\overline{\mathrm{CE}}$ is the distance between the central and eastern cell centroids. In the same manner, additional equations can be derived for the other three surrounding cells. This yields a linear system of equations of the form

$$[J] \left(\frac{\partial\varphi}{\partial x_i}\right)_{\mathrm{C}} = \Delta\varphi \,, \tag{2.19}$$

where $\Delta\varphi$ is the difference of the generic variable φ between two neighboring cell centroids and the coefficient matrix $[J]$ is purely a function of the grid geometry and determined by the latter. This system of equations is over-determined, since there are four equations for the two unknown components of the gradient. Fluent solves this system by least square fitting of the gradient vector using the Gram-Schmidt process [1] to decompose the coefficient matrix. Further information on this solution approach is found in the Fluent theory guide [3]. The extension of this approach to a three-dimensional grid is straightforward, yielding a system of six equations for the three unknown components of the gradient vector.

Numerical Interpolation To calculate the convective fluxes over the bounding surfaces of a grid cell, the value of the flux variable needs to be known at the surface S. Since the variable values are stored at the cell centroids, the value at the surface needs to be interpolated from the cell centroids of those cells that share the surface. The easiest way to do this is the first order upwind interpolation, which simply assumes that the variable value at the surface is the same as in the upstream cell centroid. Considering the example grid from Fig. 2.8 and assuming a flow in the positive x-direction, the value of the generic variable φ on the eastern cell surface (e) is determined as

$$\varphi_{\mathrm{e}} = \varphi_{\mathrm{C}} \,. \tag{2.20}$$

Based on the same idea, a second-order upwind scheme can be constructed using the first two terms of a Taylor series around the upstream cell centroid. Hence, the surface value of φ becomes

$$\varphi_{\mathrm{e}} = \varphi_{\mathrm{C}} + \left(\frac{\partial\varphi}{\partial x_i}\right)_{\mathrm{C}} \overline{\mathrm{Ce}} \,, \tag{2.21}$$

where $\overline{\mathrm{Ce}}$ is the distance between the cell centroid C of the upstream cell to the eastern face center e. Since terms of third order and higher are neglected in the used Taylor series, this scheme is of second-order accuracy. The gradient needed for this scheme at the upstream cell centroid is calculated as described above. For the numerical simulations of this work, I used the above second-order upwind scheme with the least squares gradient approximation to interpolate variable values at cell surfaces.

Numerical Integration The formulation of the conservation equations in integral form, see Eq. (2.8), requires the determination of both surface and volume integrals. Surface integrals are needed to compute the convective and diffusive fluxes through the cell's surfaces, whereas the production/destruction of a variable within a grid cell is determined via volume integrals. Both integral types are calculated using the midpoint rule, which performs the integration by simple multiplication with the appropriate cell volume or cell surface area, respectively. For the surface integrals of the convective and diffusive fluxes, this yields, exemplarily for the northern cell surface in Fig. 2.8

$$\iint_S \left(\Gamma \frac{\partial \varphi}{\partial x_j}\right) \mathrm{d}S = \left(\Gamma \frac{\partial \varphi}{\partial x_j}\right)_{\mathrm{n}} \Delta S_{\mathrm{n}} \,, \tag{2.22}$$

and

$$\iint_S \left(\rho u_j \varphi\right) \mathrm{d}S = \left(\rho u_j \varphi\right)_{\mathrm{n}} \Delta S_{\mathrm{n}} \,, \tag{2.23}$$

where the subscript n indicates a value at the center of the northern cell surface and ΔS_{n} is the area of this surface. The fluxes through the other cell surfaces are determined accordingly.

For the volume integral, which describes production/destruction of a variable inside the grid cell, the numerically approximated volume integral becomes

$$\iiint_{\mathrm{CV}} S_\varphi \, \mathrm{d}V = \left(S_\varphi\right)_{\mathrm{C}} \Delta V \,, \tag{2.24}$$

the subscript C denoting a value at the cell centroid and ΔV being the volume of the grid cell.

Solution Algorithm To solve the system of discretized equations numerically, I selected the SIMPLE algorithm in Fluent. This algorithm is specifically designed to solve pressure-linked equations in fluid dynamics for steady-state flows. To resolve pressure-velocity coupling, it employs a pressure correction equation based on the continuity equation. Using this pressure-equation, the algorithm solves the momentum equations in a predictor-corrector approach. Further information on this algorithm is provided in [63].

2.4.3 Assessment of Numerical Errors

The solution of a numerical simulation only approximates the physics of the considered flow problem, but does not exactly agree with it. Reasons for this deviation are *modeling errors* done when deriving the conservation equations, *discretization errors* due to the discretization of these equations and the discretization of the solution domain by a numerical grid, *round-off errors* owing to the floating point precision of the computer system, and *iteration errors* caused by the iterative solution of the equation system.

Modeling Errors These errors describe the difference between the actual physics and its mathematical representation by equations. They are mainly related to the assumptions made during the derivation of the conservation equations. Especially the equations for turbulence modeling, as discussed in the next section, contain many simplifications, which contribute to this type of error. Also the formulation of the initial and boundary conditions of the flow problem can add to the modeling error. To keep modeling errors low, I used a well-verified turbulence model and boundary conditions that have proven favorable for the considered flow problem.

Discretization Errors The discretization errors represent the deviation of the exact solution of the transport equations to the exact solution of the discretized equations. This error type strongly depends on the discretization schemes used for the convective and diffusive fluxes in combination with the numerical grid used for spatial discretization of the solution domain. For minimization of the discretization errors, I only used second-order accurate discretization schemes in the equations and discretized the solution domains with high resolution grids, that followed the grid quality criteria mentioned before. To quantify the discretization errors, Roache [67] established the GCI method, which has become best practice for numerical simulations. In this work, I determined the GCI for the baseline case of the flat endwall and further selected endwall contours to assess the discretization errors for the performed numerical simulations.

Iteration Errors The numerical solver does not yield an exact solution of the discretized system of equations, but iteratively approaches this solution. This means that the system of equations is solved in such a way that a residual remains in each equation, which is the difference between the exact and numerical solution of the discretized equation. This residual characterizes the iteration errors. With increasing number of iterations performed in the numerical solution process, this residual is successively lessened and the iterative solution converges towards the exact solution of the discretized equation system. In the present work, I ran all simulations for as many iterations until the residuals stopped decreasing and became constant. At this stage, all residuals had dropped at least three orders of magnitude from their initial values, often even five or six orders of magnitude, and convergence of the iterative solution could be assumed.

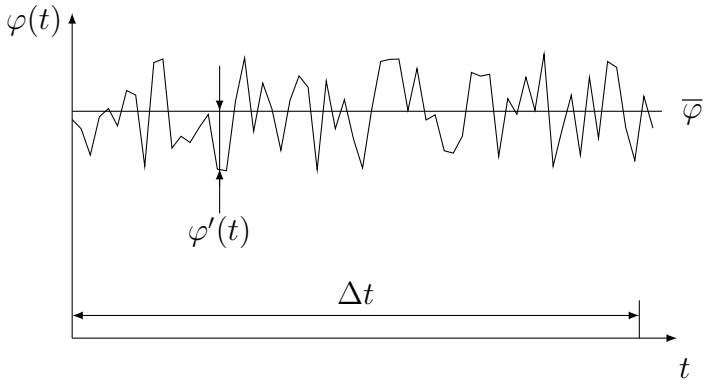

Figure 2.9: Decomposition of generic variable $\varphi(t)$

Round-off Errors Since computer systems can only store a finite number of digits for floating point values, they perform all computations with approximated instead of exact values. The digits neglected when storing or computing with the numerical values cause the round-off errors. They are diminished by using the double precision floating point format, which describes numerical values with a precision of 16 significant decimal digits. Double precision was used in all simulations of this work.

2.5 Turbulence Modeling

In general, the conservation equations from Sec. 2.3 describe all types of flows, including both laminar and turbulent ones. The latter are characterized by random fluctuations of the flow variables, which are superimposed on the mean flow motion. These fluctuations occur over a wide range of scales, from large ones to the smallest ones, the so-called Kolmogorov scale (see e. g. [64]). Describing such flows by the conservation equations requires the resolution of all these scales in time and space and hence a great effort. Therefore, this approach of Direct Numerical Simulation (DNS) is only used in fundamental research for selected flow types. In many engineering applications, however, one is rather interested in the overall effects of the flow and not in the specific details of all flow variables. Hence, instead of resolving all scales of the turbulent fluctuations, one can account for these fluctuations by modeling their effect on the mean flow. This modeling of turbulence is the subject of the following subsections.

2.5.1 Reynolds-Averaged Navier-Stokes Equations

Osborne Reynolds [66] first developed an approach for modeling the effects of turbulence on fluid flow. For a statistically steady flow, he proposed to separate the instantaneous variable $\varphi(x_i, t)$ into a time-averaged and a fluctuating part

$$\varphi(x_i, t) = \overline{\varphi}(x_i) + \varphi'(x_i, t)\,, \tag{2.25}$$

where the overbar indicates a time-averaged and the prime a fluctuating quantity. Figure 2.9 illustrates this idea. The time-averaged value is defined as

$$\overline{\varphi}(x_i) = \lim_{\Delta t \to \infty} \frac{1}{\Delta t} \int_t^{t+\Delta t} \varphi(x_i, t)\, \mathrm{d}t\,, \tag{2.26}$$

with the time interval Δt being much larger than the time scale of the turbulent fluctuations.

To apply this concept to the conservation equations, all instantaneous variables are replaced by the sum of their average and fluctuating value and the equations are time-averaged. This yields the *Reynolds-Averaged Navier-Stokes (RANS) Equations*

$$\frac{\partial}{\partial x_j}\left(\rho \overline{u}_j\right) = 0 \tag{2.27}$$

$$\frac{\partial}{\partial x_j}\left(\rho \overline{u}_j \overline{u}_i\right) = \frac{\partial}{\partial x_j}\left(\mu \frac{\partial \overline{u}_i}{\partial x_j} - \rho \overline{u_i' u_j'}\right) - \frac{\partial \overline{p}}{\partial x_i} + \overline{f}_i \tag{2.28}$$

$$\frac{\partial}{\partial x_j}\left(\rho \overline{u_j} c_p \overline{T}\right) = \frac{\partial}{\partial x_j}\left(k \frac{\partial \overline{T}}{\partial x_j} - \rho c_p \overline{u_i' T'}\right)\,. \tag{2.29}$$

These equations solely depend upon averaged flow quantities. However, due to the non-linearity of the convective fluxes, one additional term appears in both the momentum and the energy equation: the *Reynolds stress tensor* $-\rho\overline{u_i' u_j'}$ and the *turbulent heat flux vector* $-\rho c_p \overline{u_i' T'}$. These terms represent the diffusive flux of momentum and heat due to the action of the turbulent fluctuations. Note that these fluxes act both in the direction of the mean flow, i.e. along the streamlines, and perpendicular to it.

The additional terms that appear due to the time averaging render the system of equations insoluble since there are more unknowns than equations. This is known as the *closure problem* of turbulence. Hence, additional equations must be derived which describe the new unknowns by known quantities, that is the mean flow quantities. Such equations are called turbulence models and are described in the following.

2.5.2 Turbulence Models

To derive a model for the Reynolds stress tensor, Boussinesq assumed turbulence to affect the flow like an additional viscosity. This hypothesis stems from the analogy with laminar flows, for which it is the viscosity that causes a diffusive flux of momentum and energy dissipation normal to the streamlines. From the phenomenological point of view, this approach directly models the increased diffusivity observed in turbulent flow. Turbulence models which use this approach are termed *turbulent* or *eddy viscosity models*.

The following paragraphs first introduce the concept of the eddy viscosity and then present selected turbulence models which use this idea. Before presenting the shear

stress transport model (SST) that was used for the numerical simulations in this study, the k-ϵ and k-ω model are discussed, since they form the basis for the SST model.

The Eddy Viscosity Hypothesis The concept of eddy viscosity was proposed by Boussinesq in 1877 [9]. Assuming an analogy between molecular and turbulent diffusion, he suggested to model the Reynolds stress tensor as being linearly proportional to the mean rate of strain tensor S_{ij}

$$-\rho\overline{u_i' u_j'} = 2\mu_t S_{ij} - \frac{2}{3}\delta_{ij}\rho k\,, \tag{2.30}$$

with the mean rate of strain tensor being defined as

$$S_{ij} = \frac{1}{2}\left(\frac{\partial \overline{u}_i}{\partial x_j} + \frac{\partial \overline{u}_j}{\partial x_i}\right)\,. \tag{2.31}$$

This yields the Reynolds stresses

$$-\rho\overline{u_i' u_j'} = \mu_t\left(\frac{\partial \overline{u}_i}{\partial x_j} + \frac{\partial \overline{u}_j}{\partial x_i}\right) - \frac{2}{3}\delta_{ij}\rho k\,. \tag{2.32}$$

In the equation above, δ_{ij} is the Kronecker delta and k the turbulence kinetic energy, which is presented in detail later on when discussing the turbulence models. The variable μ_t is the *turbulent* or *eddy viscosity*. In contrast to the molecular viscosity μ, the eddy viscosity is not a function of the fluid but of the flow. It depends on the local flow condition and scales with the prevailing turbulence activity.

In addition to the Reynolds stress tensor, the turbulent heat flux vector is also unknown and requires modeling. Within the framework of the eddy viscosity concept, it is modeled by a gradient-diffusion approach, analogous to Fourier's law of heat conduction, as

$$-\rho c_p\overline{u_i' T'} = \rho\alpha_t\frac{\partial \overline{T}}{\partial x_i}\,, \tag{2.33}$$

with α_t being the *eddy* or *turbulent thermal diffusivity*. It is linked to the turbulent viscosity via the *turbulent Prandtl number*

$$Pr_t = \frac{\nu_t}{\alpha_t}\,, \tag{2.34}$$

where ν_t is the kinematic turbulent viscosity, $\nu_t = \mu_t/\rho$. Like the eddy viscosity, the eddy diffusivity is no material property but a function of the flow. Except for the smallest length scales, both the eddy viscosity and the eddy diffusivity are driven by the same physical process, i.e. the increased diffusivity caused by the turbulent fluctuations. For many types of flows, the turbulent Prandtl number can therefore in good approximation be assumed constant. Hence, one only needs to provide a turbulence model for the eddy viscosity.

Note that the introduction of the eddy viscosity does not constitute a solution to the closure problem yet. Although it provides a description for the Reynolds stress tensor and the turbulent heat flux vector, the eddy viscosity itself remains undefined. It is the task of the turbulence model to provide equations that allow for the calculation of this quantity. The starting point of many turbulence models thereby is a dimensional analysis. This analysis shows that the turbulent viscosity can be assumed to be proportional to a velocity and a length scale

$$\nu_t = C_\mu \times (\text{length scale}) \times (\text{velocity scale}) \,, \tag{2.35}$$

where C_μ is a dimensionless constant and the length and velocity scales are usually associated with the large scale turbulent motions of the flow. Depending on the number of transport equations used to mathematically express this equation, eddy viscosity models are divided into three categories: zero-, one-, and two-equation models. While zero-equation models only use algebraic expressions, one-equation models employ one differential equation for the velocity scale and two-equation models add a second transport equation for the turbulent length scale. The SST model, which was used in this thesis, as well as the k-ϵ and k-ω models, on which it is based, belong to the class of two-equation turbulence models. These models are presented next.

***k*-ϵ Turbulence Model** The standard k-ϵ model was introduced by Launder and Spalding [49] and is one of the most common two-equation turbulence models. It uses two additional variables to determine the eddy viscosity: the turbulence kinetic energy k and its rate of dissipation ϵ. Thus, the eddy viscosity becomes

$$\nu_t = C_\mu \frac{k^2}{\epsilon} \,. \tag{2.36}$$

In this equation, the turbulence kinetic energy k represents the velocity scale of the turbulent motion. It was originally defined by Reynolds as

$$k = \frac{1}{2}\overline{u_i' u_i'} = \frac{1}{2}\left(\overline{u_1' u_1'} + \overline{u_2' u_2'} + \overline{u_3' u_3'}\right) \,. \tag{2.37}$$

The turbulent length scale is implicitly defined by the dissipation rate ϵ. Assuming a turbulent flow with equilibrium between production and dissipation of turbulence kinetic energy, it holds

$$\epsilon \approx \frac{k^{\frac{3}{2}}}{l} \,. \tag{2.38}$$

To calculate the eddy viscosity, the following two transport equations for k and ϵ are solved

$$\frac{\partial}{\partial x_j}\left(\overline{u_j} k\right) = \nu_t \frac{\partial \overline{u}_i}{\partial x_j}\left(\frac{\partial \overline{u}_i}{\partial x_j} + \frac{\partial \overline{u}_j}{\partial x_i}\right) + \frac{\partial}{\partial x_j}\left[\left(\nu + \frac{\nu_t}{\sigma_k}\right)\frac{\partial k}{\partial x_j}\right] - \epsilon \tag{2.39}$$

$$\frac{\partial}{\partial x_j}\left(\overline{u_j} \epsilon\right) = C_{\epsilon 1} \nu_t \frac{\epsilon}{k} \frac{\partial \overline{u}_i}{\partial x_j}\left(\frac{\partial \overline{u}_i}{\partial x_j} + \frac{\partial \overline{u}_j}{\partial x_i}\right) + \frac{\partial}{\partial x_j}\left[\left(\nu + \frac{\nu_t}{\sigma_\epsilon}\right)\frac{\partial \epsilon}{\partial x_j}\right] - C_{\epsilon 2}\frac{\epsilon^2}{k} \,, \tag{2.40}$$

with the coefficients being empirically determined as

$$C_\mu = 0.09, \quad \sigma_k = 1.0, \quad \sigma_\epsilon = 1.3, \quad C_{\epsilon 1} = 1.44, \quad C_{\epsilon 2} = 1.92\,.$$

Due to its robustness and the fact that it yields good results for fully turbulent flow at high Reynolds numbers, this model is commonly used in engineering applications. However, the model has a deficiency in predicting turbulence in the near-wall region. As a consequence, it provides only poor results for heat transfer at solid walls and has problems predicting the position for detachment and reattachment of separated boundary layers, especially in the presence of adverse pressure gradients. The current thesis deals with both, heat transfer at the endwall and flow detachment, e.g. the rolling up of the boundary layer into the horseshoe vortex. Hence, the standard k-ϵ model is not used in this work.

***k*-ω Turbulence Model** Wilcox [77] proposed an alternative two-equation model, that uses a transport equation for the turbulence frequency ω instead of the dissipation rate ϵ. Thus, the eddy viscosity is evaluated from

$$\nu_t = \frac{k}{\omega}\,. \tag{2.41}$$

The variable ω represents the frequency of the smallest turbulent eddies which dissipate the turbulence kinetic energy. It is defined as

$$\omega = \frac{\epsilon}{\beta^* k}\,. \tag{2.42}$$

Hence, this variable can also be interpreted as a specific dissipation rate. The transport equations for the two variables of this model are:

$$\frac{\partial}{\partial x_j}\left(\overline{u_j} k\right) = \nu_t \frac{\partial \overline{u}_i}{\partial x_j}\left(\frac{\partial \overline{u}_i}{\partial x_j} + \frac{\partial \overline{u}_j}{\partial x_i}\right) + \frac{\partial}{\partial x_j}\left[\left(\nu + \frac{\nu_t}{\sigma_k^*}\right)\frac{\partial k}{\partial x_j}\right] - \beta^* k\omega \tag{2.43}$$

$$\frac{\partial}{\partial x_j}\left(\overline{u_j} \omega\right) = \alpha_\omega \nu_t \frac{\omega}{k}\frac{\partial \overline{u}_i}{\partial x_j}\left(\frac{\partial \overline{u}_i}{\partial x_j} + \frac{\partial \overline{u}_j}{\partial x_i}\right) + \frac{\partial}{\partial x_j}\left[\left(\nu + \frac{\nu_t}{\sigma_\omega}\right)\frac{\partial \omega}{\partial x_j}\right] - \beta\omega^2\,. \tag{2.44}$$

The empirical coefficients in these equations take the values

$$\alpha_\omega = {}^5\!/_9, \quad \beta = 0.075, \quad \beta^* = 0.09, \quad \sigma_k^* = 2.0, \quad \sigma_\omega = 2.0\,.$$

For the near-wall treatment, the k-ω model uses a low-Reynolds-number formulation and hence yields more accurate results in the near-wall region than the k-ϵ turbulence model. However, the k-ω model is strongly sensitive to free stream conditions and therefore inferior to the k-ϵ model in the fully turbulent region.

SST Turbulence Model In 1990, Menter [58] proposed two important improvements for the k-ω model: a switch to the k-ϵ model in the free stream region and a modification of the eddy viscosity definition that accounts for the transport of the main turbulent shear stress. The resulting turbulence model is called *Shear Stress Transport (SST) model*. It uses the k-ω model in the near-wall region for an accurate wall treatment and, with increasing distance to the wall, transitions into the k-ϵ model to benefit from its free stream independence in the outer boundary layer and the free shear layers. To formulate the model, Menter first transformed the k-ϵ model into a k-ω formulation. Then, he multiplied the k-ω model by a factor F_1 and the k-ϵ model by $(1 - F_1)$ and added the equations for ω from both models together. This yields

$$\frac{\partial}{\partial x_j}\left(\overline{u_j}k\right) = \nu_t \frac{\partial \overline{u}_i}{\partial x_j}\left(\frac{\partial \overline{u}_i}{\partial x_j} + \frac{\partial \overline{u}_j}{\partial x_i}\right) + \frac{\partial}{\partial x_j}\left[\left(\nu + \frac{\nu_t}{\sigma_1}\right)\frac{\partial k}{\partial x_j}\right] - \beta^* k\omega \tag{2.45}$$

$$\begin{aligned}\frac{\partial}{\partial x_j}\left(\overline{u_j}\omega\right) &= \alpha_1 \nu_t \frac{\omega}{k}\frac{\partial \overline{u}_i}{\partial x_j}\left(\frac{\partial \overline{u}_i}{\partial x_j} + \frac{\partial \overline{u}_j}{\partial x_i}\right) + \frac{\partial}{\partial x_j}\left[\left(\nu + \frac{\nu_t}{\sigma_2}\right)\frac{\partial \omega}{\partial x_j}\right] - \beta_1 \omega^2 \\ &+ 2(1 - F_1)\sigma_3 \frac{1}{\omega}\frac{\partial k}{\partial x_j}\frac{\partial \omega}{\partial x_j}\,.\end{aligned} \tag{2.46}$$

The factor F_1 is a blending function. It will be one at the wall, activating the k-ω model, and zero at the outer edge of the boundary layer to activate the k-ϵ model there. Hence, the blending takes place in between. The function F_1 is defined as

$$F_1 = \tanh\left(\arg_1^4\right)\,, \tag{2.47}$$

with the argument $\arg_1$ of the tangens hyperbolicus being defined as

$$\arg_1 = \min\left(\max\left(\frac{\sqrt{k}}{0.09\omega y}; \frac{500\nu}{y^2\omega}\right); \frac{4\rho\sigma_3 k}{\mathrm{CD}_{k\omega} y^2}\right)\,, \tag{2.48}$$

where y is the distance normal to the wall and $\mathrm{CD}_{k\omega}$ is defined as

$$\mathrm{CD}_{k\omega} = \max\left(2\sigma_3 \frac{1}{\omega}\frac{\partial k}{\partial x_j}\frac{\partial \omega}{\partial x_j}; 1 \cdot 10^{-10}\right)\,, \tag{2.49}$$

with $\sigma_3 = 0.856$. Note that the same blending approach is also used to blend the values of the coefficients in the equations.

The second step that leads to the improved performance of the SST turbulence model is the re-definition of the eddy viscosity as

$$\nu_t = \frac{a_1 k}{\max\left(a_1\omega; \Omega F_2\right)}\,, \tag{2.50}$$

with $a_1 = 0.31$, Ω being the absolute value of vorticity, and F_2 being defined as

$$F_2 = \tanh\left(\arg_2^2\right) , \tag{2.51}$$

where $\arg_2$ takes the form

$$\arg_2 = \max\left(2\frac{\sqrt{k}}{0.09\omega y}; \frac{500\nu}{y^2\omega}\right) . \tag{2.52}$$

Since the SST model combines the advantages of both the k-ω and the k-ϵ model, it overcomes the remedies of these two models and provides a two-equation eddy viscosity model applicable to a wide range from wall-bounded flows up to free shear layers. Furthermore, including the transport of the turbulent shear stresses into the eddy viscosity definition has turned out to be a major improvement in the prediction of turbulence for many types of flows. Hence, this model has become state of the art when using an eddy viscosity approach and I therefore chose this turbulence model for the present work.

Near-Wall Treatment The modeling of the near-wall region is crucial for wall-bounded turbulent flow, since this region holds very high gradients of the flow variables due to the no-slip condition at the wall. Since boundary layer flows at walls are subject to similarity laws, the velocity profile at the wall can be expressed in dimensionless form. Using the friction velocity

$$V_\tau = \sqrt{\frac{|\tau_W|}{\rho}} , \tag{2.53}$$

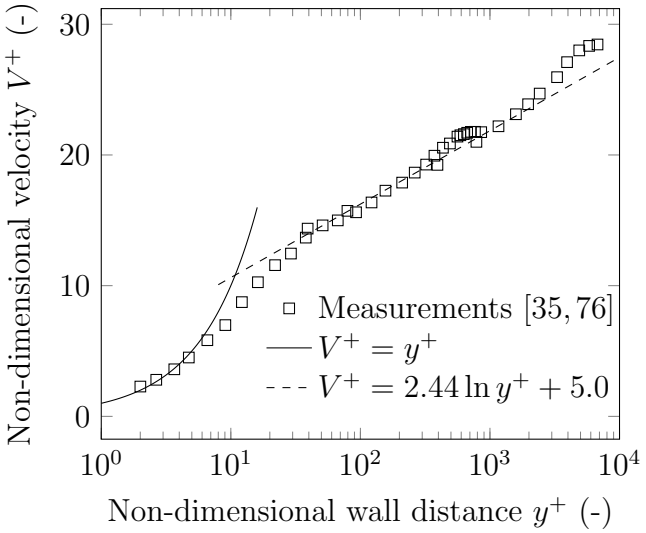

Figure 2.10: Non-dimensional velocity profile in the near-wall region

where τ_W is the wall shear stress, the dimensionless velocity becomes

$$V^+ = \frac{V}{V_\tau} \tag{2.54}$$

and the dimensionless wall distance

$$y^+ = \frac{yV_\tau}{\nu}\,, \tag{2.55}$$

with y being the distance normal to the wall. Figure 2.10 shows this non-dimensional velocity profile as it was measured by Johnson [35] and Wieghardt [76]. The profile can be subdivided into the *viscous sublayer* and the *logarithmic layer*. The viscous sublayer is a laminar layer, where molecular diffusion due to viscosity governs momentum and heat transfer. This layer extends up to $y^+ \approx 10$ and is described by a linear relation between the non-dimensional velocity and the non-dimensional wall distance, i.e. $V^+ = y^+$. In the logarithmic layer, the turbulent fluctuations dictate the transport processes. To describe the non-dimensional velocity profile for this layer, it is common to use the logarithmic law of the wall, which is $V^+ = 2.44 \ln y^+ + 5.0$. The transition region between both layers is called the *buffer layer*. Here, molecular and turbulent diffusion contribute equally to the transport processes. To correctly predict heat transfer and flow separation at the wall, the entire region of the non-dimensional velocity profile must be resolved by the numerical mesh. For the SST turbulence model, Menter suggests in [58] a value of $y_1^+ \approx 1$ and to place a minimum of 12 cells in the viscous sublayer to fully grasp the physical phenomena at the wall. Since the considered flow problems of this work involve both heat transfer and boundary layer separation, I followed this approach for all conducted numerical simulations.

2.6 Numerical Optimization

This section describes the fundamentals of the numerical optimization procedure used in this study to create the novel turbine endwall contours. The section first discusses the genetic algorithm NSGA-II, which I used as optimization tool and then explains the geometry creation process used to generate the endwall contours from the information of the genetic algorithm.

2.6.1 The NSGA-II

The Non-dominated Sorting Genetic Algorithm II (NSGA-II) by Deb et al. [21] is an evolutionary algorithm designed to solve multi-objective optimization problems. For a set of n decision variables $D_1 - D_n$ subject to M goal functions $f^{(1)} - f^{(M)}$, it determines the values of the decision variables in such a way that the M goal functions become minimum. This is done by performing a stochastic search in the n-dimensional space of the decision variables, while accounting for the dependency

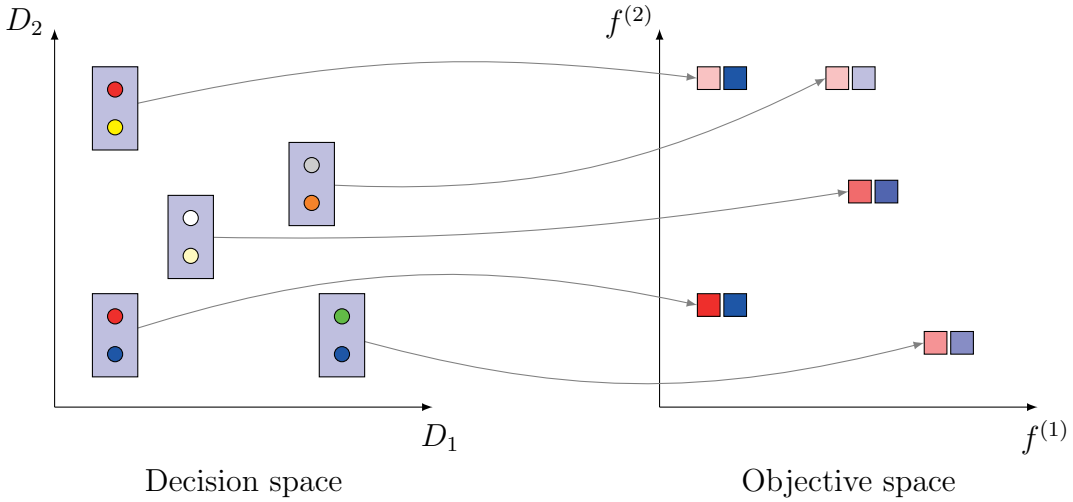

Figure 2.11: Relation between decision variables and goal functions for two-dimensional optimization problem

of the M goal functions on the n decision variables. Figure 2.11 illustrates this for a two-dimensional decision variable space and two goal functions in the objective space. Each set of decision variables in the decision space belongs to one set of goal functions in the objective space. This optimization approach is completely independent of the kind of relationship between the decision variables and the goal functions as long as there is a way to determine the goal functions from the decision variables. Hence, it is well-suited for complex problems with a highly non-linear relationship between decision variables and goal functions.

A simple way to determine the optimum values for the decision variables is to evaluate the goal functions for all possible sets of decision variables and compare the results. However, this is a very tedious approach and involves high computational effort, especially if the determination of the goal functions from the decision variables is complex. In order to avoid this slow and purely statistical approach, the NSGA-II performs a directed search in the decision variable space by mimicking a biological evolution process. The algorithm simulates the evolution of a population of individuals over several generations, imitating the concept of survival of the fittest. In this process, each set of decision variables represents an individual, with the decision variables being the individual's genes, and the goal functions represent the fitness of the individual. From one generation to the next, the parental individuals pass their genes on to the child individuals, which form the population of the next generation. To ensure convergence towards the fittest solution, the genes of the fittest parental individuals are more likely to participate in the heredity process than those of the less fit individuals. In the heredity process, operators that simulate the biological processes of recombination and mutation thereby act on the passed-on genes to create the genes of the next generation's individuals. Although the NSGA-II is tailored for multi-objective optimization problems, i.e. problems with multiple goal functions, it

can also be efficiently used for single-objective optimizations as done in this work. The next paragraph describes the NSGA-II for this special case of a single objective optimization in detail. The description of the algorithm for the more general case of a multi-objective optimization is covered in [19, 21].

Figure 2.12 shows the procedure of the NSGA-II for a single-objective optimization. In the context of this thesis, each individual represents an endwall contour, with the genes of an individual being Bézier control points used to construct the endwall contour geometry. The fitness is described by minimum endwall heat transfer. In a first step, the algorithm creates at generation zero ($i = 0$) a random parent population P_0 consisting of N individuals, each having n genes. Then the fitness of each individual of this population is determined and it becomes the parent population of the first generation. Next, the processes of selection, recombination, and mutation (explained below) are applied to this parent population to create an offspring population with N individuals from it. Both the parent and offspring population are then combined and form an intermediate population holding $2N$ individuals. This enlarged population is sorted according to the fitness of its individuals. From this, the N best individuals according to their fitness are used to form the population at the new generation $i = i + 1$. This population finally becomes the new parent population for the next iteration of the optimization loop. When the last generation ($i = m$) is reached, this population becomes the final solution of the optimization problem. For a convergent single objective optimization, the individuals of the final population are identical since only one individual is optimal for the case of a single goal function.

Combining the parent and offspring population before the best individuals are determined for the next generation constitutes an *elite-preserving* function. In the combined population, the individuals of the parent population directly compete with those of the offspring population. Hence, it is ensured that an elite individual of the parent population, that is the individual with best fitness, will also be present in the population of the next generation, unless the offspring population holds N individuals with even better fitness. In this vein, the best individual found will always be kept in the current population until N better individuals are found.

Figure 2.13 shows the processes of selection, recombination, and mutation, which are used to generate the offspring population from the parent population. These processes are performed successively and independent from each other. It starts with the selection process, in which the individuals of the parent population compete against each other in a binary tournament selection. The latter consists of N tournaments which are carried out systematically in such a way that each individual participates in exactly two tournaments with two different opponents. Every tournament is carried out between two individuals and the winner, i.e. the individual with higher fitness (lower endwall heat transfer), passes on with its genes to a mating pool holding again N individuals. Since each individual participates in two tournaments, it can have none, one, or two copies of it in the mating pool. The fittest individual ($f = f_{\max}$) of the generation thereby wins both tournaments and is represented twice in the mating pool, whereas the least fit individual ($f = f_{\min}$) loses both tournaments and is elimi-

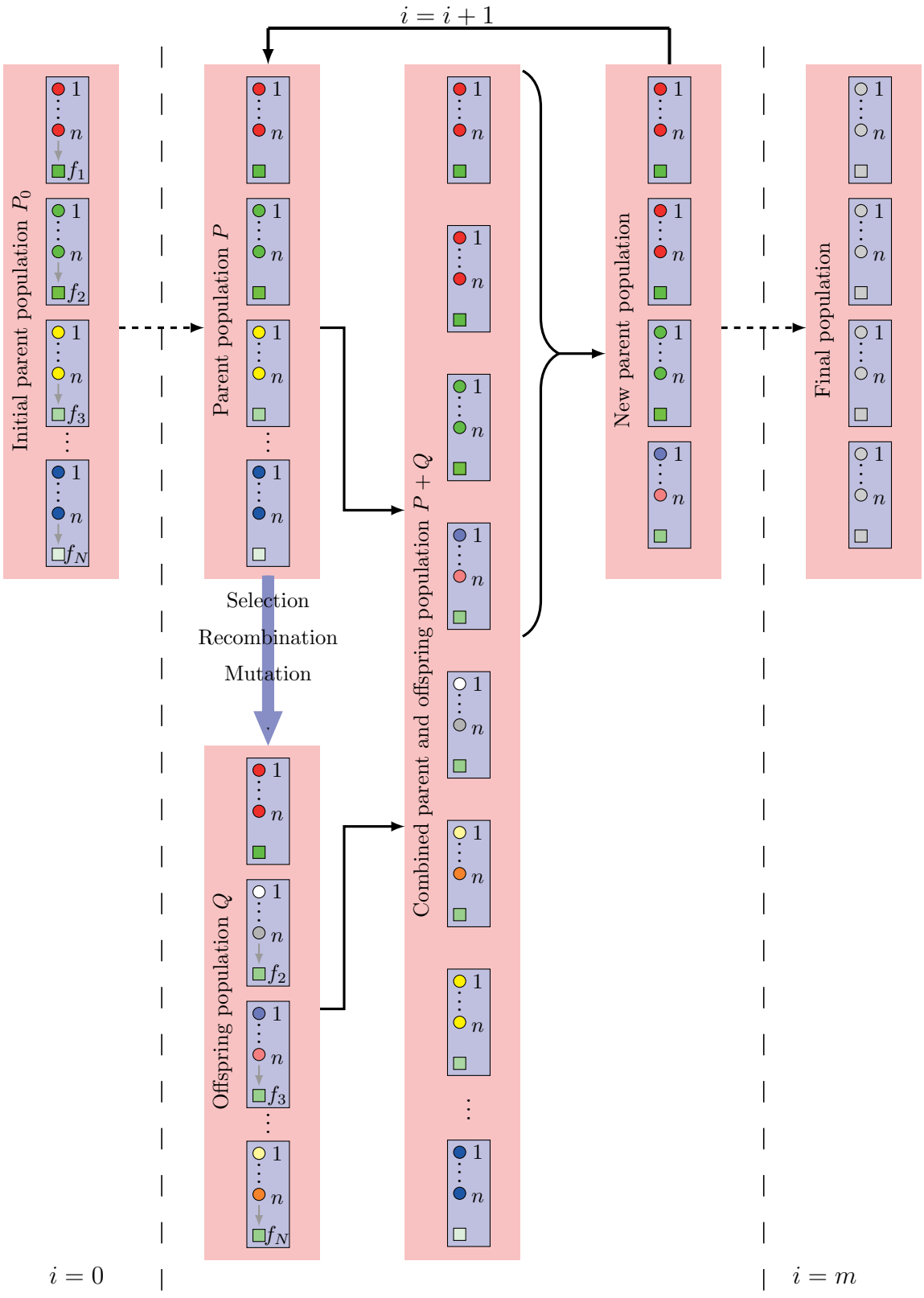

Figure 2.12: NSGA-II: Functionality for single-objective optimization

nated from the population. This ensures convergence of the optimization procedure. Appendix A.1.1 shows the binary tournament selection in further detail.

The individuals in the mating pool form the basis for the individuals of the offspring population, which are created from their genes. The recombination operator acts first on the mating pool. This operator merges all genes of two individuals from the mating pool to form two new individuals in the offspring population, which are likely to have similar features as their parent individuals. The crossover probability variable p_{cross} hereby controls if two neighboring individuals from the mating pool participate in the crossover. For each pair of individuals, a random number u is generated. If this number is smaller than p_{cross}, the crossover is performed, if not, the crossover operator does not act on the individuals. To perform the merging of the genes from two individuals in the recombination process, the NSGA-II uses the Simulated Binary Crossover (SBX). Appendix A.1.2 describes the operating mode of this algorithm.

After the crossover, the mutation operator is applied in a final step to the population's individuals. The mutation mechanism arbitrarily alters single genes. This guarantees a global convergence of the algorithm since the mutation operator consistently introduces decision variables from everywhere in the decision variable space. This operator can act on every gene of each individual. Again, a random number

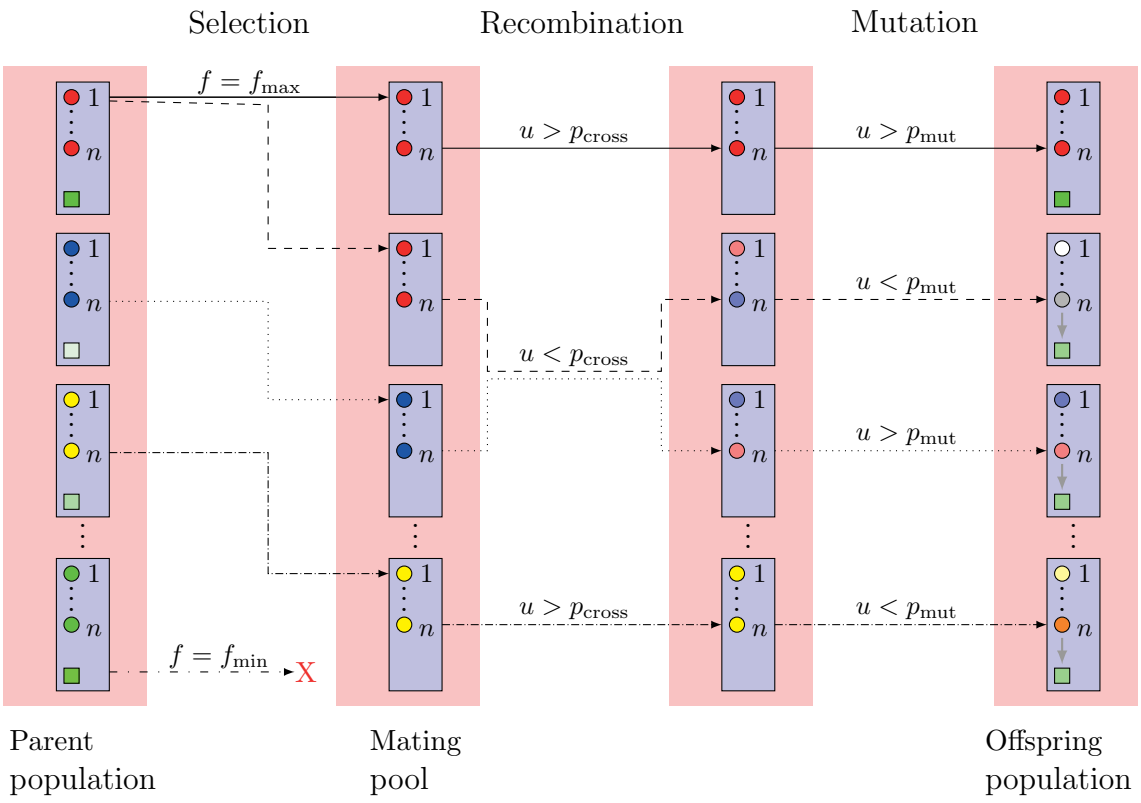

Figure 2.13: Processes used to generate the offspring population

is generated for every gene and the operator is invoked if this random number is smaller than the mutation probability p_{mut}. The mutation process itself is controlled by a mathematical function, which is described in Appendix A.1.3. The mutation mechanism counteracts the selection operator, since it extends again the solution space, which was before restricted by the directed search of the selection operator. For a correct functionality of the algorithm, these two processes must balance each other. Note that the crossover operator acts equally on all genes of two individuals, whereas the mutation operator only acts on single genes of an individual.

With the considerations above, five ways are possible for an individual between the parent and the offspring population: extinction (- · -), direct pass-through (——), selection and recombination with (- - -) and without mutation (·····), and selection without recombination but with mutation (-·-·-). In the first case, an individual becomes extinct from the population if it loses both selection tournaments. Direct pass-through describes the case, in which an individual is selected in the mating pool and neither recombination nor mutation acts on its genes. The other three cases simply represent the combinations of recombination and mutation that occur for individuals that were selected into the mating pool.

2.6.2 Endwall Geometry Creation

As stated before, each individual of the optimization process represents an endwall contour, with its genes describing the geometry of this contour. In this regard, the genes correspond to the control points of Bézier curves, which are used to construct

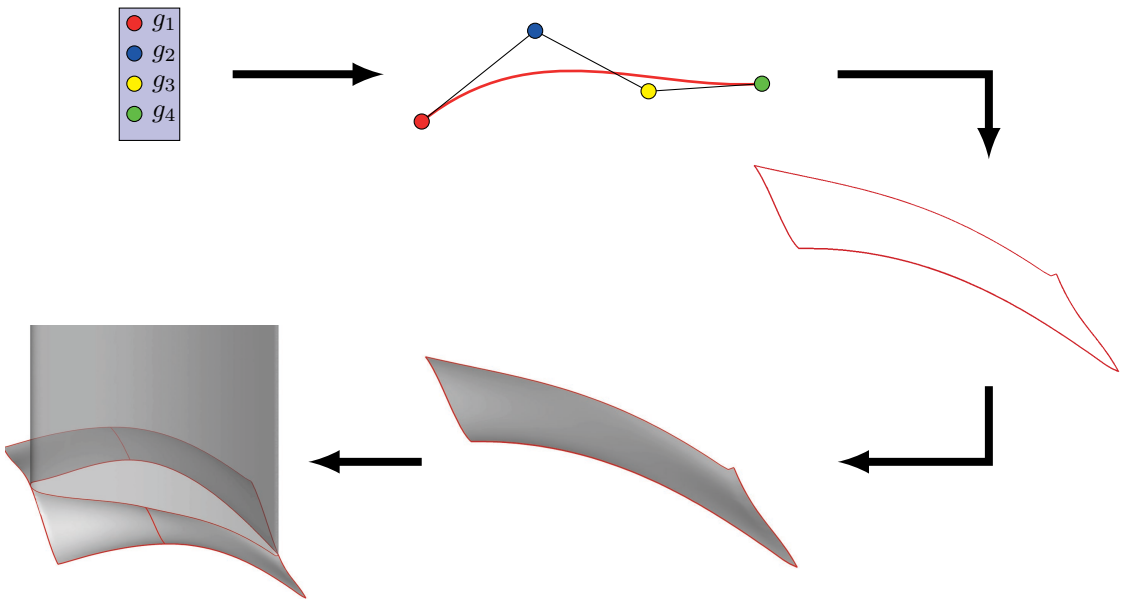

Figure 2.14: Work flow used to create the endwall contours from the individuals of the optimization process

the endwall geometry. Figure 2.14 illustrates the geometry generation process. First, the genes are interpreted as control points and used to construct cubic Bézier curves. Four such Bézier curves are then grouped together to form the boundary edges of a surface. These surfaces finally define the geometry of the endwall contour.

Bézier curves, as used in this thesis, were developed in the 1960s by Pierre Bézier [5, 6] and Paul de Casteljau [18] for the design and construction in automotive engineering. They represent a parametric definition of a mathematical curve, describing the entire curve by only few control points. The number of control points thereby determines the order of the Bézier curve, the order being the number of control points minus one. Hence, two control points result in a Bézier curve of order one (a straight line), three control points in a quadratic Bézier curve, four control points in a cubic Bézier curve, and so on. For a generic Bézier curve $C(t)$ of order h, described by $h+1$ control points P_i, each point on the Bézier curve is given by

$$C(t) = \sum_{i=0}^{h} B_{i,h}(t)\, P_i\,, \tag{2.56}$$

with $B_{i,h}(t)$ being the i-th Bernstein polynomial of order h, defined as

$$B_{i,h}(t) = \begin{pmatrix} h \\ i \end{pmatrix} t^i (1-t)^{h-i}\,, \tag{2.57}$$

and t being the Bézier parameter with $t \in [0,1]$. For cubic Bézier curves ($h=3$), as used for the geometry creation in this work, the mathematical description becomes

$$\begin{aligned} C(t) &= \sum_{i=0}^{3} \begin{pmatrix} 3 \\ i \end{pmatrix} t^i (1-t)^{3-i} P_i \\ &= (1-t)^3 P_0 + 3t(1-t)^2 P_1 + 3t^2(1-t)P_2 + t^3 P_3 \\ &= (-P_0 + 3P_1 - 3P_2 + P_3)t^3 + (3P_0 - 6P_1 + 3P_2)t^2 + (-3P_0 + 3P_1)t + P_0\,, \end{aligned} \tag{2.58}$$

where t determines the position on the Bézier curve, zero being the beginning of the curve at the first control point P_0 and unity its end at the fourth control point P_3. Figure 2.15 shows a generic cubic Bézier curve, defined by four control points.

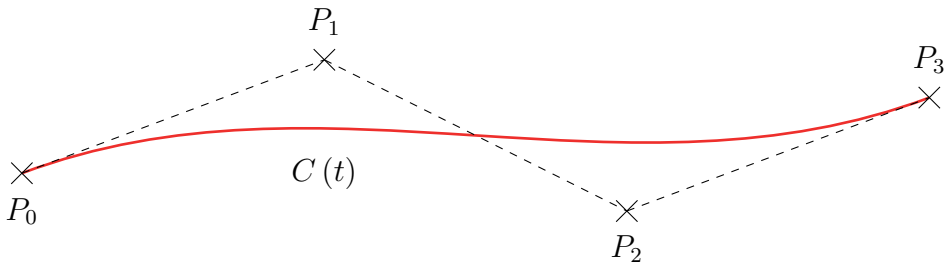

Figure 2.15: Generic cubic Bézier Curve defined by the four control points P_0 - P_3

Bézier curves have two characteristic features, which I exploited for the geometry creation. First, their first and last control point lie on the curve itself and specify their starting point and end, that is

$$C\left(t=0\right) = P_0 \tag{2.59}$$
$$C\left(t=1\right) = P_h\,. \tag{2.60}$$

This allows to easily define a Bézier curve between two characteristic points of the endwall geometry. Secondly, the straight lines between the first two (P_0, P_1) and last two control points (P_{h-1}, P_h) are tangents to the curve in its first (P_0) and last (P_h) control point and hence define the local slope of the curve at these points as

$$\left.\frac{\mathrm{d}C}{\mathrm{d}t}\right|_{t=0} = h\left(P_1 - P_0\right) \tag{2.61}$$
$$\left.\frac{\mathrm{d}C}{\mathrm{d}t}\right|_{t=1} = h\left(P_h - P_{h-1}\right)\,. \tag{2.62}$$

The characteristics above form necessary conditions for joining two Bézier curves with C^1-steadiness (First order steadiness). Figure 2.16 illustrates this for the two Bézier curves C and $\tilde{C}$. The first condition guarantees C^0-steadiness (Zeroth order steadiness). It requires the last control point P_h of the first Bézier curve C to coincide with the first control point $\tilde{P}_0$ of the second Bézier curve $\tilde{C}$, that is

$$C\left(t=1\right) = P_h \overset{!}{=} \tilde{C}\left(\tilde{t}=0\right) = \tilde{P}_0\,. \tag{2.63}$$

To make the two Bézier curves C^1-steady, the second condition demands that also the slope of the two Bézier curves are identical in their meeting point, hence

$$\left.\frac{\mathrm{d}C}{\mathrm{d}t}\right|_{t=1} = h\left(P_h - P_{h-1}\right) \overset{!}{=} \left.\frac{\mathrm{d}\tilde{C}}{\mathrm{d}\tilde{t}}\right|_{\tilde{t}=0} = \tilde{h}\left(\tilde{P}_1 - \tilde{P}_0\right)\,. \tag{2.64}$$

If both Bézier curves have the same order ($h = \tilde{h}$), the following equation needs to be satisfied for C^1-steadiness

$$\left(P_h - P_{h-1}\right) \overset{!}{=} \left(\tilde{P}_1 - \tilde{P}_0\right)\,. \tag{2.65}$$

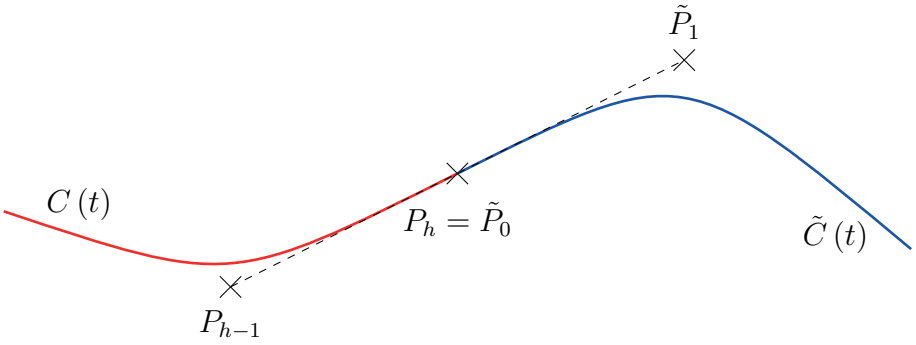

Figure 2.16: C^1-steady joining of two Bézier curves

This means that the straight line between the last two control points of P must be identical in length and orientation to that of the first two control points of $\tilde{P}$.

2.7 Parameters for Results Evaluation

This section introduces the parameters I used in this work to evaluate the performance of the created endwall contours with respect to heat transfer, flow field, and entropy production.

To assess endwall heat transfer for the contoured endwall geometries, I used the *heat transfer coefficient*, defined as

$$htc = \frac{q''}{(T_{\mathrm{EW}} - T_{\infty})} \,. \tag{2.66}$$

In this equation, q'' is the convective heat flux per area ($\mathrm{W\,m^{-2}}$) at the wall, determined from the CFD solution, T_{EW} the static temperature of the endwall, which is prescribed constant as boundary condition, and T_{∞} the flow temperature at the inlet.

To obtain a single value that characterizes endwall heat transfer, I area-averaged the local htc according to

$$\overline{htc} = \frac{\int\limits_{A_{\mathrm{EW}}} htc \, \mathrm{d}A_{\mathrm{EW}}}{\int\limits_{A_{\mathrm{EW}}} \mathrm{d}A_{\mathrm{EW}}} \,, \tag{2.67}$$

where A_{EW} denotes the area of the contoured endwall.

A further variable used in this work to evaluate the created endwall contours is the total pressure coefficient

$$C_{\mathrm{p,tot}} = \frac{\widehat{p_{\mathrm{tot}}} - \widehat{p_{\mathrm{tot,in}}}}{{}^{1}\!/_{2}\rho\overline{u_1}_{,\mathrm{in}}{}^{2}} \,, \tag{2.68}$$

where $\overline{u_1}_{,\mathrm{in}}$ is the area-averaged x-velocity component at the inlet of the numerical solution domain, defined as

$$\overline{u_1}_{,\mathrm{in}} = \frac{\int\limits_{A_{\mathrm{in}}} u_1 \, \mathrm{d}A_{\mathrm{in}}}{\int\limits_{A_{\mathrm{in}}} \mathrm{d}A_{\mathrm{in}}} \,, \tag{2.69}$$

and $\widehat{p_{\mathrm{tot}}}$ is the mass-flow-averaged total pressure according to

$$\widehat{p_{\mathrm{tot}}} = \frac{\int\limits_{A,\mathrm{in}} \rho u_1 p_{\mathrm{tot}} \, \mathrm{d}A_{\mathrm{in}}}{\int\limits_{A,\mathrm{in}} \rho u_1 \, \mathrm{d}A_{\mathrm{in}}} \,, \tag{2.70}$$

with A_{in} denoting the cross-sectional area of the numerical domain's inlet.

Accordingly, the static pressure coefficient is defined as

$$C_p = \frac{p - p_{\text{in}}}{{}^1\!/_2 \rho \overline{u_{1,\text{in}}}^2}\,, \tag{2.71}$$

where p is the static pressure and $\overline{u_{1,\text{in}}}$ again is the area-averaged x-velocity component at the inlet of the numerical solution domain.

Since the flow of a vane/endwall configuration involves strong vortex systems, I used two methods to identify vortex cores in the numerical dataset: the Q-criterion and the λ_2-method. The first was proposed by Hunt et al. [16], the latter by Jeong and Hussain [34]. Both methods are based on the fact that a vortex core has a local pressure minimum and utilize the decomposition of the velocity gradient tensor $\partial u_i/\partial x_j$ into its symmetric part

$$S_{ij} = \frac{1}{2}\left(\frac{\partial u_i}{\partial x_j} + \frac{\partial u_j}{\partial x_i}\right) \tag{2.72}$$

and its anti-symmetric part

$$\Omega_{ij} = \frac{1}{2}\left(\frac{\partial u_i}{\partial x_j} - \frac{\partial u_j}{\partial x_i}\right) \tag{2.73}$$

to create a new tensor that approximates the Hessian of the static pressure p_{ij} as

$$p_{ij} = \mathcal{H}_p = \frac{\partial^2 p}{\partial x_i \partial x_j} \approx S_{ij}^2 + \Omega_{ij}^2\,. \tag{2.74}$$

This allows to identify vortex cores from the three eigenvalues of $S_{ij}^2 + \Omega_{ij}^2$, which are given as $\lambda_1 \geq \lambda_2 \geq \lambda_3$. With these definitions, the λ_2-method specifies a vortex core as a connected region with two negative eigenvalues. This is identical with the requirement that λ_2 is smaller than zero in a vortex core. Physically, this means that regions with $\lambda_2 < 0$ indicate a local pressure minimum caused by the vortical motion of the flow around it and thus constitute the core of a vortex. The Q-criterion also uses these three eigenvalues in its definition

$$Q = -\frac{1}{2}\left(\lambda_1 + \lambda_2 + \lambda_3\right) \tag{2.75}$$

and describes a vortex core as a connected region where the variable Q is positive. This also requires $\lambda_2 < 0$ as for the λ_2-method, but additionally demands that $|\lambda_1| < |\lambda_2 + \lambda_3|$. Physically, the variable Q represents fluid regions which feature a local balance between the shear strain rate and the vorticity magnitude which is characteristic for the core of a vortex with swirling flow around it.

The ice-contoured endwalls used in this work were experimentally created with the Ice Formation Method. As a natural method, the IFM is assumed to reduce entropy production. Hence, I analyzed entropy production rates for the ice-contoured

endwalls by determining the source terms of the entropy transport equation. The latter is defined as

$$\frac{\partial \rho s}{\partial t} + \frac{\partial \rho s u_j}{\partial x_j} = \frac{\partial}{\partial x_j}\left(\frac{k}{T}\frac{\partial T}{\partial x_j}\right) + \underbrace{\frac{\sigma_{ij}}{T}\frac{\partial u_i}{\partial x_j}}_{\rho \dot{S}_{\mathrm{Diss}}} + \underbrace{\frac{k}{T^2}\left(\frac{\partial T}{\partial x_j}\right)^2}_{\rho \dot{S}_{\mathrm{Heat}}}, \tag{2.76}$$

whereas s indicates the specific entropy and σ_{ij} stands for the viscous stress tensor. In this equation, the last two terms on the right hand side describe entropy production due to viscous dissipation and irreversible heat transfer processes. After applying Reynolds-averaging to this equation, each of these entropy production terms is expanded into two expressions: one for the entropy production on molecular level and one for entropy production due to turbulent fluctuations. Hence, the following two source terms describe entropy production by viscous dissipation, first at molecular level due to mean velocity gradients

$$\begin{aligned}\dot{S}_{\mathrm{Diss,mol}} = \frac{\mu}{\overline{T}}\Bigg[2\left\{\left(\frac{\partial \overline{u_1}}{\partial x}\right)^2 + \left(\frac{\partial \overline{u_2}}{\partial y}\right)^2 + \left(\frac{\partial \overline{u_3}}{\partial z}\right)^2\right\} \\ + \left(\frac{\partial \overline{u_1}}{\partial y} + \frac{\partial \overline{u_2}}{\partial x}\right)^2 + \left(\frac{\partial \overline{u_1}}{\partial z} + \frac{\partial \overline{u_3}}{\partial x}\right)^2 + \left(\frac{\partial \overline{u_2}}{\partial z} + \frac{\partial \overline{u_3}}{\partial y}\right)^2\Bigg],\end{aligned} \tag{2.77}$$

and secondly due to fluctuating velocity gradients

$$\begin{aligned}\dot{S}_{\mathrm{Diss,turb}} = \frac{\mu}{\overline{T}}\Bigg[2\left\{\overline{\left(\frac{\partial u_1'}{\partial x}\right)^2} + \overline{\left(\frac{\partial u_2'}{\partial y}\right)^2} + \overline{\left(\frac{\partial u_3'}{\partial z}\right)^2}\right\} \\ + \overline{\left(\frac{\partial u_1'}{\partial y} + \frac{\partial u_2'}{\partial x}\right)^2} + \overline{\left(\frac{\partial u_1'}{\partial z} + \frac{\partial u_3'}{\partial x}\right)^2} + \overline{\left(\frac{\partial u_2'}{\partial z} + \frac{\partial u_3'}{\partial y}\right)^2}\Bigg].\end{aligned} \tag{2.78}$$

Similarly, two source terms arise for entropy production by heat conduction due to finite temperature gradients, again caused by mean temperature gradients at molecular level

$$\dot{S}_{\mathrm{Heat,mol}} = \frac{k}{\overline{T}^2}\left[\left(\frac{\partial \overline{T}}{\partial x}\right)^2 + \left(\frac{\partial \overline{T}}{\partial y}\right)^2 + \left(\frac{\partial \overline{T}}{\partial z}\right)^2\right], \tag{2.79}$$

and fluctuating temperature gradients

$$\dot{S}_{\mathrm{Heat,turb}} = \frac{k}{\overline{T}^2}\left[\overline{\left(\frac{\partial T'}{\partial x}\right)^2} + \overline{\left(\frac{\partial T'}{\partial y}\right)^2} + \overline{\left(\frac{\partial T'}{\partial z}\right)^2}\right]. \tag{2.80}$$

In the equations above, the primes indicate fluctuating variables due to turbulent motion. The variables u_1, u_2, and u_3 represent the velocities with respect to the

three spatial coordinates x, y, and z. Furthermore, T is the static temperature and μ and k describe the dynamic viscosity and the thermal conductivity of the fluid, respectively.

To calculate Eqs. (2.77) and (2.79), I directly used the mean velocity and temperature gradients from the numerical simulations. The fluctuating velocity and temperature gradients, which appear as new unknowns due to the time averaging of the equations, however, cannot be obtained from the numerical simulations. Hence, the turbulent entropy production terms, Eqs. (2.78) and (2.80), need to be modeled in accordance with the used turbulence model. Following Kock and Herwig [39], I modeled these terms as follows. The turbulent dissipation term, Eq. (2.78), can be related to the mean static Temperature $\overline{T}$ and the turbulence variables k and ω as

$$\dot{S}_{\mathrm{Diss,turb}} = C_\mu \frac{\rho \omega k}{\overline{T}} \,, \tag{2.81}$$

where k is again the turbulence kinetic energy and ω its dissipation rate. C_μ is a model constant ($C_\mu = 0.09$). Assuming a constant turbulent Prandtl number and an eddy-diffusivity approach according to Boussinesq for modeling the turbulent heat flux, i.e. $-\overline{u_i' T'} = \alpha_\mathrm{t} \partial \overline{T} / \partial x_i$, the turbulent heat conduction term, Eq. (2.80), can be modeled by using its mean flow counterpart, Eq. (2.79), as

$$\dot{S}_{\mathrm{Heat,turb}} = \frac{\alpha_\mathrm{t}}{\alpha} \frac{k}{\overline{T}^2} \left[\left(\frac{\partial \overline{T}}{\partial x} \right)^2 + \left(\frac{\partial \overline{T}}{\partial y} \right)^2 + \left(\frac{\partial \overline{T}}{\partial z} \right)^2 \right] , \tag{2.82}$$

where α_t/α is the ratio of turbulent to laminar thermal diffusivity. In his work, Kock [38] validated the above derived entropy production terms for the use with Computational Fluid Dynamics. Later on, Hitz [31] compared results for all four entropy production terms determined from CFD simulatons with a low Reynolds number RANS turbulence model with DNS data and thus proved the applicability of this evaluation method for the numerical setup that was also used in the present work.

3

Methodology

Contents:
Vane profile of this study and experimental test facility to create the ice contours - Derivation of the numerical setup used for the CFD simulations and the numerical optimizations of this study - Presentation of the different cases considered in the present work

3.1 Experimental Setup

The ice layers used in this study as endwall contours for the numerical simulations were taken from the experiments of Haase [26]. This section first presents the vane profile for which the endwall contours were generated. Subsequently, the test facility and the parameters of the experiments are discussed. For further details see [26].

3.1.1 Vane Profile

The endwall contours in this study were created for the guide vane of a low pressure turbine. The used vane profile is exemplary for such a turbine stage and was developed by MTU Aero Engines for a design Reynolds number of $Re_C = 200{,}000$. Figure 3.1 shows the profile with its dimensions and characteristic parameters.

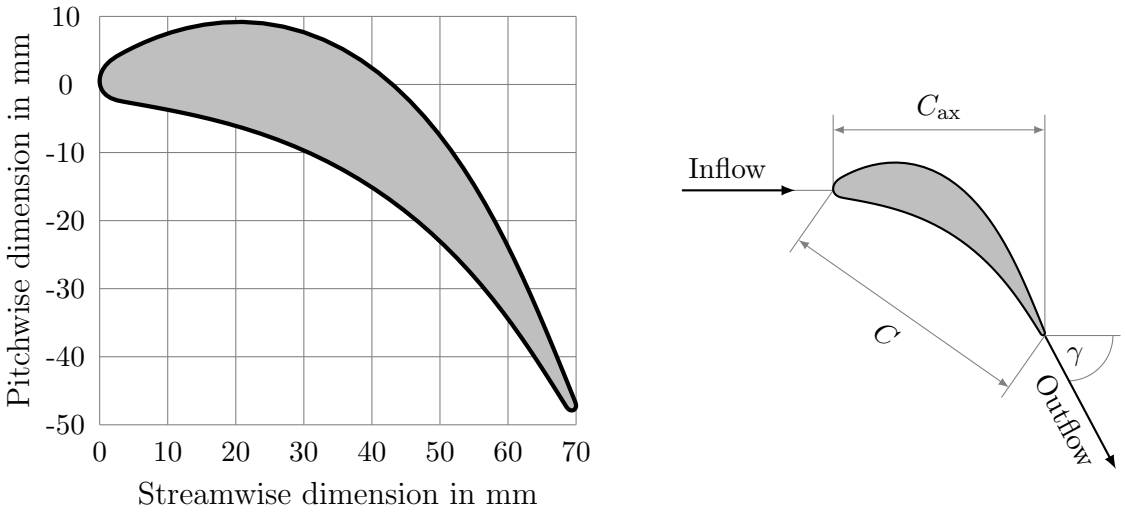

Figure 3.1: Vane profile used for this study with characteristic parameters (C - True chord, C_{ax} - Axial chord, γ - Flow turning angle)

Table 3.1 summarizes the characteristic parameters of the vane profile. In the vane row of the experimental channel, the vanes are mounted at a pitch of $P = 62.4\,\text{mm}$ and extend over the entire channel's height, i.e. they have a span of $S = 140.0\,\text{mm}$.

Table 3.1: Parameters of vane profile

True chord C	84.7 mm
Axial chord C_{ax}	70.0 mm
Flow turning angle γ	62.0°
Pitch P	62.4 mm
Span S	140.0 mm

3.1.2 Test Facility and Experiments

Figure 3.2 shows the test facility. It consists of a water cycle with a water tank, piping, and an in-line water pump to drive the flow through the test section. The latter is a three passage linear cascade of the investigated vane profile with rectangular inlet and outlet channels upstream and downstream of it.

Figure 3.3 shows the linear cascade test section in detail. It holds two full vanes and two half vanes resulting in three vane passages. The height of the test section and hence the span of the two-dimensional vanes is $S = 140\,\text{mm}$. This results in the values $S/C_{\text{ax}} = 2.0$ and $S/P = 2.24$, which ensure independency of the secondary flow structures of the top and bottom endwalls. Behind the vane cascade, tailboards are mounted. Their opening angle is adjusted to set the cascade exit pressure in such a way as to guarantee periodic flow conditions in the three vane passages. In front of the vane cascade, a 1.4 mm trip wire is installed to ensure repeatable inflow conditions with a turbulent boundary layer. At its lower endwall, the test section features a copper inlay. For the experiments, two different copper inlays were used: a short one ranging from 80 mm in front of the vanes to 80 mm behind them (shown in Fig. 3.3) and a long one extending from 280 mm in front of the vane passage to 280 mm behind it (see App. A.3). Both inlays are flush-mounted with the lower endwall of the test section.

In the experiments, the copper inlay was cooled down to temperatures below the freezing point of water and a constant water flow was set up through the test section. As a result, an ice layer developed on the cooled copper inlay. The shape of this ice

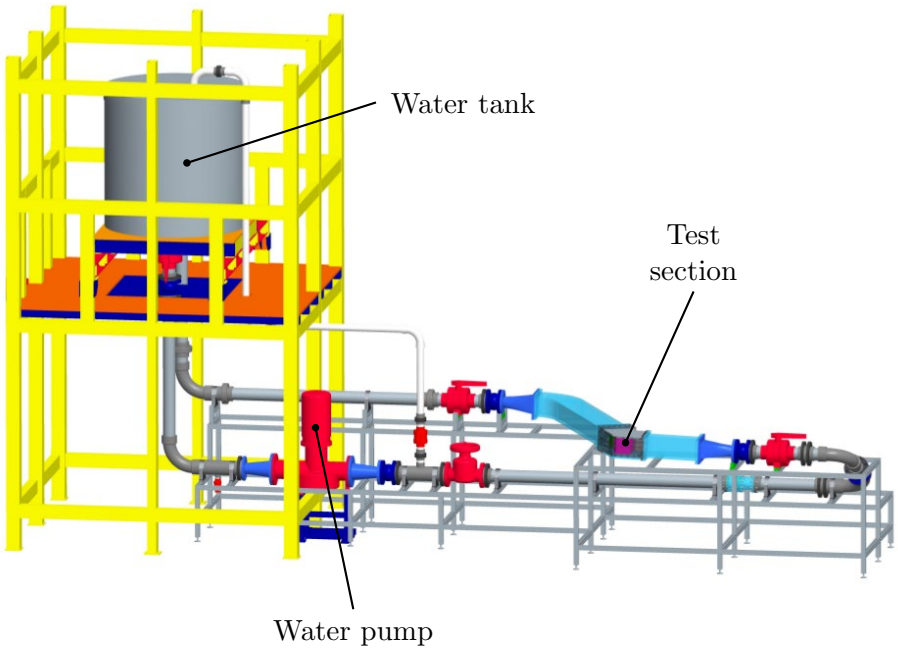

Figure 3.2: Experimental test facility (see Haase [26])

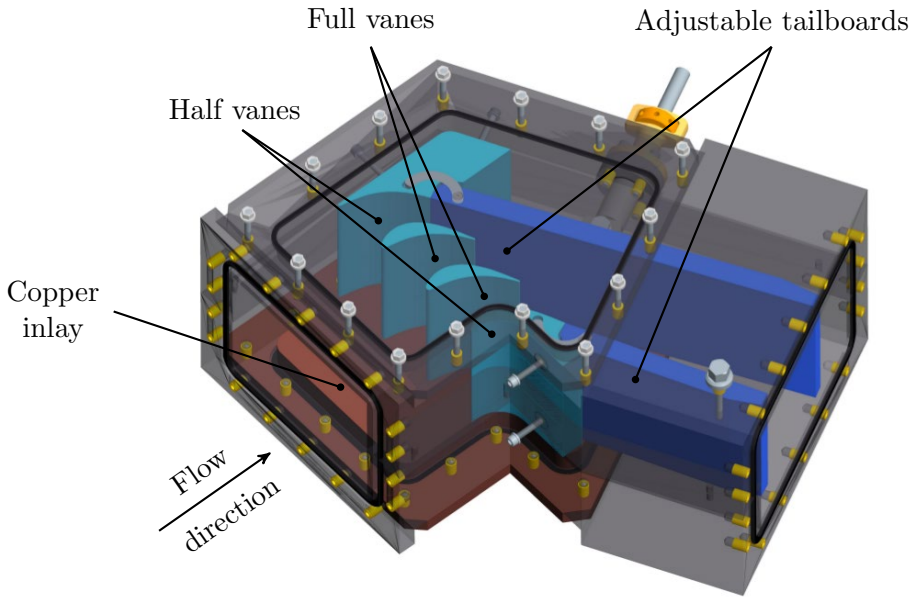

Figure 3.3: Linear cascade test section (see Haase [26])

layer emerges from the phase interface between liquid water and solid ice, which is influenced by heat removal due to the cooling of the inlay and heat addition due to the heat transfer rates caused by the flow. The experiments were run until these two processes balanced each other and steady-state was reached. In this state, the phase interface is in thermal equilibrium and the shape of the ice layer remains unchanged (see also Sec. 2.1). Since the Ice Formation Method is a natural approach, the so created ice layer represents a naturally optimized and energetically advantageous flow geometry. Hence, the steady-state ice layer is assumed to have minimum energy dissipation and thus minimum entropy production rates.

As already pointed out by LaFleur [43], the shape of the ice layer only depends on the flow velocity and the cooling of the baseline geometry, here, the temperature of the copper inlay. Hence, Haase [26] used two control parameters to create different ice layers in the experiment: the *Reynolds number* $Re_{C,\mathrm{exp}}$ and the *temperature ratio* Θ_{exp}. The Reynolds number is defined as

$$Re_{C,\mathrm{exp}} = \frac{u_{exit}\, C}{\nu_{\mathrm{water},\infty}}\,, \tag{3.1}$$

with C being the true chord of the vane profile, $\nu_{\mathrm{water},\infty}$ the kinematic viscosity of the incident water flow, and u_{exit} the velocity magnitude at the exit cross section of the vane passage without ice formation. The non-dimensional temperature ratio is defined as

$$\Theta = \frac{T_{\mathrm{f}} - T_{\mathrm{CI}}}{T_\infty - T_{\mathrm{f}}}\,, \tag{3.2}$$

where T_{f}, T_{CI}, and T_∞ denote, respectively, the freezing temperature of water, the temperature of the copper inlay, and the water temperature of the flow. Appendix A.4

holds the derivation of this variable. The test facility allows for a maximum temperature ratio of $\Theta = 12.2$. The maximum realizable Reynolds number is limited to approximately $Re_{C,\text{exp}} = 72{,}000$ due to limitations of the water pump. Hence, verification of the found geometries at the design Reynolds number of $Re_C = 200{,}000$ was done numerically.

3.2 Numerical Setup

This section describes the setup used for the numerical simulations of the endwall contours. At first, the modeling of the numerical setup for the baseline case of the flat, uncontoured endwall is presented. Next, the procedure to obtain the contoured endwalls from the experimental ice layers is discussed. The section ends by explaining the setup of the numerical optimizations.

3.2.1 Flat Endwall Baseline

The flat endwall is the baseline for comparing all created endwall contours to. Hence, I first developed a numerical setup for this baseline case. The same setup was then

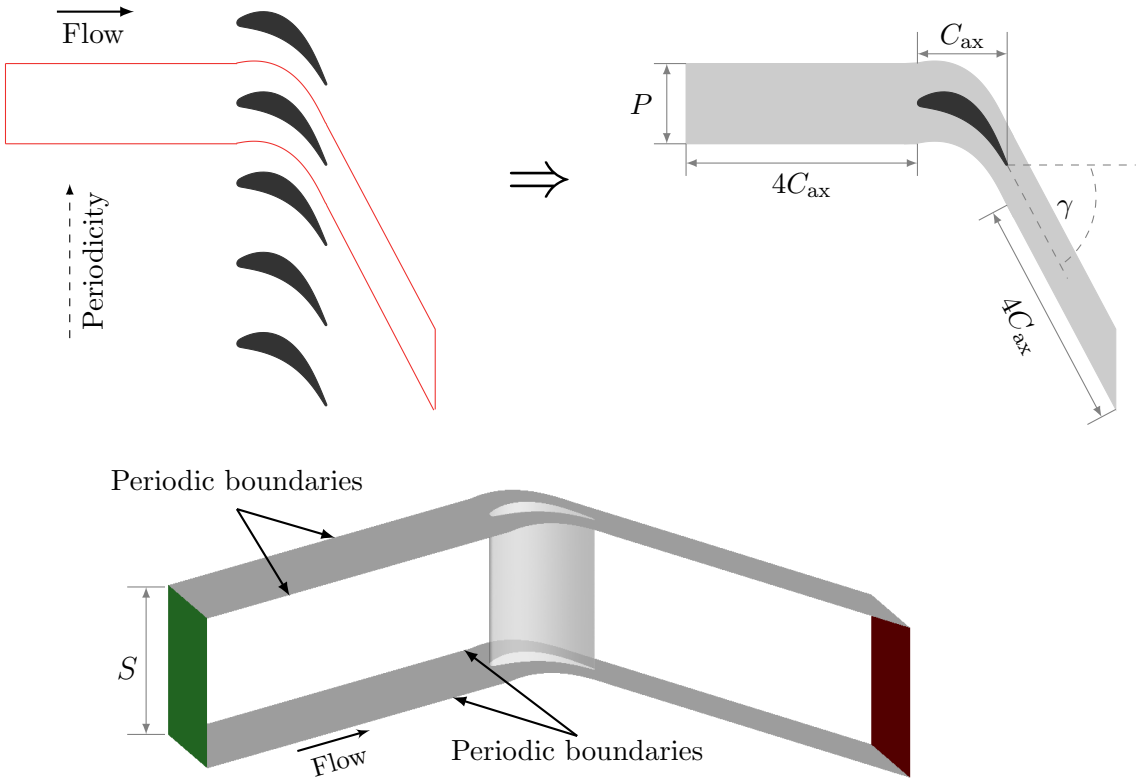

Figure 3.4: Periodic solution domain for the numerical simulations (C_{ax} - Axial chord, P - Pitch, S - Span, γ - Flow turning angle)

also used for all contoured endwalls. As solution domain for the numerical simulations, I used one periodic segment of the vane row with a vane and half a vane passage above and below it. Preliminary investigations showed that a setup with a complete vane passage between a pressure side and the adjacent vane's suction side is not suited for periodic boundary conditions. Since the periodic boundaries run directly through the wake behind the vanes, where high gradients of the flow variables occur, such a setup produces a non-periodic behavior. Figure 3.4 shows the periodic solution domain. The inlet is placed four axial chords upstream of the vane profile, the outlet four axial chords downstream of it in the outflow direction. The outflow region is inclined against the inflow region by the vane's flow turning angle γ. The vane pitch determines the width of the solution domain, the vane span its height. The latter corresponds to the height of the experimental test section.

For the numerical simulations, I spatially discretized the solution domain with a hybrid grid, created with the commercial grid generator CENTAUR [15]. At solid walls, these grids have 20 structured prism layers to resolve the entire boundary layer up to a near-wall distance of $y_1^+ \approx 1$ for the first cells at the wall. To achieve

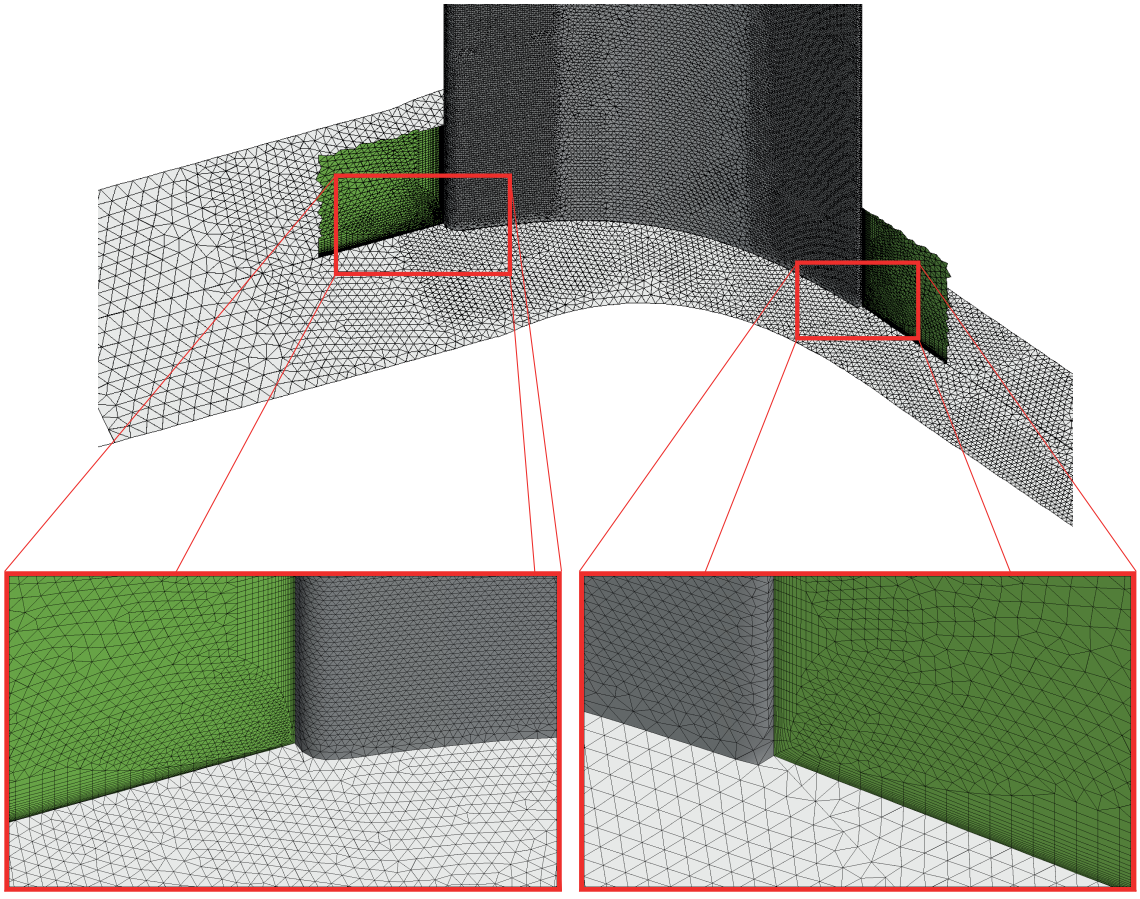

Figure 3.5: Grid used for spatial discretization of the solution domain; Cutting planes shown in green

Table 3.2: GCI study for flat endwall baseline: Grid parameters

	Fine grid (G0)	Used grid (G1)	Coarse grid (G2)
Number of cells N	9,733,451	5,754,377	3,293,029
Refinement ratio r	1.191	-	1.204
Maximum y_1^+	2.72	2.64	4.32

this, I used a dimensional height of $y_1 = 50\,\mu\text{m}$ for the first cells at solid walls. The remainder of the domain consists of unstructured tetrahedral cells. I clustered cells in regions where I expected high gradients, e.g. at the vane's leading and trailing edge and in its wake. The final grid had a total of approximately six million cells. Figure 3.5 displays this grid for the lower wall's vane/endwall junction. The figure illustrates the grid cells on the vane and the lower endwall as well as in two cutting planes (shown in green) at the vane's leading and trailing edge. These show the prism layers that are generated at the walls. Note that I used this grid to perform the numerical simulations at all Reynolds numbers from the experiments (Re_C = 34,000, 49,900, and 71,400). For the simulations at the design Reynolds number of Re_C = 200,000, I scaled down the height of the first cells at the wall to $y_1 = 20\,\mu\text{m}$ in order to maintain a non-dimensional near-wall distance of $y_1^+ \approx 1$.

To ensure that the numerical solution is grid independent, I conducted a *Grid Convergence Index (GCI)* study according to Roache [67]. Based on the grid used for the simulations (G1), I created a coarser (G2) and a finer grid (G0) and determined the flow field solution on all three grids. These three solutions were then used in a Richardson extrapolation to determine the solution for a hypothetic, infinitely fine grid with vanishing discretization error. The GCI then describes the discretization error for the used grid with respect to this infinitely fine grid. Table 3.2 shows the parameters for the three grids. I coarsened and refined the used grid by a factor of approximately 1.2, while keeping the height y_1 of the first cells at solid walls constant. Hence, the maximum y_1^+ varied between 2.72 and 4.32 for the three grids. Table 3.3 shows the results for the flat endwall GCI study. I evaluated the axial and crosswise velocities as well as the static temperature at two positions at midspan. The first position P1 lies $0.1C_{\text{ax}}$ upstream of the vane leading edge, the second position P2 lies at the same distance downstream of the trailing edge (see also App. A.2 for positions). For the velocity components, the GCI is at maximum 5%, except for the crosswise velocity component (u_2) in front of the leading edge (position P1). Here, the differences between the numerical values are too small to yield a reasonable GCI. The latter amounts to 30%, although the difference of the values between the three grids is below 1%. For the static temperature, I observed only small differences for the three grids. Upstream of the vane, the values are identical for all three grids, downstream of it, the resulting GCI is as low as 2.23e−4%. Furthermore, I determined the GCI for the area-averaged heat transfer coefficient of the lower endwall. It is below 2%, which shows that endwall heat transfer is in good approximation independent of the

Table 3.3: GCI study for flat endwall baseline: Results for axial (u_1) and crosswise (u_2) velocity components, static temperature T and area-averaged endwall heat transfer coefficient $\overline{htc}$

Position	Variable	Fine (G0)	Used (G1)	Coarse (G2)	GCI
P1	u_1 ($\mathrm{m\,s^{-1}}$)	6.35	6.33	6.34	2.89e−3
	u_2 ($\mathrm{m\,s^{-1}}$)	0.163	0.162	0.161	0.30
	T (K)	349.98	349.98	349.98	-
P2	u_1 ($\mathrm{m\,s^{-1}}$)	6.92	6.97	7.00	0.034
	u_2 ($\mathrm{m\,s^{-1}}$)	12.87	12.95	13.05	0.051
	T (K)	349.88	349.87	349.86	2.23e−6
Endwall	$\overline{htc}$ ($\mathrm{W\,m^{-2}\,K^{-1}}$)	38.98	38.80	38.52	0.017

used grid. In addition, I also evaluated the grid influence in a plane that is located $0.5C_{\mathrm{ax}}$ downstream of the trailing edge and perpendicular to the outflow direction (see App. A.2). This wake region features high flow gradients and is hence crucial for determining grid independence. Figure 3.6 shows the local distribution of the Darcy friction factor f and the heat transfer coefficient htc in this plane. The friction factor is virtually independent of the used grid. For the htc, the results of the used grid are in good agreement with those of the fine grid. The average GCI in this plane is 0.47% for the htc of the used grid. Appendix A.2 holds the full data set that forms the basis of this GCI study.

For the CFD simulations of this study, I used ANSYS® Fluent [4] version 12.1. It uses a pressure-based approach to solve the set of governing equations with the SIM-

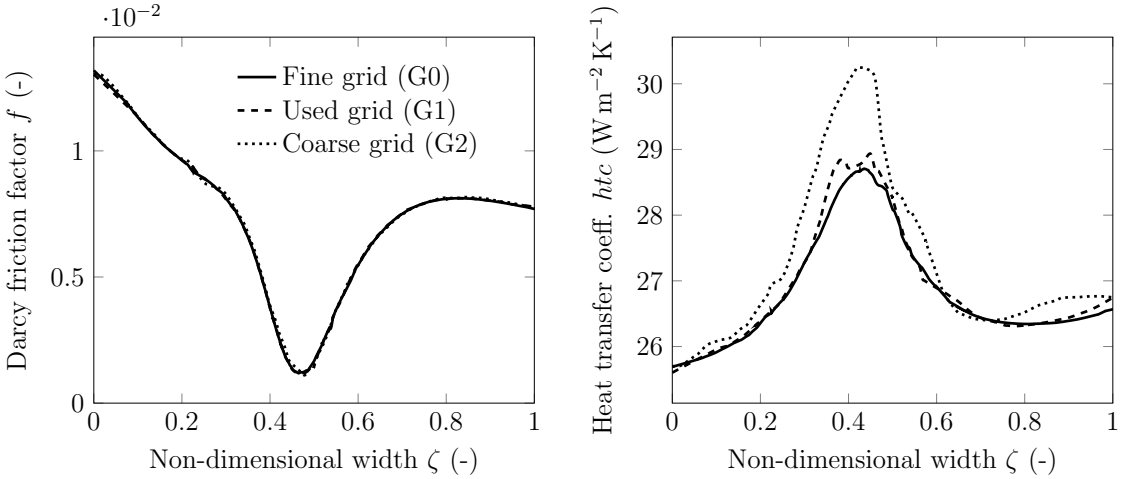

Figure 3.6: GCI study for flat endwall baseline: Darcy friction factor f (left) and htc (right) in plane located in vane wake flow, see App. A.3 for coordinate ζ

PLE algorithm. To model turbulence, I employed Menter's SST turbulence model (see [58]) in low-Reynolds formulation and a constant turbulent Prandtl number $Pr_{\mathrm{t}} = 0.85$ to link momentum and thermal turbulence diffusivity. For discretization of the equations, I employed second order schemes. Simulations were all done steady-state. To judge convergence of the simulations, I consulted the normalized residuals and monitor points for the flow variables at different positions of the solution domain. All simulations were run until the flow variables became constant for the monitor points and the normalized residuals stopped decreasing. At this point, residuals had dropped at least three orders of magnitude. As fluid for the numerical simulations, I used compressible air as an ideal gas to determine the fluid's density and Sutherland's law with three coefficients (see App. A.5) to obtain the fluid's viscosity. For the fluid's thermal conductivity and its specific heat, I prescribed constant values, since the temperature variation in the solution domain was within a range of only 50 K. Figure 3.7 shows the solution domain and the boundary conditions used for the numerical simulations. As hydrodynamic boundary conditions, I prescribed a constant mass flow rate at the inlet, with a turbulence intensity of $Tu_{\mathrm{in}} = 5\%$ and a constant static pressure at the outlet. The mass flow rate at the inlet was determined from the numerical Reynolds number used for the simulation. It is defined as

$$Re_{C,\mathrm{num}} = \frac{u_{exit}\, C}{\nu_{\mathrm{air},\infty}}\,, \tag{3.3}$$

where C is the true chord of the vane profile, $\nu_{\mathrm{air},\infty}$ the kinematic viscosity of the incident air flow and u_{exit} the velocity magnitude at the exit cross section of the vane passage for the flat endwall baseline. Note that the definition of this numerical Reynolds number differs from the one of the experimental Reynolds number, Eq. (3.1), only by the different viscosities for water and air. As thermal boundary conditions, I used a constant static temperature of the fluid at the inlet and a constant temperature boundary condition at the lower endwall. To simulate endwall heat transfer, the fluid temperature at the inlet was 50 K above the temperature of

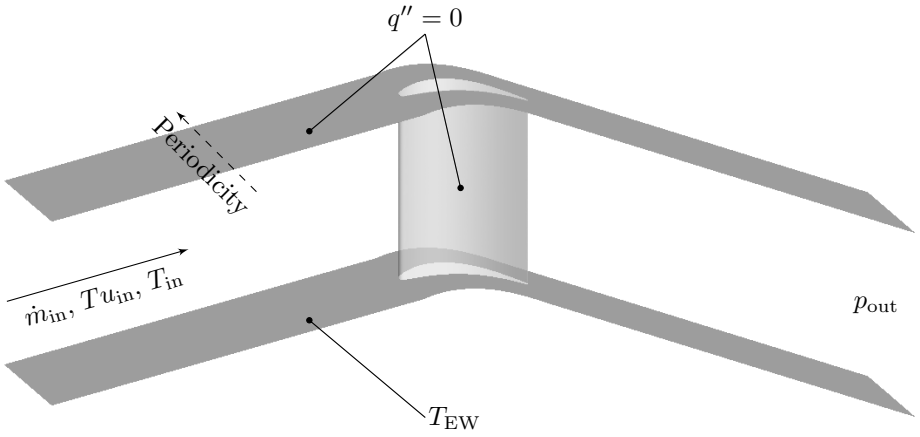

Figure 3.7: Boundary conditions for numerical solution domain

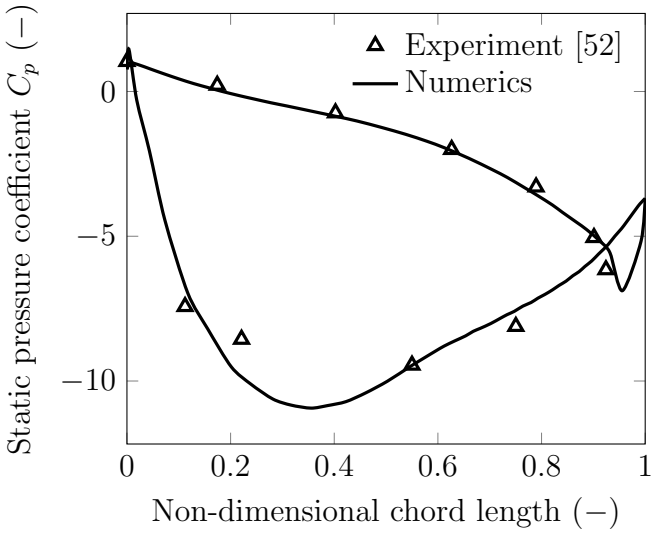

Figure 3.8: Distribution of static pressure coefficient around vane profile of Ligrani and Jin [52]: numerical prediction and experimental data

the lower endwall. Heat transfer was only simulated for the lower endwall, the vane and the upper endwall were prescribed as adiabatic. Note that for the simulations at the design Reynolds number (Re_C = 200,000), I prescribed fully developed velocity and temperature profiles at the inlet, since the inlet region was too short to attain fully developed flow profiles for this Reynolds number.

The above described numerical setup for the flat endwall needed to be validated in order to prove that it yields reliable results. Since no experimental data is available for the vane profile used in this work, I conducted the validation using a similar two-dimensional vane profile from an experimental study of Ligrani and Jin [52]. This study was conducted at similar Reynolds numbers as the ones used in the present work. Figure 3.8 shows the distribution of the static pressure coefficient around the vane profile as obtained with the numerical setup of this work and compares it to the experimental data from [52]. The used numerical setup predicts the distribution of the static pressure coefficient along the vane pressure side (upper line in plot) very well. For the vane suction side, the numerical results are also in good agreement with the experimental data. Merely at the rear suction side part of the profile the numerical prediction differs slightly from the experiment. This validation proves that the employed numerical setup of this work is capable of correctly predicting the flows around turbine vanes.

3.2.2 Ice Contours

To utilize the experimentally created ice layers as endwall contours for the numerical simulations, these needed to be digitized and processed for the numerical treatment. The digitization was done by Haase [26] at the end of each experiment. He used a

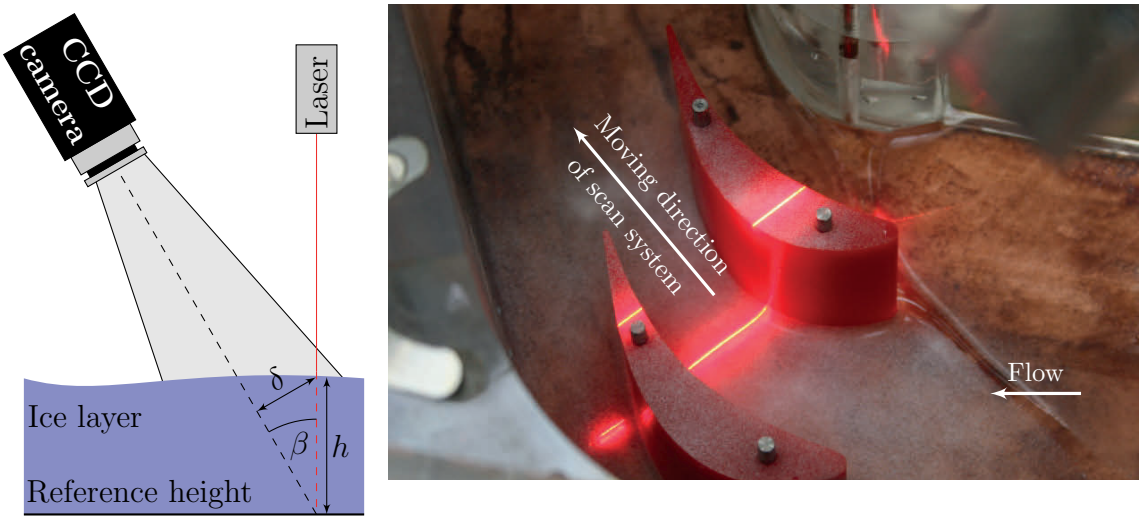

Figure 3.9: Laser triangulation method (left) and laser scanning of ice layer (right)

laser scan system from the company *in-situ* [32], which employs a laser triangulation method to measure the height of the ice layer. Figure 3.9 (left) shows a schematic of the laser triangulation method. The system uses a diode laser and a camera, which is tilted by the angle β. It is calibrated to the copper endwall of the channel as reference height. The system determines the local height of a point on the ice layer by projecting a laser beam onto the ice surface and recording the lateral displacement δ on the camera picture. With the known angle β between laser and camera, the height h then simply results from the displacement δ by using trigonometry ($h = \delta/sin\beta$). This height measurement has an accuracy of 0.094 mm.

Figure 3.9 (right) shows an ice layer during the scan process. The scan system digitizes the ice layer along a projected laser line. The system resolves 426 pixels on this line with a distance of 0.129 mm between the pixels. To scan the complete surface of an ice layer, it moves on a linear traverse over the ice layer perpendicular to the projected laser line and digitizes the ice layer line by line with a resolution of 0.2 mm between two adjacent laser lines.

The outcome of this digitization is a three-dimensional scatter plot of the scanned ice layer. Hence, I used MathWorks® Matlab [57] to reconstruct the surface of this ice layer. I then employed the so digitized ice layer as endwall contour for the lower endwall of the solution domain. Figure 3.10 exemplarily shows such a solution domain with a digitized ice layer as endwall contour. For the numerical simulations with these ice-contoured endwalls, I used the same parameters for grid generation and the same setup for the CFD as for the flat endwall baseline.

To validate the endwall heat transfer distribution predicted by the used numerical setup, I compared it against experimental data from Haase [26]. For this purpose, I simulated one exemplary experiment using the geometry of the entire test section including an ice layer at $Re_{C,\mathrm{exp}} = 49{,}900$ and $\Theta = 8.5$. However, since the laser scan system only digitizes the ice layer on two of the three vane passages, I needed

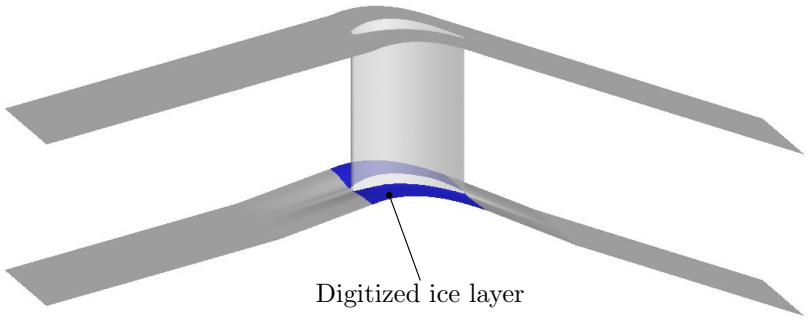

Figure 3.10: Solution domain with digitized ice layer as lower endwall

to model the remaining parts by periodically extending the digitized data. This replicated geometry then allowed for a simulation of the experiment using water as fluid and the experimental boundary conditions. Figure 3.11 shows the distribution of the heat transfer coefficient as predicted by the numerical model (left) and compares it to the one obtained from the experiment (right top). The latter was obtained from the thickness of the ice layer (Fig. 3.11, right bottom) using one-dimensional

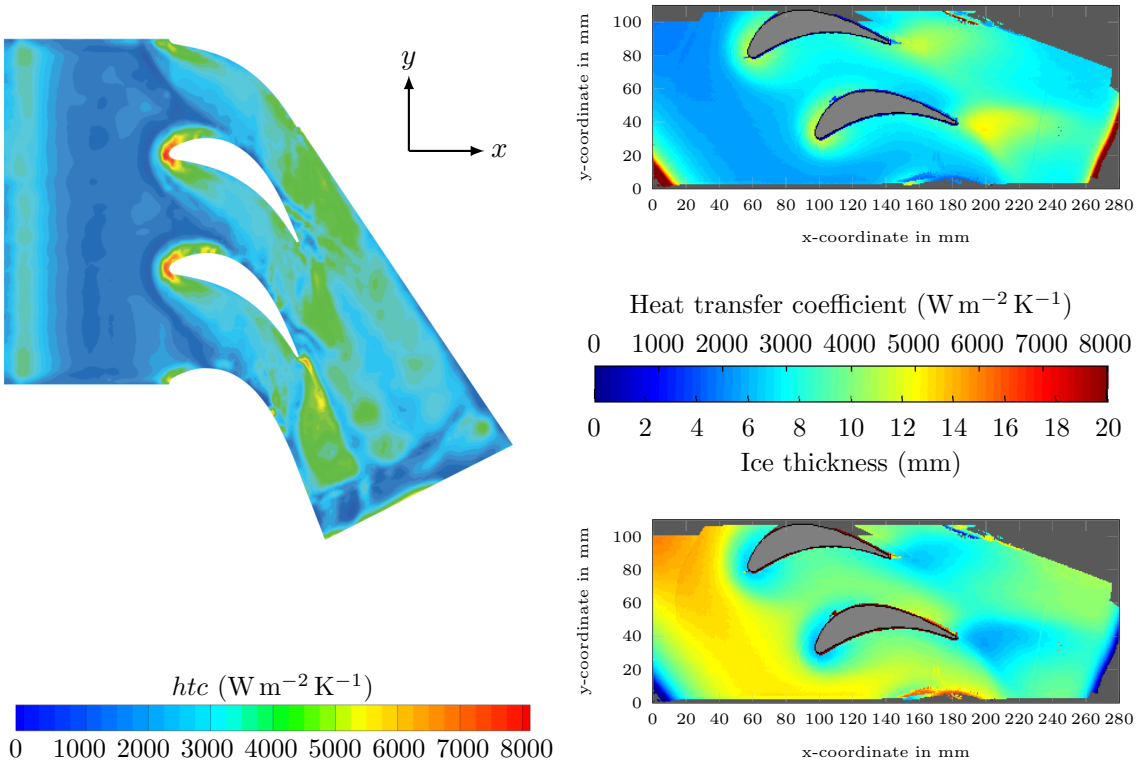

Figure 3.11: Distribution of heat transfer coefficient on ice contour obtained from numerics (left) and from experiments (right)

heat conduction (see [26]). Comparing the heat transfer distributions verifies that the numerical setup predicts all relevant features of endwall heat transfer. These are increased heat transfer around the vane leading edges, along the pressure sides, and in the wakes of the vanes as well as reduced heat transfer along the rear part of the vane suction sides. However, the numerical simulation overpredicts the maximal heat transfer at the vane leading edges. For a quantitative comparison, I averaged the heat transfer coefficient for the numerical and experimental data over both the full ice layer and the ice layer in the middle vane passage. Considering the full ice layer, the average *htc* predicted by the numerical simulation differs by 10.98% from the one obtained from the experiment. For the heat transfer coefficient averaged over the middle vane passage, the difference between numerics and experiment is 9.62%. These results prove that the numerical setup reliably predicts the heat transfer distribution on the endwall. Appendix A.6 holds the full data set of this validation.

In the present work, ice layers that have been experimentally created in water flow were employed as endwall contours for numerical simulations of a gas turbine that uses air as working medium. It was assumed that the changes in heat transfer that occur due to the ice layer that develops in water flow are reflected likewise for air flow. To validate this assumption, I again used the replicated experimental geometry with ice layer (described above) and performed numerical simulations using both water and air as fluid. In addition, I also simulated the reference case without ice layer for both media. From these simulations I determined the average Nusselt number on the endwall and calculated the ratio of ice layer to flat endwall for both water and air. This yields a Nusselt number ratio of 1.095 for water flow and 1.079 for air flow. Hence, the observed changes in heat transfer caused by the ice layers are similar for water and air flow. This allows for the use of the ice layers created in water flow as endwall contours for a gas turbine that operates with air.

3.2.3 Numerical Optimization

To optimize the endwall contours with the numerical optimization algorithm, I needed to parametrize the endwall geometry in the region that should be optimized. The parametrization serves the purpose to define the geometry of the endwall by only a few parameters. In the present thesis, I used Bézier splines, which describe an entire curve by only a few control points (see also Sec. 2.6.2). For each parametrization, I kept the x- and y-coordinates of these control points fixed. Hence, only the z-coordinates of the control points, which describe the distance normal to the flat endwall, define the geometry of the endwall contour. Figure 3.12 shows an endwall geometry created with such a parametrization. Note that the parametrization is a crucial part of the optimization process. It must be able to reproduce every possible geometry from the entire decision space, in order not to preclude parts of it from the optimization process. Hence, where applicable, I based the parametrization of the endwall contours on the ice-contoured endwall geometries. Since the ice layers do not have any restrictions on the decision space, a parametrization based on them is also free of restrictions.

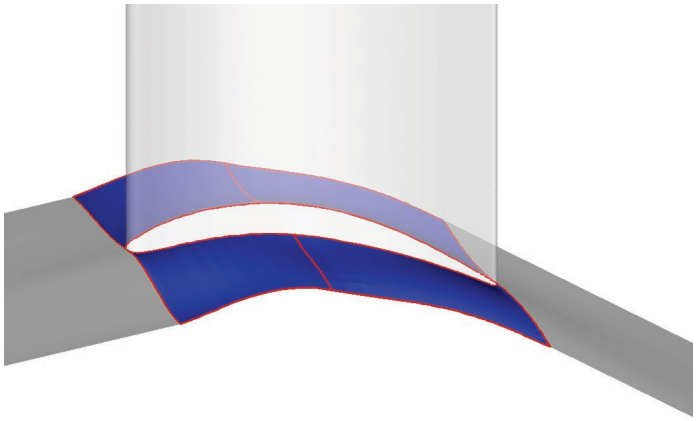

Figure 3.12: Generic parametrization of endwall contour; Bézier curves in red

For the numerical optimizations of this study, I used the genetic algorithm NSGA-II from Deb et al. [21] as described in Sec. 2.6.1. Here, the endwall contours represent the individuals of the genetic algorithm with the z-coordinate of the Bézier control points (height above flat endwall) being the genes or decision variables, respectively. These describe the characteristics of each individual, i.e. the geometry of the endwall contour. During the optimization process, the genetic algorithm creates several individuals and assigns a fitness based on a specified goal function to each individual. At the end of the optimization process the fittest individual is found, which is optimal with respect to the goal function. In this study, I used CFD simulations

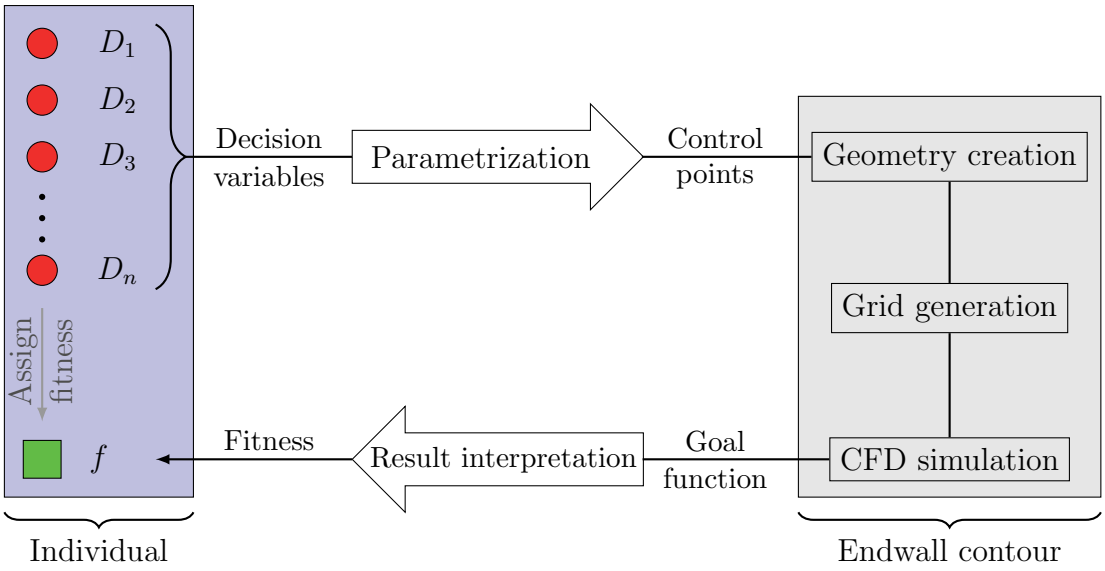

Figure 3.13: Procedure used to assign the fitness to an individual

to assign the fitness to each individual. Figure 3.13 shows the complete procedure used for this fitness assignment. It first uses the parametrization to interpret the decision variables as Bézier control points and hence transforms the individual into an endwall contour. Then, a grid is created and a CFD simulation is performed for this geometry. The simulation is finally evaluated with respect to the desired goal function, for example heat transfer at the lower endwall, and the result is assigned as fitness to the individual. For the CFD simulations of the numerical optimization, I used the same numerical setup as for the ice-contoured endwalls and the flat endwall baseline.

The CFD simulations to evaluate the fitness of the individuals consume most of the optimization's runtime. Hence, in order to obtain a convergent flow field solution as fast as possible, I used two speed-ups for the simulations during the numerical optimization: a smaller spatial grid and an initialization approach for the flow domain. The GCI study for the flat endwall, see Sec. 3.2.1, shows that the results obtained on the coarse grid (G2) are very similar to those of the grid which I used for the numerical simulations of this study (G1). Especially the average heat transfer coefficient differs by only 0.7%. Thus, for the geometries created during the optimization process, I applied the parameters from the coarse grid for grid generation.

In order to obtain the flow field solution with this grid fast, I tested different techniques to initialize the solution domain of these geometries. For this test, I used an endwall contour from a preliminary optimization run with the genetic algorithm and the parametrization explained before. I then performed CFD simulations for this geometry in Fluent, using three different techniques to initialize the flow field: initialization with inlet values, interpolation from flow field solution of ice-contoured endwall, and Fluent's fast multigrid (FMG) initialization. For simulations with these

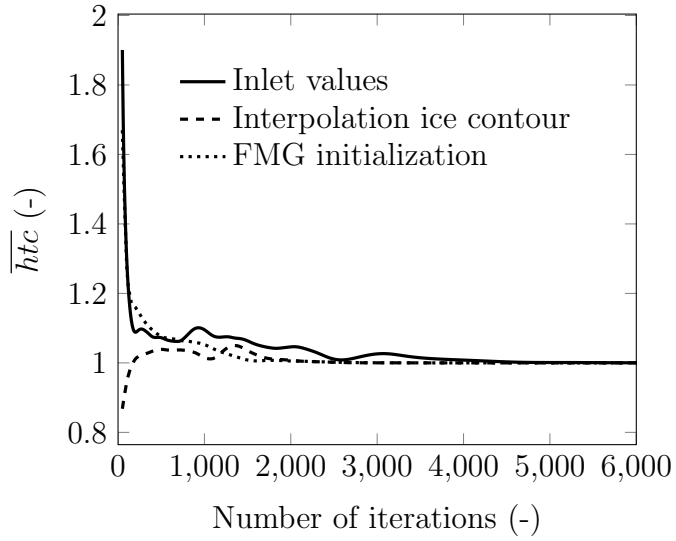

Figure 3.14: Convergence behavior of area-averaged heat transfer coefficient for different flow field initialization techniques

Table 3.4: Settings for NSGA-II

Crossover probability p_{cross}	0.8
Crossover distribution index η_C	50
Mutation probability p_{mut}	0.2
Distribution index for mutation η_m	10

three initialization techniques, Figure 3.14 shows the normalized, area-averaged htc at the lower endwall versus the number of iterations. All values were normalized with that of the fully converged solution. Initializing the flow field by interpolating from a converged solution or by using Fluent's FMG initialization shows a significant speed-up of convergence. With these two initialization techniques, the flow field converges within less than 2,000 iterations, whereas a simulation initialized with inlet values needs more than 4,000 iterations until convergence. Since the FMG initialization is quite time-consuming, I initialized the flow field for all geometries of the optimization process by interpolating from the flow field solution of the corresponding ice contour. For optimizations that were not based on an ice contour, I interpolated from the flow field solution of the flat endwall baseline instead.

To verify the results from the numerical optimizations, I performed a concluding CFD simulation for the final endwall contour of each optimization. For this simulation, I applied the parameters of the used grid (G1) for grid generation, initialized the flow field with inflow values and simulated as many as 8,000 iterations until complete convergence of the solution.

For the NSGA-II algorithm, Deb at al. [19] suggest a population size of 2^d, with d being the dimension of the considered optimization problem. However, the dimension of the optimization problem is not known a priori. Therefore, I assumed it to be three and performed a preliminary test run of the numerical optimization, using a population size of $2^3 = 8$ individuals and 20 generations. A further test run with the next higher dimension of $d = 4$ and hence a population size of 16 showed an improvement of only 0.07%, however, at double runtime. Also, an increase in the number of generations from 20 to 30 improved the goal function only by 3%. Hence, for all numerical optimizations in this study, I used a population size of 8 individuals and simulated 20 generations. Table 3.4 lists the remaining settings used for the NSGA-II optimization algorithm. An explanation of these variables is found in App. A.1.2 and A.1.3.

3.3 Considered Cases

In this study, I considered three different cases, which combine the application of the Ice Formation Method and of numerical optimization to create endwall contours with reduced heat transfer. The first case initially uses ice layers from the experiments as

endwall contours, which are afterwards used as starting points for further numerical optimizations. The second case employs only ice layers resulting from experiments with an enlarged copper inlay in the test section. For the third case I used solely numerical optimization based on the flat endwall to create optimized endwall contours. The following subsections describe these three cases in detail.

3.3.1 Ice Contours - Short Cooling Length

This is the most fundamental case of this study. For the numerical simulations of the ice-contoured endwalls, I processed the ice layers that Haase [26] created with the short copper inlay shown in Fig. 3.3 and embedded them into the lower endwall of the numerical solution domain. Those parts of the ice layer that develop on the cooled copper inlay up- and downstream of the vane passage are subject to constraints imposed by the finite length of the cooled area. Hence, in these regions the ice layer cannot evolve free of restrictions and I only took the ice layer within the vane passage as endwall contour. The omitted areas up- and downstream of it, I replaced by linear transitions. Figure 3.15 shows the final solution domain for an ice-contoured endwall created with the short cooling length. For reference, the figure also includes the dimension of the copper inlay for the short cooling length.

For this case, I also performed numerical optimizations using a parametrization of the endwall contour based on the digitized ice layer. Figure 3.16 depicts the parametrized endwall contour. In crosswise direction, the parametrization features six Bézier curves, that is two Bézier curves at the three axial positions: $0\%\,C_{\mathrm{ax}}$ (profile leading edge), $50\%\,C_{\mathrm{ax}}$ (mid of vane passage), and $100\%\,C_{\mathrm{ax}}$ (profile trailing

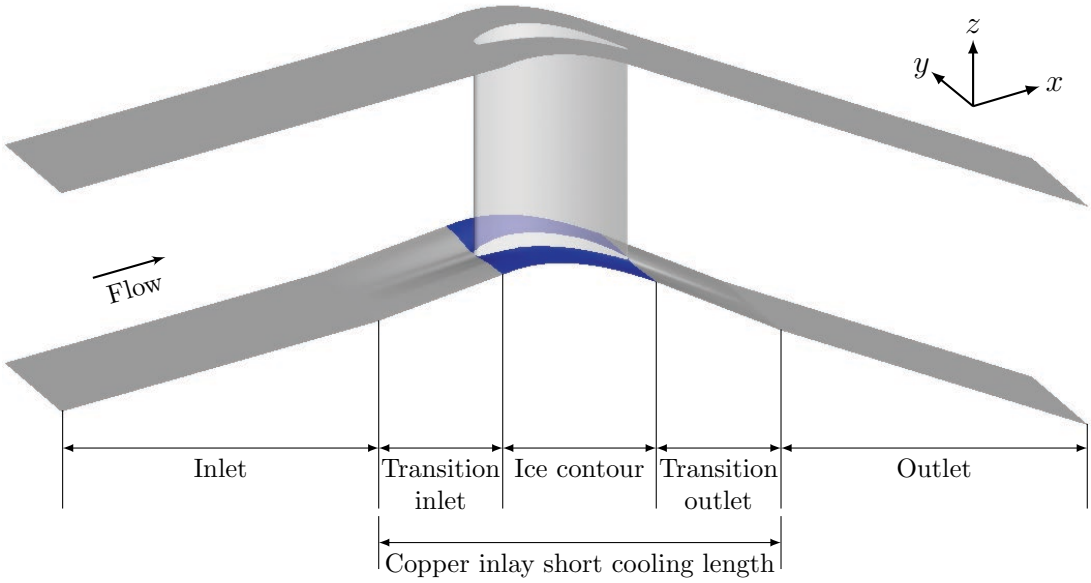

Figure 3.15: Ice contours short cooling length: Solution domain

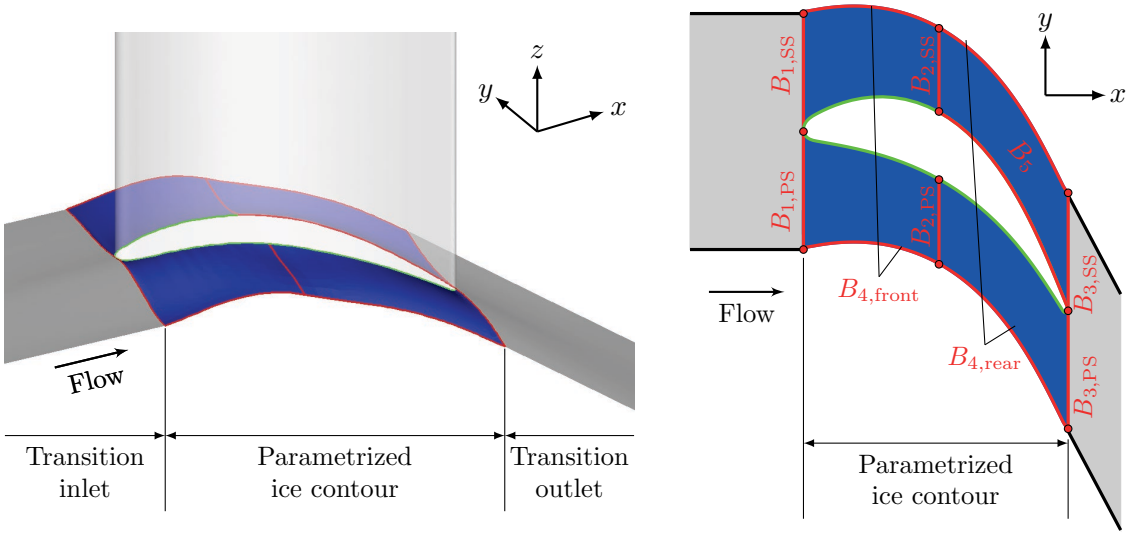

Figure 3.16: Ice contours short cooling length: Parametrized contour in isometric (left) and top view (right) with Bézier curves (—), edges of transition region (—), edges from ice layer (—), and curve junctions (●)

edge). Each axial position thereby features two curves, one in the pressure side (PS) region and one in the suction side (SS) region. For reasons of periodicity, the suction and pressure side Bézier curves share a common point at the periodic boundary. In streamwise direction, I used two Bézier curves, $B_{4,\mathrm{front}}$ and $B_{4,\mathrm{rear}}$. These curves lie directly at the periodic boundaries, where they connect the Bézier curves running in crosswise direction. Note that the Bézier curves in streamwise direction are the same at the upper and lower periodic boundary of the solution domain. Furthermore, I parametrized the rear suction side of the vane profile with an additional Bézier curve (B_5), since the experiments indicated that this region can be crucial for the contouring. This Bézier curve connects $B_{2,\mathrm{SS}}$ and $B_{3,\mathrm{SS}}$ at the rear suction side meeting points. The remaining edges at the vane were not parametrized. Instead, I took the geometry of these edges from the digitized ice layer to keep the benefits from the ice contouring. To ensure steadiness of the parametrized endwall contour, I prescribed C^1-steadiness (see Sec. 2.6.2 for definition) at all curve junctions. Figure 3.17 (left) illustrates this for the junction of two Bézier curves. The latter is a control point of both curves and I specified it to lie midway in between the two neighboring control points. Since both Bézier curves are of the same order, this ensures that they are C^1-steady. At the leading and trailing edge, where the transition regions merge into the parametrized endwall contour, see middle sketch in Fig. 3.17, I prescribed C^1-steadiness. For this purpose I used the z-coordinate of the first control point of the Bézier curve (a decision variable determined by the optimization algorithm) and the axial length of the transition region. From these values, I determined the slope at the merge position and hence calculated the z-coordinate of the Bézier curve's second control point according to Eq. (2.62). At the

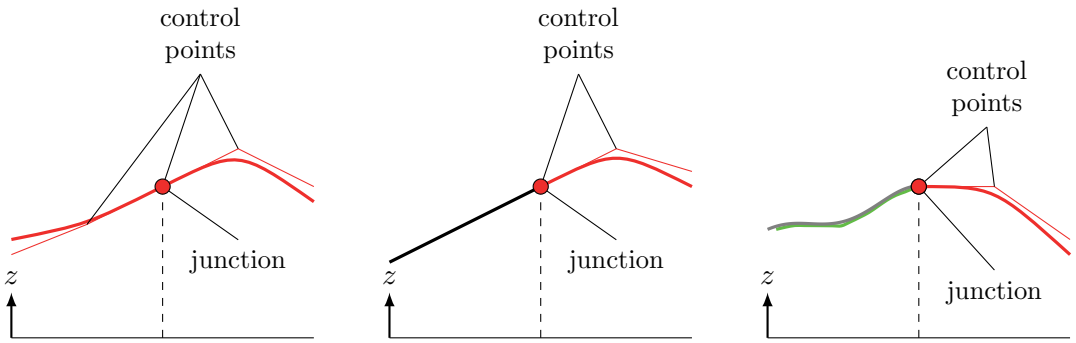

Figure 3.17: C^1-steadiness at junction of two curves (left), merge position of transition regions and parametrized contour (middle), and rear suction side (right) with edge from ice layer (—) and polynomial function (—)

rear suction side (Fig. 3.17, right), I obtained the slope at the end of the edge from the ice layer by calculating it from a polynomial function that approximates this edge. Using this slope, I then determined the first two control points of the adjacent Bézier curve. Note that, for this considered case, the region of the contouring is restricted to the vane passage, the transition regions are only the result of this contouring.

The parametrization of this case has a total of twelve decision variables, which the optimization algorithm uses to create the different endwall contours during the optimization process. The upper and lower limit of these decision variables I set to 0 mm (height of flat endwall) and 10 mm (≈ 7% span), respectively. Thus, the values for the z-coordinates of the control points lie within the range $0\,\text{mm} < z < 10\,\text{mm}$ and all endwall contours lie within a 10 mm thick block above the vane passage of the flat endwall baseline. Figure 3.18 shows the optimization space for this case.

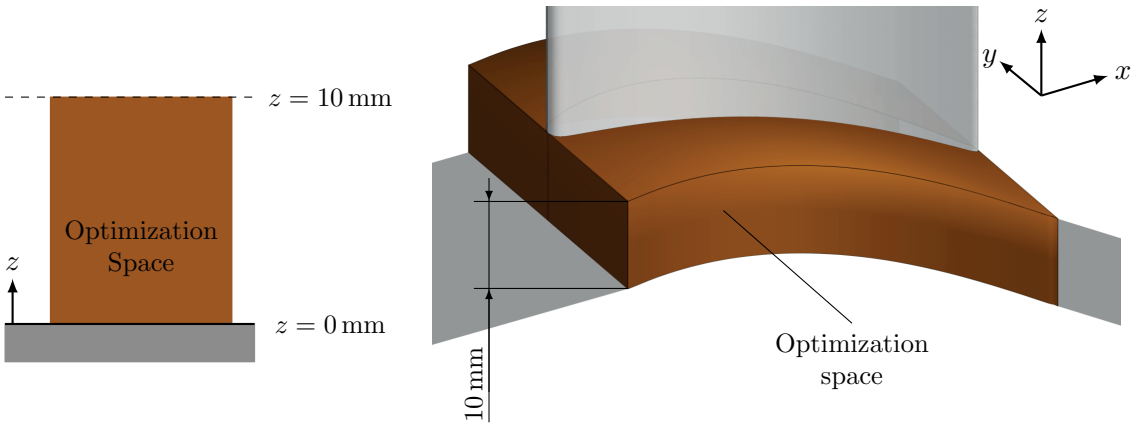

Figure 3.18: Ice contours short cooling length: Optimization space

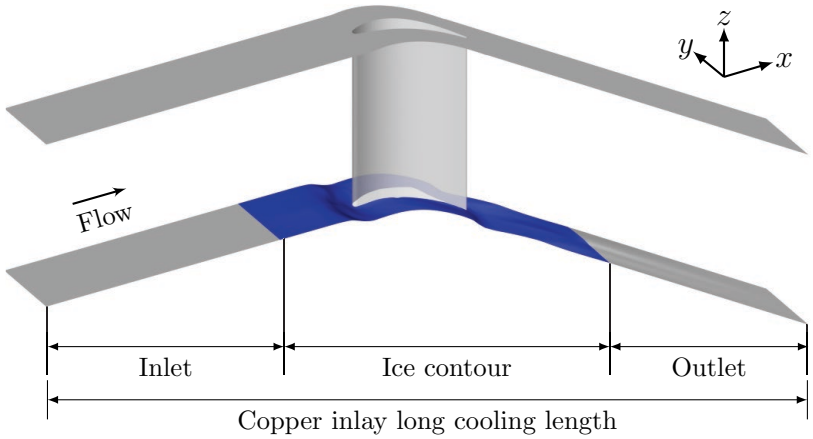

Figure 3.19: Ice contour long cooling length: Solution domain

3.3.2 Ice Contours - Long Cooling Length

In the experiments, Haase [26] additionally used an enlarged cooled copper inlay to create ice layers that are restriction-free for a larger area of the flow geometry (see App. A.3 for the copper inlay). I also processed these ice layers and embedded them into the solution domain for numerical simulations. Figure 3.19 shows the solution domain for such an ice-contoured endwall with long cooling length. The figure also indicates the dimension of the enlarged copper inlay used in the experiment. For this case, the ice layer ranges from $0.5\,C_{\mathrm{ax}}$ upstream of the vane passage to $1.5\,C_{\mathrm{ax}}$ downstream of it. At its beginning, upstream of the vane passage, this ice layer grows to a constant height in pitchwise direction. Hence, for the numerical simulations, I shifted the digitized ice layer down by this height in order to make it even with the flat endwall in the inlet region. Thus, a slight transition was necessary in the outlet region to bring the geometry back to the height of the flat endwall. Note that I did not perform numerical optimizations for the ice-contoured endwalls of this case.

3.3.3 Numerical Optimization from Flat Endwall

In addition to the optimizations based on the ice-contoured endwalls, I also performed numerical optimizations for which the parametrization of the endwall contour is based on the flat endwall. Figure 3.20 shows the used parametrization. As for the ice contours, I only parametrized the vane passage and applied linear transitions up- and downstream of it. This parametrization also uses six Bézier curves in crosswise direction (one Bézier curve each in both the pressure (PS) and suction side (SS) region) and two Bézier curves at the periodic boundaries of the vane passage. In contrast to the parametrization of the ice contours, I fully parametrized the vane profile for this case. This yields the additional Bézier curves B_6, B_7 and B_8. Hence, the parametrization of this case has a total of 21 decision variables. To obtain a steady endwall contour, this parametrization also uses C^1-steadiness at all curve

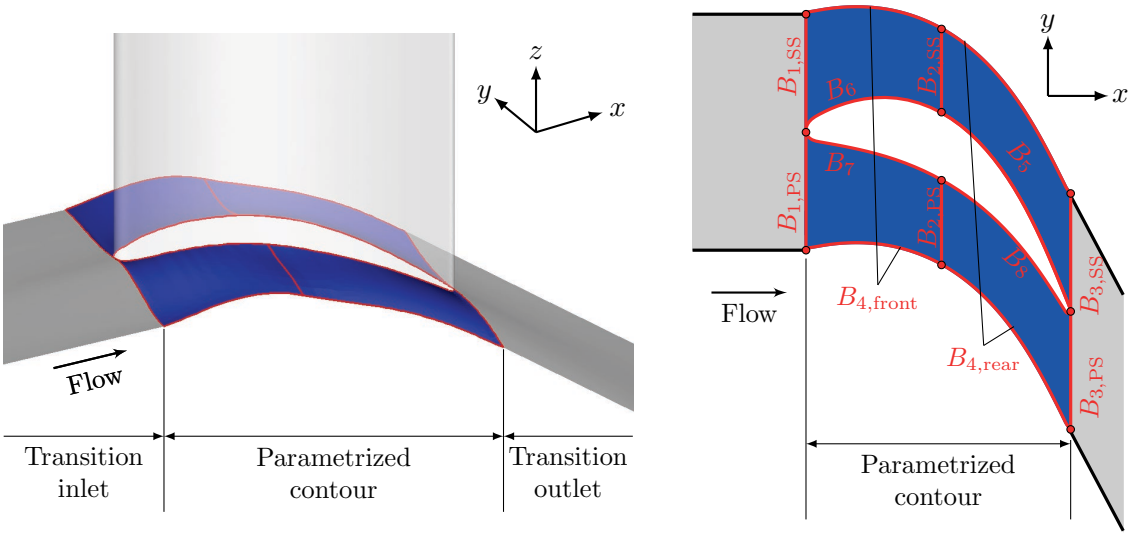

Figure 3.20: Optimization flat endwall: Param. contour in isometric (left) and top view (right) with Bézier curves (—) and edges of transition region (—)

junctions (see also Fig. 3.17). As for the optimizations based on the ice-contoured endwalls, the optimization space for this case has a height of 10 mm. However, for this case, the optimization ranges from 5 mm above the flat endwall baseline to 5 mm below it (see Fig. 3.21). This allows for an endwall contour with local heights below the flat endwall baseline. Furthermore, for this case, I also performed a numerical optimization with the optimization space being extended to 30 mm, i.e. ranging from 15 mm above to 15 mm below the flat endwall baseline.

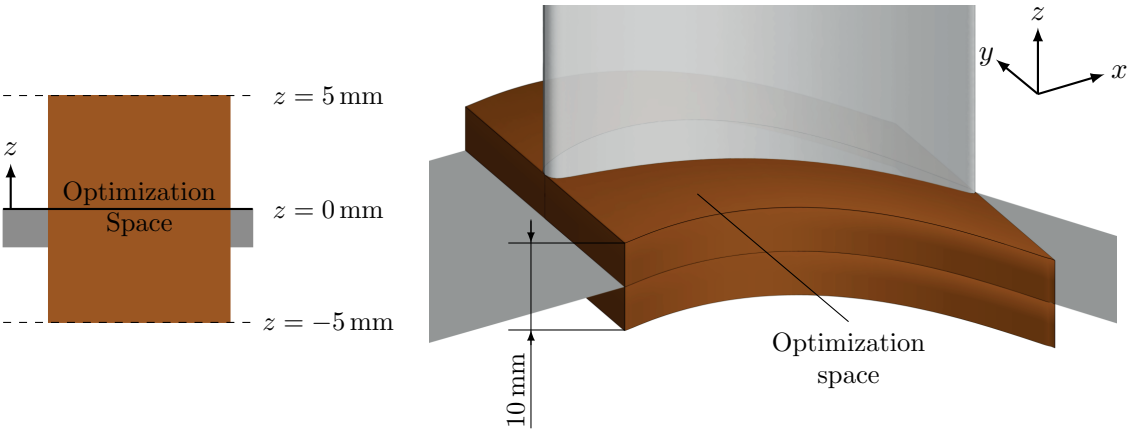

Figure 3.21: Optimization from flat endwall: Optimization space

4

Results Ice Contours Short Cooling Length

Contents:
Flow features and associated endwall heat transfer for flat endwall baseline - Flow field and heat transfer results for ice-contoured endwalls - Entropy production rates for ice-contoured endwalls and comparison to baseline - Results for endwall contours created from numerical optimizations on basis of ice-contoured endwalls

4.1 Flat Endwall Baseline

The flat endwall serves as the baseline for this study and all contoured endwalls are compared to this baseline case. Therefore, I present in this section the heat transfer characteristics of the flat endwall and outline the underlying flow field with its vortical structures. This is done for $Re_C = 49{,}900$. Results showed that flow and heat transfer characteristics are similar for the other Reynolds numbers.

For vane cascades, the flow features of the vane/endwall configuration dominate endwall heat transfer. The flow behavior near the endwall thereby is essential to understand the heat transfer. Figure 4.1 illustrates this near-endwall flow in terms of numerical oil flow visualization on the flat endwall baseline. The numerical data show all relevant flow phenomena, as presented in Figs. 2.4 and 2.5: the saddle point region in front of the leading edge, the separation lines of horseshoe and passage vortex and the shear flow downstream of the trailing edge.

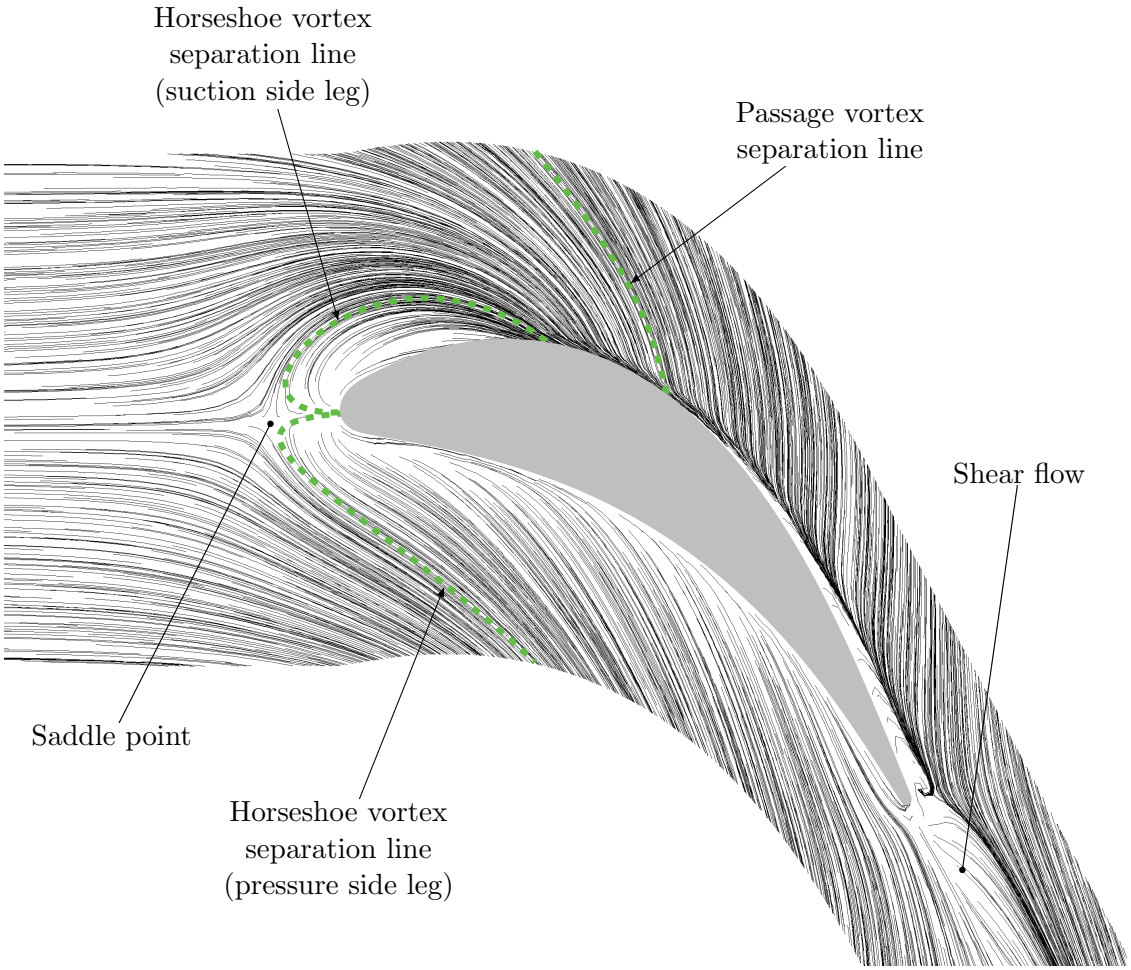

Figure 4.1: Numerical oil flow visualization on flat endwall

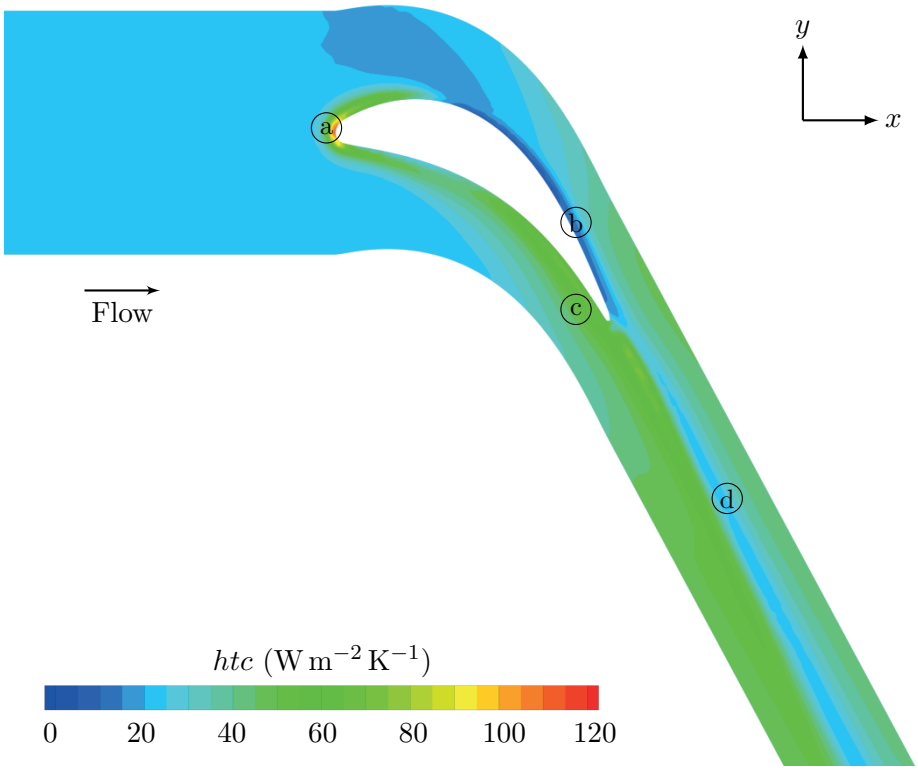

Figure 4.2: Distribution of heat transfer coefficient for flat endwall

Figure 4.2 shows the distribution of the heat transfer coefficient (htc) on the endwall, which results from the flow field near the endwall. It features maximum heat transfer at the leading edge (a), minimum heat transfer at the rear suction side (b), a region with high heat transfer at the rear pressure side (c), and, except for a small stripe (d), increased heat transfer in the vane's wake. Figure 4.3 illustrates the associated vortex system by path lines of the near-endwall flow. At the leading edge,

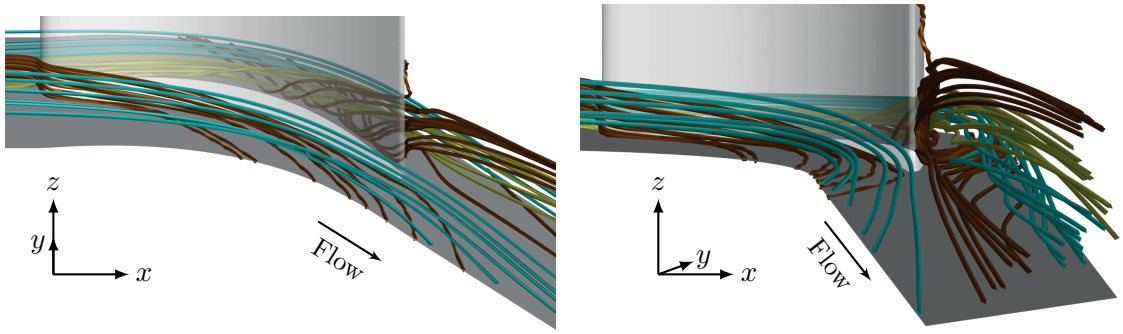

Figure 4.3: Vortex system for flat endwall baseline

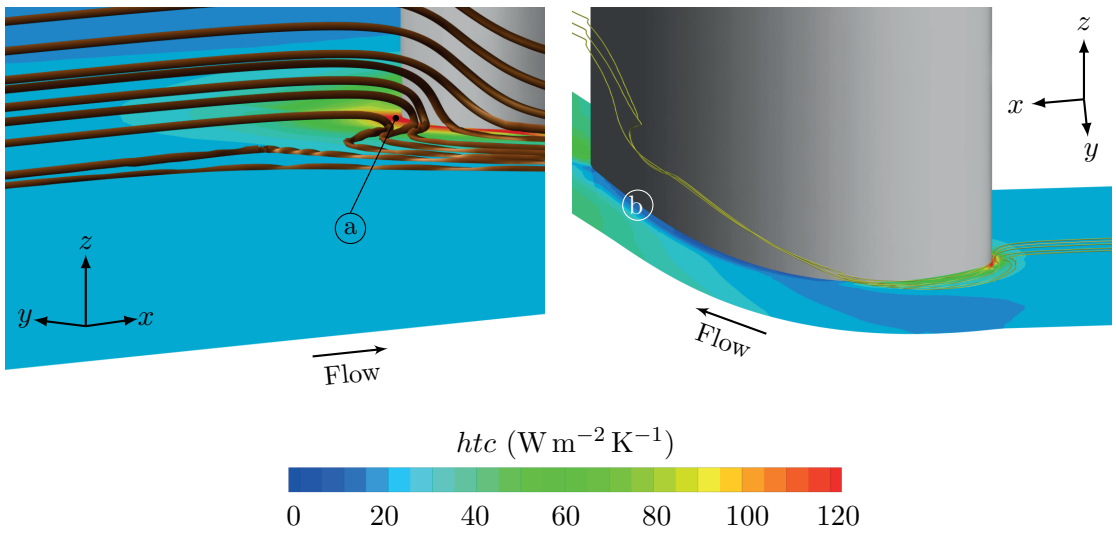

Figure 4.4: Flat endwall baseline: Heat transfer and path lines at leading edge (left) and at suction side of the vane (right)

the boundary layer rolls up into the horseshoe vortex, consisting of a pressure side (brown) and a suction side leg (yellow). The pressure side leg evolves into the passage vortex as it moves across the vane passage and, when it encounters the rear suction side of the vane, it is deflected upwards (positive z-direction) along the vane. This also causes the suction side leg to move upwards. Together with fluid from the mean flow (blue), the suction side leg then merges into the passage vortex. The latter extends from the rear vane passage downstream to the outlet.

Figure 4.4 (left) shows endwall heat transfer and path lines in the stagnation region at the leading edge. Due to the pressure gradient, the incoming flow is deflected downwards at the leading edge and impinges on the endwall, causing the maximum heat transfer (a) at this position. At the suction side, see Fig. 4.4 (right), heat transfer is high in the front region, where the suction side leg of the horseshoe vortex forms. However, heat transfer drastically decreases as soon as the vortex leg moves upwards along the vane and hence away from the endwall. Thus, minimum endwall heat transfer is found at the rear suction side (b).

Figure 4.2 indicated high heat transfer along the whole pressure side due to the pressure side leg of the horseshoe vortex, which evolves into the passage vortex on its way through the vane passage. The highest heat transfer rates thereby occur at the rear third of the pressure side. For this region, Fig. 4.5 (top) shows iso-surfaces of the vertical velocity component. These reveal that the high heat transfer rates are caused by the vortex inducing the highest velocities towards the endwall in this region. In the vane wake, endwall heat transfer is governed by the passage vortex, which remains until the outlet. Figure 4.5 (bottom) illustrates this by showing path lines and velocities normal to the endwall in planes downstream of the vane. All planes are perpendicular to the outflow direction. The vortex extends in outflow

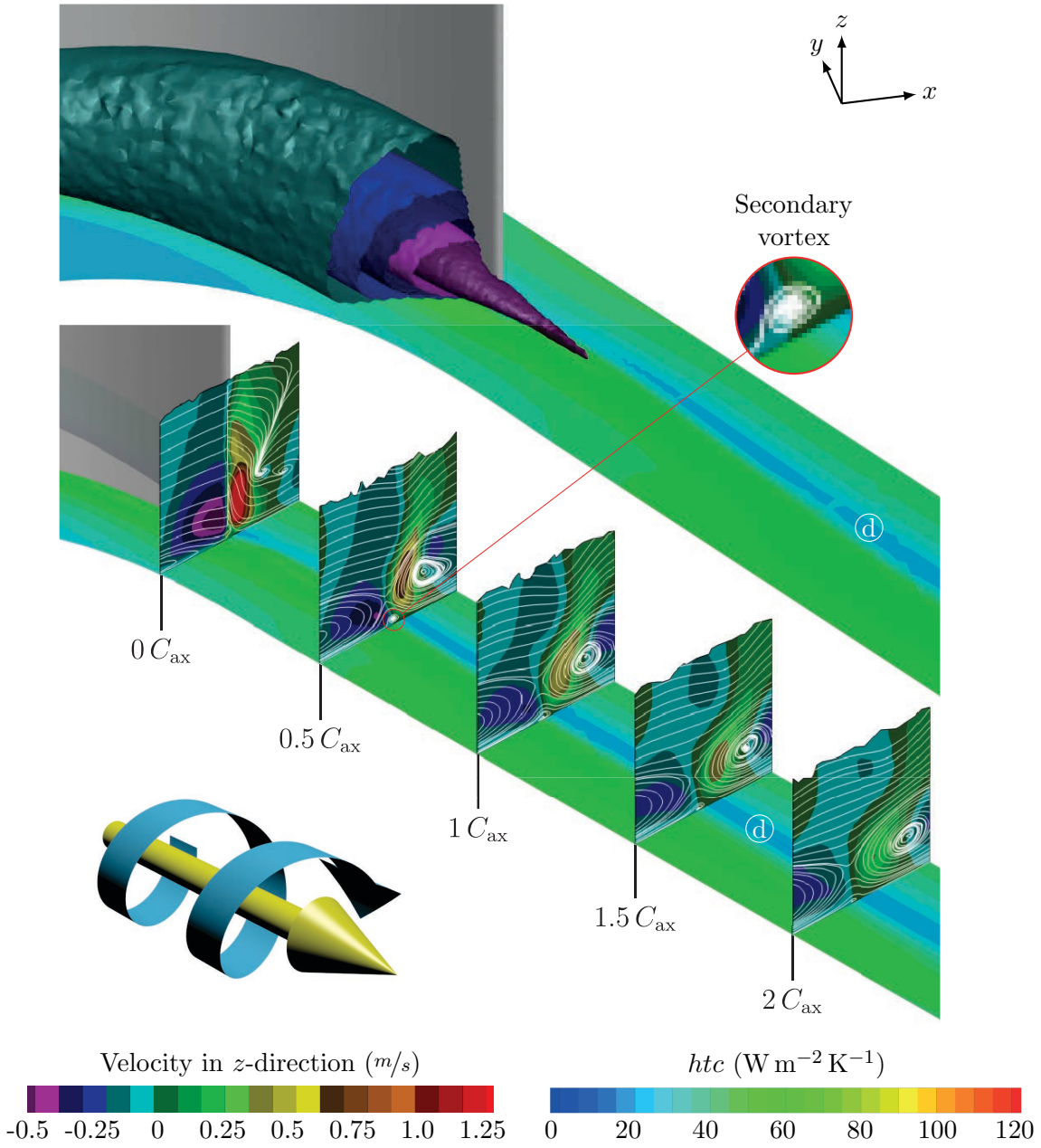

Figure 4.5: Flat endwall baseline: Heat transfer and velocity component in z-direction at rear pressure side (top) and downstream of vane (bottom)

direction and rotates counter-clockwise in flow direction (see sketch on lower left). Due to its rotation, it induces both upwards and downwards velocities close to the endwall. The upwards velocities accelerate fluid close to the endwall away from it and hence cause reduced heat transfer. The downwards velocities, in contrast, cause fluid to impinge on the endwall and hence create regions with high heat transfer. Note also the small secondary vortex (see magnification) induced by the vertical velocities

at the endwall. As explained in Sec. 2.2 (see also Fig. 2.6), this vortex results from the shear layer in between the two neighboring passage vortices. The vortex strength and thus the induced velocities are highest at the vane's trailing edge. This explains the regions with maximum and minimum *htc* directly downstream of the vane. With increasing distance to the vane, the strength of the vortex decreases, leading to lower velocities in z-direction. Thus, heat transfer becomes more balanced towards the outlet, however, a small stripe of low heat transfer (d) remains. This stripe indicates the outer edge of the vortex, where the induced upwards velocities are maximal.

4.2 Ice-contoured Endwalls

For the short cooling length, Haase [26] created nine different ice layers in the test facility, using three temperature ratios ($\Theta_{\text{exp}} = 6.5$, 8.5, and 12.2) at each of the three Reynolds numbers $Re_{C,\text{exp}} = 34{,}000$, 49,900, and 71,400. This section presents the results for the numerical simulations with these endwall contours at the experimental Reynolds numbers.

To obtain the numerical solution domains with the ice-contoured endwalls, I processed the digitized ice layers as described in Sec. 3.2.2. The numerical simulations were then performed using the gas turbine medium air. Since the ice layers were created in water flow, Reynolds number similarity was applied for all simulations, that is $Re_{C,\text{exp}} = Re_{C,\text{num}}$. Results are first presented in terms of heat transfer and later on in terms of entropy production, always beginning with the results for all nine ice-contoured endwalls and subsequently analyzing one selected contour in detail.

4.2.1 Heat Transfer

To evaluate heat transfer for the ice-contoured endwalls, I compared their heat transfer coefficients to the one of the flat endwall baseline at the same Reynolds number. All heat transfer coefficients were obtained from the CFD simulations and were area-averaged over the entire lower endwall. Figure 4.6 shows the percentaged reductions which the ice contours achieve compared to the baseline. It is notable that all ice-contoured endwalls reduce average heat transfer compared to the baseline. This shows that the Ice Formation Method reliably creates contours adapted to the vane/endwall flow field and hence capable of reducing endwall heat transfer. The degree of *htc* reduction thereby depends on the two competing parameters temperature ratio Θ and Reynolds number Re_C. The former determines ice growth on the cooled copper inlay, i.e. the higher Θ, the colder the temperature of the copper for a constant water temperature and the more ice grows on it. The latter determines the melting rate of the ice due to heat transfer rates induced by the flow. That is, with higher Reynolds number the flow induced heat transfer rates increase and the contouring of the ice layer becomes more pronounced. For the lowest Re_C (34,000), the velocities of the flow and hence the induced heat transfer are only moderate and therefore the grown ice cannot be contoured effectively by the flow. Thus, for

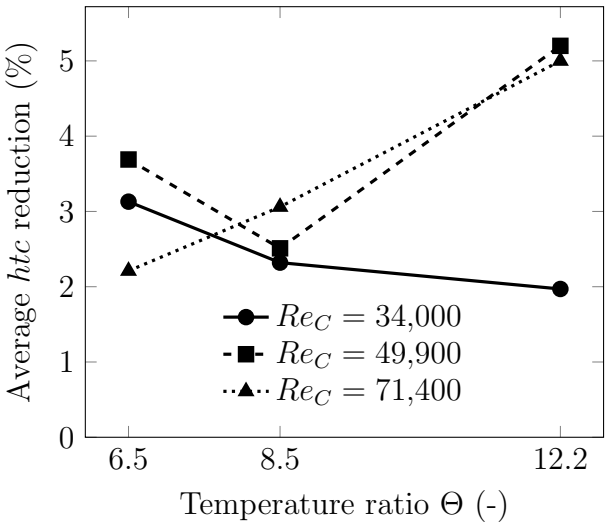

1

Figure 4.6: Average heat transfer reductions of ice-contoured endwalls compared to flat endwall baseline

Re_C = 34000 the reduction in area-averaged *htc* declines with increasing Θ since ice growth becomes too dominant. For the highest Reynolds number (71,400), heat transfer outbalances ice growth at the lowest temperature ratio of $\Theta = 6.5$, resulting in an endwall contour with low *htc* reduction. However, for this Reynolds number, the flow's heat transfer rates are high enough to also effectively contour thicker ice layers. Hence, contouring becomes more pronounced with increasing Θ, which yields ice-contoured endwalls with high heat transfer reductions. For the ice layers of the mid Reynolds number (Re_C = 49,900), ice growth and flow induced melting rates are more balanced than for the other Reynolds numbers. Hence, the heat transfer reductions for the ice layers of this Reynolds number do not have a clear trend. Heat transfer reduction for the ice layer at $\Theta = 8.5$ is lower than for the one at $\Theta = 6.5$, while the ice contour at the highest temperature ratio holds the lowest heat transfer of all ice-contoured endwalls. Compared to the flat endwall, it reduces average heat transfer by 5.20%. In the remainder, I refer to this contour as $\mathrm{IC_{IFM}}$.

Figure 4.7 depicts this contour in terms of its height levels (left) and in a three-dimensional view (right). It features concave regions with low heights around the leading edge (A), where the boundary layer rolls up into the horseshoe vortex causing high heat transfer rates and thus low ice thickness. In the middle of the vane passage, heat transfer is low, and hence the ice grows high at this position (B). The passage vortex, which evolves from the pressure side leg of the horseshoe vortex, mainly governs flow and heat transfer in the vane passage. Due to its rotational direction, fluid impinges on the ice layer and causes high heat transfer rates at the rear pressure side and hence low ice thickness. At the rear suction side, the passage vortex induces velocities away from the endwall, resulting in low heat transfer. Hence, melting rates are low and a height maximum (C) develops at this position. Note that this

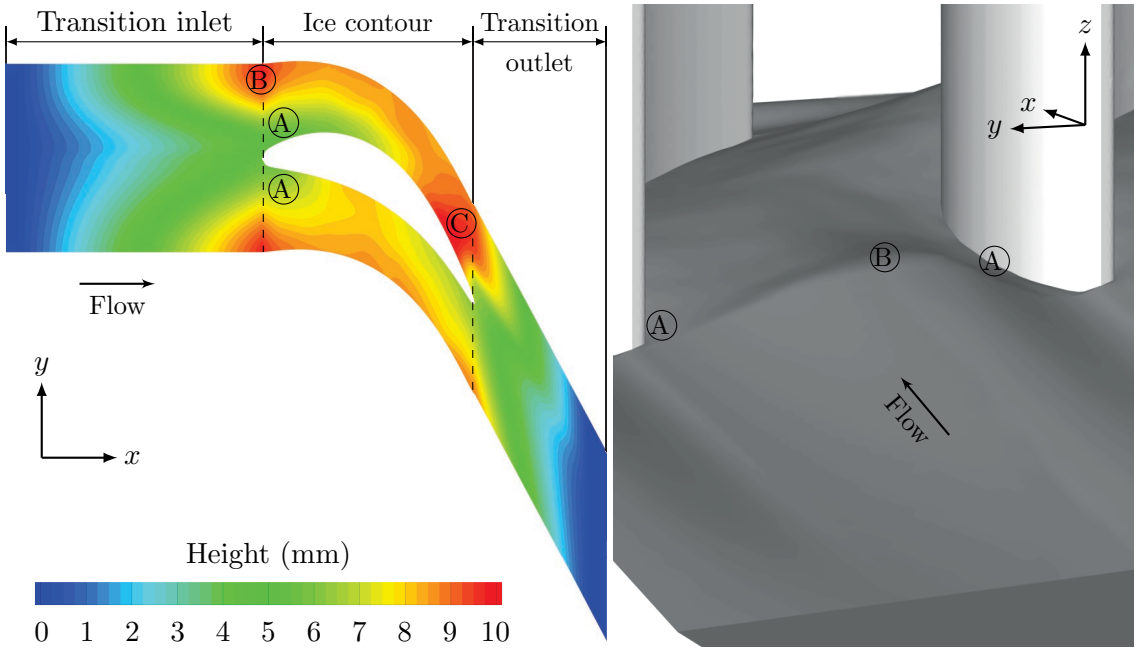

Figure 4.7: Ice-contoured endwall with short cooling length at Re_C = 49,900 and $\Theta = 12.2$ (IC_{IFM}): Height levels (left) and three-dimensional view (right)

steady-state ice layer is the result of a mutual interaction between flow field and flow geometry. That is, both the geometry and the flow field differ from that of the flat endwall baseline, thus causing a change in the heat transfer distribution.

Figure 4.8 shows the heat transfer distribution obtained for this ice-contoured endwall from the CFD simulation (left) and compares it to the flat endwall by showing the *htc* ratio of contoured to flat endwall (right). In this ratio, values above unity indicate increased heat transfer for the ice contour, whereas values below unity show regions where the ice-contoured endwall features lower heat transfer than the baseline. The contouring significantly alters the heat transfer distribution, with local heat transfer rates being both lower and higher than for the baseline. The most prominent changes are a region with low heat transfer at the rear suction side (e), a band with high and low heat transfer side by side in the rear pressure side passage exit (f), and low heat transfer in the outflow region (g), which is, except for a small stripe (h), lower than for the baseline.

The changes in endwall heat transfer are closely linked to the altered flow field due to the contouring. Figure 4.9 shows the vortex system for the ice-contoured endwall in terms of path lines (compare also to Fig 4.3). The contouring shifts the turning of the passage vortex from pressure to suction side further downstream to the rear part of the vane passage. As for the flat endwall, the passage vortex also impinges at the rear suction side. However, due to the diverging geometry downstream of the height maximum (see (C) in Fig 4.7), a recirculation zone develops at the end of the suction side. This recirculation zone holds only low momentum fluid, resulting in the

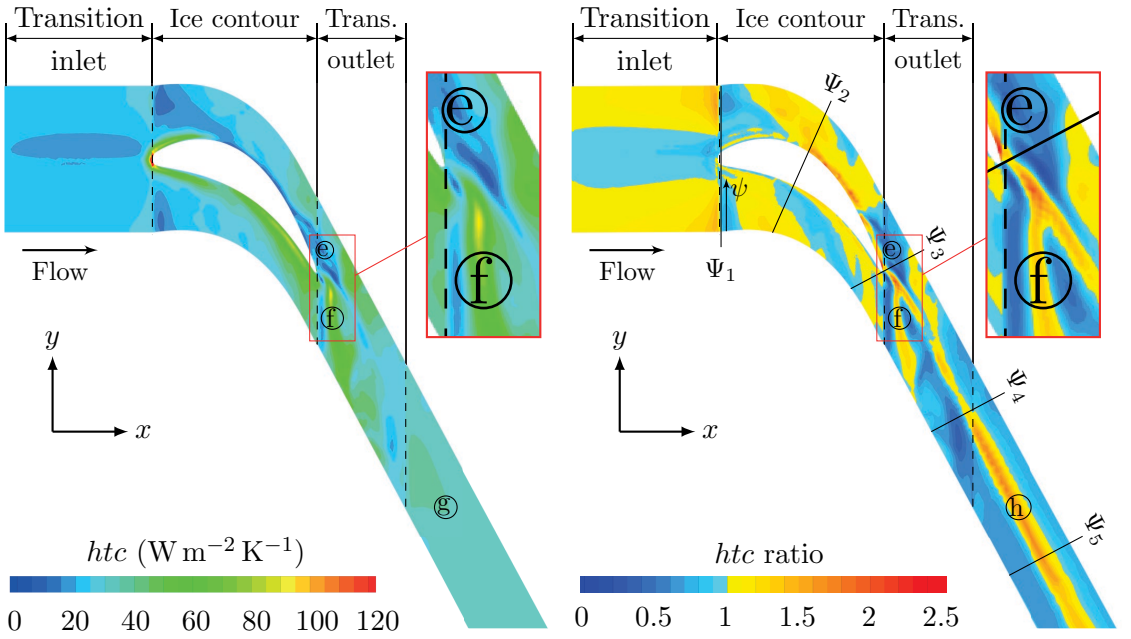

Figure 4.8: *htc* distribution for ice-contoured endwall IC_{IFM} (left) and *htc* ratio of contoured to flat endwall (right) at $Re_C = 49{,}900$

low heat transfer rates (e) in this region. Furthermore, it causes a strong deflection of the passage vortex directly behind the trailing edge and hence produces the band (f) with increased *htc*, where the vortex induces impinging flow, and reduced heat transfer where the vortex induces velocities away from the endwall. In addition, it breaks up the vortex structures and inhibits that the pressure and suction side legs of the horseshoe vortex form a strong passage vortex as this is the case for the baseline.

To outline these changes in the vortex structure, I extracted vortex cores using the Q-criterion (see Sec. 2.7). Figure 4.10 shows the vortex cores for the contoured endwall IC_{IFM} and the baseline as iso-surfaces of $Q = 8{,}000$. The figure clearly shows

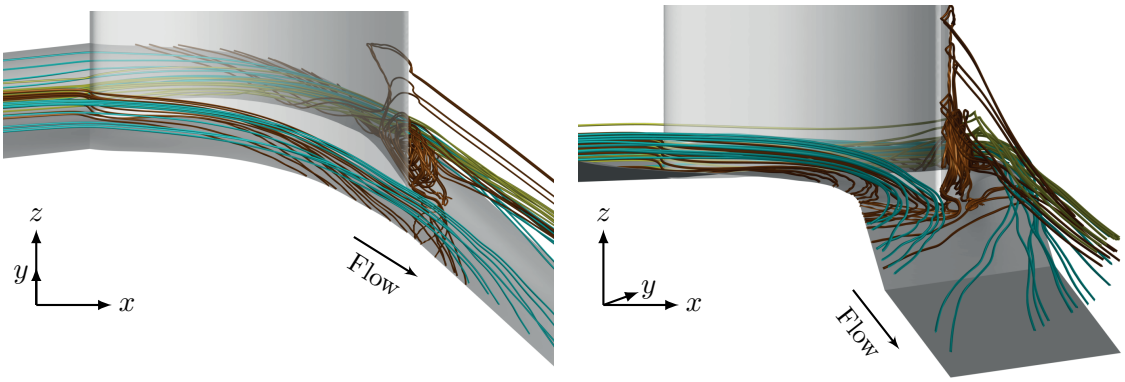

Figure 4.9: Vortex system for ice-contoured endwall IC_{IFM} at $Re_C = 49{,}900$

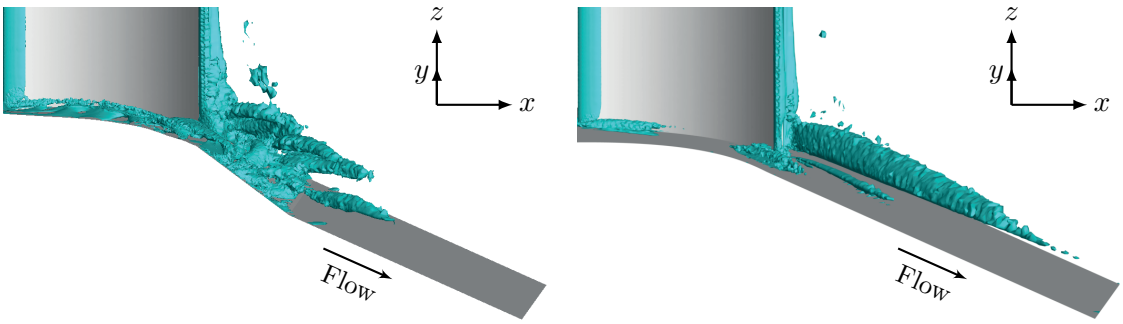

Figure 4.10: Vortex cores for contour IC_{IFM} (left) and for flat endwall (right) at $Re_C = 49{,}900$

that, for the baseline, the passage vortex runs in outflow direction and exists almost until the outlet. Due to this course of the passage vortex, heat transfer is high in the outflow region for the baseline, except for the small stripe at the outer edge of the vortex (see (d) in Fig. 4.2). For the ice-contoured endwall, the passage vortex does not run as far downstream as for the baseline, since the contouring breaks up the vortex system at the trailing edge by diffusing it. This causes an upwards shift of the vortex system away from the endwall and a shorter spread of it in downstream direction. This explains the low endwall heat transfer for the ice-contoured endwall in the outflow region (g). In the latter, heat transfer rates are much lower for the ice-contoured endwall than for the baseline, except for the small stripe (h). Note that for this stripe, heat transfer is very low for the baseline. Hence, although heat transfer is increased by the contouring, heat transfer rates are still low in this region.

To point out the local relationship between flow and heat transfer, I analyzed heat transfer rates and the near-endwall flow field at the five cross-sections Ψ_1-Ψ_5 (see Fig. 4.8, right). Figure 4.11 shows the local *htc* distribution on the endwall along the dimensionless cross-section width ψ and the vertical velocity component (z-direction) for the two cross-sections Ψ_1 and Ψ_2. The velocity contours are enhanced by path lines which indicate the secondary flows in these cross-sections. As indicated in Fig. 4.8, Ψ_1 is located directly downstream of the leading edge and Ψ_2 at $0.5\,C_{ax}$, being perpendicular to the local flow direction. For comparison, results are shown for both the ice-contoured endwall IC_{IFM} and the baseline (BSL). In Ψ_1, heat transfer is maximal at the vane for both cases, since here the formation of the horseshoe vortex induces high velocities towards the endwall. With increasing distance from the vane, the *htc* significantly decreases, the ice contour having lower heat transfer rates since the contouring alters the near-endwall flow field and induces upwards velocities. Towards the periodic boundaries ($\psi \to 0$ and $\psi \to 1$), the contoured endwall causes again downwards velocities and heat transfer rates approach those of the baseline. In cross-section Ψ_2, heat transfer rates are much lower. Here, heat transfer is higher in the pressure side region than in the suction side region. The highest heat transfer is located close to the pressure side and is caused by the pressure

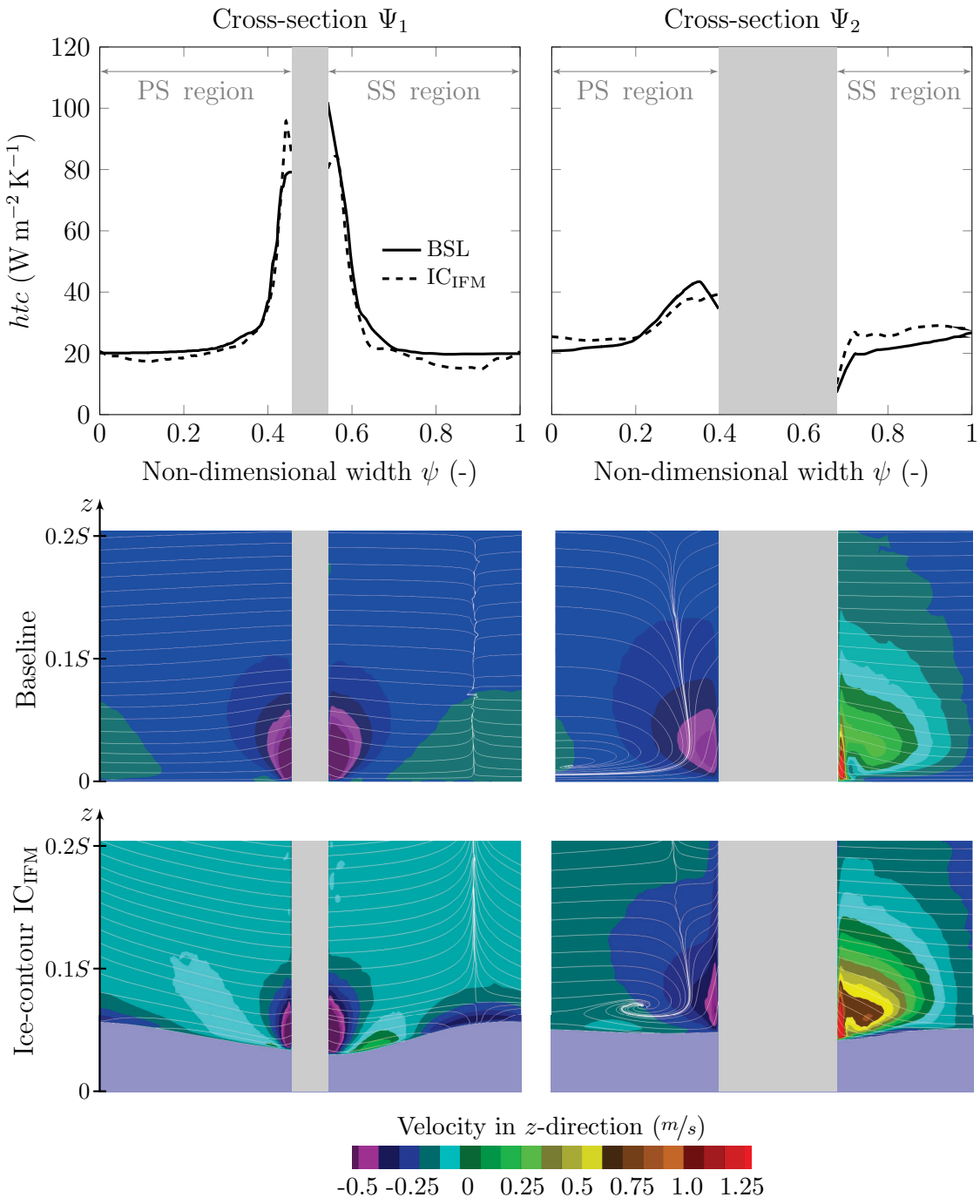

Figure 4.11: Distribution of heat transfer coefficient and near-endwall flow field for baseline and ice contour IC$_{\text{IFM}}$ in cross-sections Ψ_1 and Ψ_2

side leg of the horseshoe vortex. Although the contouring pushes the vortex leg closer to the vane in this region, it reduces the induced downwards velocities. This results in a lower maximum heat transfer. Furthermore, the ice-contoured endwall reduces the amplitude of the *htc* in the pressure side region. In the suction side region, the contouring produces slightly higher heat transfer than the baseline, however, heat transfer rates are comparably low in this region.

Figure 4.12 shows endwall heat transfer and z-velocities plus path lines for the three cross-sections Ψ_3-Ψ_5 in the outflow region (see Fig. 4.8, right), again for the ice-contoured endwall $\mathrm{IC_{IFM}}$ and the baseline. The cross-sections are perpendicular to the outflow direction and located directly at the trailing edge, as well as at distances of 1 and $2\,C_{\mathrm{ax}}$ downstream of it. For the flat endwall baseline, the heat transfer distributions exhibit a distinct trend at all cross-sections. It features a maximum in the pressure side region ($0 < \psi < 0.5$) and a minimum in the suction side region ($0.5 < \psi < 1$). For each cross-section, solid lines indicate the positions of these extrema in the near-endwall flow field. The path lines show that the suction side leg of the horseshoe vortex merges into the passage vortex at the vane's trailing edge (cross-section Ψ_3). This vortex is still present two axial chords downstream of the trailing edge (cross-section Ψ_5). The velocity contours also indicate the reasons for the extrema observed in the heat transfer distribution. Maximum heat transfer occurs at the position where the vortex induces the highest downwards velocities, minimum heat transfer where it induces the highest upwards velocities. The induced downward velocities are highest at the trailing edge and hence also the heat transfer maximum attains the highest value in this cross-section. In the cross-sections further downstream, the induced downwards velocities are clearly smaller and the value for the heat transfer maximum decreases. In contrast, the upwards velocities do not decrease that much with increasing downstream distance and the heat transfer minimum has approximately the same value in all cross-sections. Note that this minimum represents the small stripe of low heat transfer (d) in the outflow region (see e.g. Fig. 4.2).

For the contoured endwall, both heat transfer and the near-endwall flow field differ from the baseline. In the first cross-section (Ψ_3), the contoured endwall also exhibits an absolute maximum and minimum of *htc* in the pressure and suction side region, respectively. The maximum is located at about the same position as for the baseline, but takes a slightly higher value, since the contoured endwall features high downwards velocities at this position. The absolute minimum is shifted to a higher ψ and holds a smaller value than the baseline. Dashed lines indicate the positions of these extrema. The velocity plot shows that the shift of the heat transfer minimum is caused by the recirculation zone at the rear suction side, which pushes the pressure side leg of the horseshoe vortex towards $\psi = 1$. Furthermore, the velocity field of the contoured endwall is less homogeneous than for the baseline. It has small spots of positive and negative z-velocities, which cause further local extrema in the heat transfer distribution. Due to the deflection and breakup of the vortex system for the contoured endwall, heat transfer is much lower in the cross-sections Ψ_4 and Ψ_5 than for the baseline. In addition, heat transfer is more evenly distributed for the contoured

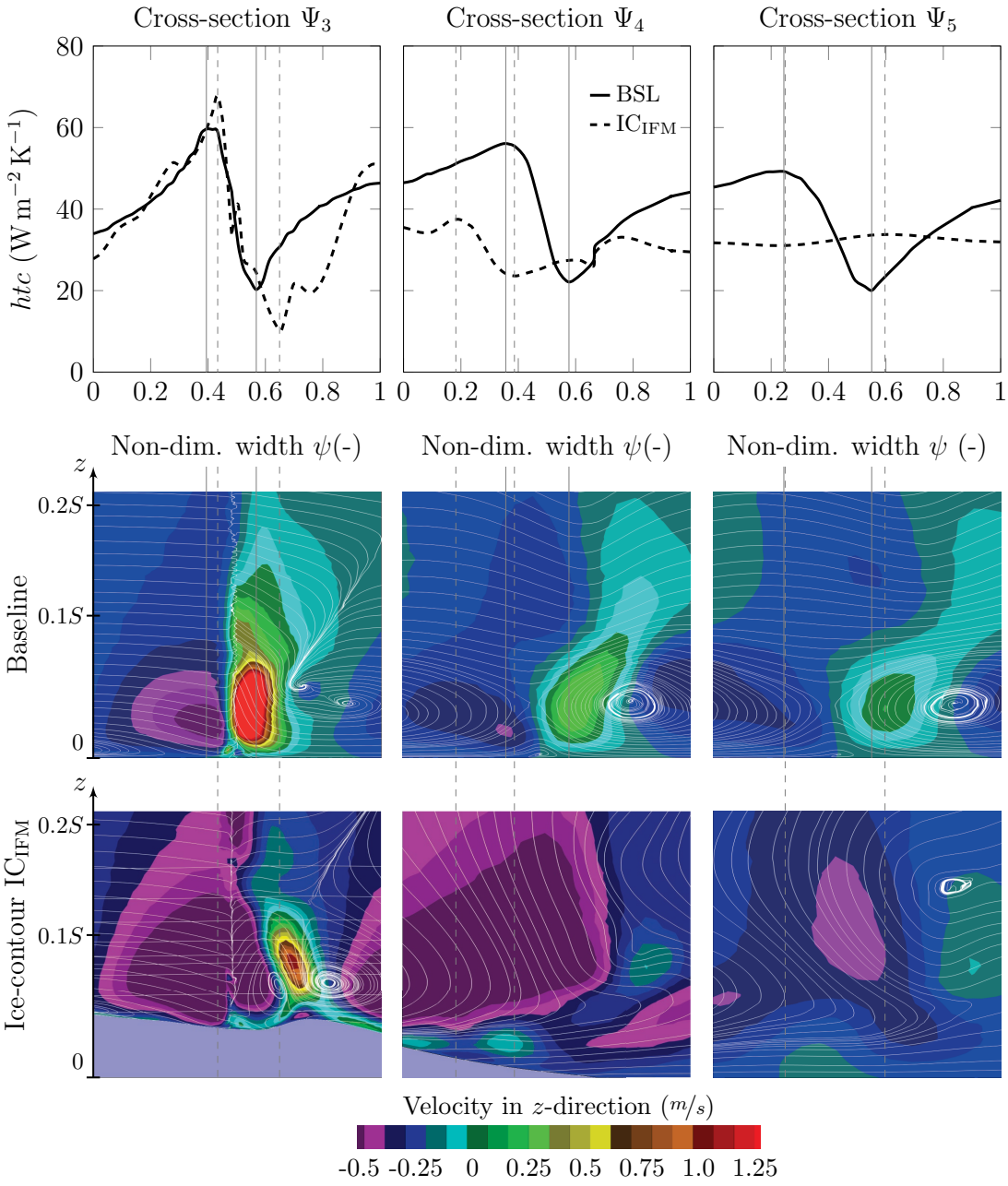

Figure 4.12: Distribution of heat transfer coefficient and near-endwall flow field for baseline and ice contour IC$_{\mathrm{IFM}}$ in cross-sections Ψ_3, Ψ_4, and Ψ_5

endwall. The velocity plots show that in these cross-sections no vortices are present near the contoured endwall and hence the heat transfer distribution does not have a distinct maximum and minimum as for the baseline. For the contoured endwall, a vortical structure is present though in Ψ_5, however, it is too far away from the endwall to influence near-endwall flow and heat transfer.

The last paragraphs outlined the effects of the ice-contouring on flow and heat transfer both globally for the entire domain and locally for different positions on the endwall. In order to further identify the regions that the contouring influences most, I area-averaged the heat transfer coefficient over each of the five endwall segments shown in Fig. 3.15. The same regions were used for the flat endwall baseline. Table 4.1 presents the results for both contours and the percentaged differences of contoured to flat endwall, with positive values indicating increased heat transfer for the contoured endwall. The contoured endwall achieves the highest heat transfer reduction in the two regions downstream of the vane passage, due to the ice contour causing the turning and break-up of the passage vortex. In the *Transition outlet* region, the *htc* is reduced by more than 20%, in the *Outlet* region the reduction is over 13%. Hence, these regions contribute the most to the total reduction of 5.20%. The *Vane passage* itself, where the actual contouring is situated, exhibits a higher heat transfer than the comparable region for the flat endwall. This is due to the fact that the Ice Formation Method is a global optimization method, which creates an optimum solution for the entire system, i.e. the complete endwall. The contouring in the vane passage is just means to an end, to alter the passage vortex system and in this vein create an endwall contour which globally reduces heat transfer.

Moreover, one must also consider that the ice contour in the vane passage has a mean thickness of approximately 8 mm, corresponding to 5.7% of the vane span S. This reduction in cross-sectional area causes an acceleration of the flow and thus a higher Reynolds number in the vane passage for the ice-contoured endwall. As known from Reynolds analogy, this increased Reynolds number also increases heat transfer. For turbulent flow, many correlations, such as Dittus and Boelter ($Nu_D = 0.023 Re_D^{0.8} Pr^{0.3}$, see [33]) or Kays et al. ($Nu_x = 0.0287 Re_x^{0.8} Pr^{0.4}$ [36]), suggest that heat transfer, i.e. the Nusselt number, scales with the Reynolds number to the power of 0.8, that is $Nu \sim Re^{0.8}$. Therefore, to compare vane passage heat transfer for the ice-contoured and the flat endwall independent of the Reynolds num-

Table 4.1: Heat transfer coefficients area-averaged over endwall segments for ice-contoured endwall $\mathrm{IC_{IFM}}$ and flat endwall baseline at $Re_C = 49{,}900$

	Inlet	Transition inlet	Vane passage	Transition outlet	Outlet	Total
$\mathrm{IC_{IFM}}$	27.38	22.37	30.27	34.59	31.32	28.25
BSL	27.66	21.38	29.76	43.50	36.09	29.80
Difference	−1.02%	4.63%	1.71%	−20.48%	−13.22%	−5.20%

ber in the vane passage, I consulted $Nu/Re^{0.8}$. This yields $Nu/Re^{0.8} = 0.016{,}019$ for the vane passage of the baseline and $Nu/Re^{0.8} = 0.015{,}692$ for the ice-contoured vane passage and hence a reduction of 2.04% for the ice-contoured endwall in this region. These considerations exemplify the complexities that arise when comparing the ice contours in the vane passage to the flat endwall. Furthermore, the fact that the ice growth yields an elevated endwall in the vane passage not only affects heat transfer rates in the vane passage but also influences flow and heat transfer for the entire flow domain. The next section addresses this in detail.

Finally, it needs to be mentioned that the distinct geometrical features A, B, and C (see Fig. 4.7) and their effect on flow and heat transfer, as described above for the contour $\mathrm{IC}_{\mathrm{IFM}}$, are present for all experimentally created ice contours. That is, all combinations of Re_C and Θ produce similar ice-contoured endwalls. However, the magnitude of the contouring depends on these two parameters. That is, smaller

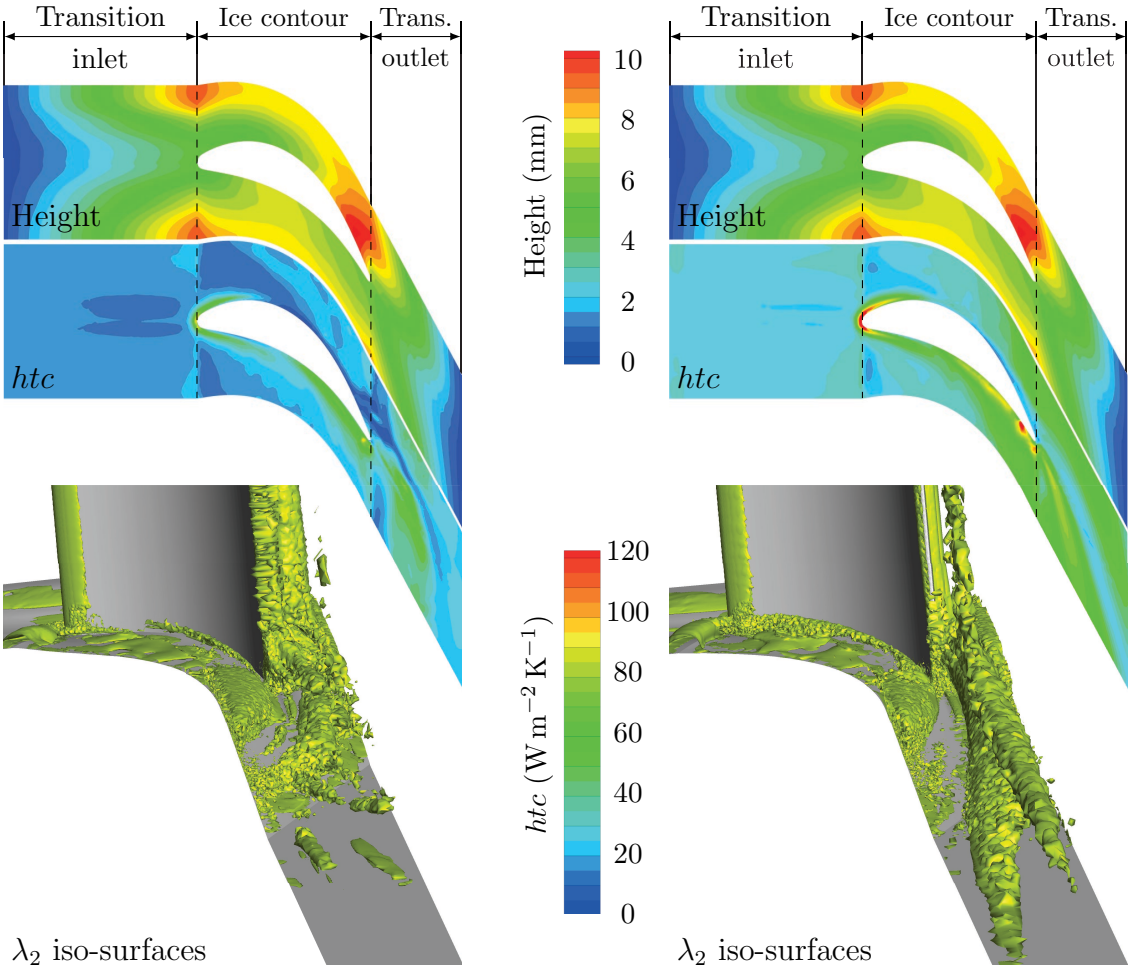

Figure 4.13: Height levels, *htc* distribution, and iso-surfaces of $\lambda_2 = -4{,}000$ for ice contours at $Re_C = 34{,}000$ and $\Theta = 8.5$ (left) and $Re_C = 71{,}400$ and $\Theta = 12.2$ (right)

Reynolds numbers and higher temperature ratios yield more pronounced contours with increasing amplitude between maximum and minimum occurring height. Figure 4.13 shows two further ice contours in terms of their height levels. Furthermore, it displays the local *htc* distributions and the passage vortices in the outflow region for these contours. Appendix A.7 shows the same plots for the remaining contours of the short cooling length for completeness. All contours have in common that the contouring, especially the height maximum at the rear suction side, causes an overturning of the passage vortex in the outflow region and hence reduced heat transfer rates downstream of the vane passage. The recirculation zone downstream of the height maximum, which results in a further break-up of the vortex structure, however, is only present for highly contoured ice layers. These are all contours at the lowest Reynolds number of $Re_C = 34{,}000$ and the one contour at $Re_C = 49{,}900$ and $\Theta = 12.2$. Note that the contour at $Re_C = 71{,}400$ and $\Theta = 12.2$ does not feature this recirculation zone, but also achieves a heat transfer reduction of 5.0%.

Influence of Endwall Elevation in Vane Passage In the experimental facility, the cooled copper inlay is flush-mounted with the remaining lower endwall of the test section. Hence, the ice layer, which grows on the endwall during the experiment, protrudes into the channel. Together with the transition regions, the digitized ice contour thus forms a trapezoidal endwall shape, the contour in the vane passage being elevated compared to the flat endwall baseline. To assess the influence of such an elevated endwall in the vane passage, I performed numerical simulations with trapezoidal endwalls and evaluated their effect on flow and heat transfer. To create these endwalls, I raised the flat endwall in the vane passage by the elevation height h and used linear transitions of 80 mm up- and downstream of it (see Figure 4.14).

For these trapezoidal endwalls, Fig. 4.15 displays the resulting area-averaged *htc* values for the five endwall segments and the entire endwall versus the elevation h. The graphs show that elevating the endwall in the vane passage leads to contours with reduced total heat transfer compared to the flat endwall baseline. As for the ice contours, the rear endwall segments downstream of the vane passage feature

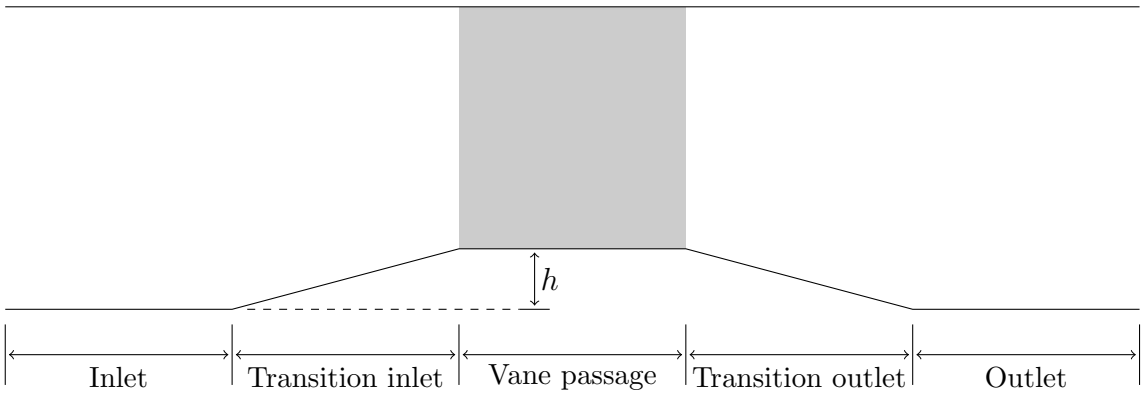

Figure 4.14: Trapezoidal endwall contour with elevation h in vane passage

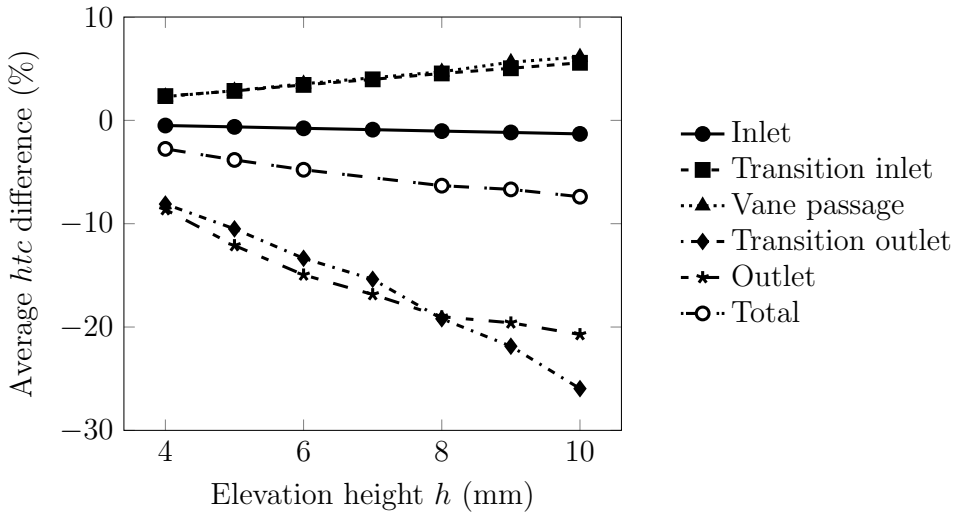

Figure 4.15: Averaged heat transfer difference with respect to baseline for a trapezoidal endwall with vane passage being elevated by height h

the highest reductions in heat transfer, whereas the htc in the passage increases. With increasing h, total heat transfer decreases, whereas vane passage heat transfer increases. The latter observation results from the fact that the vane passage cross-section reduces with increasing h, leading to higher velocities and hence increased heat transfer rates.

Figure 4.16 shows endwall heat transfer and the core of the passage vortex for the trapezoidal endwall with $h = 8\,\text{mm}$ at $Re_C = 49{,}900$. The figure illustrates that the

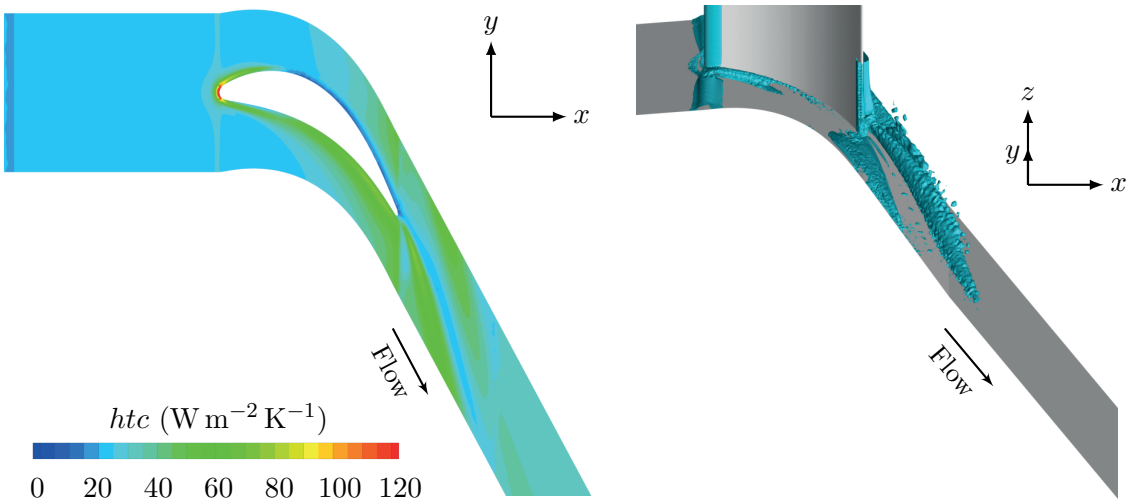

Figure 4.16: Endwall heat transfer coefficient distribution (left) and passage vortex core at $Q = 8{,}000$ (right) for trapezoidal endwall with $h = 8\,\text{mm}$ at $Re_C = 49{,}900$

Table 4.2: Heat transfer coefficients area-averaged over endwall segments for contour IC_{IFM} and trapezoidal endwall with $h = 8\,mm$ at $Re_C = 49{,}900$

	Inlet	Transition inlet	Vane passage	Transition outlet	Outlet	Total
IC_{IFM}	27.38	22.37	30.27	34.59	31.32	28.25
$h = 8\,mm$	27.02	21.93	30.92	36.63	29.65	27.92
Difference	−1.31%	−4.63%	2.15%	5.90%	−5.33%	−1.17%

elevation of the endwall in the vane passage causes an overturning of the passage vortex, which reduces heat transfer rates downstream of the vane passage and hence leads to the reduction in total heat transfer. This yields two conclusions: First, although the ice contouring contributes to the overturning of the passage vortex by forming the height maximum at the rear suction side, this overturning is mainly caused by the elevated endwall in the vane passage. Secondly, only elevating the endwall in the vane passage already causes reductions in total endwall heat transfer, however, inside the vane passage, the elevated flat endwall causes higher heat transfer than the ice-contoured endwalls. To illustrate this last point, Tab. 4.2 shows the averaged heat transfer coefficients for the ice-contoured endwall IC_{IFM} (average height approx. 8 mm) and the comparable trapezoidal endwall at $h = 8\,mm$ and outlines the difference for the endwall segments. The trapezoidal endwall indeed features slightly lower total heat transfer than the ice-contoured endwall, however, in the ice-contoured vane passage, the ice contour holds smaller average heat transfer.

Note that the selection of the trapezoidal endwall at 8 mm was logical but arbitrary. Using another reasoning, one could have just as well selected a trapezoidal endwall at a higher or lower elevation h, which for example corresponds to the maximum or minimum occurring height level of the ice contour. However, the trapezoidal endwall shall not constitute a further reference to compare the ice-contoured endwall to. It is rather intended to show the influence of the elevated vane passage endwall on heat transfer and to illustrate the difficulties that occur when comparing different endwall contours amongst each other.

4.2.2 Entropy Production

Like every natural process, the Ice Formation Method tends to minimize the losses of a system. Such losses convert parts of the available exergy into anergy. The amount of converted exergy thereby corresponds to the produced entropy. This means that the IFM creates contours with reduced entropy production. This was proven by LaFleur [41] for a Couette flow. Lyulinetskyy [54] showed that ice layers in a channel flow also feature reduced entropy production compared to the baseline geometry. Hence, in this section, I present results for entropy production of the ice-contoured vane endwalls and how these relate to the observed reductions in heat transfer. For

Table 4.3: Averaged rates of terms contributing to entropy production for ice-contoured endwalls with short cooling length and baseline at Re_C = 49,900, in e$-4\,\mathrm{W\,K^{-1}}$

Θ	$\dot{S}_{\mathrm{Diss,mol}}$	$\dot{S}_{\mathrm{Diss,turb}}$	$\dot{S}_{\mathrm{Heat,mol}}$	$\dot{S}_{\mathrm{Heat,turb}}$	$\dot{S}_{\mathrm{total}}$
6.5	3.122	3.191	98.518	58.044	162.875
	(0.081)	(0.321)	(−6.526)	(−0.043)	(−6.167)
8.5	3.179	3.115	100.283	58.851	165.428
	(0.138)	(0.245)	(−4.761)	(0.764)	(−3.614)
12.2	3.188	3.282	96.444	60.894	163.808
	(0.147)	(0.412)	(−8.600)	(2.807)	(−5.234)
BSL	3.041	2.870	105.044	58.087	169.042

brevity, I only show results for the ice contours at Re_C = 49,900. Appendix A.8 gives results for the other Reynolds numbers.

Table 4.3 holds entropy production rates for the three ice contours with short cooling length and the flat endwall baseline (BSL) at Re_C = 49,900. Shown are the values for the four terms that contribute to total entropy production: molecular dissipation $\dot{S}_{\mathrm{Diss,mol}}$, turbulent dissipation $\dot{S}_{\mathrm{Diss,turb}}$, molecular heat transfer $\dot{S}_{\mathrm{Heat,mol}}$, and turbulent heat transfer $\dot{S}_{\mathrm{Heat,turb}}$ (see Sec. 2.7 for the definition of these terms). All values are averaged over the entire numerical domain. For all endwall contours, including the baseline, entropy production due to heat transfer is more than one order of magnitude higher than entropy production due to dissipation. This indicates that

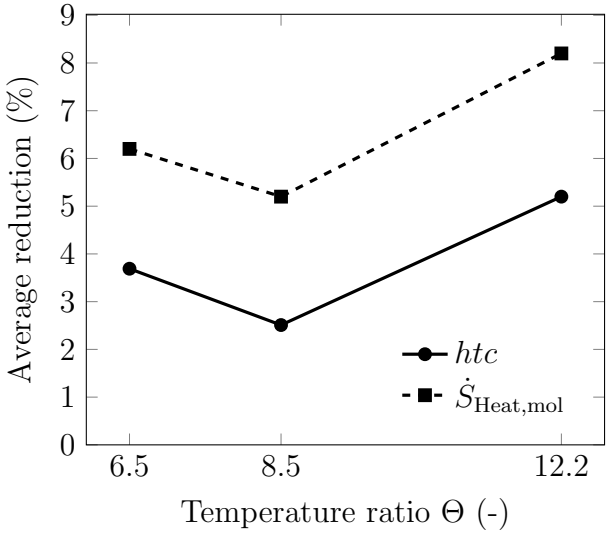

Figure 4.17: Average reductions in heat transfer and entropy production rates due to molecular heat transfer with respect to baseline at Re_C = 49,900

heat transfer is the predominant source of losses for this type of flow. Furthermore, molecular heat transfer contributes almost double to entropy production than turbulent heat transfer. Comparing the ice-contoured endwalls to the baseline reveals that the Ice Formation Method diminishes this biggest source of loss. Hence, entropy production due to molecular heat transfer is reduced the most for the ice-contoured endwalls, thus yielding a reduction of total entropy production.

For the three ice contours at $Re_C = 49{,}900$, Fig. 4.17 shows the average reductions in both heat transfer and entropy production due to molecular heat transfer. As can be seen, the heat transfer reductions for the ice-contoured endwalls directly relate to the reductions in entropy production. The higher the reduction in $\dot{S}_{\mathrm{Heat,mol}}$ for an endwall contour, the higher also the average heat transfer reduction for this contour. From one contour to another, both variables even scale with approximately the same ratio. Thus, the heat transfer reductions achieved by the IFM directly result from the method's natural character to reduce entropy production for the main source of loss, here entropy production due to molecular heat transfer.

Figure 4.18 shows the local, cross-section averaged entropy production rates due to mean and turbulent heat transfer along the numerical domain for the ice-contoured endwall $\mathrm{IC_{IFM}}$. This contour features the lowest entropy production ($\dot{S}_{\mathrm{Heat,mol}}$) and hence the highest reduction in heat transfer. Values are again normalized with the flat endwall baseline; the gray background indicates the position of the vane. In the inflow region, values for the contoured endwall are at the same level as those for the baseline. Towards the leading edge, entropy production rates due to molecular heat transfer increase, since the flow encounters the transition region. With the beginning of the ice contour at the vane's leading edge, these entropy production rates significantly decrease due to the contouring. Downstream of the trailing edge, they

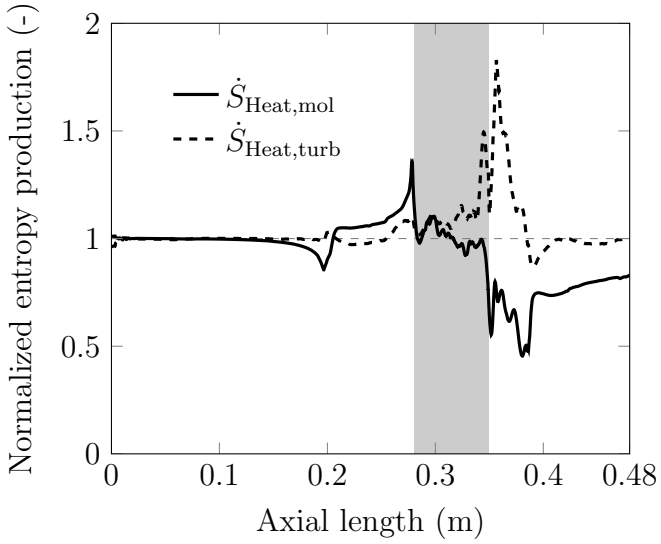

Figure 4.18: Local, cross-section averaged entropy production rates due to mean and turbulent heat transfer for ice-contoured endwall $\mathrm{IC_{IFM}}$ at $Re_C = 49{,}900$

remain at about 20% below the value of the baseline since the Ice Formation Method diminishes the vortical structures in this region. In contrast, entropy production rates due to turbulent heat transfer are increased downstream of the vane passage. However, these rates are much lower than those due to molecular heat transfer (see also Tab. 4.3) and hence have only minor influence on heat transfer. This local distribution shows again that the IFM significantly reduces entropy production due to molecular heat transfer and thus causes a heat transfer reduction in the region of the contouring and even downstream of it.

As stated above, the IFM reduces endwall heat transfer by minimizing entropy production rates due to molecular heat transfer. Since Sec. 4.2.1 also showed a reduction of endwall heat transfer for a trapezoidal endwall, it is interesting to compare entropy production rates due to molecular heat transfer $\dot{S}_{\mathrm{Heat,mol}}$ for the ice-contoured endwall to those of the trapezoidal endwall. Thus, for the Reynolds number of $Re_C = 49{,}900$, Fig. 4.19 shows the ratio of this variable for the ice contour $\mathrm{IC_{IFM}}$ to the trapezoidal endwall with $h = 8\,\mathrm{mm}$. The values are plotted against the axial length of the numerical domain; at each axial position, the values are integrated over the local cross-section of the domain. Values above and below unity indicate, respectively, higher and lower entropy production rates for the ice-contoured endwall. In the vane passage, the ice contour features mostly lower $\dot{S}_{\mathrm{Heat,mol}}$ than the trapezoidal endwall due to the contouring and hence lower heat transfer, as shown in Tab. 4.2. This also results in lower entropy production rates for the ice-contoured endwall directly downstream of the vanes. In the outflow region, however, the ratio lies above unity, i.e. $\dot{S}_{\mathrm{Heat,mol}}$ is higher for the ice contour than for the trapezoidal endwall. These entropy production results confirm the trend that was seen for heat transfer. Compared to

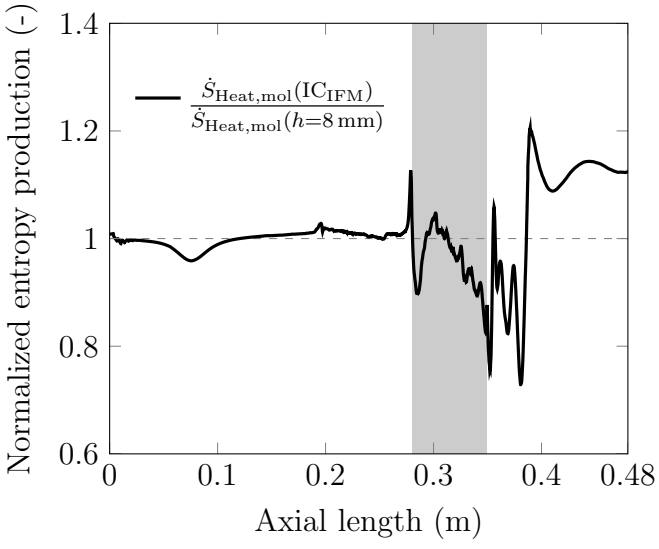

Figure 4.19: Ratio of entropy production rates due to molecular heat transfer for ice contour $\mathrm{IC_{IFM}}$ to trapezoidal endwall at $h = 8\,\mathrm{mm}$ ($Re_C = 49{,}900$)

the trapezoidal endwall, $\dot{S}_{\mathrm{Heat,mol}}$ and the average *htc* are lower for the ice-contoured endwall in the vane passage and the transition outlet region, but higher in the outlet region.

4.3 Endwall Contours from Numerical Optimization

The section above already showed that the ice-contoured endwalls reduce average heat transfer compared to the flat endwall baseline. Hence, these endwalls are well-suited as starting points for subsequent numerical optimizations. Using the NSGA-II algorithm, I performed such numerical optimizations starting from the three ice contours at Re_C = 49,900 and Θ = 6.5, 8.5, and 12.2. In each optimization, I parametrized the ice contour with nine Bézier curves and used an optimization space ranging from 0 to 10 mm above the vane passage, as described in Sec. 3.3.1. This section presents the endwall contours obtained from the numerical optimizations and describes their heat transfer behavior. First, I show results for optimizations which aim at minimizing global average heat transfer for the entire endwall. Afterwards, results are presented for optimizations that pursued the goal to reduce average heat transfer in the vane passage only.

4.3.1 Reducing Global Endwall Heat Transfer

As shown in the previous section, the Ice Formation Method's goal function for this type of flow is the global minimization of entropy production rates, especially those

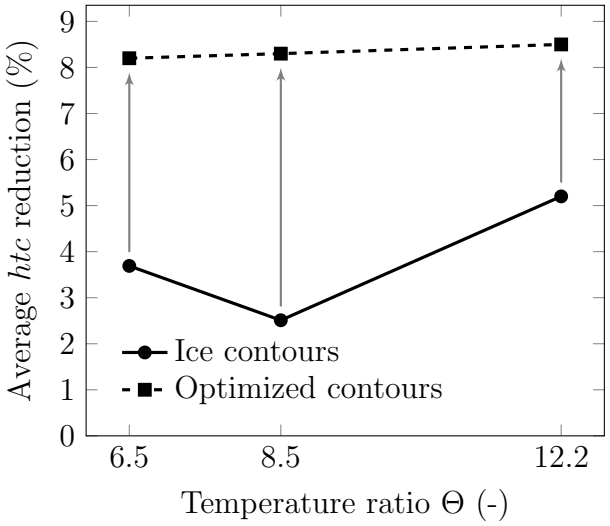

Figure 4.20: Average heat transfer reductions for endwall contours optimized on the basis of ice-contoured endwalls at Re_C = 49,900

due to molecular heat transfer. This corresponds to an optimization with respect to minimum global heat transfer. Therefore, I also used global heat transfer, averaged over the entire endwall, as goal function for the numerical optimizations of this section. Figure 4.20 shows the globally averaged reductions in *htc* for the three endwall contours obtained from the numerical optimizations. The heat transfer reductions for the ice-contoured endwalls, which form the basis of the numerically optimized contours, are also included for reference. For all ice contours as initial geometries, the subsequent numerical optimization yields endwall contours with similar reductions in average heat transfer. Hence, it can be assumed that the optimization algorithm creates endwall contours that are close to the global optimum for this flow configuration, that is a global *htc* reduction of approximately 8% compared to the baseline. Yet, there is the tendency that ice contours with higher non-dimensional temperature ratio as starting geometries yield slightly higher heat transfer reductions after the optimization.

Figure 4.21, which shows the endwall contours after optimization for all three ice contours as starting geometries, confirms these observations. All optimized endwall geometries exhibit a similar contouring. Compared to the ice-contoured endwalls, see Fig. 4.7 and App. A.7, two changes are noticeable. First, the optimization lowers the elevation at the vane passage entry and, secondly, it shifts the height maximum in the rear vane passage from the suction side further into the vane passage. Moreover, the higher the temperature ratio of the initial ice-contoured endwall, the more pronounced is the contouring after the optimization. This is especially visible for the height maximum of the contouring. Hence, as for the ice-contoured endwalls, the optimized endwall contour started from $\Theta = 12.2$, in the following termed $\mathrm{OC}_{\mathrm{IFM}}$, yields the highest reduction in endwall heat transfer, which amounts to 8.49%. The

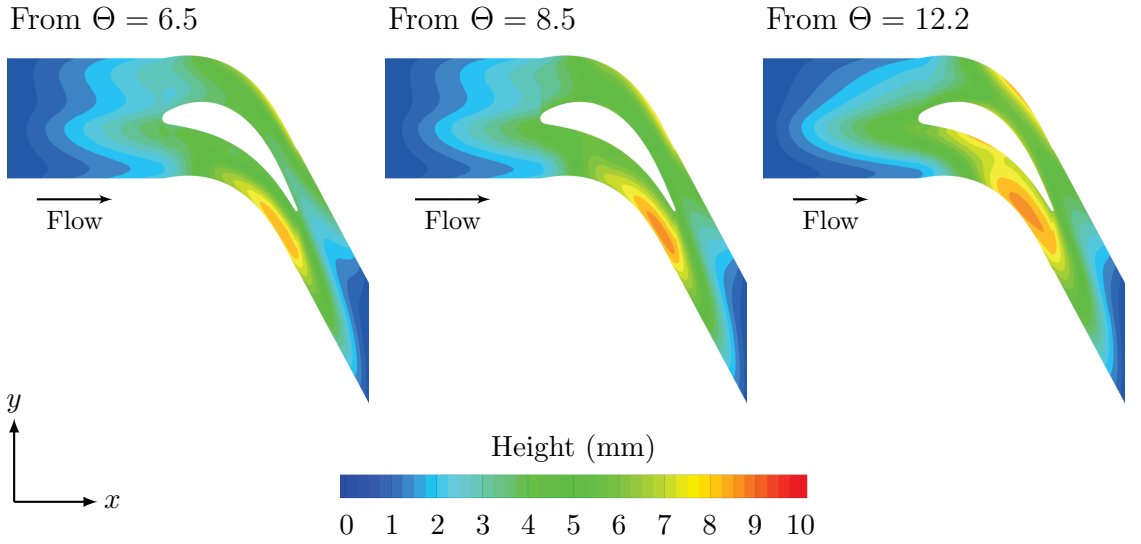

Figure 4.21: Height levels of endwall contours optimized on the basis of ice-contoured endwalls at $Re_C = 49{,}900$

next paragraphs describe the numerical optimization process that yields this endwall contour and explain how this contour alters the flow field and hence further reduces heat transfer.

In order to find an optimum endwall contour, the NSGA-II creates a multitude of endwall geometries and analyzes each with respect to the desired goal function, here global, average endwall heat transfer. On the basis of this information, the algorithm constantly refines the endwall geometry during the optimization process, thus converging towards an optimum solution. For the contour OC_{IFM}, Figure 4.22 characterizes this process by showing a bar plot of average endwall heat transfer for each endwall geometry creted over the 20 generations of the optimization process. Every generation thereby holds a population consisting of eight different endwall contours, each represented by one bar. All values are normalized with the baseline. For further reference, the value obtained for the ice-contoured endwall is also displayed. During the first generations, the optimization algorithm generates contours with both higher and lower endwall heat transfer than the ice-contoured endwall. However, these contours all have lower heat transfer than the flat endwall baseline, since they originate from the ice-contoured endwall. For the contours of the following generations, endwall heat transfer ever declines until the optimum contour with minimum heat transfer is found in generation 15.

For this optimized contour OC_{IFM}, Fig. 4.23 shows the Bézier splines of the parametrized endwall after the numerical optimization (see Fig. 3.16 (right) for Bézier spline position). Together with the edges from the ice contour, these describe the geometry of the optimized endwall contour, as it is shown in Fig. 4.21, right. The

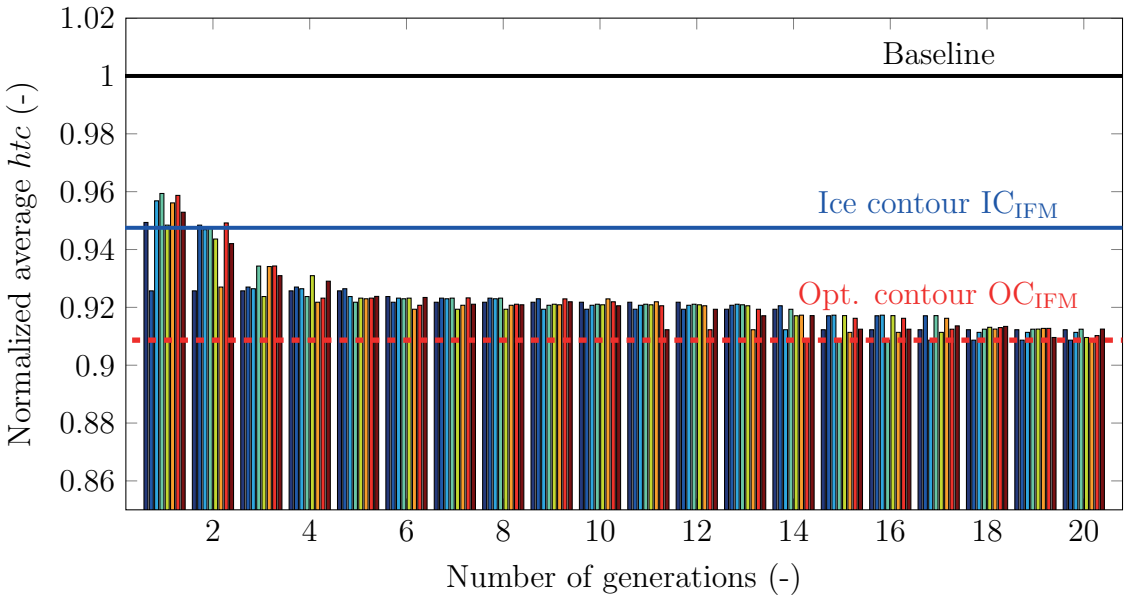

Figure 4.22: Average *htc* for all endwall contours created over the 20 generations of the numerical optimization process, referred to flat endwall baseline

six Bézier splines in crosswise direction (B_1-B_3) all exhibit a similar trend, having a convex shape in the pressure side region, which turns into a concave shape in the suction side region. The Bézier spline in streamwise direction at half pitch (B_4) starts at a low height at the vane passage entry and constantly increases in height forming a convex bump in the rear vane passage. This bump defines the height maximum in the rear vane passage for the optimized endwall contour. The Bézier spline (B_5) at the

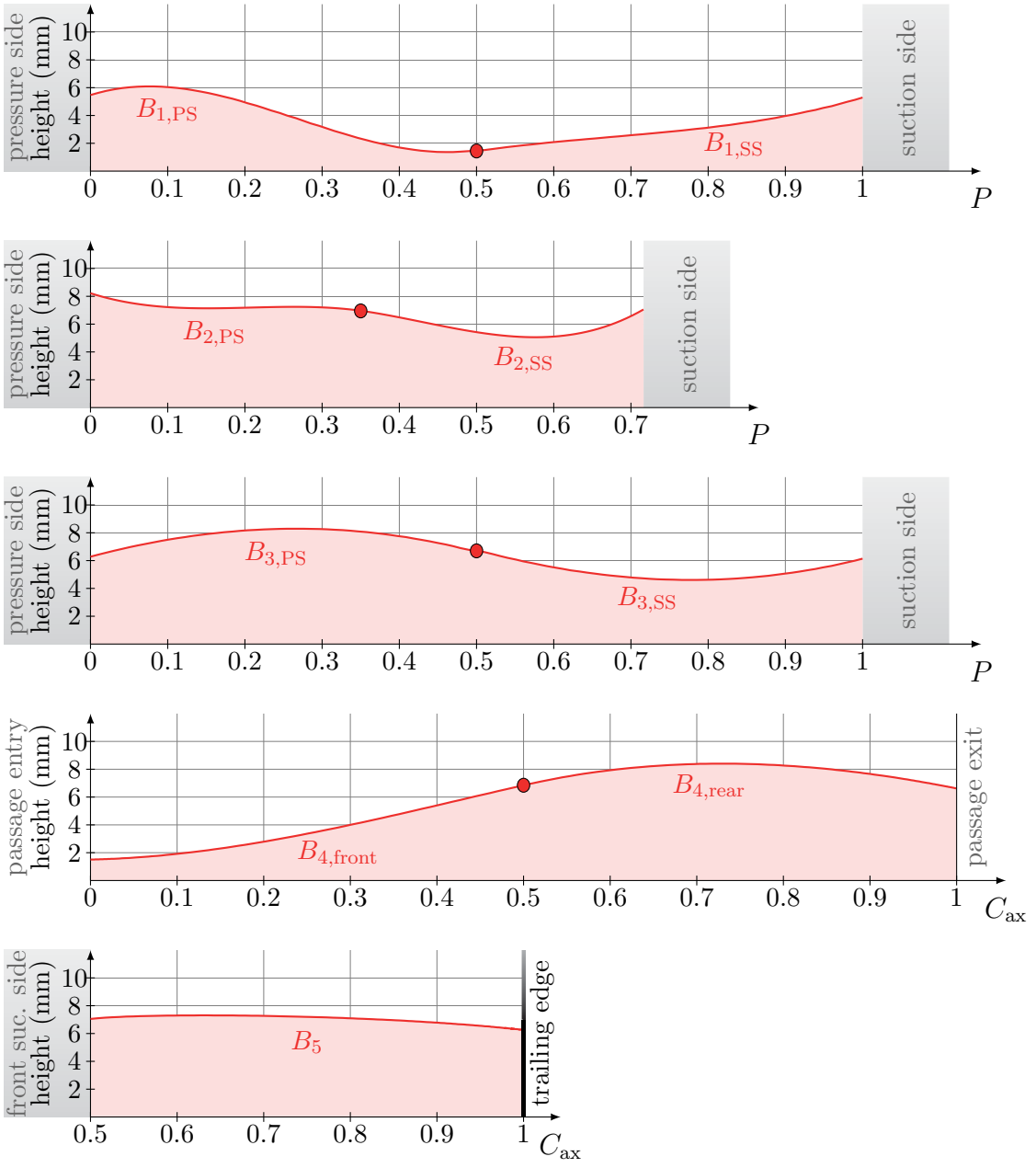

Figure 4.23: Bézier splines B_1-B_5 for endwall contour OC_{IFM}, optimized from ice-contoured endwall at $Re_C = 49{,}900$ and $\Theta = 12.2$

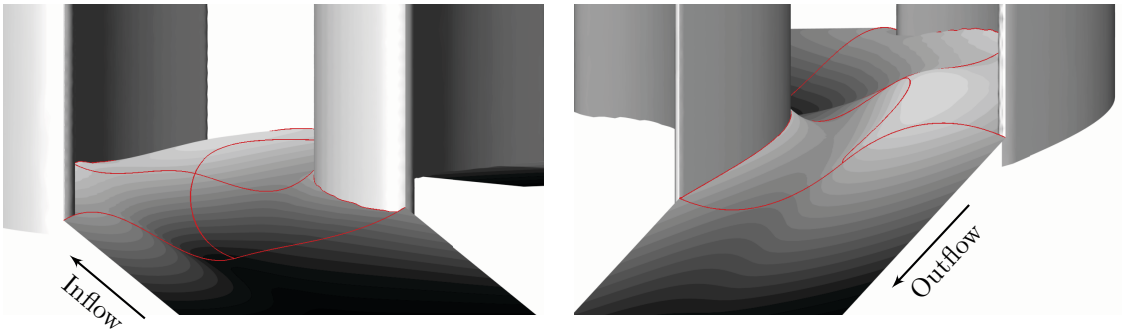

Figure 4.24: Endwall contour OC_{IFM}, optimized on basis of ice-contoured endwall at $Re_C = 49{,}900$ and $\Theta = 12.2$

rear suction side exhibits a slight convex curvature, which is less pronounced than for the ice-contoured endwall, hence contributing to the shift of the height maximum in pitchwise direction. Figure 4.24 depicts the optimized endwall contour OC_{IFM} with these Bézier splines and the edges from the ice contour as three-dimensional views. For the left image, the viewing direction is in flow direction and shows the geometry at the front vane passage, for the right image it is against the flow direction and shows the rear vane passage.

The above presented geometry of the optimized endwall contour further changes the flow field, thus leading to the increased heat transfer reduction. To exemplify

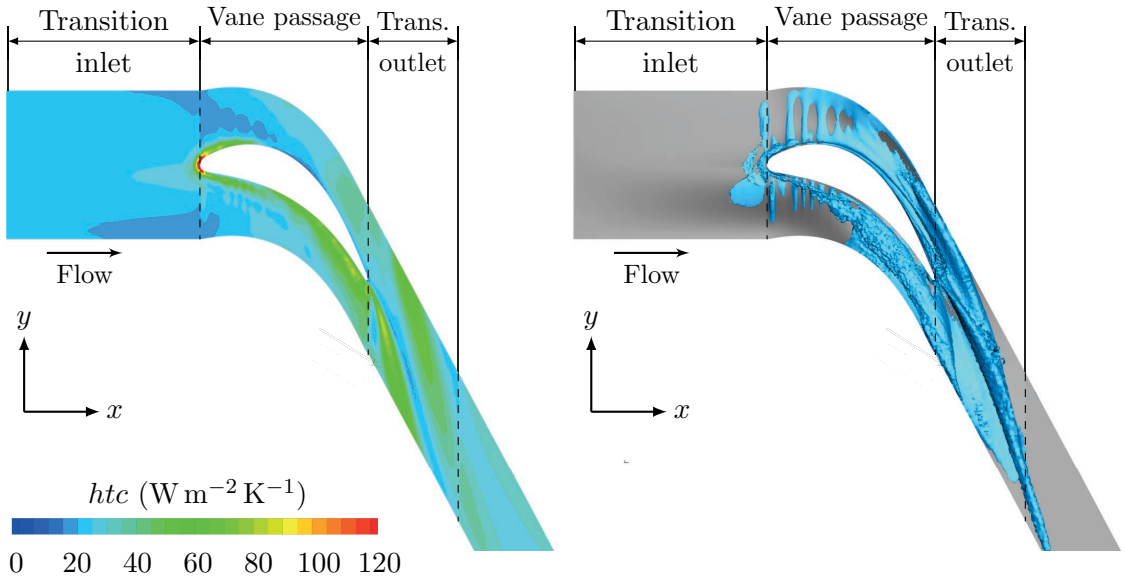

Figure 4.25: Distribution of heat transfer coefficient on endwall (left) and passage vortex as $Q = 8{,}000$ (right) for optimized endwall contour OC_{IFM} at $Re_C = 49{,}900$

Table 4.4: Percentaged difference of area-averaged endwall heat transfer with respect to baseline for ice-contoured endwall IC_{IFM} and endwall contour OC_{IFM} optimized on basis of it

	Inlet	Transition inlet	Vane passage	Transition outlet	Outlet	Total
IC_{IFM}	−1.02%	4.63%	1.71%	−20.48%	−13.22%	−5.20%
OC_{IFM}	−0.51%	1.17%	1.68%	−21.74%	−24.42%	−8.49%

the flow field and its effect on heat transfer, Fig. 4.25 shows the optimized contour's *htc* distribution (left) and the passage vortex as iso-surface of Q = 8,000 (right). Both images reveal that the optimization leads to an even stronger overturning of the passage vortex than for the ice contour. Thus, the optimization amplifies the effect that was already seen for the ice-contoured endwall and, in that vein, causes the further reduction in heat transfer. Table 4.4 shows heat transfer averaged over the five endwall segments described in Fig. 3.15 for both the optimized contour OC_{IFM} and the initial ice-contoured endwall IC_{IFM}, which forms the basis for this optimization. All values are in relation to the baseline and describe the percentaged difference to it. In the front regions of the endwall, the optimization reduces heat transfer only marginally in the *Transition inlet* region. Like the ice-contoured endwall, the optimized endwall contour reduces heat transfer the most in the outflow regions downstream of the vane passage since it displaces the position of the passage vortex by deflecting it. In the vane passage, the optimized contour features higher heat transfer than the baseline. However, this is not astonishing, since the goal function for the optimization was heat transfer averaged over the entire endwall and not only over the vane passage. Hence, the optimization algorithm accepts the increased heat transfer in the vane passage in favor of a high heat transfer decrease downstream.

Note that this optimized endwall contour has a lower average height in the vane passage than the initial ice contour, but features higher heat transfer reduction. In addition, a trapezoidal endwall with a comparable elevation reduces the globally averaged *htc* by only 4.51% compared to the flat endwall baseline, whereas the optimized contour's *htc* reduction amounts to almost twice this value. Therefore, the optimization achieves the further heat transfer reduction by emphasizing the contouring in the vane passage, while reducing the elevation of the endwall in the vane passage.

4.3.2 Reducing Vane Passage Endwall Heat Transfer

So far, I created all endwall contours with the goal to reduce average heat transfer for the entire endwall of the numerical domain. Considering a real engine application, however, endwall heat transfer is most important in the vane passage, since up- and downstream of it rotating blade rows are present. Hence, I performed a numerical optimization that used vane passage heat transfer as goal function to be minimized by the optimization algorithm. For this optimization, I used the ice-contoured end-

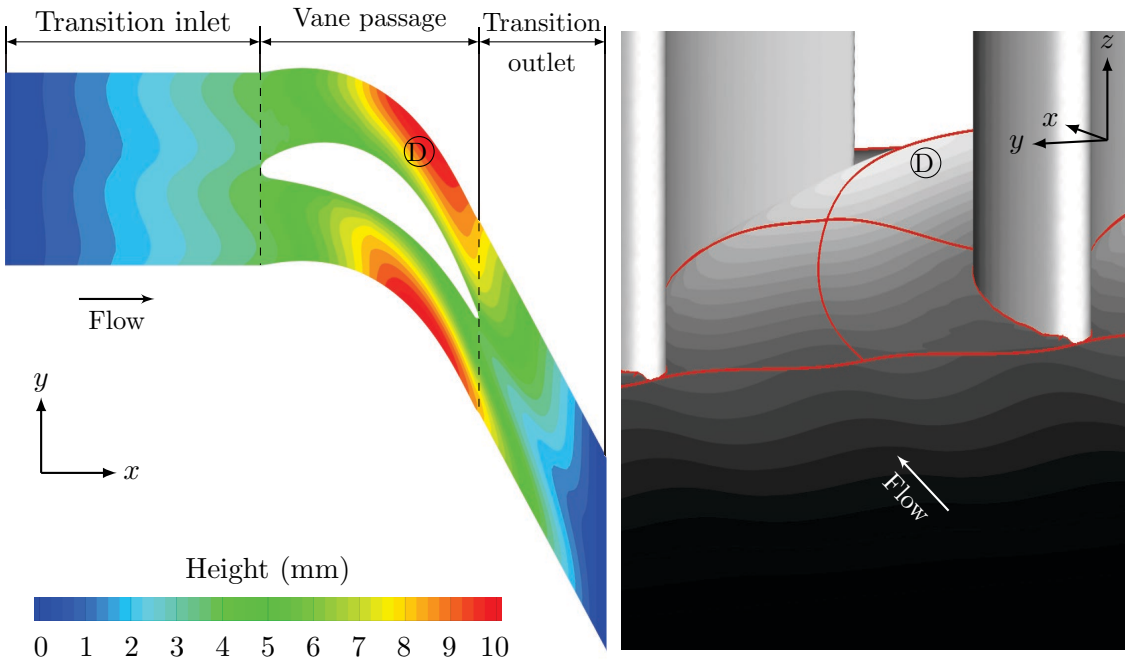

Figure 4.26: Endwall contour optimized with respect to minimum vane passage heat transfer; based on ice contour at $Re_C = 49{,}900$ and $\Theta = 8.5$

wall at $Re_C = 49{,}900$ and $\Theta = 8.5$ as basis, applying the same parametrization as before. Figure 4.26 shows the endwall contour that results from this optimization; Appendix A.9.1 shows the underlying Bézier curves. Its main feature is an elongated elevation in the vane passage (D), which ranges from about 40% axial chord to the end of the vane passage. In pitchwise direction, this elevation stretches across a great part of the vane passage. At its beginning, the elevation lies closer to the vane pressure side, but it turns towards the suction side in the rear vane passage.

Compared to the flat endwall baseline, this endwall contour achieves an average *htc* reduction of 2.62% in the vane passage. For completeness, App. A.9.2 holds average heat transfer rates for the remaining endwall segments of this contour in comparison with the baseline. To outline the reasons for the heat transfer reduction in the vane passage, Fig. 4.27 shows endwall heat transfer in the vane passage for the optimized contour (left), the baseline (middle) and the heat transfer ratio of optimized to baseline endwall (right). The optimized endwall significantly changes the *htc* distribution in the rear vane passage, reducing heat transfer in the suction side region and, more importantly, lowering heat transfer in the rear pressure side region, where *htc* values are high for the baseline. However, at the very end of the pressure side a small hot spot appears for the contoured endwall, which holds even higher heat transfer than the baseline at this position. For this contour though, vane passage heat transfer is also influenced by the reduced passage cross-section and the resulting flow acceleration. Hence, consulting $Nu/Re^{0.8}$, this results in an average value of $Nu/Re^{0.8} = 0.015{,}038$ for the vane passage of the contoured endwall, while

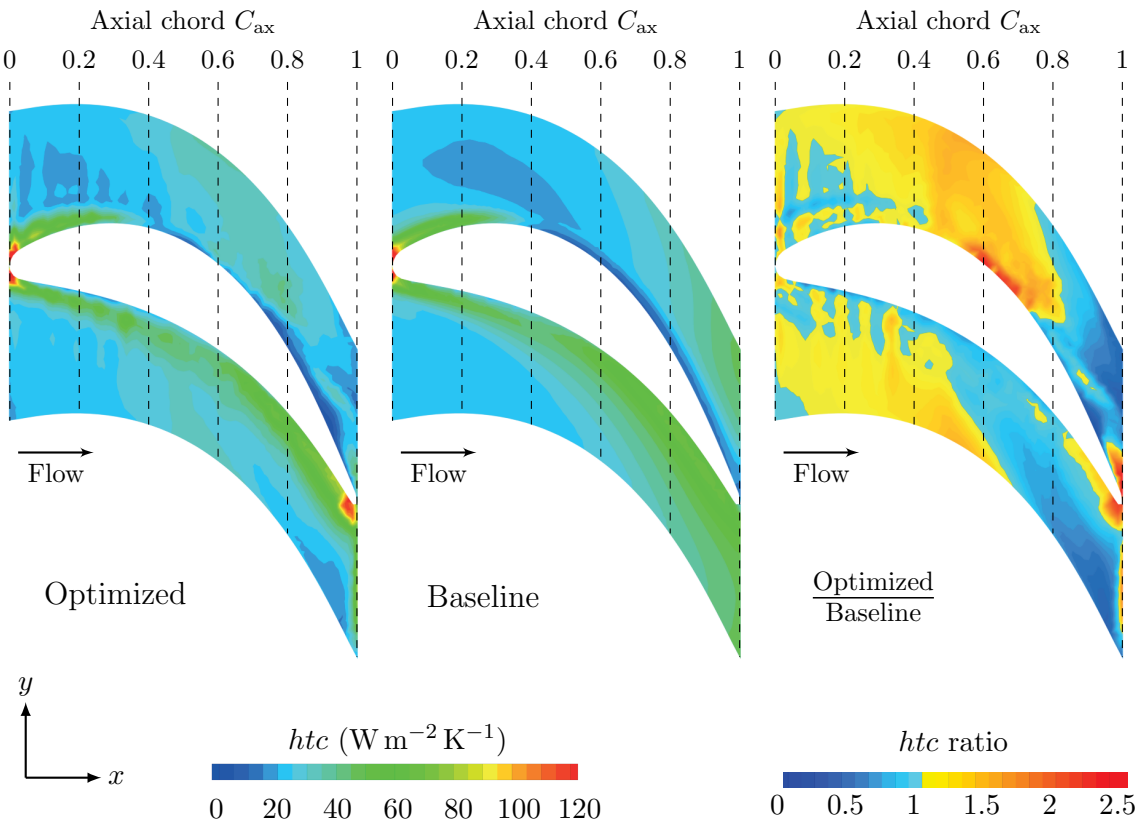

Figure 4.27: Distribution of heat transfer coefficient for contour optimized with respect to minimum vane passage heat transfer (left), flat endwall baseline (middle), and *htc* ratio of both contours (right) at $Re_C = 49{,}900$

the comparable value for the baseline is $Nu/Re^{0.8} = 0.016{,}019$. This corresponds to a reduction of 6.1% for the optimized endwall contour.

These changes in heat transfer are closely linked to the altered flow field in the contoured vane passage. Since the elevation of the contoured endwall runs close to the suction side in the rear vane passage, the contouring locally accelerates the flow and extends the low pressure region at the suction side further downstream. Subsequently, the decreasing height of the elevation towards the passage exit creates a diverging geometry and hence causes a steep increase in static pressure in the vane wake. As the rear suction side is sensitive to flow detachment, this pressure increase leads to a region of separated flow at the suction side vane/endwall junction. Figure 4.28 (left) illustrates this detached flow in terms of path lines colored by velocity magnitude. The latter is low for the fluid flow in this recirculation zone. The right image of Fig. 4.28 confirms this by showing the velocity magnitude in cross-sections along the rear suction side. Hence, this recirculation zone only holds low momentum fluid and thus reduces heat transfer in the rear suction side vane passage.

In the rear pressure side part of the vane passage, the elevation changes the velocity component in z-direction. Figure 4.29 shows this velocity component at the rear

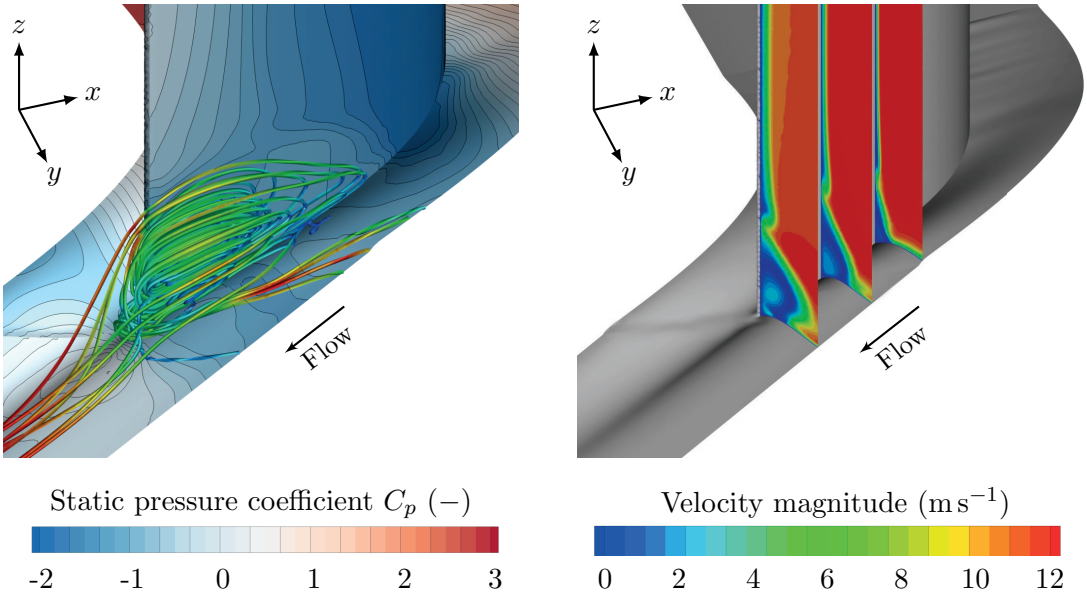

Figure 4.28: Recirculation zone at rear suction side for contour optimized for vane passage heat transfer from ice contour at $Re_C = 49{,}900$ and $\Theta = 8.5$

pressure side for the optimized endwall and the baseline. Due to the trench that forms in between the rear pressure side and the elevation, the contouring yields strongly increased downwards velocities at the rear pressure side/endwall junction.

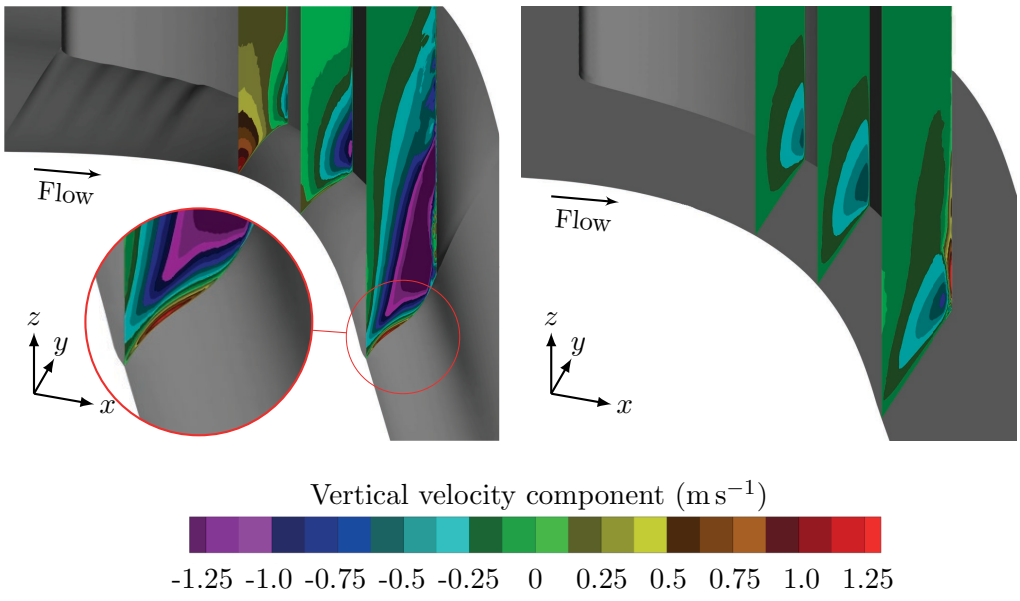

Figure 4.29: Vertical velocity component close to rear pressure side for contour optimized with respect to minimum vane passage heat transfer (left) and flat endwall baseline (right) at $Re_C = 49{,}900$

Hence, at this position heat transfer is increased for the contoured endwall resulting in the local hot spot at the very end of the pressure side. Towards the mid of the vane passage in pitchwise direction, the present elevation induces upwards velocities away from the endwall, which stretch the thermal boundary layer and thus reduce endwall heat transfer in the rear pressure side vane passage. Note that the lowest heat transfer also occurs at the position where the contouring induces maximum upwards velocities.

5

Results Other Cases

Contents:
Flow and heat transfer results for ice-contoured endwall with extended cooling length - Results for endwall contours created from numerical optimizations on basis of flat endwall

5.1 Ice Contour Long Cooling Length

For the case with the short cooling length, the ice layers grew only in the vane passage free of restrictions; outside of it, ice growth was influenced by the finite length of the cooled copper inlay. Hence, to create the numerical solution domain from the experimental ice layers, I used linear transitions up- and downstream of the vane passage to connect the ice layer to the remaining endwall. This also resulted in an increased height of the endwall contour in the vane passage. As the preceding chapter showed, it is hardly possible to use such an endwall configuration for reducing average heat transfer in the vane passage.

Therefore, in order to get a larger restriction-free ice layer and thus avoid the linear transitions and the elevation of the endwall in the vane passage, Haase [26] used a significantly longer copper inlay, as described in Sec. 3.1.2. With this extended cooling length, he created further ice layers in the test facility. These ice layers were also digitized by the laser scanner, embedded in the numerical solution domain and used for simulations with air as gas turbine medium. This section discusses the results of the numerical simulation for one selected endwall contour with enlarged ice layer. Results are first presented in terms of heat transfer; subsequently, the underlying flow field is analyzed and the relations between flow features and the resulting heat transfer rates are identified.

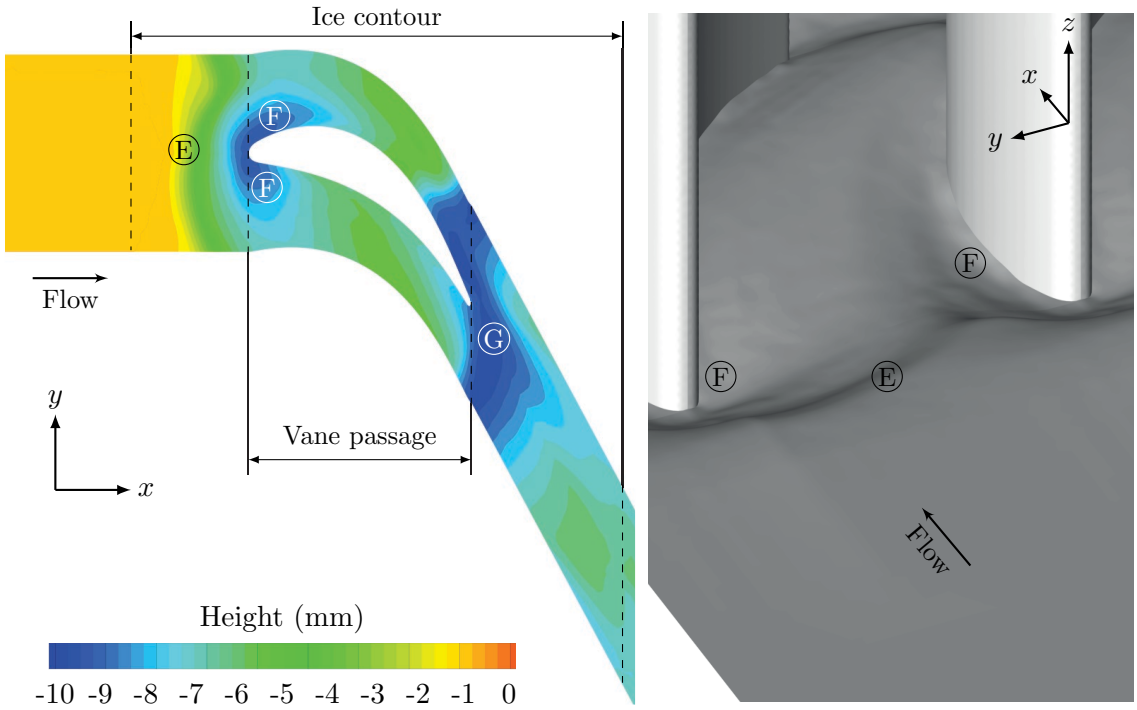

Figure 5.1: Ice-contoured endwall with long cooling length at Re_C = 49,900 and Θ = 12.2: height levels (left) and three-dimensional view (right)

5.1.1 Heat Transfer

Figure 5.1 shows the ice-contoured endwall with long cooling length at $Re_C = 49{,}900$ and $\Theta = 12.2$. The ice contour starts $0.5\,C_{\mathrm{ax}}$ upstream of the vane passage and extends until $1.5\,C_{\mathrm{ax}}$ downstream of it. In order to avoid an elevation of the endwall and hence a reduced cross-sectional area as for the endwalls of the short cooling length, I shifted the digitized ice layer in spanwise direction so that its horizontal beginning ($0.5\,C_{\mathrm{ax}}$ upstream of vane passage) was at the same height as the lower endwall of the solution domain. Hence, the span in the inlet region was equal to that of the flat endwall baseline. Note that this caused a slightly higher cross-sectional area in the vane passage than for the baseline. Upstream of the passage, the vanes only affect flow and hence ice growth in the vicinity of the leading edge, where the horseshoe vortex forms. Thus, at its beginning, the digitized ice layer is uniform in pitchwise direction. Downstream of the vane passage, the passage vortex is still present and only decays slowly, influencing ice growth far downstream. At the end of the digitized ice layer, $1.5\,C_{\mathrm{ax}}$ downstream of the vane passage, the height still varies in pitchwise direction with an amplitude of 1.1 mm. This required a slight transition region up to the end of the solution domain. Note that, in contrast to the contours of the short cooling length, this ice-contoured endwall increases the cross-section of the vane passage. However, this change in cross-sectional area is significantly smaller than for the short cooling length.

At the beginning of the ice-contouring (E), the height of this endwall contour rapidly decreases due to the forming horseshoe vortex, which causes high heat transfer and hence low ice thickness in front of the vane in the experiment. The contour starts to decline approximately$0.35\,C_{\mathrm{ax}}$ upstream of the leading edge and the lowest height is reached directly at the leading edge (F), where the horseshoe vortex is strongest and thus induces the highest heat transfer rates. In the middle part of the passage, the height of the contour grows again, similar to the short cooling length. In the rear vane passage and downstream of the trailing edge (G), the interaction of the vortices once more causes high heat transfer and thus low heights. However, with increasing distance from the trailing edge, the vortex system weakens and the height of the contouring grows towards the outlet of the solution domain. Note that this contour is different from the ice-contoured endwall of the short cooling length for the same Re_C and Θ (compare also Fig. 4.7). Especially between the leading edges and at the rear suction side it features a much lower height than the contour created with the short cooling length.

For this enlarged endwall contour, Figure 5.2 shows the heat transfer distribution resulting from the numerical simulation and compares it to the flat endwall baseline. At the beginning of the contouring upstream of the vane (i), the ice-contoured endwall holds lower heat transfer than the baseline over the entire pitch due to the rapidly diverging geometry at this position. Directly downstream, however, heat transfer is significantly increased around the vane leading edge. At the suction side, the region of high heat transfer persists until 50% axial chord and hence further downstream as for the baseline. At the pressure side, the region of high heat transfer that moves

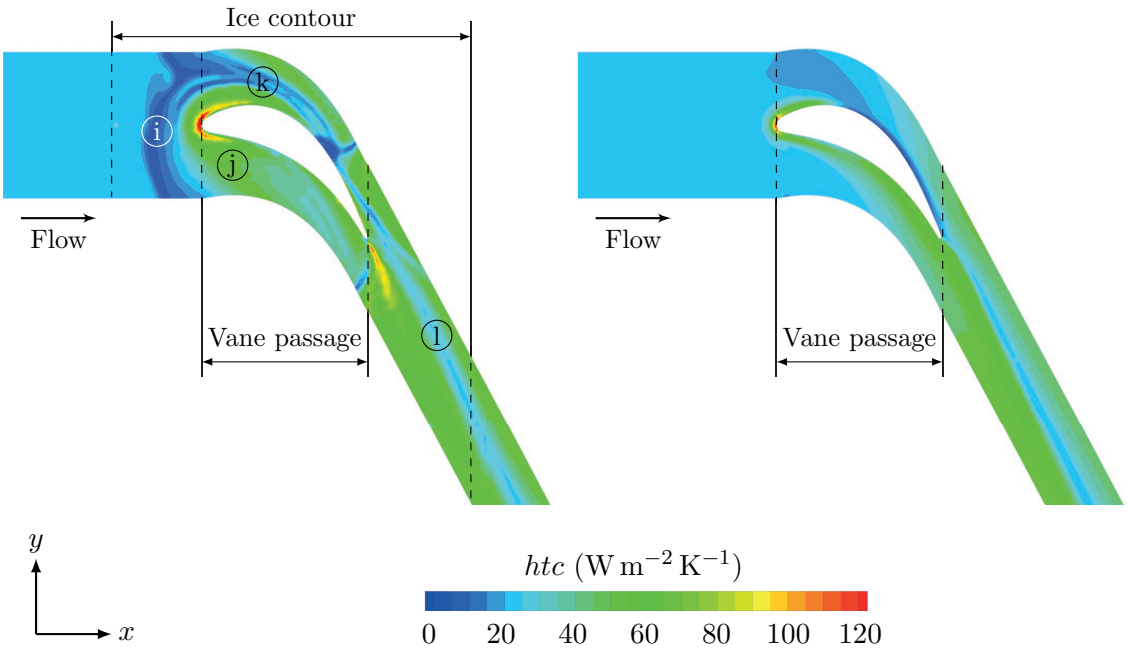

Figure 5.2: *htc* distribution for ice contour with long cooling length at $Re_C = 49{,}900$ and $\Theta = 12.2$ (left) and flat endwall baseline (right)

across the vane passage (j), starts further upstream as for the baseline. In between these two regions of high heat transfer, a strip with lower heat transfer (k) exists until it encounters the suction side at approximately 70% axial chord. In the rear vane passage and downstream of it, heat transfer is both higher and lower for the contoured endwall since the contouring changes the vortex system in this region. The strip of low heat transfer that exists until the outlet (l), indicates that the passage vortex is not deflected as was observed for the ice contours of the short cooling length. In average, heat transfer for this ice-contoured endwall is significantly higher compared to the flat endwall baseline. Considering the entire endwall, the area-averaged *htc* is 5.52% higher than for the baseline, in the vane passage, the contour even features an increase in heat transfer of 33.60%. The following section presents and discusses the flow features that lead to such a drastic increase in heat transfer.

5.1.2 Flow Field

For the present flow configuration, endwall heat transfer is to a great extent governed by the vortex system that develops around the vanes and in the vane passage. Figure 5.3 shows the vortex systems for the enlarged ice contour and the baseline in terms of iso-surfaces of Q (top row) and path lines around the vane (bottom row). For the iso-surfaces, I used $Q = 8{,}000$ for the baseline and $Q = 20{,}000$ for the ice contour, since the vortex system is much stronger and vortex cores are hence identified by higher values of Q. Additionally, the endwalls are colored by their respective

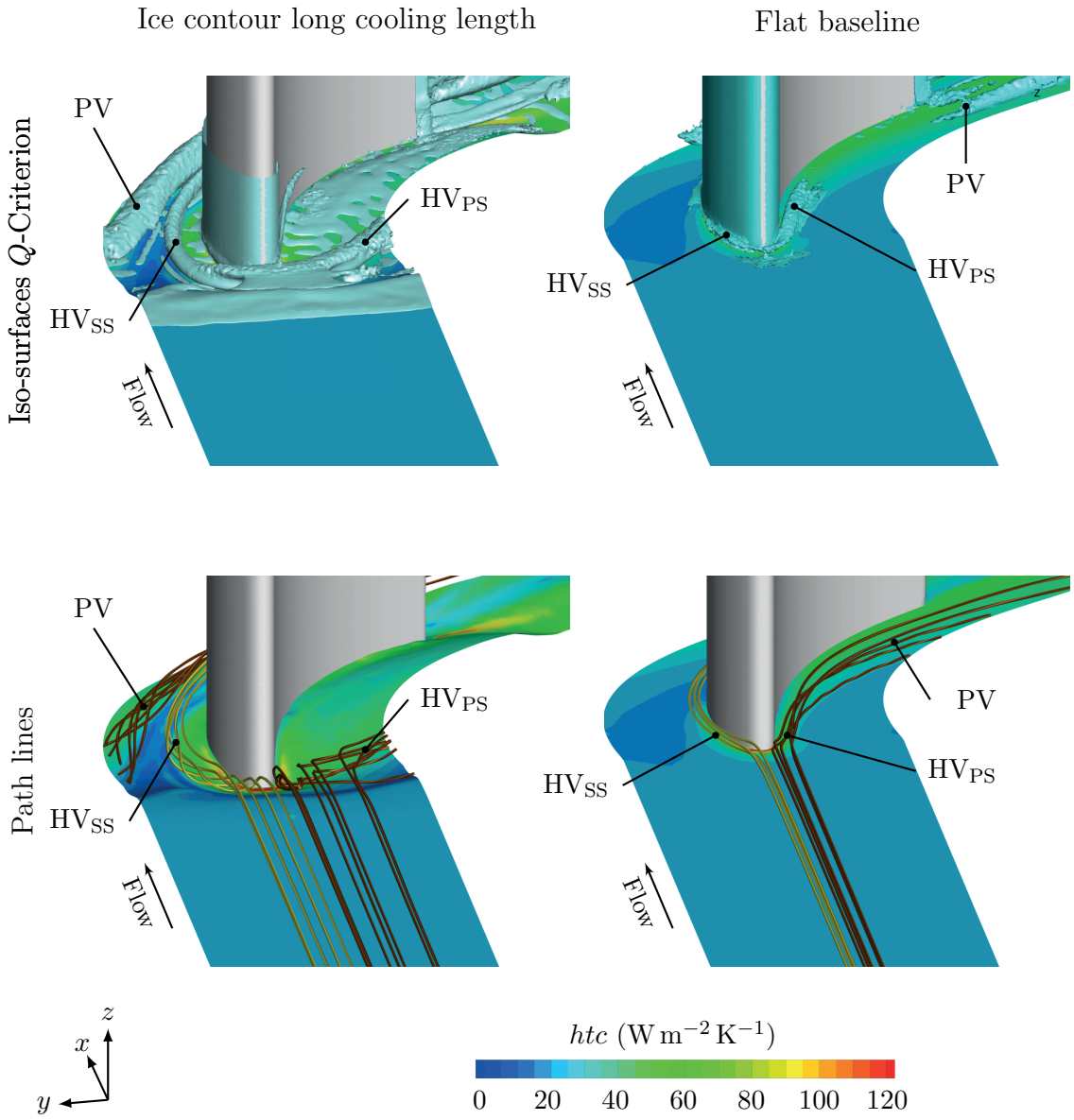

Figure 5.3: Vortex cores (upper row) and corresponding path lines (lower row) for ice-contoured endwall with long cooling length at $Re_C = 49{,}900$ and $\Theta = 12.2$ and flat endwall baseline

htc-distribution. The plots show that the flow of the ice-contoured endwall features a clearly stronger horseshoe vortex than the baseline. That is, both the pressure (HV_{PS}) and the suction side leg of this vortex (HV_{SS}) are more strongly pronounced for the ice contour. This also leads to a stronger passage vortex, which develops from the pressure side leg. Furthermore, the contouring changes the course of the pressure side leg. Instead of running close to the front pressure side as for the baseline, it runs rather in pitchwise direction almost perpendicular to the inflow direction. Therefore,

also the position of the passage vortex (PV) is shifted. From the path line plot, it becomes obvious how this changed vortex system affects heat transfer for the ice contour. In the suction side region, the suction side leg of the horseshoe vortex and the passage vortex cause the regions of high heat transfer at the vane and at mid pitch. In between, both vortices induce upwards velocities, resulting in the strip of low heat transfer (k). In the pressure side region, the position of the horseshoe vortex pressure side leg causes high heat transfer in the front part of the vane passage (j). Downstream of the vortex leg, the pitchwise pressure gradient drives a new boundary layer across the vane passage which causes a moderate increase of heat transfer in the pressure side region. In comparison, the vortices of the baseline and hence the regions of increased heat transfer run closer to the vane in the front vane passage and the passage vortex only causes high heat transfer in the rear pressure side region. This explains the significant increase in average *htc* for the vane passage of the ice-contoured endwall.

As discussed for Fig. 2.3, the horseshoe vortex develops because of the velocity distribution in the boundary layer. Velocities close to the endwall are much smaller than those in the free stream with greater distance from the endwall. When approaching the leading edge, the flow is slowed down and the higher velocities in the free stream result in a higher stagnation pressure than in the boundary layer close to the endwall. Hence, a downwards pressure gradient develops, which causes secondary flow towards the endwall at the leading edge and hence a rolling up of the boundary layer. Together with the main flow, this secondary flow forms the pressure and suction side leg of the horseshoe vortex. Therefore, the formation and strength of the horseshoe vortex depends on the pressure distribution and thus the induced vertical velocities at the leading edge. Figure 5.4 shows these vertical velocities at the leading edge for both the enlarged ice-contoured endwall and the flat endwall baseline. The plot additionally holds the endwalls' *htc* distributions. The rapidly diverging geometry of

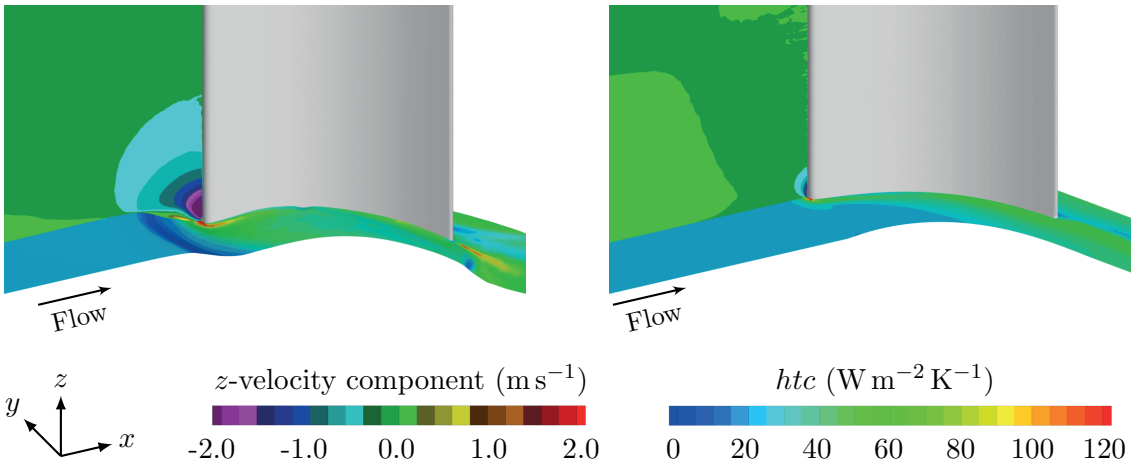

Figure 5.4: Vertical velocities at leading edge for ice contour with long cooling length at $Re_C = 49{,}900$ and $\Theta = 12.2$ (left) and flat endwall baseline (right)

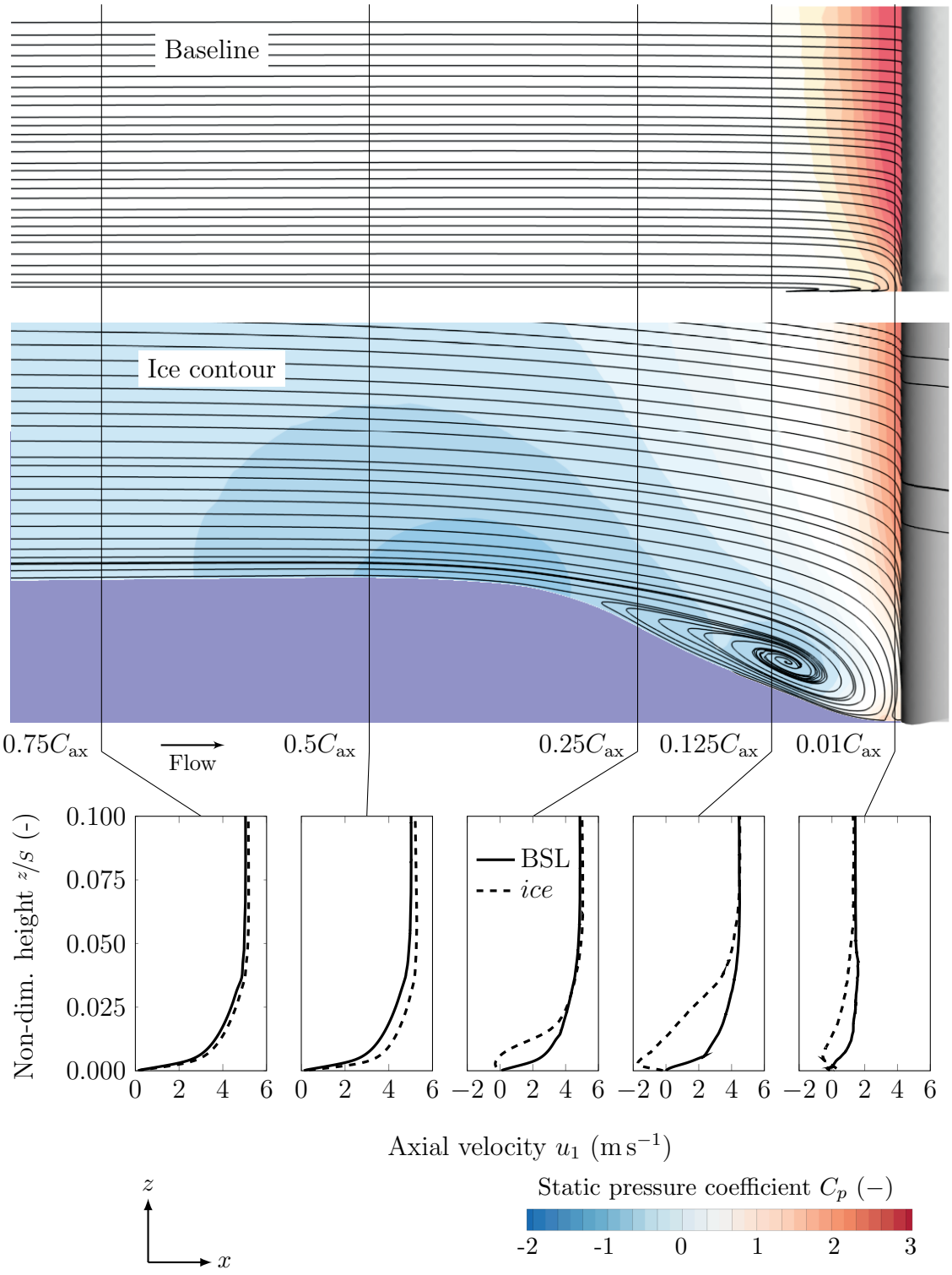

Figure 5.5: Distribution of static pressure coefficient C_p, path lines and velocity profiles in near-endwall region in front of vane leading edge for baseline and ice-contoured endwall with long cooling length at $Re_C = 49{,}900$

the ice-contoured endwall in front of the vane slows down the flow in the boundary layer close to the endwall and hence increases the pressure gradient normal to the endwall. This yields higher downwards velocities at the leading edge and forces more fluid into the secondary motion of the horseshoe vortex.

Figure 5.5 shows the distribution of the static pressure coefficient C_p, flow path lines and the endwall boundary layers in a plane upstream of the vane for both the enlarged ice-contoured endwall and the baseline. The displayed plane lies at the vane leading edge with a normal vector in y-direction. For the ice-contoured endwall, the divergent region in front of the vane causes very low velocities in the lower part of the boundary layer close to the wall. Hence, the boundary layer for the ice-contoured endwall features a significantly higher gradient of kinetic energy normal to the wall than the baseline boundary layer. This causes the higher downwards pressure gradient at the vane leading edge for the ice contour and thus yields a strong horseshoe vortex, which forms in the cavity in front of the vane. Note that this horseshoe vortex itself is the reason for the changes in the boundary layer of the ice-contoured endwall. Due to these changes, the ice-contoured endwall amplifies both dimension and intensity of the horseshoe vortex, resulting in a more strongly pronounced vortex system in the vane passage.

The higher downwards velocities predicted by the numerical simulations at the leading edge of this ice-contoured endwall could also be confirmed by Particle Image Velocimetry (PIV) measurements in the experiment (see Haase [26]). Figure 5.6 shows these measurements in the entry plane of the vane cascade for the flat endwall baseline (top) and the ice contour with the long cooling length at $Re_C = 49{,}900$ and $\Theta = 12.2$ (bottom). The plots are colored by the vertical velocity component u_3 and hold arrows indicating the local flow direction in the plane. A comparison of the vertical velocity components at the leading edges ($y/P = -0.5$ and $y/P = 0.5$) shows that the concave regions, which develop with the ice-contouring around the leading edges, significantly increase the downwards velocities at this position. This verifies the numerical findings and indicates that the horseshoe vortex at the leading edge becomes stronger due to the ice-contouring.

Chapter 4 as well as this chapter both revealed that it is difficult to use the Ice Formation Method for creating ice-contoured endwalls with the goal of a reduced endwall heat transfer for the flow around a turbine guide vane. The short cooling length yielded ice contours with globally reduced average *htc*, however, similar *htc* reductions could also be achieved by elevating the endwall in the vane passage. For the long cooling length, average heat transfer was even higher than for the flat endwall baseline. Especially in the vane passage heat transfer was substantially increased. This resulted from the concave region, which the ice layer features around the front part of the vane profile. This region proved to increase the strength of the horseshoe vortex, leading to an intensified vortex system and hence increased heat transfer in the vane passage. Note that this concave region was only partly present for the endwall contours of the short cooling length and hence these contours did not intensify the vortex system in the vane passage.

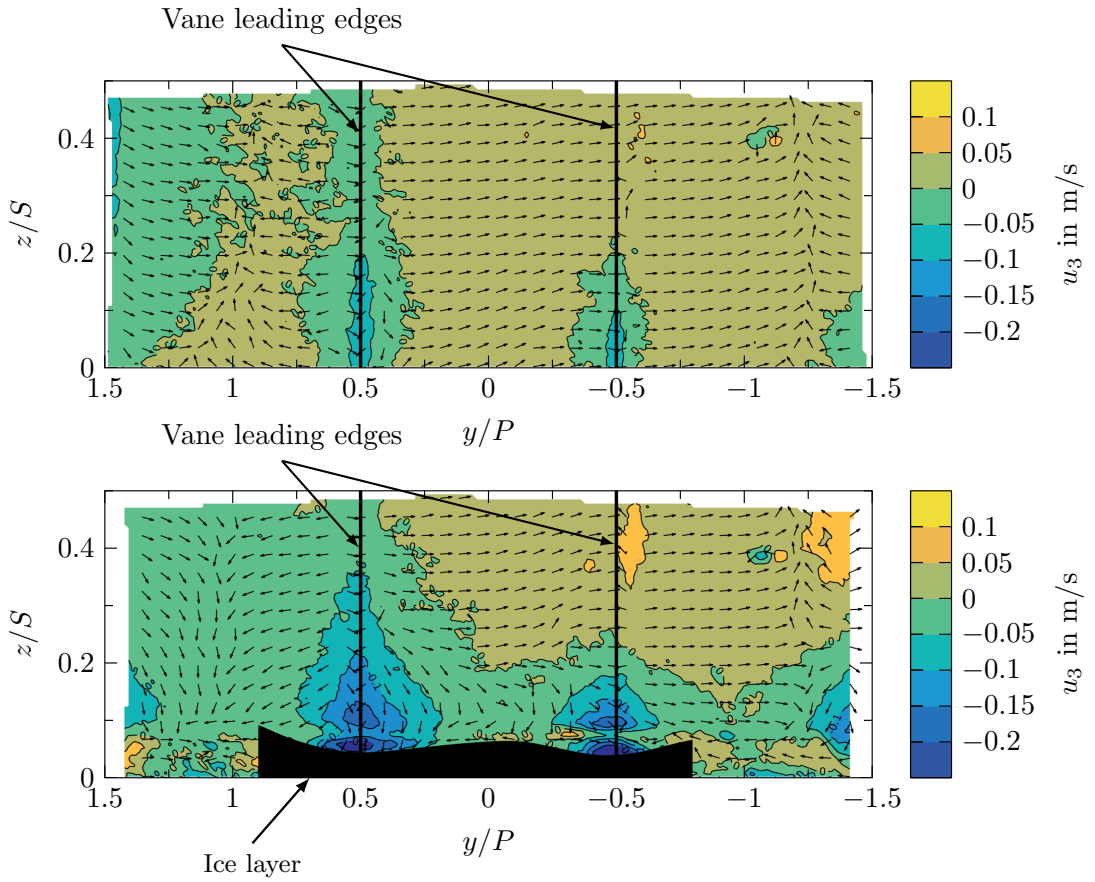

Figure 5.6: PIV measurements of vertical velocity component at vanes' leading edges for baseline (top) and experimental ice layer with long cooling length at $Re_C = 49{,}900$ and $\Theta = 12.2$ (bottom) [26]

Based on the above results, it must be concluded at this stage that the Ice Formation Method can only be used with reservations for the optimization of the considered vane endwall. Two possible explanations for this might be the influence of the inflow boundary layer condition on the behavior of the heat transfer in the cascade and the definition of the baseline geometry. In contrast to other applications of the IFM for a 180° bend [73] or a cylinder in cross-flow [13], the heat transfer behavior in the region of the forming ice strongly depends on the condition of the inlet boundary layer for the here considered vane endwall flow. For the bend, ice growth on the separating web is independent of the boundary layer condition at the inflow, since the boundary layer is already fully developed upstream of the web. For the cylinder in cross-flow, the boundary layer starts to develop at the cylinder and not upstream of it. Therefore, the flow at the cylinder and hence ice growth are also rather independent of the inflow conditions. This is different for the vane endwall flow considered in this work. Since the horseshoe vortex arises from the incoming boundary layer,

the vortex system and hence heat transfer in the vane passage strongly depend on the condition of the boundary layer upstream of the vane. The growing ice at the beginning of the cooled copper inlay, however, accelerates the flow, thus changing the state of the incoming boundary layer. Hence, the contoured ice layer that grows in the vane passage forms on the basis of this boundary layer, which has a different condition than the incoming boundary layer of the flat endwall. This needs to be kept in mind when comparing the ice-contoured endwalls to the flat endwall. The latter was though used as baseline geometry for this study, since it constitutes the most fundamental endwall for comparison. For consistency, I always used this flat endwall with a span of S, to compare all created endwall contours to. The ice contours of the short cooling length already showed that the evaluation of their heat transfer performance is significantly different if it is compared to this flat endwall or to a trapezoidal endwall with elevated vane passage. For the long cooling length, I shifted the ice layer down in spanwise direction, so that the ice layer in the inlet region had the same span as the baseline. However, I could have also constructed the ice-contoured endwall in such a vein that the ice layer of the outlet region has the same span as the baseline. Associated to this is the fact that it is also difficult to compare the different endwalls at the same flow parameters. Since the growing ice reduces the cross-section of the test section, it increases flow velocity and hence also heat transfer. This causes different flow parameters in the region of ice growth and hinders the comparison of different endwall contours. All these considerations illustrate the complexities that arise when comparing the contoured endwalls created by the Ice Formation Method to a baseline geometry.

5.2 Optimization from Flat Endwall Baseline

The chapters before showed that with the current experimental setup of the IFM, it is very difficult to reduce endwall heat transfer in the passage between the vanes. Even with a subsequent numerical optimization based on the ice-contoured endwalls, vane passage heat transfer could only be reduced by about 2.68% compared to the flat endwall baseline (see Sec. 4.3.2). One reason for this is the reduction of the cross-section in the vane passage, which increases flow velocity and thus heat transfer. Therefore, I performed a numerical optimization based on the flat endwall in order to reduce vane passage heat transfer. For the parametrization of the vane passage, this optimization used the same Bézier curves in pitchwise direction as the parametrization of the ice-contoured endwalls. However, instead of using the height information at the vane's pressure and front suction side from the ice contour, I parametrized the entire vane profile with Bézier curves. Furthermore, the optimization space for this case extends from 5 mm below the flat endwall to 5 mm above it, so that the height of the resulting endwall contour can locally be both higher and lower than the flat endwall baseline. Section 3.3.3 describes the used parametrization in detail.

Figure 5.7 shows the resulting endwall contour OC_{BSL}, created with this parametrization and the goal function of minimum vane passage heat transfer. The contouring

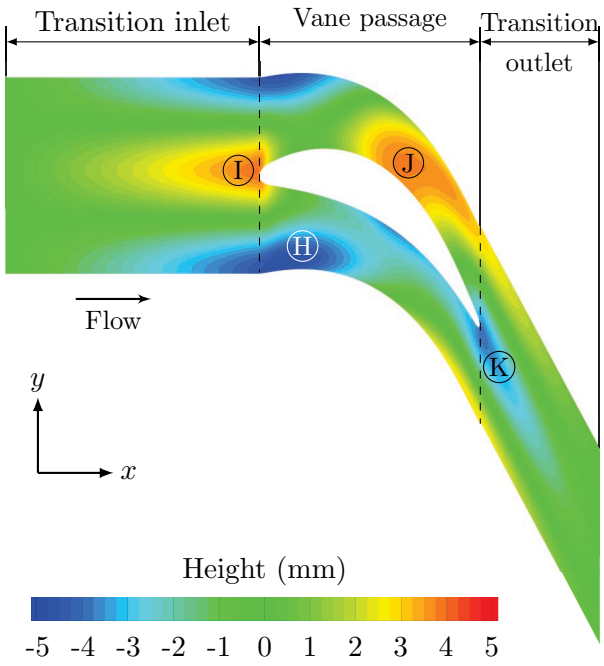

Figure 5.7: Endwall contour optimized from flat endwall baseline at $Re_C = 49{,}900$

has four distinct regions: two convex regions with maximum height, as well as two concave regions with minimum height. Upstream of the vane passage, a large concave region (H) develops at half pitch and reaches into the front vane passage until the vane's pressure side. In between this region, a convex bump (I) is present at the leading edge. A further convex elevation at the rear suction side (J) determines

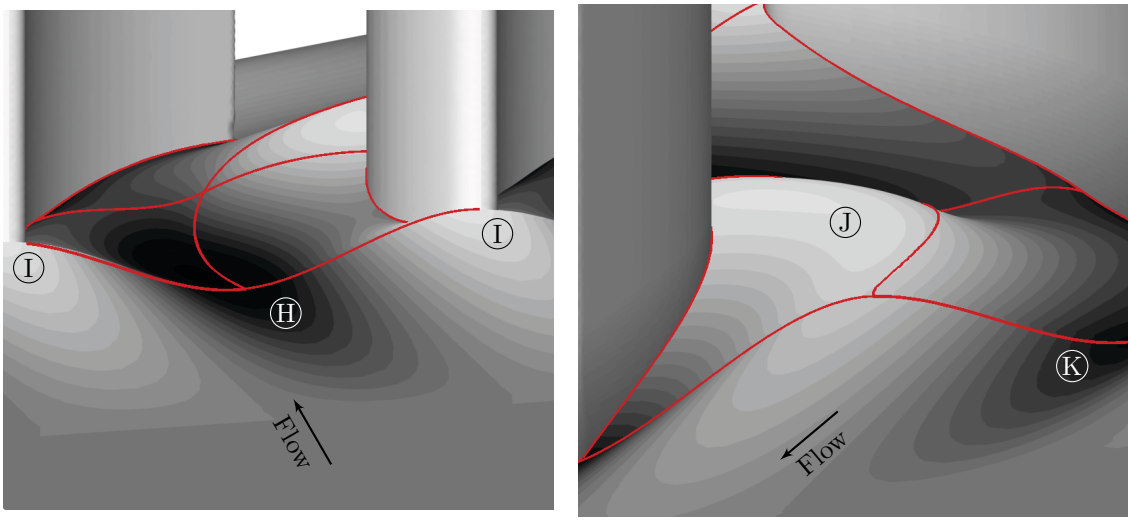

Figure 5.8: Three-dimensional view of endwall contour $\mathrm{OC_{BSL}}$ at $Re_C = 49{,}900$

the contouring of the suction side vane passage. In contrast to the contouring at the leading edge, the trailing edge features a small concave height minimum (K). Note that all Bézier curves for the contouring lie within the vane passage. Up- and downstream of the vane passage, the contouring smoothes out in the transition regions. Appendix A.10.1 holds the Bézier curves for this contour as obtained from the numerical optimization. Figure 5.8 shows a three-dimensional view of this contour in streamwise direction upstream of the vane passage (left) and against the streamwise direction downstream of it (right).

For this optimized endwall contour $\mathrm{OC_{BSL}}$, Fig. 5.9 shows the heat transfer distribution in the vane passage (top) and compares it to the baseline (middle). Furthermore, the figure displays the *htc* ratio in the suction and pressure side region (bottom). The optimized endwall reduces heat transfer in large parts of the vane passage, especially close to the front suction side (m) and along the pressure side (n), where heat transfer is high for the baseline. Only at the two spots (o) and (p), heat transfer close to the vane is increased for the optimized contour. The latter also exhibits an *htc* increase in the front suction side region (s), however, heat transfer rates are very low in this region. In average, this contour reduces heat transfer in the vane passage by 7.07% compared to the baseline. Outside the vane passage, this endwall contour increases heat transfer close to the leading edge (q) and in the pressure side region downstream of the trailing edge (r). This is due to the fact that only average heat transfer in the vane passage was prescribed as goal function to be reduced in the optimization. The increased heat transfer at the leading edge is undesirable, since this is the position of maximum heat transfer for the flat baseline. Considering the average *htc* over the entire endwall, the optimized contour yields a reduction of 1.20% with respect to the baseline. For completeness, App. A.10.2 holds the average *htc* values for all endwall segments of this contour.

The reduced vane passage heat transfer for the optimized endwall can be traced back to the contouring changing the structure of the horseshoe and the passage vortex. Figure 5.10 outlines these changes by comparing the vortex structure for the flat baseline and the optimized contour in terms of iso-surfaces of $Q = 8{,}000$. The latter are plotted together with the *htc* distributions of the two endwalls. The contouring of the optimized endwall, primarily the convex elevation at the leading edge (I) (see Fig. 5.7), clearly reduces the formation of the horseshoe vortex around the front part of the vane, both at the suction (1) and the pressure side (2). The increasing height towards the leading edge locally accelerates the flow near the endwall and narrows the boundary layer in front of the leading edge, causing less fluid to roll up into the horseshoe vortex. To exemplify this point, Fig. 5.11 shows the near-endwall flow field upstream of the vane for the optimized contour $\mathrm{OC_{BSL}}$ and the flat baseline. The flow is shown in an x-z-plane at the vane leading edge, including velocity boundary layers at selected positions. The boundary layer plots clearly show the effect of the contour's increasing height towards the vane leading edge. That is, the convergent endwall geometry accelerates the lower part of the boundary layer close to the endwall and hence adds kinetic energy to it. This results in a flatter velocity profile for the optimized endwall contour with a reduced difference of kinetic energy in wall

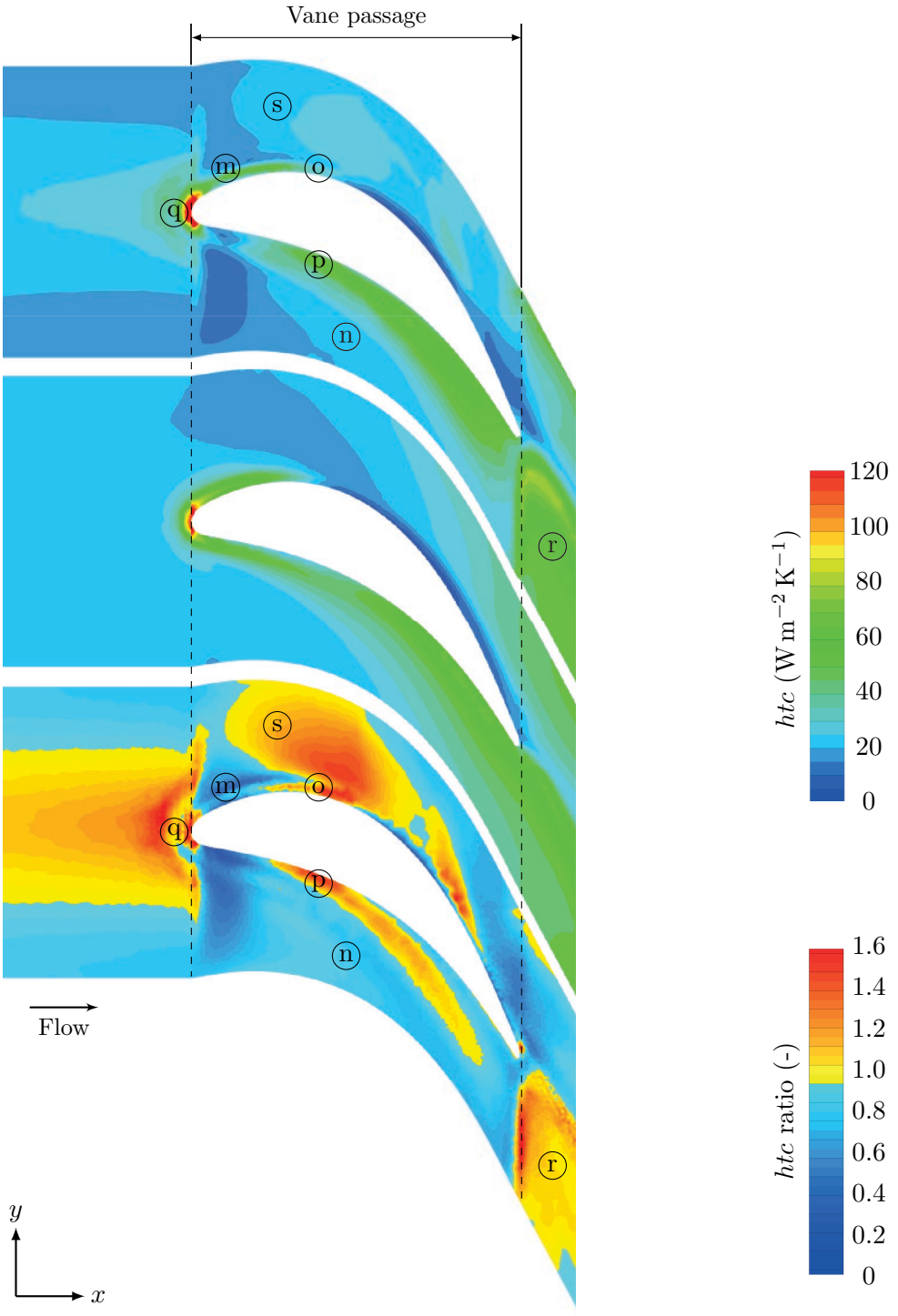

Figure 5.9: Distribution of heat transfer coefficient for optimized endwall OC_{BSL} (top), flat endwall baseline (middle) and *htc* ratio of both contours (bottom) at $Re_C = 49{,}900$

normal direction. Thus, when approaching the vane leading edge, the rise in static pressure is similar in large parts of the boundary layer, reducing the pressure gradient towards the endwall. The reduced pressure gradient lessens fluid flow towards the endwall at the leading edge and thus weakens the formation of the horseshoe vortex. In addition, the convex elevation rapidly decreases in height downstream of the leading edge, decelerating the flow close to the vane endwall junction. Both these facts damp the formation of the horseshoe vortex for the optimized geometry. This finding agrees well with the results obtained by Zess and Thole [84]. They reported that the horseshoe vortex can be eliminated by applying a leading edge fillet to a vane profile. The geometry of this fillet was similar to the convex region (I) at the leading edge obtained from the optimization of the present endwall contour. Further publications [24, 51, 55] also observed a weakening of the horseshoe vortex by fillets located at the front part of different vane profiles. The weakening of the vortex system by these fillets thereby depends on the same physical principles as those observed for the convex elevation of the present endwall contour.

However, the convex elevation also increases maximum heat transfer at the leading edge, since the axial flow has a component normal to the endwall, due to the inclination of the endwall at this position. As the boundary layer plots in Fig. 5.11 show, this narrows the thermal boundary layer at the endwall. Similar to the velocity profiles, also the temperature profiles become flatter in the convergent region of the ice-contoured endwall. The flatter temperature profiles feature higher temperature

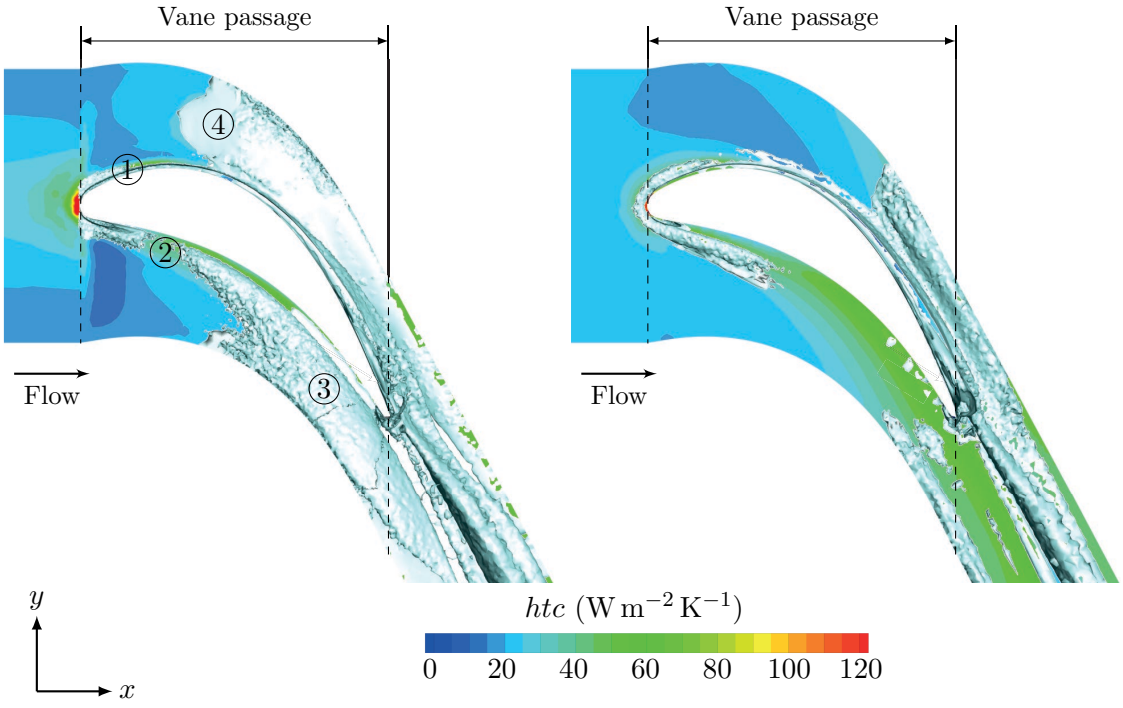

Figure 5.10: *htc* distribution and vortex system in terms of $Q = 8{,}000$ for endwall contour $\mathrm{OC_{BSL}}$ (left) and baseline (right) at $Re_C = 49{,}900$

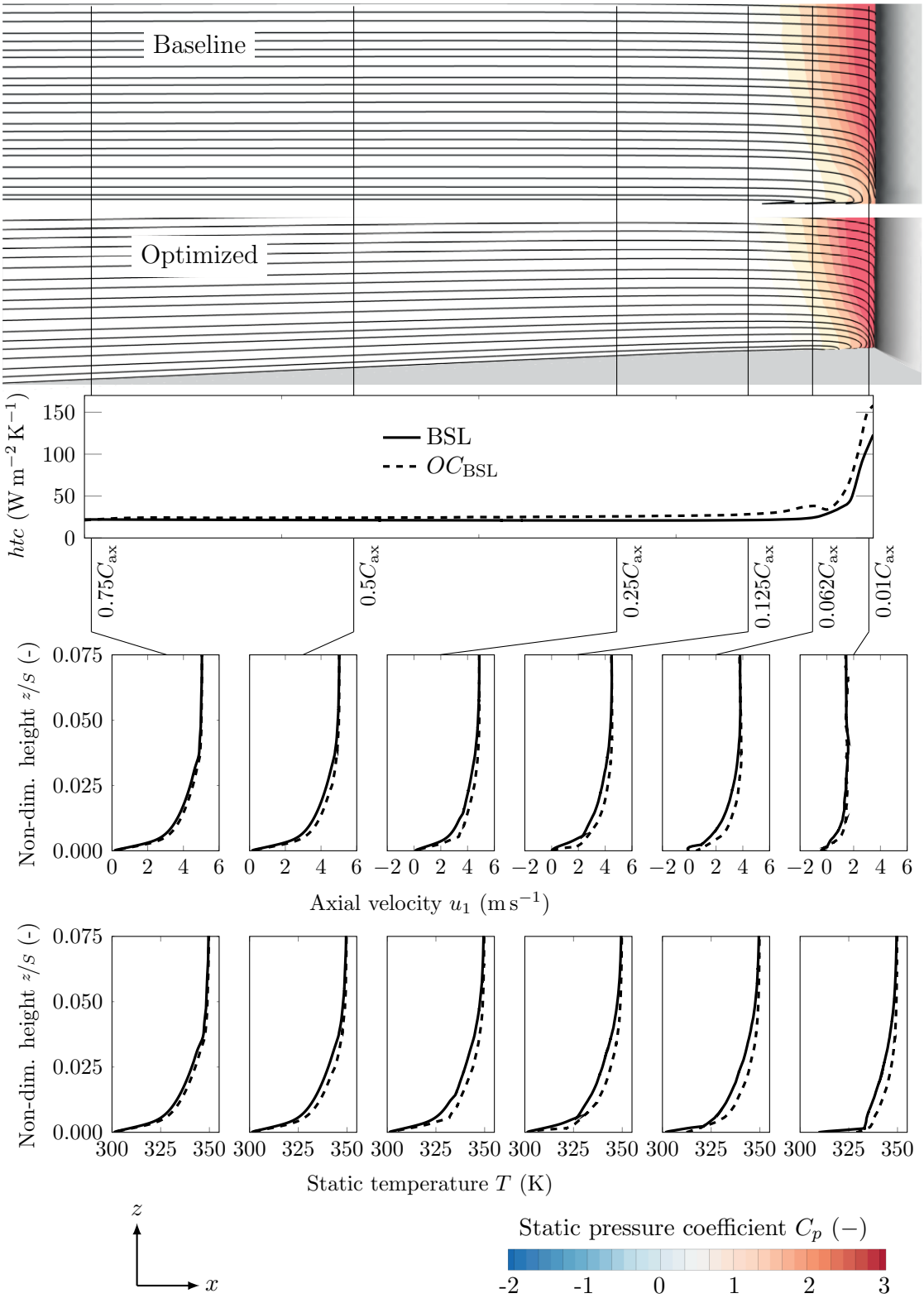

Figure 5.11: Near endwall flow with velocity and thermal boundary layer in front of vane for baseline and optimized contour $\mathrm{OC_{BSL}}$ at $Re_C = 49{,}900$

gradients at the wall and hence cause the increased heat transfer at the leading edge. Hence, for using this endwall design in an engine application, further local optimization of the endwall in the vicinity of the leading edge is required to reduce maximal heat transfer at this position.

As the vortex cores in Fig. 5.10 show, the contouring also changes the structure of the passage vortex in the rear vane passage. Due to the contouring, the passage vortex extends over the entire pitch in the rear part of the vane passage. Thus, this vortex becomes stronger at the rear pressure side (3), resulting in the increased heat transfer rates compared to the baseline (p). Furthermore, the passage vortex for the contoured endwall also reaches further upstream in the suction side region (3), resulting in the increased heat transfer rates at this position (s).

In the paragraphs above, the parametrization based on the flat endwall proved successful for reducing endwall heat transfer inside the vane passage. In order to see if this parametrization allows for an even higher heat transfer reduction in the vane passage, I conducted a further optimization with an enlarged optimization space. The latter has a height of 30 mm and ranged from 15 mm below the flat endwall to 15 mm above it. Hence, the optimization space is three times as high as for the endwall contour OC_{BSL} and enables a more pronounced contour in the vane passage to develop during the numerical optimization. Figure 5.12 shows the optimized endwall contour with these settings; in the remainder referred to as $OC_{BSL,2}$. Due to the similar parametrization, the geometry of this endwall contour is similar to the one of the contour OC_{BSL}. It also features a convex elevation at the leading edge (L), a

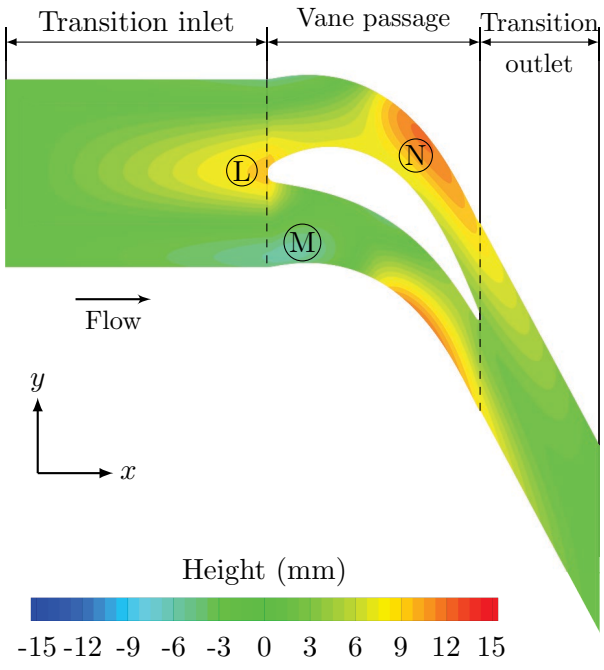

Figure 5.12: Endwall contour optimized from flat endwall baseline with extended optimization space at $Re_C = 49{,}900$

height minimum in the front pressure side region (M), and a height maximum that extends from the rear pressure side into the vane passage (N). However, the contour is in average at higher z-levels, which magnifies the height maxima and lessens the height minima.

For this endwall contour $\mathrm{OC}_{\mathrm{BSL},2}$, Fig. 5.13 shows the heat transfer distribution in the vane passage and compares it to the baseline. Due to the convex elevation at the leading edge, the contour holds increased heat transfer at this position (t), as discussed before for the contour $\mathrm{OC}_{\mathrm{BSL}}$. Downstream of the leading edge, heat transfer is reduced along the front suction side and along most of the pressure side, which is a region of high *htc* for the baseline. Especially in the front pressure side region (u), heat transfer is significantly lowered compared to the baseline. In the suction side region, the contour increases heat transfer rates slightly (v) and hence homogenizes the *htc* in the vane passage. Downstream of the vane passage, however, this contour also induces a region of increased heat transfer in the pressure side region (w). The most beneficial feature of this contour is the significantly reduced heat transfer in the pressure side region of the vane passage.

To understand the reasons for this local *htc* reduction, Fig. 5.14 shows the vortex system in the pressure side region of this contour (left) and associated path lines

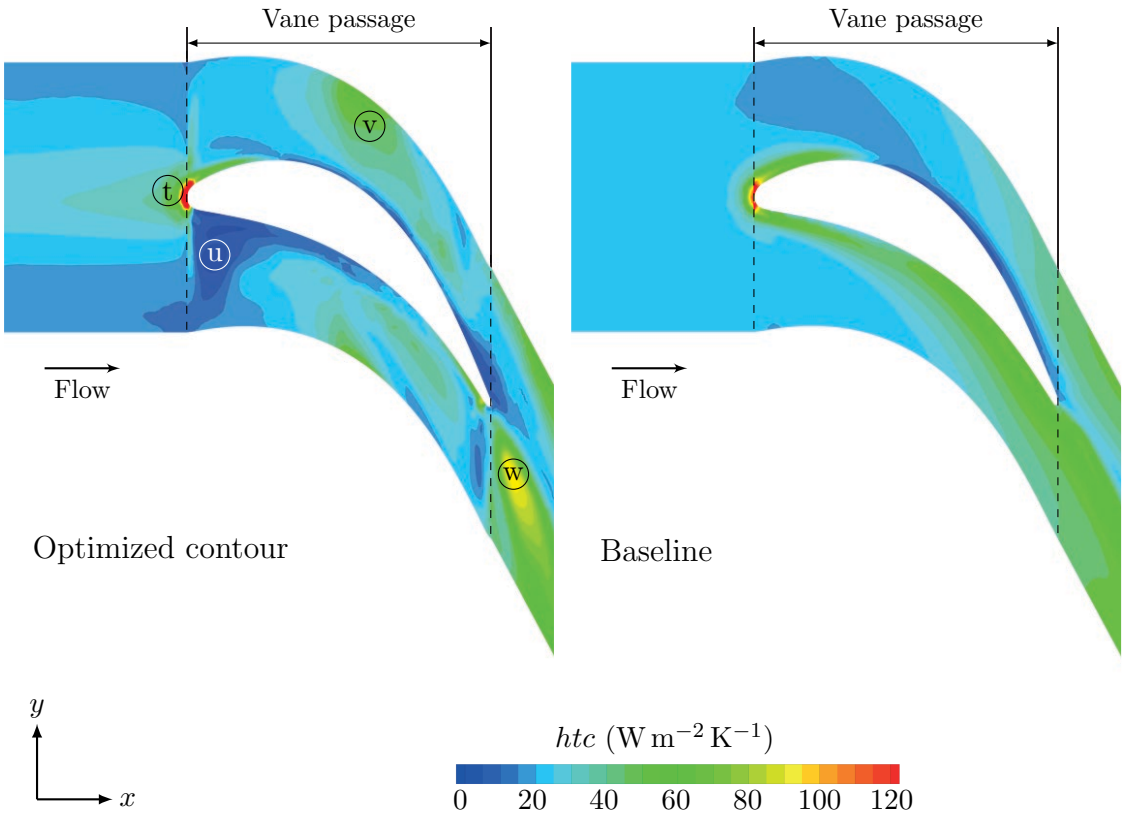

Figure 5.13: *htc* distribution for optimized endwall $\mathrm{OC}_{\mathrm{BSL},2}$ (left) and flat baseline (right) at $Re_C = 49{,}900$

(right). The figure clearly shows a recirculation zone at the height minimum in the front pressure side region. Its low momentum fluid isolates the endwall from the hot gas of the core flow and hence causes the observed low heat transfer rates. Furthermore, the recirculation zone shifts the pressure side leg of the horseshoe vortex and thus also the passage vortex upwards and hence away from the endwall. This explains the low heat transfer along the vane pressure side. Note that the passage vortex is also weakened since the convex elevation in front of the leading edge weakens the pressure side leg of the horseshoe vortex. Based on the explained heat transfer distribution, the endwall contour $\mathrm{OC}_{\mathrm{BSL},2}$ decreases heat transfer in the vane passage by 13.22% compared to the baseline. This constitutes a considerable reduction in vane passage heat transfer. If heat transfer is averaged over the entire endwall, this contour achieves a reduction of 6.90% with respect to the flat endwall (see Appendix A.11.2 for more details). The high reduction in overall heat transfer thereby results from the fact that the height maximum at the rear pressure side causes an overturning of the passage vortex and hence reduces heat transfer downstream of the vane passage, as was already observed for the ice-contoured endwalls. Contrary to the heat transfer reductions, which this contour achieves compared to the baseline, is however the increased maximum heat transfer at the leading edge, which requires additional cooling. Furthermore, from an aerodynamic point of view, the recirculation zone in the front pressure side region is undesirable because it increases aerodynamic loss.

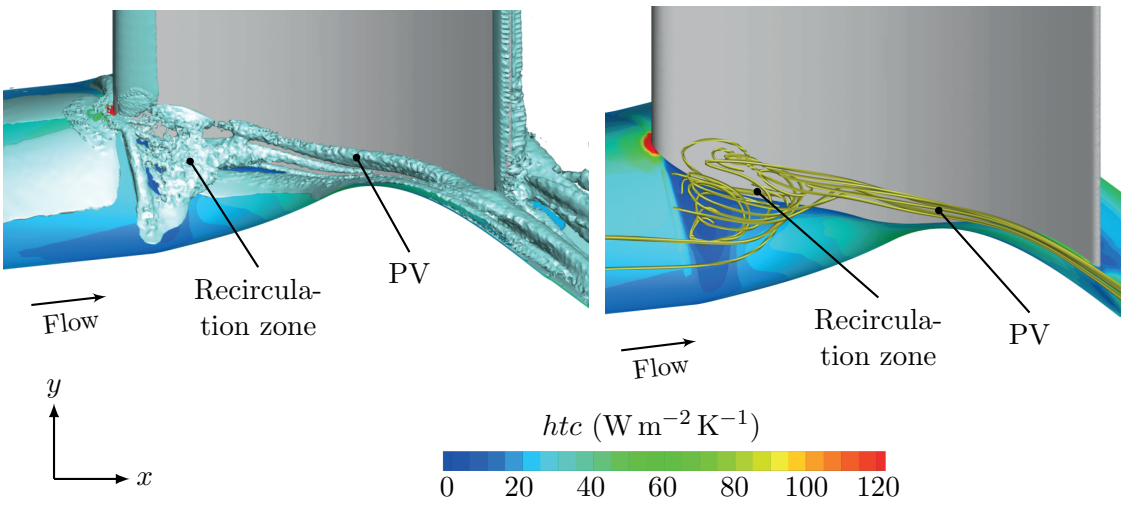

Figure 5.14: *htc* distribution with vortex system as $Q = 8{,}000$ (left) and path lines of recirculation zone (right) for contour $\mathrm{OC}_{\mathrm{BSL},2}$ at $Re_C = 49{,}900$

6

Results at Design Reynolds Number

Contents:
Flow and heat transfer for flat endwall baseline at design Reynolds number - Behavior of ice-contoured endwalls and optimized endwall contours at design Reynolds number with respect to endwall heat transfer and total pressure loss

6.1 Flat Endwall Baseline

Before I discuss the behavior of the novel endwall contours at the design Reynolds number, I show in this section the effect of the higher Reynolds number on endwall heat transfer for the flat baseline. Figure 6.1 shows the local distribution of this endwall's heat transfer coefficient at the experimental Reynolds number (Re_C = 49,900) and the design Reynolds number of Re_C = 200,000. For the latter, heat transfer increases due to two reasons. First, as known from the Reynolds analogy, heat transfer scales with the flow velocity and hence with the Reynolds number. This explains the higher heat transfer rates for the boundary layer type flow upstream of the vane. Second, the higher Reynolds number also increases the strength of the vortices. These induce higher vertical velocities near the endwall and thus enhance heat transfer. Since the vortex system dominates endwall heat transfer, the last effect has a great impact on heat transfer for the design Reynolds number.

To demonstrate this last point, Tab. 6.1 shows the average *htc* for the endwall segments of the flat baseline for Re_C = 49,900 and Re_C = 200,000 plus additionally the factor by which heat transfer increases. In the *Inlet* region, before the flow encounters the vane, heat transfer is only governed by a boundary layer flow and hence the heat transfer increase is lowest in this region. As soon as the vortex system around the vane starts to play a role for heat transfer, the factor for the heat transfer increase grows. Thus, it is already higher for the *Transition inlet* region, since this region contains the rolling-up of the boundary layer at the leading edge. For the

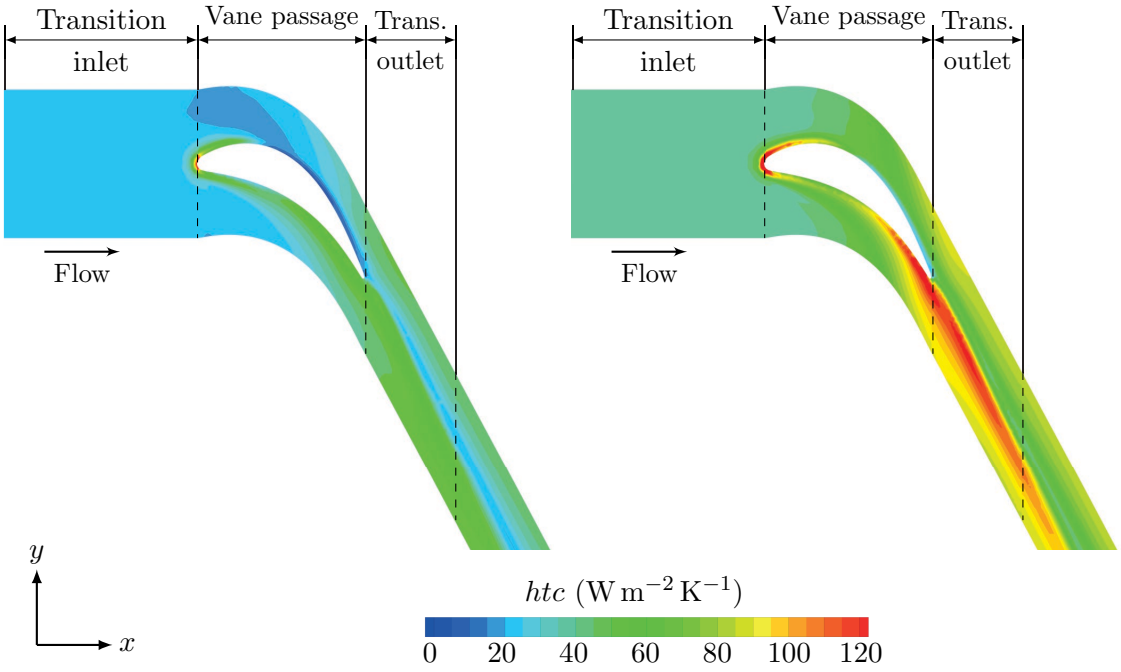

Figure 6.1: Distribution of heat transfer coefficient for flat baseline at experimental, Re_C = 49,900, (left) and design Reynolds number Re_C = 200,000 (right)

Table 6.1: Average *htc* for endwall segments of flat baseline at experimental Reynolds number ($Re_C = 49{,}900$) and at design Reynolds number ($Re_C = 200{,}000$)

Re_C	Inlet	Transition inlet	Vane passage	Transition outlet	Outlet	Total
49,900	27.66	21.38	29.76	43.50	36.09	29.80
200,000	36.45	37.36	58.48	85.30	72.99	50.49
Factor	1.31	1.73	1.94	1.93	1.98	1.67

Vane passage and the regions downstream of it, heat transfer increase for the design Reynolds number is highest, since these are the regions that are mostly affected by the increased strength of the passage vortex. Heat transfer in these regions is for the design Reynolds number approximately twice as high as for the experimental Reynolds number. In total, endwall heat transfer at the design Reynolds number is approximately 1.7 times higher than for the experimental one.

6.2 Ice Contours Short Cooling Length

This section first presents results at the design Reynolds number for all ice-contoured endwalls from the experiments with short cooling length and then for the endwall contour $\mathrm{IC_{IFM}}$, optimized on basis of the ice contour at $Re_{C,\mathrm{exp}} = 49{,}900$ and $\Theta = 12.2$.

6.2.1 Ice-contoured Endwalls

To examine their performance at the design Reynolds number, I used the endwall contours from the experiments with the short cooling length (see Sec. 4.2) and simulated them numerically for $Re_C = 200{,}000$. Figure 6.2 shows the average reductions in endwall heat transfer for these contours, referred to the baseline at the design Reynolds number. Note that $Re_{C,\mathrm{exp}}$ only indicates the Reynolds number at which the contours were created in the experiment; all contours were simulated at $Re_C = 200{,}000$. Also for the design Reynolds number, all ice-contoured endwalls have lower average heat transfer than the flat endwall baseline. For the different combinations of Reynolds number and non-dimensional temperature ratio, these reductions exhibit a similar trend as for the experimental Reynolds numbers (see also Fig. 4.6). However, heat transfer is reduced even more at the design Reynolds number. As for the experimental Reynolds numbers, the ice-contoured endwall $\mathrm{IC_{IFM}}$, created in the experiment at $Re_{C,\mathrm{exp}} = 49{,}900$ and $\Theta = 12.2$, reduces heat transfer the most. This reduction amounts to 9.05% and is thus higher than the reduction of 5.20% at the experimental Reynolds number.

For this contour, Tab. 6.2 shows the percentaged *htc* differences for the different endwall segments, both at the experimental Reynolds number of $Re_C = 49{,}900$ and

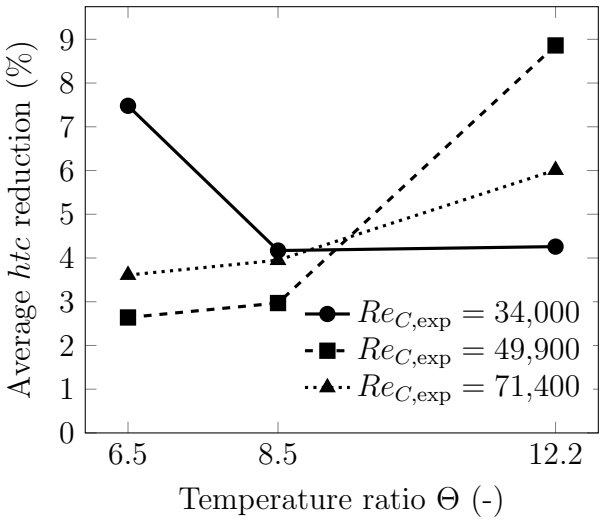

Figure 6.2: Average heat transfer reductions of ice-contoured endwalls with short cooling length at design Reynolds number

the design Reynolds number $Re_C = 200{,}000$. The higher Reynolds number intensifies the heat transfer characteristics observed for the experimental Reynolds number. Regions with increased heat transfer compared to the baseline at $Re_C = 49{,}900$ feature an even higher increase for $Re_C = 200{,}000$, whereas the higher Reynolds number further reduces the *htc* for regions with lowered heat transfer at the experimental Reynolds number. Thus, the endwall contour achieves the additional heat transfer reduction for the design Reynolds number in the segments downstream of the vane passage, whereas heat transfer in the vane passage slightly increases. Especially in the *Transition outlet* region, the heat transfer reduction is considerably higher at the design Reynolds number than at the experimental one. This endwall segment also features the highest reduction in *htc* for the experimental Reynolds number.

To outline the reasons for the further reduction in heat transfer at the design Reynolds number, Fig. 6.3 shows the *htc* distribution on the ice-contoured endwall and the flat baseline at $Re_C = 200{,}000$. In general, the higher Reynolds number increases flow velocities and hence heat transfer on the endwall for both contours. The

Table 6.2: Difference in average *htc* with respect to baseline for endwall segments of ice-contoured endwall $\mathrm{IC_{IFM}}$ at experimental ($Re_C = 49{,}900$) and design Reynolds number ($Re_C = 200{,}000$)

Re_C	Inlet	Transition inlet	Vane passage	Transition outlet	Outlet	Total
49,900	−1.02%	4.63%	1.71%	−20.48%	−13.22%	−5.20%
200,000	−1.26%	4.73%	2.30%	−34.01%	−17.21%	−9.05%

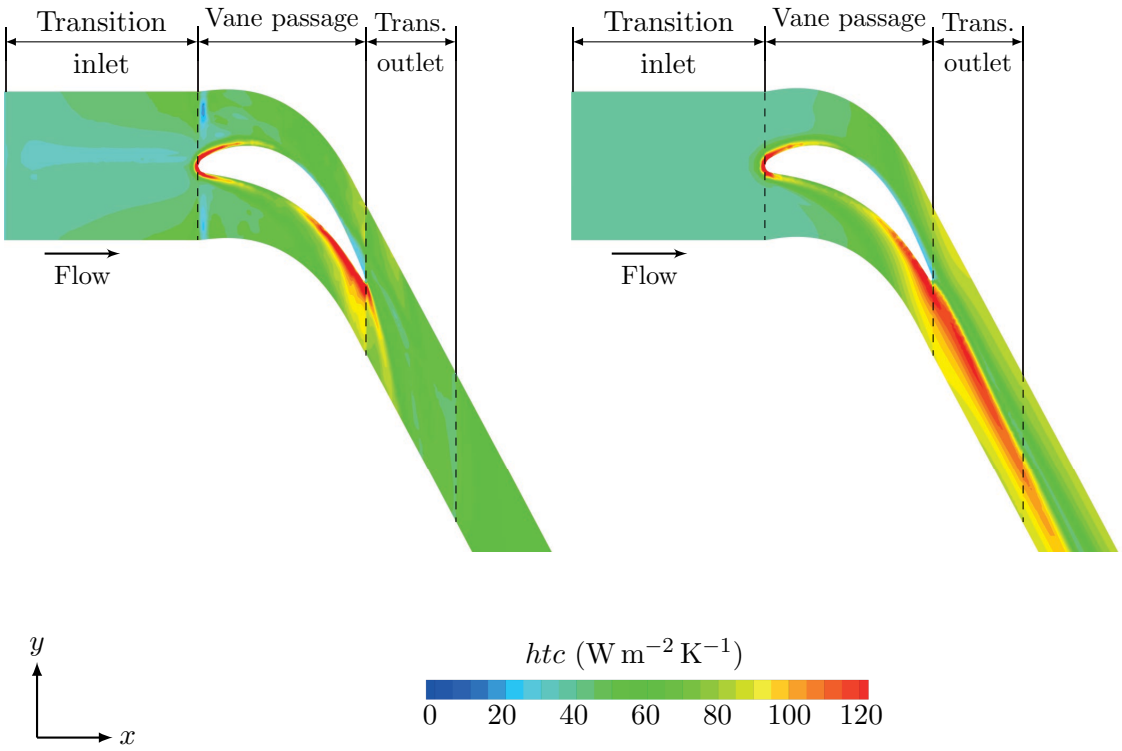

Figure 6.3: *htc* distribution for ice-contoured endwall $\mathrm{IC_{IFM}}$ (left) and flat endwall baseline (right) at $Re_C = 200{,}000$

local *htc* distribution, however, strongly depends on the vortex system. For the flat endwall, the passage vortex forms in the rear vane passage and runs in outflow direction. Due to its direction of rotation, it induces downwards velocities and therefore increased heat transfer rates at the rear pressure side and in the pressure side region downstream of it. In contrast, the contoured endwall causes the overturning of the passage vortex and thus reduces the vortex's influence on heat transfer downstream of the vane passage. As I showed for the flat endwall, the higher Reynolds number significantly increases the strength of the passage vortex and thus the induced heat transfer rates. Thus, the absence of this vortex downstream of the vane for the ice-contoured endwall has a greater effect on heat transfer at the design Reynolds number than at the experimental one. Hence, the heat transfer reduction compared to the baseline is higher at the design Reynolds number.

Although this study focuses on heat transfer, also total pressure loss should be considered when evaluating the performance of the contoured endwalls. Total pressure losses are very small at the experimental Reynolds numbers and hence a comparison of total pressure is more reasonable at the design Reynolds number. For the latter, Tab. 6.3 shows the total pressure coefficient $C_{\mathrm{p,tot}}$ for the ice contours and its percentaged difference with respect to the flat baseline (BSL). Again, the experimental Reynolds numbers are only shown to identify the ice contours. Due to the blockage

Table 6.3: Total pressure coefficients with percentaged difference to baseline for ice-contoured endwalls with short cooling length at design Reynolds number

Θ	$Re_{C,\text{exp}} = 34{,}000$	$Re_{C,\text{exp}} = 49{,}900$	$Re_{C,\text{exp}} = 71{,}400$
6.5	0.261 (4.99%)	0.268 (7.66%)	0.259 (4.18%)
8.5	0.268 (7.50%)	0.269 (8.09%)	0.259 (4.08%)
12.2	0.282 (13.37%)	0.278 (11.65%)	0.269 (7.94%)
BSL		0.249	

effect of the ice layers in the vane passage and its impact on the vortex structure, all ice-contoured endwalls feature a higher total pressure coefficient, that is higher total pressure loss than the flat baseline. Since the thickness of the ice layer, and with it the blockage effect, rises with higher non-dimensional temperature ratio, the ice-contoured endwalls at $\Theta = 12.2$ increase the total pressure coefficient the most. At the same time, these contours also reduce heat transfer the most. Thus, the ice-contoured endwalls achieve the reduced heat transfer rates at the expense of a higher total pressure loss.

To understand the reasons for the increase in total pressure loss for the ice contours, Fig. 6.4 compares the local total pressure coefficient for the ice-contoured endwall IC_{IFM} and the baseline. For both endwalls, total pressure loss is low upstream of the vane passage and not affected by the contouring. Over the vane passage, the formation of the vortices generates high total pressure loss and hence a steep decrease

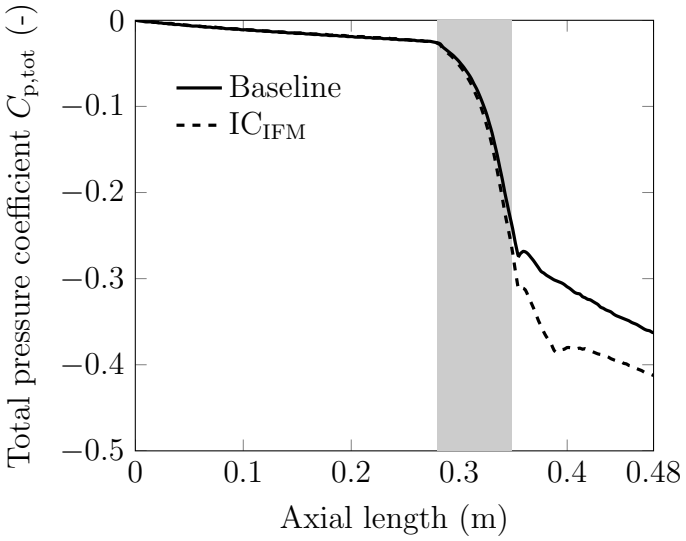

Figure 6.4: Total pressure coefficient along numerical domain for ice-contoured endwall IC_{IFM} and flat endwall baseline at design Reynolds number

Table 6.4: Averaged rates of terms contributing to entropy production for ice-contoured endwall IC_{IFM} and baseline at $Re_C = 200{,}000$, in e$-2\,\mathrm{W\,K^{-1}}$

Θ	$\dot{S}_{\mathrm{Diss,mol}}$	$\dot{S}_{\mathrm{Diss,turb}}$	$\dot{S}_{\mathrm{Heat,mol}}$	$\dot{S}_{\mathrm{Heat,turb}}$	$\dot{S}_{\mathrm{total}}$
IC_{IFM}	1.103	1.728	0.780	1.714	5.325
BSL	1.049	1.543	0.942	1.701	5.236
Difference	0.054	0.185	−0.162	0.013	0.089

of $C_{\mathrm{p,tot}}$. These losses are higher for the ice-contoured endwall due to its blockage effect. Downstream of the vane passage, total pressure losses become significantly smaller for both contours, but are still higher than in the inflow region. From the vanes' trailing edges until approximately one axial chord downstream of it ($x \approx 0.42$), $C_{\mathrm{p,tot}}$ decreases more for the ice-contoured endwall than for the baseline. As I showed in Fig. 4.10 for the experimental Reynolds number, the contoured endwall causes a diffusion and break-up of the vortex structure in this region and hence the higher total pressure loss. Downstream of this region, total pressure loss is about the same for the ice-contoured endwall and the baseline. This is indicated by the same slope of both curves in this region.

The last paragraphs demonstrated that the ice-contoured endwalls on the one hand reduce heat transfer compared to the baseline, but on the other hand increase total pressure loss. With the help of entropy production these two parameters can be related to each other in order to comment on the thermo-hydraulic efficiency of the endwall contours. Table 6.4 shows the different entropy production rates at the design Reynolds number, exemplarily for the ice-contoured endwall IC_{IFM} and the baseline, as well as their difference. For $Re_C = 200{,}000$, the contouring further reduces entropy production due to molecular heat transfer (≈ -17%), explaining the higher *htc* reduction than for the experimental Reynolds number of $Re_C = 49{,}900$. However, dissipative effects also strongly increase at the design Reynolds number (compare also Tab. 4.3) and entropy production rates due to dissipation grow to the same order of magnitude than those due to heat transfer. For the ice-contoured endwall, dissipative entropy production is higher than for the baseline, especially caused by increased turbulence dissipation effects. $\dot{S}_{\mathrm{Diss,turb}}$ is approximately 12% higher for the contoured endwall than for the baseline. Altogether, these increased dissipation rates outbalance the reductions in entropy production due to heat transfer. Thus, total entropy production is higher for the contoured endwall than for the baseline, yielding a slight decrease in thermo-hydraulic efficiency. In contrast to this, however, heat transfer at the design Reynolds number is significantly reduced for the ice-contoured endwall.

Table 6.5: Percentaged difference in average *htc* with respect to baseline for endwall segments of optimized endwall OC_{IFM} at experimental (Re_C = 49,900) and design Reynolds number (Re_C = 200,000)

Re_C	Inlet	Transition inlet	Vane passage	Transition outlet	Outlet	Total
49,900	−0.51%	1.17%	1.68%	−21.74%	−24.42%	−8.49%
200,000	−0.65%	1.71%	1.74%	−25.64%	−19.87%	−8.85%

6.2.2 Optimized Endwall Contour OC_{IFM}

For the experimental Reynolds number of Re_C = 49,900, I showed in Sec. 4.3.1 that a subsequent numerical optimization based on the ice contours generates endwall contours with further decreased heat transfer. From the ice contour at Re_C = 49,900 and Θ = 12.2, the optimization yielded the endwall geometry OC_{IFM}, which reduces the average *htc* by 8.49% compared to the baseline. This endwall contour was also numerically simulated at Re_C = 200,000 to assess its performance at the design Reynolds number. Table 6.5 shows the results as average *htc* for the different endwall segments of this contour. Results for the experimental Reynolds number are also included for reference. For both Reynolds numbers, the optimized endwall contour reduces heat transfer in the regions downstream of the vane passage. However, the regions where the *htc* reductions occur shift. Compared to the experimental Reynolds number, *htc* reduction becomes higher in the *Transition outlet* region for the design Reynolds number, but lower in the *Outlet* endwall segment. On the whole, this optimized endwall contour decreases global average heat transfer at the design Reynolds number to approximately the same amount as for the experimental Reynolds number, i. e. slightly more than 8%. This is also the highest reduction in average endwall *htc* observed for the experimental Reynolds numbers. Hence, one can conclude that for both the experimental Reynolds numbers and the design Reynolds number, an *htc* reduction of about 8% constitutes a global minimum in endwall heat transfer for the optimization of the considered vane profile with the approach used in this work.

Considering total pressure loss, this optimized endwall contour has a $C_{p,tot}$ of 0.27% and hence lower total pressure loss than the ice-contoured endwall that formed the basis for the optimization. Compared to the flat endwall at Re_C = 200,000, this corresponds to an increase in $C_{p,tot}$ of 7.39%.

6.3 Optimization from Baseline

As Section 5.2 showed, heat transfer in the vane passage can effectively be reduced by using numerical optimization with a parametrization based on the flat endwall. For a Reynolds number of Re_C = 49,900, the endwall contour OC_{BSL} created in this vein reduced average heat transfer in the vane passage by 7.07%, while having an

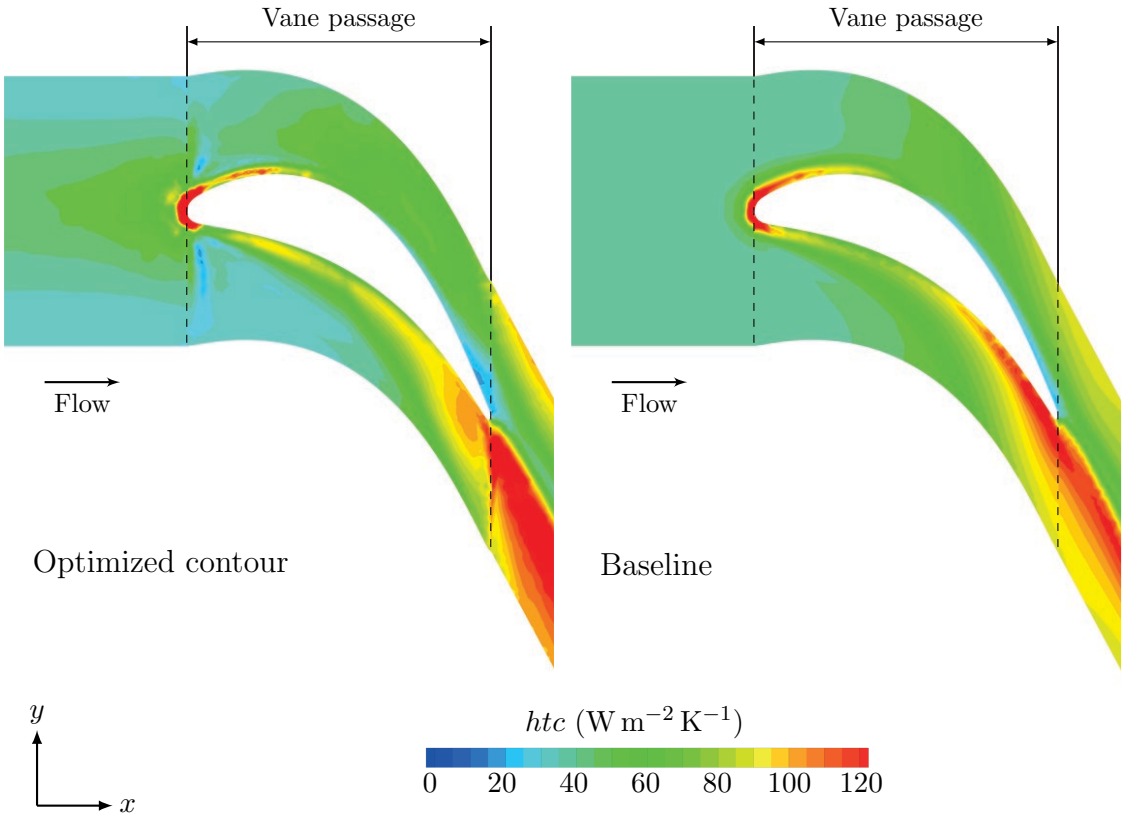

Figure 6.5: Vane passage *htc* distribution for optimized endwall contour OC_{BSL} (left) and flat baseline (right) at design Reynolds number

average *htc* reduction of 1.20% for the entire endwall. This contour was also analyzed numerically for the design Reynolds number. For this Reynolds number, the contour yields a similar *htc* reduction in the vane passage of 6.84%, however, average heat transfer for the entire endwall increases by 0.75% compared to the baseline.

Figure 6.5 shows the local heat transfer distribution for this endwall and the baseline at the design Reynolds number. In the vane passage heat transfer is locally reduced in the front suction side region and to a large extent in the pressure side region, yielding the average reduction of 6.84%. Note that especially at the rear pressure side, heat transfer is significantly reduced compared to the baseline. However, downstream of the vane passage, the increased heat transfer rates for this endwall contour are intensified at the higher Reynolds number and hence heat transfer in the outflow region is increased compared to the baseline. This results in the small overall *htc* increase for the complete endwall and underlines that this endwall contour was specifically optimized to reduce vane passage heat transfer. For completeness, App. A.10.2 holds the average heat transfer rates for all endwall segments of the contour OC_{BSL} at the design Reynolds number.

This optimized contour has a total pressure coefficient of $C_{p,tot} = 0.257$ and hence an increase in total pressure loss of only 3.21% compared to the flat endwall baseline.

This is the lowest total pressure loss of all contoured endwalls and results from the fact that the parametrization based on the flat endwall yields a smaller blockage effect.

The endwall contour $OC_{BSL,2}$, optimized from the flat endwall baseline with enlarged optimization space, yields, at the design Reynolds number, a reduction of 10.67% for vane passage heat transfer and reduces global endwall heat transfer by 5.68%. However, due to its increased extent in spanwise direction, it has a total pressure coefficient of $C_{p,tot} = 0.278$ and hence causes an increase of 11.81% compared to the baseline. For quick reference, Tab. A.10 in App. A.12 finally summarizes the features of all endwall contours created in this study.

7 Conclusion and Outlook

Over the past decades, the aim for higher gas turbine efficiency led to a constant increase in the turbine inlet temperature. This causes a high thermal loading on the turbine stages. Due to the flat turbine inlet temperature profiles and the secondary flows in their vicinity, the vane endwalls are especially affected by these thermal loads. The present work focused on creating contoured vane endwalls that alter the near-endwall flow in a favorable way and hence reduce heat transfer rates on the endwall. This diminishes the thermal loading of the endwall, which reduces cooling needs and enhances component lifetime.

In the present study, the Ice Formation Method (IFM), numerical optimization, and a combination of both were used to create novel endwall contours which reduce heat transfer. The IFM thereby is a natural optimization approach that generates restriction-free endwall contours in terms of ice layers, which globally optimize the flow system. The numerical optimization used a genetic algorithm in combination with CFD simulations to create optimized endwall contours, allowing to specifically select the region of optimization and the desired goal function. All endwall contours created in this study were examined using numerical simulations and the impact of the endwall contours' geometry on flow and heat transfer was carefully analyzed. Results were compared to the flat endwall, which served as baseline for this study.

The used numerical setup was validated for a vane profile at similar Reynolds numbers. To validate the endwall heat transfer obtained from the CFD simulations, it was compared against experimental data of Haase [26]. This showed that the numerical model used in this work correctly predicts all relevant vane/endwall flow features and yields a reasonable heat transfer distribution. For the flat endwall it was seen that the heat transfer distribution on the endwall strongly depends on the vortex system that develops in the vane passage. The strongest vortex of this system, the passage vortex, still exists far downstream of the vane passage and influences heat transfer until the outlet of the numerical domain.

To create the nine ice-contoured endwalls of this study, experimental ice layers from the study of Haase [26] were employed. These were created in an experimental water flow test facility using three Reynolds numbers (Re_C = 34,000, 49,900, and 71,400)

and three temperature ratios (Θ_{exp} = 6.5, 8.5, and 12.2). During the experiments, these ice layers grew on a cooled copper inlay that ranged from one chord length upstream of the vane to one cord length downstream of it, which is referred to as *short cooling length* in this work. After each experiment, the ice layers were digitized, utilized as endwall contours in the vane passage and simulated at the same Reynolds numbers, however, using air as gas turbine medium. All ice-contoured endwalls showed a reduction in global endwall heat transfer up to 5.20%. The regions downstream of the vane passage thereby contributed the most to the heat transfer reduction since the contouring overturns the passage vortex downstream of the vane passage and hence diminishes its impact on heat transfer in these regions. A convex elevation on the endwall at the rear suction side of the vane profile proved to promote the overturning of the passage vortex. Results further showed that the elevated endwall in the vane passage, caused by the ice growth in the experiment, influences endwall heat transfer in two ways. First, it increases vane passage heat transfer since it increases flow velocity in the vane passage due to the reduced cross-section. Secondly, it also contributes to the overturning of the passage vortex.

Examining entropy production rates validated the assumption that the IFM creates optimized endwall contours with reduced total entropy production rates. All nine ice-contoured endwalls showed a significant decrease in entropy production due to molecular heat transfer. This reduction mostly occurs in the regions downstream of the vane passage, where the contouring weakens the vortex system and also causes the reductions in heat transfer.

The three ice-contoured endwalls at Re_C = 49,900 were used as starting geometries for numerical optimizations to further reduce global endwall heat transfer. For the optimizations, the ice contours were parametrized with Bézier curves in the vane passage and at the rear suction side and optimized with the genetic algorithm NSGA-II. After the optimization, all three endwall contours yielded similar reductions in global heat transfer, the highest reduction being 8.50% for the contour at Θ = 12.2. The optimized endwall contours showed a shift of the convex elevation at the rear suction side further into the vane passage. This intensified the overturning of the passage vortex and increased heat transfer reductions downstream of the vane passage, leading to the higher reduction in global endwall heat transfer. Hence, the optimization amplified the features that lead to the reduced heat transfer of the ice-contoured endwalls.

Since in a real engine application, endwall heat transfer is more important in the vane passage than on the entire endwall, the ice-contoured endwall at Re_C = 49,900 and Θ = 8.5 was also used as starting geometry for a numerical optimization with the goal to reduce vane passage heat transfer. This optimization, however, yielded only a small reduction in vane passage heat transfer. Since the parametrization was based on the ice-contoured endwall, the elevation of the contour in the vane passage was still present in the optimized contour and prevented a higher reduction.

To remedy the elevated endwall in the vane passage, a longer ice layer from the study of Haase [26] was used as endwall contour. For this ice contour, a longer cooled copper inlay (termed *long cooling length*) was used in the experiment which

ranged from three axial chords upstream of the vane passage to three axial chords downstream of it. Upstream of the vane passage, the ice layer created with this longer cooled copper inlay grew to a constant height in pitchwise direction. The ice layer was translated down by this height to be at the level of the lower endwall and to avoid the elevation of the endwall in the vane passage. Further, this ice layer did not only describe the contouring of the endwall in the vane passage, but also up- and downstream of it, especially including the cavity that forms around the leading edge in the experiment. Results of the numerical simulations of this endwall contour however showed that the cavity amplifies the horseshoe vortex and hence increases heat transfer in the vane passage. This leads to the conclusion that, with the experimental setup of the IFM as used in this work, it is not possible to create endwall contours with reduced heat transfer in the vane passage. A reason for this is the fact that the growth of the ice layer significantly changes the state of the boundary layer upstream of the vane passage, which has great impact on the forming vortex system and hence heat transfer in the passage.

Finally, a numerical optimization based on the flat endwall was performed to create an endwall contour with reduced vane passage heat transfer. For this optimization, the vane passage was parametrized with Bézier curves and the optimization space ranged from 5 mm below the flat endwall to 5 mm above it. This allowed for an endwall contour with local heights being both above and below the flat endwall. The resulting endwall contour reduced average heat transfer in the vane passage by 7.07% compared to the baseline. An analysis of the flow and thermal fields showed that the contour holds a convex elevation at the vane leading edge, which weakens the horseshoe vortex and hence the vortex system in the vane passage. This leads to the reduced vane passage heat transfer. However, the elevation also increases maximum heat transfer in front of the leading edge. This is undesirable and, for using the design in an engine application, would require further local optimization to reduce heat transfer at this position. An increase of the optimization space's height showed an even higher reduction in vane passage heat transfer of 13.22%.

Since all endwall contours were created at the same Reynolds numbers as in the experiments of the IFM, the contours were at last verified for the vane profile's design Reynolds number of $Re_C = 200{,}000$. For this Reynolds number, the ice-contoured endwalls featured higher heat transfer reductions than for the experimental Reynolds numbers, indicating their wide range of validity. For the endwall contours from the numerical optimizations, heat transfer reductions were slightly lower than those at the experimental Reynolds numbers. This reveals that these contours were specifically optimized for the Reynolds numbers used in the optimization process. Considering the total pressure coefficient showed that all contoured endwalls achieve their heat transfer reductions at the expense of an increased total pressure loss.

The present study showed that the IFM can successfully be used to create vane endwall contours with reduced global heat transfer compared to a flat endwall baseline. Furthermore, if only a reduction of vane passage heat transfer is desired, this can be achieved by numerical optimizations with a parametrization based on the flat endwall. For future research, it is recommended to verify the numerically gener-

ated endwall contours with experiments that investigate these contours for air flow. Moreover, one can think about using more sophisticated turbulence models for the numerical simulations, such as Reynolds stress turbulence models. This would allow to consider the anisotropy of turbulence and render more accurate heat transfer results, however, at increased computational cost. Regarding the numerical optimizations it would be advisable to use a different averaging technique for the goal function of heat transfer in order to avoid the occurrence of local hot spots in the optimized contour. For example, root mean square (rms) averaging could be used, which rates regions of high heat transfer in an average more than those of low heat transfer. Furthermore, critical regions, such as the endwall at the vane leading edge, could be considered more explicitly in the optimization process. In this respect it would also be imaginable to employ penalty functions in the numerical optimization, which preclude endwall contours with undesired heat transfer features from the further optimization process.

Bibliography

[1] W. K. Anderson and D. L. Bonhaus. *An Implicit Upwind Algorithm for Computing Turbulent Flows on Unstructured Grids.* Computers & Fluids, **23**(1):pp. 1–21, 1994.

[2] J. D. Anderson Jr. *Computational Fluid Dynamics - The Basics with Applications.* McGraw-Hill Incorporated, 1995.

[3] ANSYS® Inc. *ANSYS FLUENT 12.1 Theory Guide*, 2009.

[4] ANSYS® Inc. *ANSYS Fluent User's Guide*, release 12.1 ed., 2010.

[5] P. E. Bézier. *Définition numérique des courbes et surfaces I.* Automatisme, **11**:pp. 625–632, 1966.

[6] P. E. Bézier. *Définition numérique des courbes et surfaces II.* Automatisme, **12**:pp. 17–21, 1967.

[7] J. A. Bilenas and L. M. Jiji. *Variational solution of axisymmetric fluid flow in tubes with surface solidification.* Journal of the Franklin Institute, **289**(4):pp. 265–279, 1970.

[8] A. Boelcs. *Flow Investigations in a Water Channel at Subsonic and Supersonic Velocities.* Escher Wyss News, 1969.

[9] J. Boussinesq. *Essai sur la theorie des eaux courantes.* Mémoires présentés par divers savants à l'Académie des Sciences XXIII, 1887.

[10] W. W. Bowley. *Unpublished Ice Formation Model of a 90 degree elbow.* Fluid Machinery Labaratory, ME Department, University of Connecticut.

[11] J. Braun and H. Beer. *Ice formation for turbulent flow in curved rectangular channels.* International Journal of Heat and Mass Transfer, **38**(8):pp. 1505–1515, 1995.

[12] G. Brennan, N. W. Harvey, M. G. Rose, N. Fomison, and M. D. Taylor. *Improving the Efficiency of the Trent 500-HP Turbine Using Nonaxisymmetric End Walls - Part 1: Turbine Design*. Journal of Turbomachinery, **125**(3):pp. 497–504, 2003.

[13] F. M. Carlson. *An investigation of the solidification of a flowing liquid on a circular cylinder in crossflow and its effects on the drag coefficient*. PhD Thesis, University of Connecticut, Storrs, CT, 1975.

[14] I. B. Celik, U. Ghia, P. J. Roache, C. J. Freitas, H. Coleman, and P. E. Raad. *Procedure for Estimation and Reporting of Uncertainty Due to Discretization in CFD Applications*. Journal of Fluids Engineering, **130**:pp. 078001–078004, 2008.

[15] CentaurSoft. *Centaur Manual*. Centaur Software, Austin, latest ed., 2013. See also URL `www.centaursoft.com`.

[16] Center for Turbulence Research. *J. C. R. Hunt and A. A. Wray and P. Moin*, Proceedings of the 1988 Summer Program. N.A.S.A., 1988. CTR-S88.

[17] K. Chida. *Blockage of Laminar Pipe Flow in a Piping System by Internal Fluid Solidification*. Heat Transfer - Japanese Research 15, 1986.

[18] P. de Casteljau. *Courbes et surfaces a pôles*. Technical report Citroen, 1963.

[19] K. Deb. *Multi-Objective Optimization using Evolutionary Algorithms*. John Wiley & Sons, LTD, New York, 2001.

[20] K. Deb and S. Agarwal. *A Niched-Penalty Approach for Constraint Handling in Genetic Algorithms*. In *Artificial Neural Nets and Genetic Algorithms - Proceedings of the International Conference in Portoro, Slovenia, 1999*, pp. 235–243. Springer Vienna, 1999.

[21] K. Deb, A. Pratap, S. Agarwal, and T. Meyarivan, editors. *A Fast and Elitist Multiobjective Genetic Algorithm: NSGA-II*, vol. 6 of *IEEE Transactions on Evolutionary Computation*. IEEE, 2002.

[22] J. H. Ferziger and M. Peric. *Computational Methods for Fluid Dynamics*. Springer Verlag Berlin Heidelberg, 2002.

[23] S. Friedrichs, H. Hodson, and W. Dawes. *Distribution of Film-Cooling Effectiveness on a Turbine Endwall Measured Using the Ammonia and Diazo Technique*. Journal of Turbomachinery, **118**(4):pp. 613–621, 1996.

[24] S. A. G. I. Mahmood. *Experimental Investigation of Secondary Flow Structure in a Blade Passage With and Without Leading Edge Fillets*. Journal of Fluids Engineering, **129**:pp. 253–262, 2007.

[25] R. R. Gilpin. *The Morphology of Ice Structure in a Pipe At or Near Transition Reynolds Numbers*. In R. W. Lyczkowski, editor, *Heat Transfer - San Diego 1979: AICHE Symp. Series*, vol. 75 of *189*, pp. 89–94. AICHE, 1979.

[26] K. Haase. *Experimental investigation of the Ice Formation Method applied to the endwall of a turbine stator vane row*. PhD Thesis, University of Stuttgart, Stuttgart, Germany, 2016.

[27] K. Haase, S. Winkler, E. Lutum, and B. Weigand. *Wärmeübergang in 3D Schaufelkanälen - Zwischenbericht über das Vorhaben 1049*. In *Heft R559*. Forschungsvereinigung Verbrennungskraftmaschinen e.V., 2012. Informationstagung Turbomaschinen, Frühjahr 2012, Bad Neuenahr.

[28] K. Haase, S. Winkler, S. O. Neumann, and B. Weigand. *Novel Turbine Endwall Contours For The Reduction Of Heat Transfer Generated Using The Ice Formation Method*. In *Proceedings of ASME IMECE 2012*. ASME, 2012. IMECE2012-87430.

[29] N. W. Harvey, M. G. Rose, M. D. Taylor, S. Shaphar, J. Hartland, and D. G. Gregory-Smith. *Nonaxisymmetric Turbine End Wall Design: Part 1 - Three-Dimensional Linear Design System*. Journal of Turbomachinery, **122**(2):pp. 278–285, 2000.

[30] W. R. Hawthorne. *Rotational flow through cascades - Part II: The circulation about the cascade*. The Quarterly Journal of Mechanics & Applied Mathematics, **8**(3):pp. 280–292, 1955.

[31] T. Hitz. *Numerical Simulation of Entropy Production in Turbulent Flow Around a Turbine Vane*. Diploma thesis, University of Stuttgart, Institute of Aerospace Thermodynamics (ITLR), 2015.

[32] in situ. *ITLR-EDM-1 Dual Scanner für Eisdickenmessung*, 2007. See also URL `www.in-situ.com`.

[33] F. P. Incropera, D. P. DeWitt, T. L. Bergmann, and A. S. Lavine. *Fundamentals of Heat and Mass Transfer*. John Wiley & Sons, 2007.

[34] J. Jeong and F. Hussain. *On the identification of a vortex*. Journal of Fluid Mechanics, **285**:pp. 69–94, 1995.

[35] P. Johnson and J. Johnston, editors. *Seventh Symposium on Turbulent Shear Flows*. Stanford University, Department of Mechanical Engineering, 1989.

[36] W. Kays, M. Crawford, and B. Weigand. *Convective Heat and Mass Transfer*. McGraw Hill, 2012.

[37] D. Knezevici, S. A. Sjolander, T. J. Praisner, E. Allen-Bradley, and E. A. Grover. *Measurements of Secondary Losses in a Turbine Cascade With the Implementation of Nonaxisymmetric Endwall Contouring.* Journal of Turbomachinery, **132**(1), 2010.

[38] F. Kock. *Bestimmung der lokalen Entropieproduktion in turbulenten Strömungen und deren Nutzung zur Bewertung konvektiver Transportprozesse.* Phd thesis, University of Hamburg-Harburg, 2003.

[39] F. Kock and H. Herwig. *Entropy production calculation for turbulent shear flows and their implementations in CFD codes.* International Journal of Heat and Fluid Flow, **26**(4):pp. 672–680, 2005.

[40] R. S. LaFleur. *A Basis for Iceformation Design.* In *Computers in engineering 1990; Proceedings of the ASME International Computers in Engineering Conference and Exposition*, vol. 2 of *A92-14526 03-61*, pp. 393–401. American Society of Mechanical Engineers, 1990.

[41] R. S. LaFleur. *Example of the Couette iceform design model: flat plate iceformation.* International Journal of Heat and Mass Transfer, **35**(10):pp. 2631–2642, 1992.

[42] R. S. LaFleur. *Second Vane Total Pressure Loss Due to Endwall Iceform Contouring.* In *Proceedings of the ASME Turbo Expo 2008: Power for Land, Sea, and Air*, vol. 6, pp. 1097–1107. ASME, 2008. GT2008-50439.

[43] R. S. LaFleur and L. S. Langston. *Ice formation design of a cylinder/hull juncture with horseshoe vortices and unsteady wake.* In R. H. Nadolink, editor, *Proceedings of the 2nd International Symposium on Performance Enhancement for Marine Applications.* Kingston, RI: The University of Rhode Island, Newport, Rhode Island, 1990.

[44] R. S. LaFleur and L. S. Langston. *Drag Reduction of a Cylinder/Endwall Junction Using the Iceformation Method.* Journal of Fluids Engineering, **115**(1):pp. 26–32, 1993.

[45] R. S. LaFleur, T. S. Whitten, and J. A. Araujo. *Second Vane Endwall Heat Transfer Reduction by Iceform Contouring.* In *Proceedings of the International Gas Turbine and Aeroengine Congress.* ASME, Indianapolis, In, 1999. 99-GT-422.

[46] L. Langston. *Secondary Flows in Axial Turbines - A Review.* Annals New York Academy of Sciences.

[47] L. Langston. *Crossflows in a Turbine Cascade Passage.* Journal of Engineering for Power, **102**(1):pp. 866–874, 1980.

[48] L. Langston, M. Nice, and R. Hooper. *Three-Dimensional Flow Within a Turbine Cascade Passage*. Journal of Engineering for Power, **99**(1):pp. 21–28, 1977.

[49] B. Launder and D. Spalding. *The numerical computation of turbulent flows*. International Journal of Heat and Mass Transfer, **3**(2):pp. 269–289, 1973.

[50] B. Laveau, R. S. Abhari, M. E. Crawford, and E. Lutum. *High Resolution Heat Transfer Measurement on Flat and Contoured Endwalls in a Linear Cascade*. Journal of Turbomachinery, **135**(4), 2013.

[51] A. T. Lethander, K. A. Thole, G. Zess, and J. Wagner. *Vane-Endwall Junction Optimization to Reduce Turbine Vane Passage Adiabatic Wall Temperatures*. Journal of Propulsion and Power, **20**(6):pp. 1105–1115, 2004.

[52] P. Ligrani and J. S. Jin. *Second law analysis of aerodynamic losses: Results for a cambered vane with and without film cooling*. Journal of Turbomachinery, **135**(4), 2013.

[53] S. P. Lynch, K. A. Thole, A. Kohli, and C. Lehane. *Computational Predictions of Heat Transfer and Film-Cooling for a Turbine Blade With Nonaxisymmetric Endwall Contouring*. Journal of Turbomachinery, **133**(4), 2011.

[54] R. Lyulinetskyy. *Analytical study of entropy production rates for a natural optimization method (ice formation method) for the case of a channel flow*. Study thesis, University of Stuttgart, Institute of Space Systems, Stuttgart, Germany, 2013.

[55] S. Mank, L. Duerrwaechter, M. Hilfer, R. Williams, S. Hogg, and G. Ingram. *Secondary Flows and Fillet Radii in a Linear Turbine Cascade*. In *Proceedings of ASME Turbo Expo 2014*. ASME, 2014. GT2014-25458.

[56] P. Marchal and C. Sieverding. *Secondary Flows Within Turbomachinery Bladings*. Secondary Flows in Turbomachines, 1977. AGARD CP No. 214 Paper No. 11.

[57] MathWorks. *Matlab Manual*, latest ed., 2013.

[58] F. R. Menter. *Two-Equation Eddy-Viscosity Turbulence Models for Engineering Applications*. AIAA Journal, **32**(8):pp. 1598–1605, 1994.

[59] M. G. Nagel and R.-D. Baier. *Experimentally Verified Numerical Optimization of a Three-Dimensional Parametrized Turbine Vane With Nonaxisymmetric End Walls*. Journal of Turbomachinery, **127**(2):pp. 380–387, 2005.

[60] S. O. Neumann and H. Beer. *The formation of ice layers in a straight walled, rectangular diffuser*. In *International Symposium on Thermal Engineering and Sciences for Cold Regions*, pp. 324–330. 1996.

[61] M. N. Oezisik and J. Mulligan. *Transient Freezing of Liquids in Forced Flow Inside Circular Tubes.* Journal of Heat Transfer, **91**(3):pp. 385–390, 1969.

[62] K. Panchal, S. Abraham, S. V. Ekkad, W. Ng, A. S. Lohaus, and A. Malandra. *Effect of Endwall Contouring on a Transonic Turbine Blade Passage: Part 2 - Heat Transfer Performance.* In *Proceedings of ASME Turbo Expo 2012*, vol. 4, pp. 151–162. ASME, 2012. GT2012-68405.

[63] S. Patankar and D. Spalding. *A calculation procedure for heat, mass and momentum transfer in three-dimensional parabolic flows.* International Journal of Heat and Mass Transfer, **15**(10):pp. 1787–1806, 1972.

[64] S. B. Pope. *Turbulent Flows.* Cambridge University Press, 2000.

[65] T. J. Praisner, E. Allen-Bradley, E. A. Grover, D. C. Knezevici, and S. A. Sjolander. *Application of non-axisymmetric endwall contouring to conventional and high-lift turbine airfoils.* Journal of Turbomachinery, **135**(6), 2013.

[66] O. Reynolds. *On the dynamical theory of incompressible viscous fluids and the determination of the criterion.* Philosophical Transactions of the Royal Society of London, **186**:pp. 123–164, 1895.

[67] P. J. Roache. *Perspective: A method for uniform reporting of grid refinement studies.* Journal of Fluids Engineering, **116**(3):pp. 405–413, 1994.

[68] A. K. Saha and S. Acharya. *Computations of Turbulent Flow and Heat Transfer Through a Three-Dimensional Nonaxisymmetric Blade Passage.* Journal of Turbomachinery, **130**(3):pp. 031008–1–031008–10, 2008.

[69] R. Schwarze. *CFD Modellierung - Grundlagen und Anwendungen bei Strömungsprozessen.* Springer Verlag Berlin Heidelberg, 2013.

[70] C. Sieverding. *Recent Progress in the Understanding of Basic Aspects of Secondary Flows in Turbine Blade Passages.* Journal of Turbomachinery, **107**(1):pp. 248–257, 1985.

[71] C. Sieverding. *Secondary flows in straight and annular turbine cascades.* Thermodynamics & Fluids of Turbomachinery, NATO, Vol. II, pp 621-624, 1985.

[72] C. Sieverding. *Understanding secondary flows in turbine bladings.* Review of State-of-the-Art & Impact on Blade Design, Gas Turbine Engineering Lecture Series, 2004. Siemens, Orlando, Florida.

[73] H. Steinbrueck, S. Zehner, B. Weigand, S. Neumann, and J. Gier. *Optimization of the web geometry of a 180-degree bend using an experimentally determined ice layer as starting contour: Part 2 - Numerical simulation and optimization.* In *Proceedings of the 12th International Symposium on Transport Phenomena and Dynamics of Rotating Machinery.* 2008. ISROMAC12-2008-20053.

[74] B. Weigand and H. Beer. *Transient freezing of liquids in forced laminar flow inside a parallel plate channel.* Wärme - und Stoffübertragung, **27**(1):pp. 77–84, 1992.

[75] B. Weigand and H. Beer. *Freezing in turbulent flow inside tubes and channels.* Wärme - und Stoffübertragung, **28**(1):pp. 57–64, 1993.

[76] Wieghardt. *Data Set used at the 1968 Stanford University AFOSR Conference*, 1968.

[77] D. Wilcox. *Re-assessment of the scale-determining equation for advanced turbulence models.* AIAA Journal, **26**(11):pp. 1299–1310, 1988.

[78] S. Winkler, K. Haase, J. Brucker, and B. Weigand. *Turbine Endwall Contouring for the Reduction of Endwall Heat Transfer Using the Ice Formation Method Along with Computational Fluid Dynamics.* In *Proceedings of ASME Turbo Expo 2014*. ASME, 2014. GT2014-25655.

[79] S. Winkler, K. Haase, E. Lutum, and B. Weigand. *Wärmeübergang in 3D Schaufelkanälen - Abschlussbericht über das Vorhaben 1049.* In *Heft R565*. Forschungsvereinigung Verbrennungskraftmaschinen e.V., 2013. Informationstagung Turbomaschinen, Herbst 2013, Bad Neuenahr.

[80] S. Winkler, K. Haase, E. Lutum, and B. Weigand. *Wärmeübergang in 3D Schaufelkanälen II - Abschlussbericht über das Vorhaben 1135.* In *Heft R573*. Forschungsvereinigung Verbrennungskraftmaschinen e.V., 2015. Informationstagung Turbomaschinen, Herbst 2015, Würzburg.

[81] S. Winkler, K. Haase, R. Lyulinetskyy, S. O. Neumann, and B. Weigand. *On the optimization of 3D-flow and heat transfer by using the Ice Formation Method: Vane endwall heat transfer.* International Journal of Heat and Mass Transfer, **88**:p. 957964, 2015.

[82] S. Zehner, H. Steinbrueck, B. Weigand, and S. O. Neumann. *The Ice Formation Method: A Natural Approach to Optimise Turbomachinery Components.* International Journal of Design & Nature, **3**(4):p. 259272, 2009.

[83] S. Zehner, H. Steinbrueck, B. Weigand, S. O. Neumann, and J. Gier. *Optimization of the web geometry of a 180-degree bend using an experimentally determined ice layer as starting contour: Part 1 - Experimental results.* In *Proceedings of the 12th International Symposium on Transport Phenomena and Dynamics of Rotating Machinery*. 2008. ISROMAC12-2008-20049.

[84] G. A. Zess and K. A. Thole. *Computational Design and Experimental Evaluation of Using a Leading Edge Fillet on a Gas Turbine Vane.* Journal of Turbomachinery, **124**(2):pp. 167–175, 2002.

A

Appendix

Contents:

Operators of genetic algorithm - Definition and data basis for GCI study - Experimental test section with enlarged copper inlay - Derivation of non-dimensional temperature ratio used in experiment - Definition of Sutherland's law - Geometries and endwall heat transfer for ice-contoured endwalls with short cooling length - Entropy production rates for ice-contoured endwalls with short cooling length - Bézier curves and average heat transfer rates for endwall contours from numerical optimization - Overview of endwall contours created in this study

A.1 NSGA-II Operators

A.1.1 Binary Tournament Selection

The figure below shows the binary tournament selection operator acting on a population of six individuals. Each individual participates in exactly two tournaments with different opponents. In total, six tournaments are performed and the resulting mating pool holds six individuals, as does the population itself. Since the optimization is designed to minimize the goal function, in each tournament, the individual with the higher fitness (lowest goal function value) wins and is copied into the mating pool. For the example below, the fitness values of the individuals are ordered as $f_1 < f_2 < f_3 < f_4 < f_5 < f_6$. Note that the fittest individual with the highest fitness (f_6) has two copies in the mating pool, whereas the least fit individual with the lowest fitness (f_1) is removed from the population.

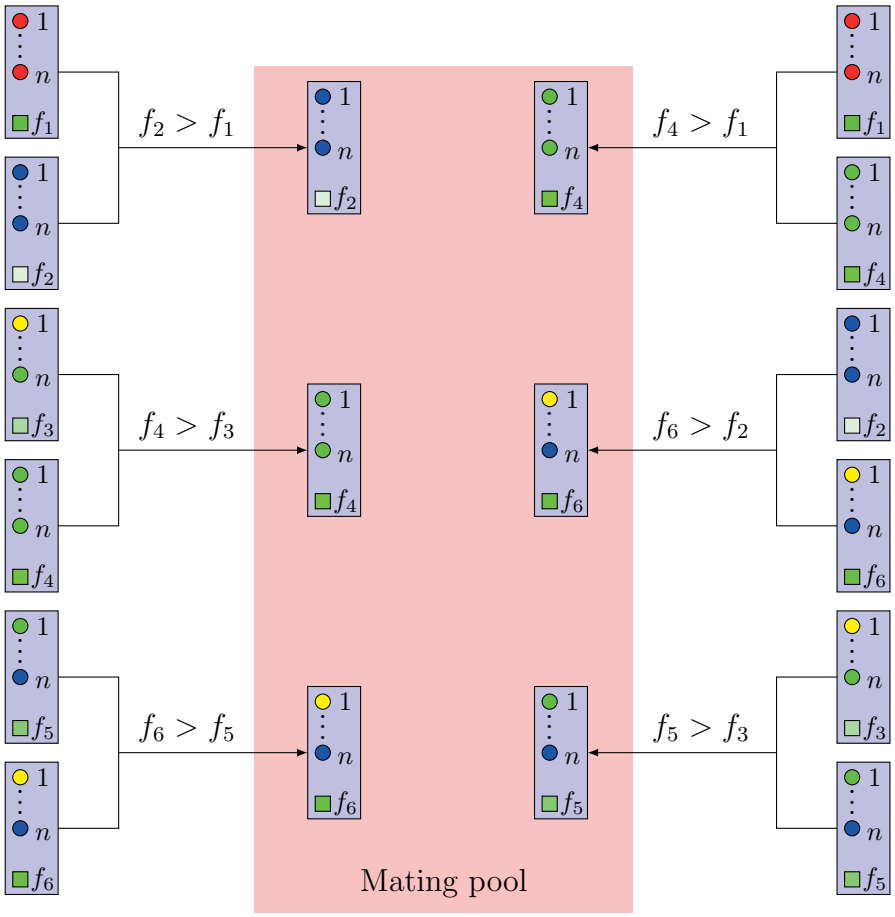

Figure A.1: Binary tournament selection for a population of six individuals

A.1.2 Simulated Binary Crossover (SBX) Operator

This operator performs a crossover between two parent individuals of the mating pool to create two offspring individuals. By doing so, each gene $g_i^{(Q,1)}$ and $g_i^{(Q,2)}$ of the two offspring individuals is created by combining the genes $g_i^{(P,1)}$ and $g_i^{(P,2)}$ of the two parent individuals as [20]

$$g_i^{(Q,1)} = \frac{1}{2}\left(g_i^{(P,1)} + g_i^{(P,2)}\right) - \frac{1}{2}\beta_i^Q\left(g_i^{(P,2)} - g_i^{(P,1)}\right) \tag{A.1}$$

$$g_i^{(Q,2)} = \frac{1}{2}\left(g_i^{(P,1)} + g_i^{(P,2)}\right) + \frac{1}{2}\beta_i^Q\left(g_i^{(P,2)} - g_i^{(P,1)}\right), \tag{A.2}$$

with β_i^Q being a weighting factor which characterizes the distance of the offspring genes to the parent genes.

The factor β_i^Q is determined from a probability density function, defined as

$$\mathcal{P}(\beta_i) = \begin{cases} \frac{1}{\alpha_i}(\eta_C+1)\beta_i^{\eta_C} & \text{if } \beta_i \leq 1 \\ \frac{1}{\alpha_i}(\eta_C+1)\frac{1}{\beta_i^{\eta_C+2}} & \text{if } \beta_i > 1\,. \end{cases} \tag{A.3}$$

In the equation above, β_i is a metric that relates the two parent genes to their variable bounds, and α a further metric derived from it. These variables take the forms

$$\beta_i = \begin{cases} 1 + 2\frac{g_i^{(U)} - g_i^{(P,2)}}{g_i^{(P,2)} - g_i^{(P,1)}} & \text{if } g_i^{(P,1)} - g_i^{(L)} > g_i^{(U)} - g_i^{(P,2)} \\ 1 + 2\frac{g_i^{(P,1)} - g_i^{(L)}}{g_i^{(P,2)} - g_i^{(P,1)}} & \text{if } g_i^{(P,1)} - g_i^{(L)} < g_i^{(U)} - g_i^{(P,2)}\,, \end{cases} \tag{A.4}$$

where the variables $g_i^{(L)}$ and $g_i^{(U)}$ define the lower and upper bounds of g_i, i.e. $g_i^{(L)} < g_i < g_i^{(U)}$, and

$$\alpha_i = 2 - \frac{1}{\beta_i^{\eta_C+1}}\,. \tag{A.5}$$

In the definition of the probability function (Eq. A.3), the crossover distribution index η_C is a non-negative real number, which controls the probability that the offspring genes lie in the vicinity of the parent genes. The higher η_C is, the more likely it is that the offspring genes take similar values than the parent genes, since the probability density function narrows around the value of the parent gene. Figure A.2 (left) illustrates this for $\alpha_i = 1$ and $\eta_C = 2$ and 5.

From the above described probability density function, β_i^Q is determined using u_i, a random variable between zero and unity, see Fig. A.2 (right). This variable relates to the area underneath the probability density function

$$\int_0^{\beta_i^Q} \mathcal{P}(\beta_i)\,\mathrm{d}\beta_i = u_i\,, \tag{A.6}$$

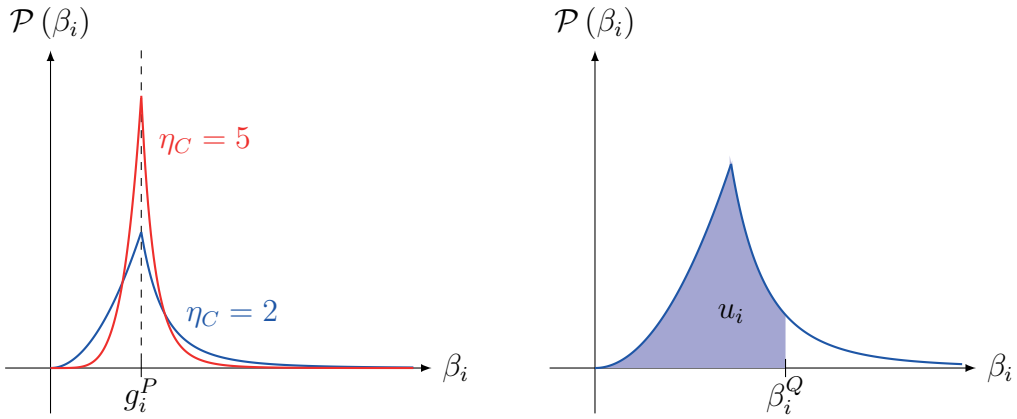

Figure A.2: Probability density function used to determine the variable β_i^Q

whereas a value of $u_i = 1$ relates to the full area under the function and values of $0 < u_i < 1$ to the appropriate fraction of the full area. Hence, the variable β_i^Q is determined from the following relationship

$$\beta_i^Q = \begin{cases} (\alpha_i u_i)^{\frac{1}{\eta_C+1}} & \text{if } \alpha_i u_i \leq 1 \\ \left(\frac{1}{2-\alpha_i u_i}\right)^{\frac{1}{\eta_C+1}} & \text{if } \alpha_i u_i > 1\,. \end{cases} \tag{A.7}$$

Note that due to the definitions of α_i and u_i, their product is bounded between zero and two, i.e. $0 < \alpha_i u_i < 2$. Hence, β_i^Q can theoretically take any value from zero to infinity. However, with increasing crossover distribution index η_C, β_i^Q approaches unity asymptotically

$$\lim_{\eta_C \to \infty} \beta_i^Q = 1\,, \tag{A.8}$$

and hence the offspring genes are the same as the parent genes

$$g_i^{(Q,1)}\left(\beta_i^Q = 1\right) = g_i^{(P,1)} \quad \text{and} \quad g_i^{(Q,2)}\left(\beta_i^Q = 1\right) = g_i^{(P,2)}\,. \tag{A.9}$$

A.1.3 Mutation Operator

The mutation operator perturbs single genes of individuals from the mating pool and hence creates mutated offspring individuals. The mutated offspring gene is thereby calculated from the parent gene according to

$$g_i^{(Q,m)} = g_i^{(P)} + \delta_i^Q \left(g_i^{(U)} - g_i^{(L)}\right)\,, \tag{A.10}$$

where the variables $g_i^{(L)}$ and $g_i^{(U)}$ define the lower and upper bounds of g_i, i.e. $g_i^{(L)} < g_i < g_i^{(U)}$. Similar to the crossover operator, the mutation factor δ_i^Q is determined by

relating the area underneath a probability density function to the random variable u_i. Hence, δ_i^Q is calculated from u_i as

$$\delta_i^Q = \begin{cases} \left[2u_i\left(1-2u_i\right)\left(1-\delta_i\right)^{\eta_m+1}\right]^{\frac{1}{\eta_m+1}} - 1 & \text{if } u_i \leq 0.5 \\ 1 - \left[2\left(1-u_i\right) + 2\left(u_i - 0.5\right)\left(1-\delta_i\right)^{\eta_m+1}\right]^{\frac{1}{\eta_m+1}} & \text{if } u_i > 0.5\,, \end{cases} \tag{A.11}$$

where δ_i is a variable that relates the parent gene to the variable bounds

$$\delta_i = \begin{cases} \frac{g_i^{(P)} - g_i^{(L)}}{g_i^{(U)} - g_i^{(L)}} & \text{if } g_i^{(P)} - g_i^{(L)} < g_i^{(U)} - g_i^{(P)} \\ \frac{g_i^{(U)} - g_i^{(P)}}{g_i^{(U)} - g_i^{(L)}} & \text{if } g_i^{(P)} - g_i^{(L)} > g_i^{(U)} - g_i^{(P)}\,, \end{cases} \tag{A.12}$$

and η_m is the distribution index for mutation, that takes any non-negative value. Note that δ_i^Q is defined between zero and unity, whereas the distance of the mutated gene to the parent gene is controlled by the distribution index η_m. The higher this index, the further δ_i^Q approaches zero

$$\lim_{\eta_m \to \infty} \delta_i^Q = 0\,. \tag{A.13}$$

Hence, with a higher distribution index, the mutated genes are more likely to lie in the vicinity of the parent genes.

A.2 Grid Convergence Index

The Grid Convergence Index (GCI) is a method to assess the discretization error due to the used spatial grid in a numerical simulation. To determine the GCI for a flow variable, Celik et al. [14] propose the following procedure.

The solution for the flow field is obtained on three different grids: a fine grid (index 1), a medium grid (index 2), and a coarse frid (index 3). Each grid has the representative grid size h

$$h = \left[\frac{1}{N}\sum_{i=1}^{N}\left(\Delta V_i\right)\right]^{1/3}, \tag{A.14}$$

where N is the total number of cells and ΔV_i the volume of the i-th cell. The grid refinement ratios between the grids are

$$r_{21} = \frac{h_2}{h_1} \quad \text{and} \quad r_{32} = \frac{h_3}{h_2}\,. \tag{A.15}$$

Let ϕ_1, ϕ_2, and ϕ_3 be the solutions for a generic flow variable on the three grids, then the differences for this flow variable on the three grids are

$$\epsilon_{21} = \phi_2 - \phi_1 \qquad \text{and} \qquad \epsilon_{32} = \phi_3 - \phi_2 \,, \tag{A.16}$$

The apparent order p of the method is calculated by iteratively solving the following set of equations

$$p = \frac{1}{ln\,(r_{21})} |ln\left(\left|\frac{\epsilon_{32}}{\epsilon_{21}}\right|\right) + q(p)| \tag{A.17}$$

$$q(p) = ln\left(\frac{r_{21}^p - s}{r_{32}^p - s}\right) \tag{A.18}$$

$$s = 1 \cdot sgn\left(\frac{\epsilon_{32}}{\epsilon_{21}}\right) . \tag{A.19}$$

Using the apparent order p, an extrapolated value for an infinite fine grid ($N \to \infty$, $h \to 0$) with vanishing discretization error can be derived for the generic flow variable ϕ as

$$\phi_{ext}^{32} = \frac{1}{r_{32}^p - 1}\left(r_{32}^p \phi_2 - \phi_3\right) . \tag{A.20}$$

This allows for calculating error estimates which describe the discretization error for the used grid. These estimates are the approximate relative error

$$e_a^{32} = \left|\frac{\phi_2 - \phi_3}{\phi_2}\right| \quad , \tag{A.21}$$

the extrapolated relative error

$$e_{ext}^{32} = \left|\frac{\phi_{ext}^{32} - \phi_2}{\phi_{ext}^{32}}\right| , \tag{A.22}$$

and the fine-grid convergence index

$$\mathrm{GCI}_{fine}^{32} = \frac{1.25 e_a^{32}}{r_{32}^p - 1} \quad . \tag{A.23}$$

Similarly, the extrapolated variable ϕ_{ext}^{21} and the fine-grid GCI, GCI_{fine}^{21}, are calculated from the equations above. Note that the three used grids for the GCI study must lie in the asymptotic range. This is true if the following difference is close to zero

$$\mathrm{GCI}_{fine}^{32}\, r_{32}^p - \mathrm{GCI}_{fine}^{21} \approx 0 \,. \tag{A.24}$$

Furthermore, note that if either one of the differences ϵ_{32} or ϵ_{21} becomes very small, the GCI does not yield a reasonable result.

Table A.1 holds the full data set for the GCI study of the flat endwall baseline from Sec. 3.2.1. For all calculated GCI values, Eq. (A.24) was in good approximation

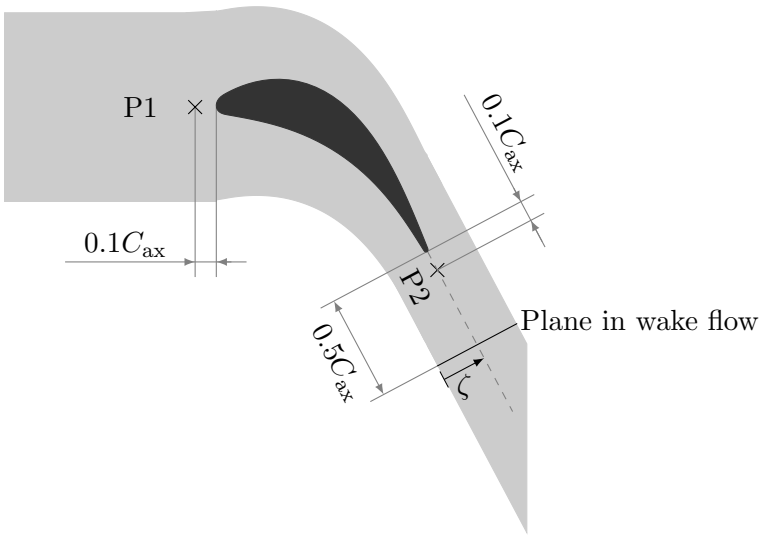

Figure A.3: GCI study for flat endwall baseline; Positions P1 and P2, and plane in vane wake flow used for calculation of GCI

true, with a maximum residual of 0.015 on its right-hand-side. Hence, the three grids of the GCI study were in the asymptotic range. Figure A.3 shows the positions P1 and P2 which I used to determine the GCI of the flow variables u_1, u_2 and T. For the GCI of $\overline{htc}$, I averaged the local htc values over the entire lower endwall of the solution domain.

Table A.1: Data set of GCI study for flat endwall baseline (P1 - Position 1 upstream of leading edge, P2 - Position 2 downstream of trailing edge, EW - Lower endwall of solution domain)

Pos.	Var.	ϕ_1	ϕ_2	ϕ_3	p	ϕ_{ext}^{32}	e_a^{32}	e_{ext}^{32}	GCI_{fine}^{32}
P1	u_1	6.35	6.33	6.34	2.57	6.31	1.41e-3	2.31e-3	2.89e-3
	u_2	0.163	0.162	0.161	0.16	0.20	7.45e-3	0.19	0.304
	T	349.98	349.98	349.98	-	-	-	-	-
P2	u_1	6.92	6.97	7.00	1.06	6.78	5.85e-3	2.77e-2	0.0336
	u_2	12.87	12.95	13.05	0.93	12.42	7.78e-e	4.28e-2	0.0514
	T	349.88	349.87	349.86	5.13	349.89	2.86e-6	1.79e-6	2.23e-6
EW	$\overline{htc}$	38.98	38.80	38.52	2.38	39.32	7.43e-3	1.31e-2	0.0167

A.3 Long Copper Inlay

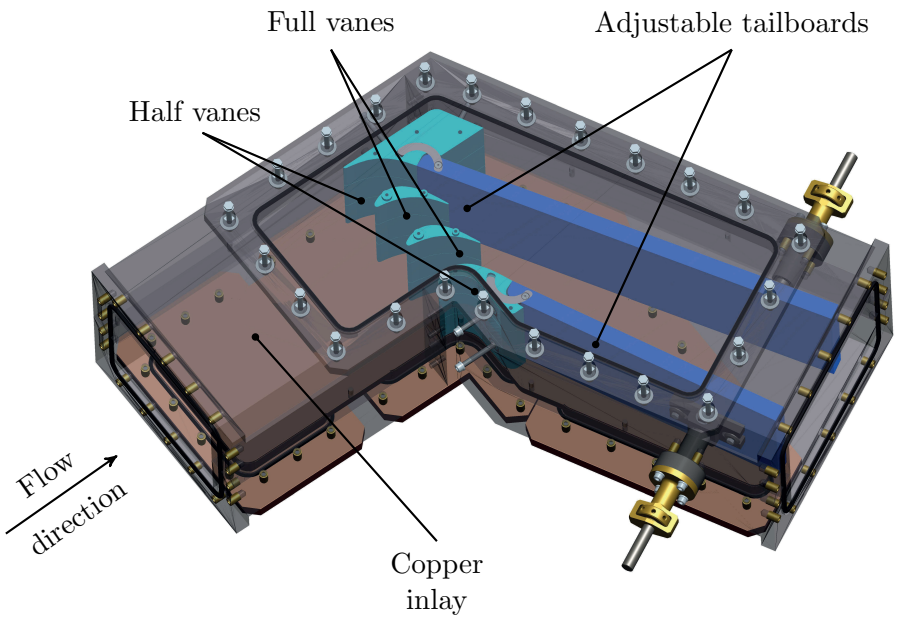

Figure A.4: Linear cascade test section with long copper inlay (see Haase [26])

A.4 Non-dimensional Temperature Ratio

For a steady-state ice layer without phase change, the heat fluxes into the ice and from the water become identical. That is, the heat flux in the ice between the cooled copper inlay and the ice/water interface

$$q''_{\text{ice}} = \frac{k_{\text{ice}}}{L_{\text{ice}}} \left(T_{\text{f}} - T_{\text{CI}}\right) \,, \tag{A.25}$$

with L_{ice} being the thickness of the ice layer, and the convective heat flux at the ice/water interface

$$q''_{\text{water}} = htc \left(T_{\infty} - T_{\text{f}}\right) \tag{A.26}$$

equal each other, i.e. $q''_{\text{ice}} = q''_{\text{water}}$. This yields the following Biot number

$$Bi = \frac{htc\, L_{\text{ice}}}{k_{\text{ice}}} = \frac{T_{\text{f}} - T_{\text{CI}}}{T_{\infty} - T_{\text{f}}} \quad , \tag{A.27}$$

with the right hand side being the dimensionless temperature ratio

$$\Theta = \frac{T_\mathrm{f} - T_\mathrm{CI}}{T_\infty - T_\mathrm{f}} \tag{A.28}$$

used to characterize the ice layers in the experiment. Note that this parameter is similar to the freezing parameter B of Oezisik and Mulligan [61]

$$B = \frac{k_\mathrm{ice}}{k_\mathrm{water}} \frac{T_\mathrm{f} - T_W}{T_0 - T_\mathrm{f}} \quad . \tag{A.29}$$

The latter additionally accounts for the thermal conductivities of the water and ice phase. In the experiments performed by Haase [26], the temperature variations in the ice and water were sufficiently small to assume these two parameters constant. Hence, the dimensionless temperature ratio Θ was enough to describe the created ice layers.

A.5 Sutherland's Law

The Australian physicist William Sutherland published in 1893 a relation between the dynamic viscosity and the absolute temperature of an ideal gas, based on kinetic theory of ideal gases and idealized intermolecular-force potential. Sutherland's law takes the form

$$\mu = \mu_\mathrm{Ref} \left(\frac{T}{T_\mathrm{Ref}} \right)^{3/2} \frac{T_\mathrm{Ref} + S}{T + S} \,, \tag{A.30}$$

with μ being the dynamic viscosity and T the static temperature. The reference values are

$$\mu_\mathrm{Ref} = 1.716\mathrm{e}{-5}\,\mathrm{kg\,m^{-1}\,s^{-1}}, \quad T_\mathrm{Ref} = 273.11\,\mathrm{K}, \quad S = 110.56\,\mathrm{K}\,. \tag{A.31}$$

A.6 Validation endwall heat transfer

Table A.2: Endwall heat transfer predicted by numerical simulation and calculated from ice layer thickness in experiment

	Averaged heat transfer coefficient ($\mathrm{W\,m^{-2}\,K^{-1}}$)		
	Experiment	Numerics	Difference (%)
Full ice layer	3,010.90	2,680.20	10.98%
Middle vane passage	3,309.40	2,991.67	9.62%

A.7 Ice Contours Short Cooling Length

A.7.1 $Re_C = 34{,}000$

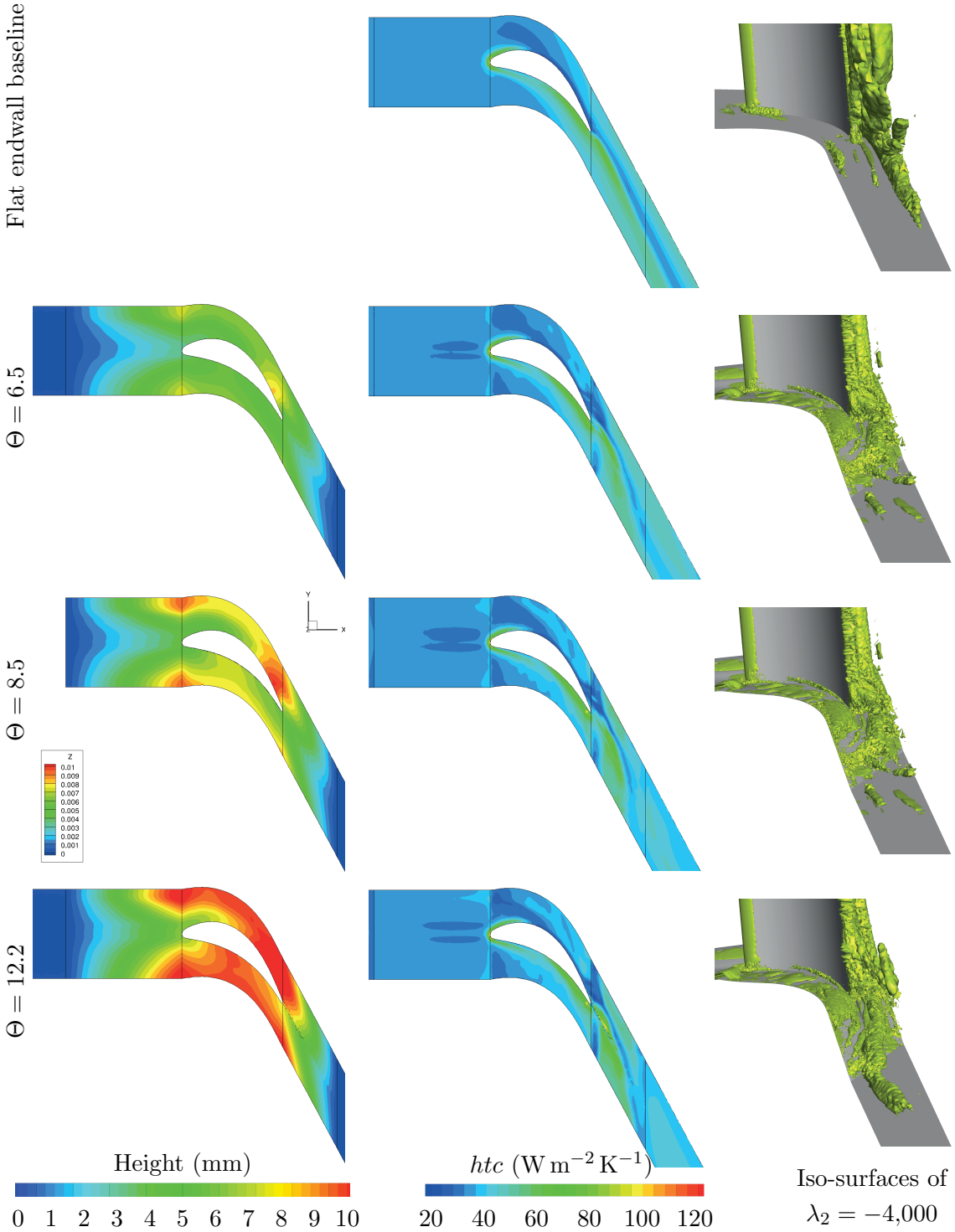

A.7.2 $Re_C = 49{,}900$

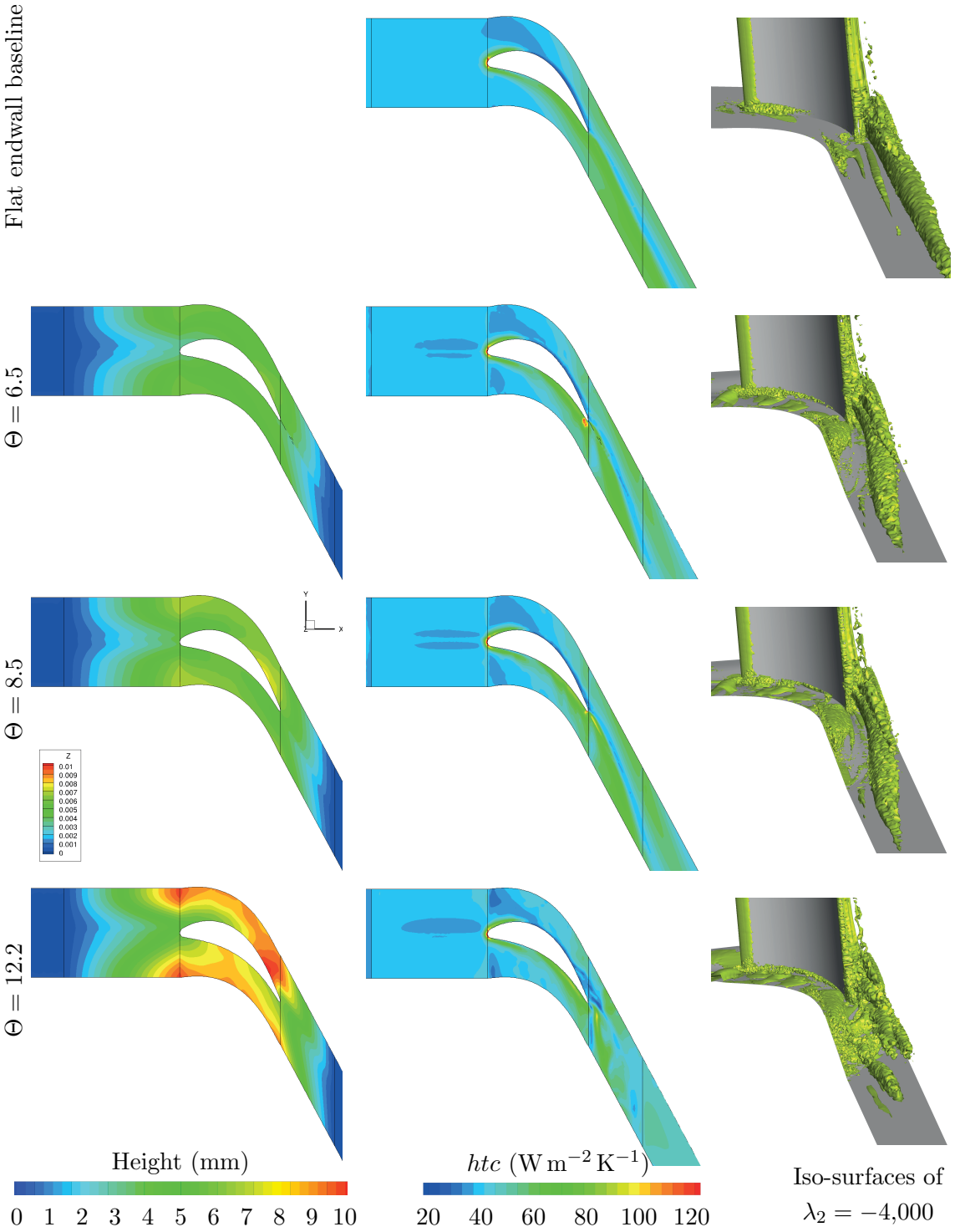

A.7.3 $Re_C = 71{,}400$

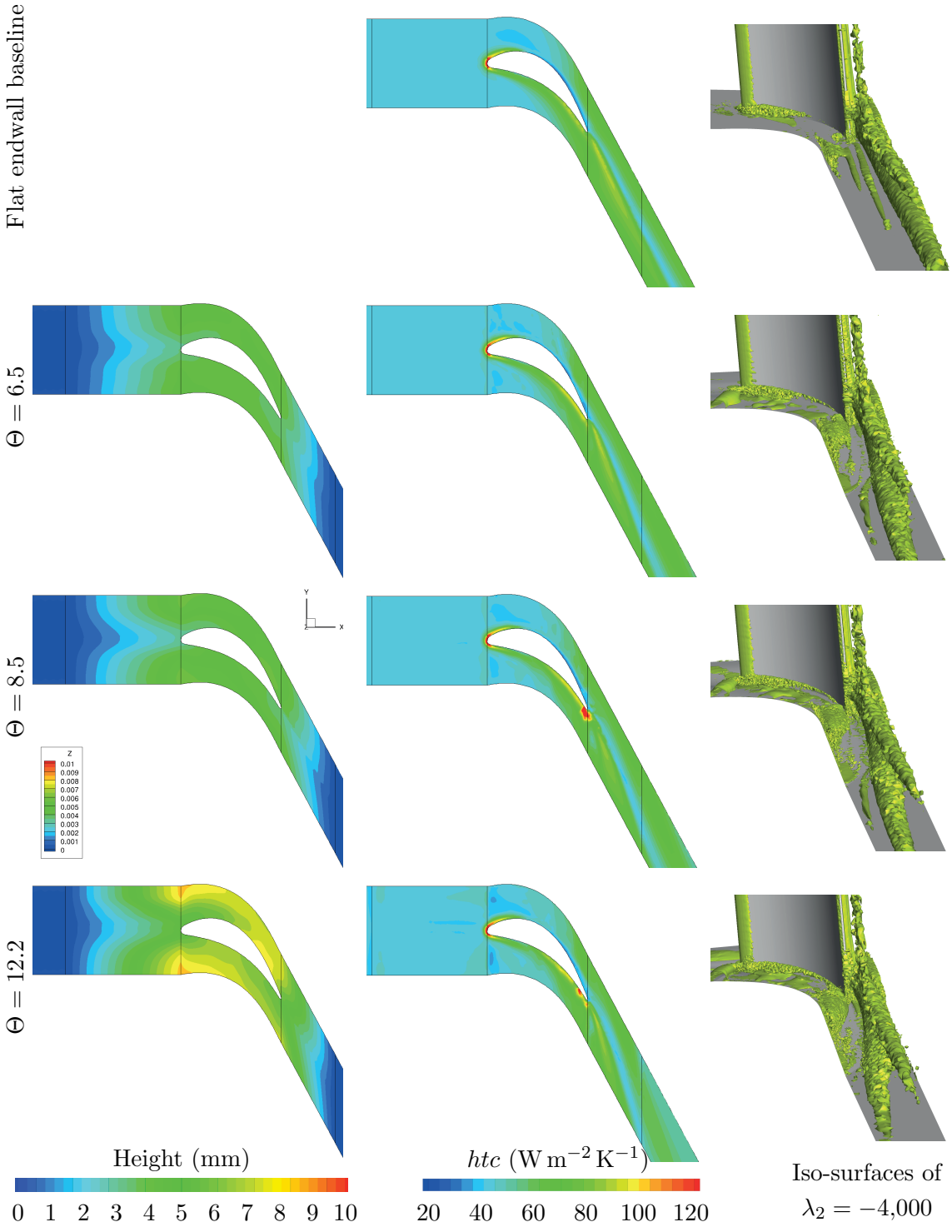

A.8 Entropy Production Rates

A.8.1 $Re_C = 34{,}000$

Table A.3: Averaged rates of terms contributing to entropy production for ice-contoured endwalls and baseline at $Re_C = 34{,}000$, in e$-4\,\mathrm{W\,K^{-1}}$; numbers in brackets indicate difference to baseline

Θ	$\dot{S}_{\mathrm{Diss,mol}}$	$\dot{S}_{\mathrm{Diss,turb}}$	$\dot{S}_{\mathrm{Heat,mol}}$	$\dot{S}_{\mathrm{Heat,turb}}$	$\dot{S}_{\mathrm{total}}$
6.5	1.211	1.530	78.914	40.000	121.656
	(0.048)	(0.164)	(−3.533)	(2.013)	(−1.307)
8.5	1.252	1.433	78.941	38.855	120.481
	(0.089)	(0.067)	(−3.506)	(0.868)	(−2.482)
12.2	1.285	1.483	78.313	38.867	119.948
	(0.122)	(0.117)	(−4.134)	(0.880)	(−3.015)
BSL	1.163	1.366	82.447	37.987	122.963

A.8.2 $Re_C = 71{,}400$

Table A.4: Averaged rates of terms contributing to entropy production for ice-contoured endwalls and baseline at $Re_C = 71{,}400$, in e$-4\,\mathrm{W\,K^{-1}}$; numbers in brackets indicate difference to baseline

Θ	$\dot{S}_{\mathrm{Diss,mol}}$	$\dot{S}_{\mathrm{Diss,turb}}$	$\dot{S}_{\mathrm{Heat,mol}}$	$\dot{S}_{\mathrm{Heat,turb}}$	$\dot{S}_{\mathrm{total}}$
6.5	7.425	8.108	123.984	85.615	225.133
	(0.243)	(0.419)	(−4.770)	(1.140)	(−2.968)
8.5	7.415	8.109	121.023	84.274	220.821
	(0.232)	(0.421)	(−7.731)	(−0.201)	(−7.280)
12.2	7.527	8.317	118.657	84.529	219.030
	(0.345)	(0.628)	(−10.097)	(0.054)	(−9.071)
BSL	7.183	7.688	128.754	84.476	228.100

A.9 Contour Optimized with Respect to Vane Passage Heat Tranfer

A.9.1 Bézier Curves after Optimization

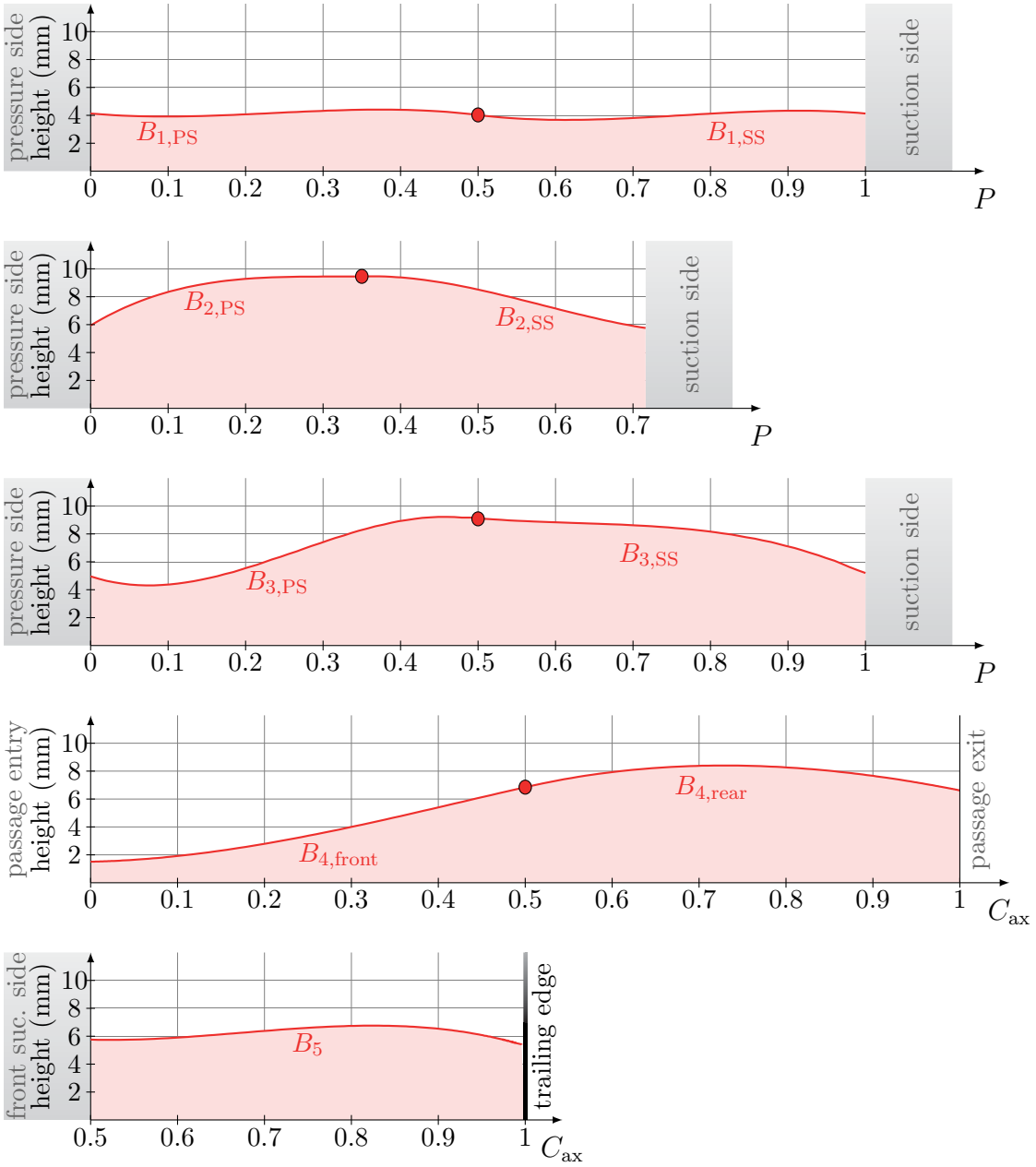

Figure A.5: Bézier splines B_1-B_5 for endwall contour optimized with respect to minimum vane passage heat transfer; optimized from ice-contoured endwall at $Re_C = 49{,}900$ and $\Theta = 8.5$

A.9.2 Average Heat Transfer Coefficients

Table A.5: Heat transfer coefficients area-averaged over endwall segments for contour optimized with respect to vane passage heat transfer, based on ice-contoured endwall with short cooling length at $Re_C = 49{,}900$ and $\Theta = 8.5$; values for baseline included for comparison

	Inlet	Transition inlet	Vane passage	Transition outlet	Outlet	Total
Optimized	27.49	21.40	28.98	47.38	36.92	30.17
BSL	27.66	21.38	29.76	43.50	36.09	29.80
Difference	−0.61%	0.10%	−2.62%	8.91%	2.28%	1.24%

A.10 Optimized Endwall Contour OC_{BSL}

A.10.1 Bézier Curves after Optimization

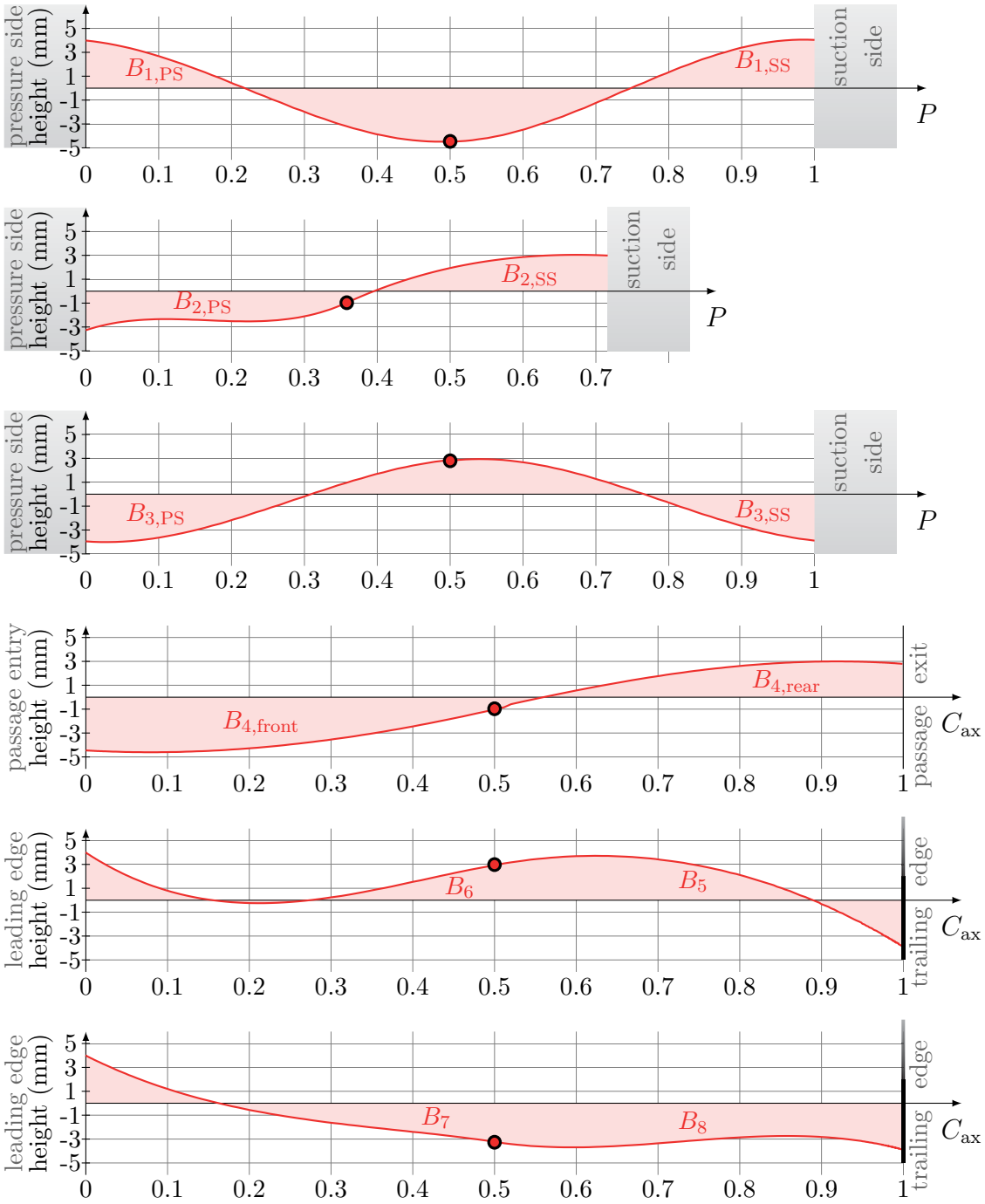

Figure A.6: Bézier splines B_1-B_8 for optimized contour OC_{BSL} at $Re_C = 49{,}900$

A.10.2 Average Heat Transfer Coefficients

Table A.6: Heat transfer coefficients area-averaged over endwall segments for optimized contour OC_{BSL} at Re_C = 49,900; values for baseline included for comparison

	Inlet	Transition inlet	Vane passage	Transition outlet	Outlet	Total
OC_{BSL}	27.66	21.99	27.65	43.90	34.76	29.45
BSL	27.66	21.38	29.76	43.50	36.09	29.80
Difference	0.00%	2.85%	−7.07%	0.92%	−3.69%	−1.20%

Table A.7: Heat transfer coefficients area-averaged over endwall segments for optimized contour OC_{BSL} at design Reynolds number Re_C = 200,000; values for baseline included for comparison

	Inlet	Transition inlet	Vane passage	Transition outlet	Outlet	Total
OC_{BSL}	36.45	38.83	54.45	88.68	74.02	50.87
BSL	36.45	37.36	58.48	85.30	72.99	50.49
Difference	0.0%	3.94%	−6.84%	3.96%	1.41%	0.75%

A.11 Optimized Endwall Contour $OC_{BSL,2}$

A.11.1 Bézier Curves after Optimization

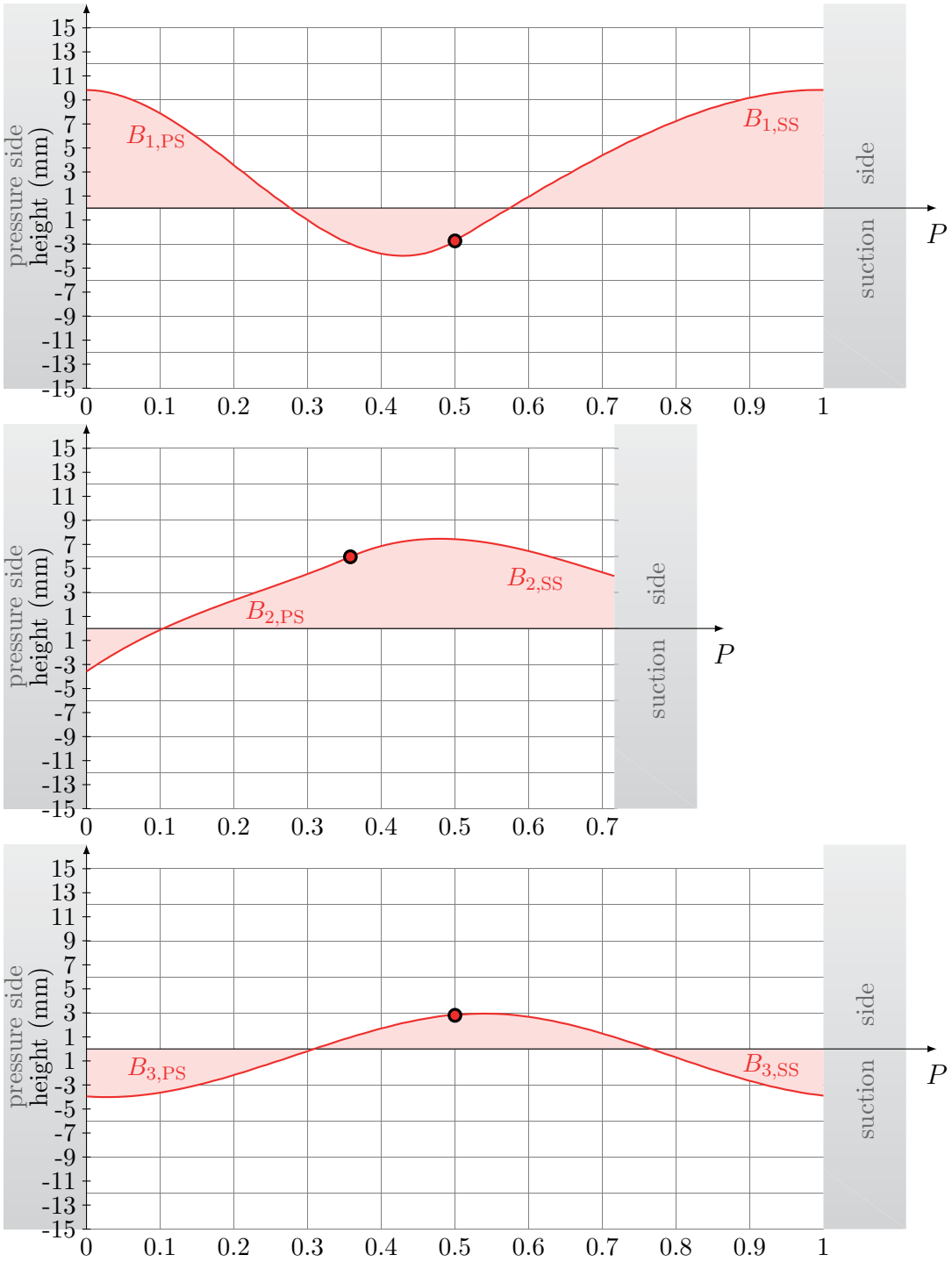

Figure A.7: Bézier splines B_1-B_3 for optimized contour $OC_{BSL,2}$ at $Re_C = 49{,}900$

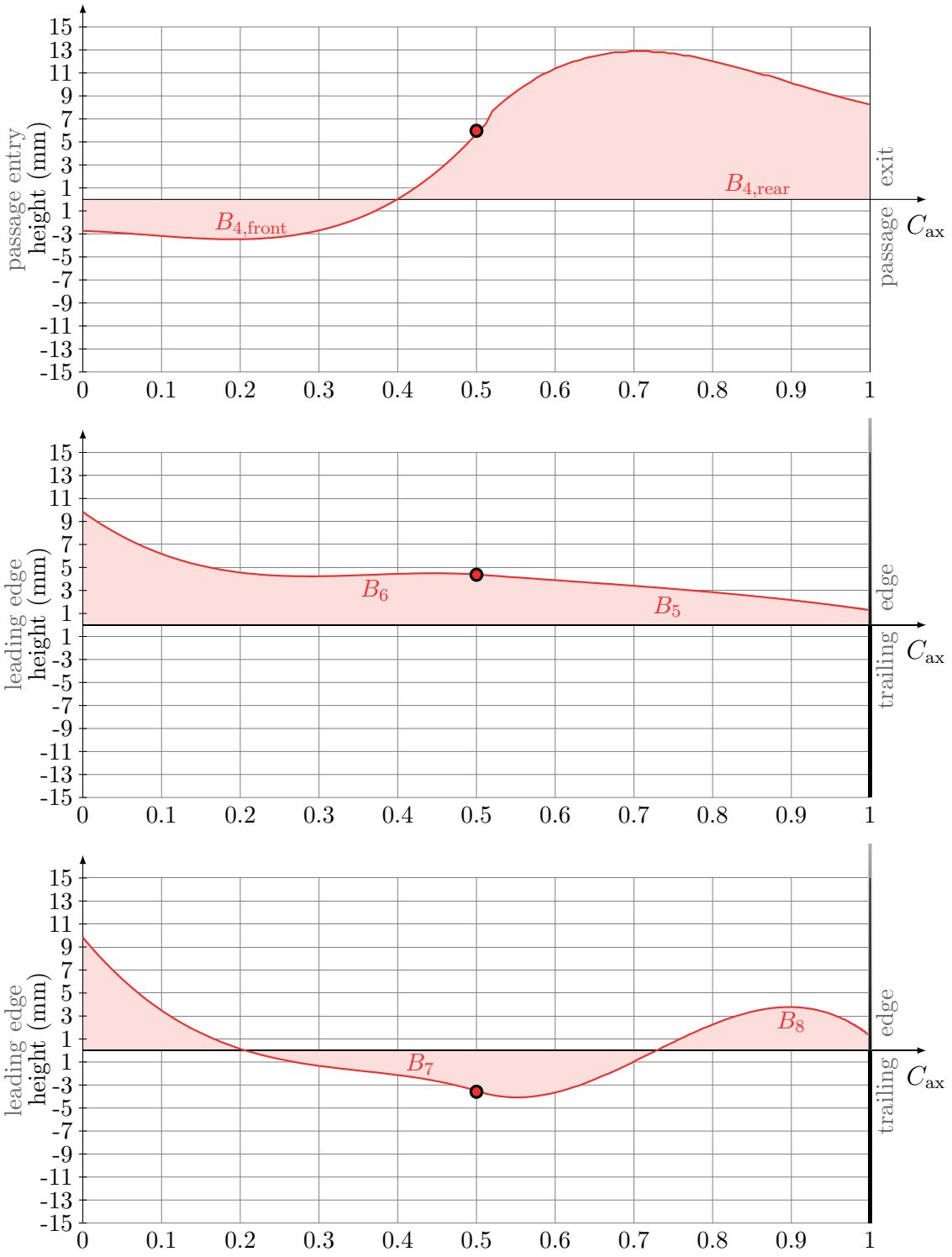

Figure A.8: Bézier splines B_4-B_8 for optimized contour $OC_{BSL,2}$ at $Re_C = 49{,}900$

A.11.2 Average Heat Transfer Coefficients

Table A.8: Heat transfer coefficients area-averaged over endwall segments for optimized contour $OC_{BSL,2}$ at $Re_C = 49{,}900$; values for baseline included for comparison

	Inlet	Transition inlet	Vane passage	Transition outlet	Outlet	Total
$OC_{BSL,2}$	27.54	22.50	25.82	40.45	28.86	27.76
BSL	27.66	21.38	29.76	43.50	36.09	29.80
Difference	−0.43%	5.23%	−13.22%	−7.02%	−20.06%	−6.90%

Table A.9: Heat transfer coefficients area-averaged over endwall segments for optimized contour $OC_{BSL,2}$ design Reynolds number $Re_C = 200{,}000$; values for baseline included for comparison

	Inlet	Transition inlet	Vane passage	Transition outlet	Outlet	Total
$OC_{BSL,2}$	36.26	39.68	52.24	77.78	63.22	47.62
BSL	36.45	37.36	58.48	85.30	72.99	50.49
Difference	−0.52%	6.21%	−10.67%	−8.82%	−13.38%	−5.68%

A.12 Overview of Created Endwall Contours

Name	Type	Goal function	Experimental parameters	Parametrization	Optimization space
Ice contour short cooling length IC_{IFM}	Ice contour	$\dot{S}$ global	$Re_C = 49{,}900$ $\Theta = 12.2$	-	-
Optimized contour global heat transfer OC_{IFM}	Optimized contour	*htc* entire endwall	-	Based on IC_{IFM}	$0 < z < 10$ (in mm)
Optimized contour vane passage heat transfer	Optimized contour	*htc* vane passage	-	Based on ice contour short cooling length at $Re_C = 49{,}900$ and $\Theta = 8.5$	$0 < z < 10$ (in mm)
Ice contour long cooling length	Ice contour	$\dot{S}$ global	$Re_C = 49{,}900$ $\Theta = 12.2$	-	-
Optimized contour from baseline OC_{BSL}	Optimized contour	*htc* vane passage	-	Based on flat endwall	$-5 < z < 5$ (in mm)
Optimized contour from baseline $OC_{BSL,2}$	Optimized contour	*htc* vane passage	-	Based on flat endwall	$-15 < z < 15$ (in mm)

Table A.10: Overview of endwall contours created with the Ice Formation Method and with numerical optimization

Name	$Re_C = 49{,}900$		$Re_C = 200{,}000$		
	htc difference entire endwall	*htc* difference vane passage	*htc* difference entire endwall	*htc* difference vane passage	Difference $C_{\mathrm{p,tot}}$
Ice contour short cooling length $\mathrm{IC_{IFM}}$	**-5.20%**	1.71%	**-9.05%**	2.30%	11.65%
Optimized contour global heat transfer $\mathrm{OC_{IFM}}$	**-8.49%**	1.68%	**-8.85%**	1.74%	7.39%
Optimized contour vane passage heat transfer	1.24%	−2.62%	-	-	-
Ice contour long cooling length	5.52%	33.60%	-	-	-
Optimized contour from baseline $\mathrm{OC_{BSL}}$	−1.20%	**-7.07%**	0.75%	**-6.84%**	3.21%
Optimized contour from baseline with extended optimization space $\mathrm{OC_{BSL,2}}$	−6.90%	**-13.22%**	−5.68%	**-10.67%**	11.81%

Table A.11: Overview of endwall contours created with the Ice Formation Method and with numerical optimization (Continued from page before)

A.13 Publications and Related Work

Parts of the present work have been published in [28], [78], and [81]. Further information on the project, which this work was part of, can be found in contributions to the Research Association for Combustion Engines (Forschungsvereinigung Verbrennungskraftmaschinen e.V., FVV) [27, 79, 80].

Within the framework of the present work, the following student theses emerged:

- Ryusuke Daniel Kambara Martin: Optimization of the flow field around a cars tail; Bachelor Thesis, 2011
- Andreas Grybos: Numerische Untersuchung der Umstrmung verschiedener experimentell erzeugter Heckgeometrien einer Mercedes-Benz E-Klasse; Studienarbeit,2011
- Gabriele Frank: Implementierung und Validierung des SST-Zwei-Gleichungs-Modells nach Menter in OpenFOAM; Diplomarbeit, 2012
- Janosch Brucker: Numerische Untersuchung experimentell erzeugter Seitenwandtopologien mit OpenFOAM; Bachelor Thesis, 2013
- Anton Kierig: Numerische Optimierung der Schaufelseitenwand einer Niederdruckturbinenschaufel; Bachelor Thesis, 2013
- Timon Hitz: Numerical Simulation of Entropy Production in Turbulent Flow Around a Turbine Vane; Diplomarbeit, 2015